2020

Lattice Boltzmann Method For Multiphase Flows With High Density Ratios

Jumaa, Norjan

Lattice Boltzmann Method For Multiphase Flows With High Density Ratios

by

Norjan Hassan Jumaa

A thesis submitted to the University of Plymouth

in partial fulfilment for the degree of

DOCTOR OF PHILOSOPHY

School of Engineering, Computing and Mathematics

July 2020

Dedication

I dedicate this work to my father Hassan Jumma (may Allah rest his soul), without his encouragement and faith in me, I would not have found the motivation to finish my studies.

Acknowledgements

A sincere thank and gratitude to my supervisor Dr David Graham for his dedicated support and patience throughout my studies. Completing this thesis could not have been possible without his guidance. Dr David continuously provided encouragement and was always prepared and enthusiastic to help in any way he could.

I would like to thank all my colleagues, staff and Doctoral college in the school of Engineering, computing and mathematics for all the mental and considerate guidance

My deepest gratitude to my lovely Mother, Brothers (Falah, Ali and Mustafa) and sisters (Guney, Maral, Demet) for their encouraging, supporting and standing by me during my studies.

My unreserved love, thanks, and appreciation must go to my gorgeous family: my husband (Mohammed) and my son (Hassan) who have been very patient, understanding, and inspiring to me throughout this hard journey. I hope the potential success of this research will compensate some of what they have missed.

Additionally, I would like to thank my mother and sisters- in- law for their role in encouraging me to finish this study.

Special thanks are extended to PhD student (Ruaa Wana, Zainab Bu Sinnah, Omar al-Tameemi, Hassan Sdiq, Akeel Noor) for sharing their time and invaluable expertise with me.

I would like to thank the Ministry of Higher Education and Scientific Research (MOHESR) and University of Kirkuk for their support thought my PhD studies.

Norjan Hassan Jumma

Author's Declaration

At no time during the registration for the degree of Doctor of Philosophy has the author been registered for any other University award without prior agreement of the Doctoral College Quality Sub-Committee.
Work submitted for this research degree at university of Plymouth has not formed part of any other degree either at university of Plymouth or at another establishment.

Conferences:

- UK Consortium on Mesoscale Engineering Sciences Workshop (UKCOMES) (12th-13th December 2016).
- Attend the V International Conference on Particle-based Methods. Fundamentals and Applications. Hannover, Germany (PARTICLES) (26-28 September 2017).
- Attend the Society for Underwater Technology Evening Meeting (University of Exeter) (17th January 2018).
- Attend Society for Underwater Technology: South West Evening, Meeting Advances in Marine Measurements, Portland Square Building (Plymouth Lecture Theatre), (Plymouth University) (29 November 2018).

Presentations:

- The British Applied Mathematics Colloquium (BAMC) conference 2018. 26th-29th March 2018, University of St Andrews, Scotland, UK.
- Proceeding of the 5th IAHR Europe Congress — New Challenges in Hydraulic Research and Engineering. Trento, Italy, June 13th-15th, 2018.

- 29th International Conference on the Discrete Simulation of Fluid Dynamics (DSFD 2020) (Viterbo,Italy), Technical Session 14 - Fluid-Structure Interaction - virtual room Palma, 16th- 17th July 2020.

Word count for the main body of this thesis: **63921**

Signed: Norjan Hassan Jumaa

Date: 26/08/2020

Abstract

THIS thesis describes the Lattice Boltzmann Method (LBM) and its application to single and multiphase flows. The LBM algorithm using Single Relaxation Time (SRT) and Multi Relaxation Time (MRT) models are studied. In particular, a new MRT multiphase model is developed, based upon the SRT multiphase model of Banari et al. (2014). A unified LBM approach is used with separate formulations for the phase field, the pressureless Naiver-Stokes (NS) equations and the correction of the pressureless velocity field by solving a Poisson equation.

To validate the current model, computations for various Reynolds numbers (Re) were performed to simulate 2D lid driven cavity flow. Results show excellent comparison with those in the literature. The multiphase model was verified with two fluid Poiseuille flow, static and rising bubbles. The method was also used to simulate 2D single and multiple mode Rayleigh-Taylor instability (RTI). A good comparison between the present numerical results and those in the literature at large Re with high density ratio and various values of surface tension coefficient in single mode and multiple mode RTI are made, respectively.

The multiphase LB model has been extended using MRT collision operator to study various breaking dam problems with both dry and wet bed, expanding the range of the possible density ratios and Re which was impossible with SRT. The simulations show agreement with those in the literature. Moreover, grid convergence was studied using both acoustic and diffusive scaling for standing wave simulations with high density ratios. The use of MRT was found to improve the stability for high density ratio. Results with density ratio up to 1000 at large $Re = 1000$ were obtained using MRT model.

Table of Contents

List of Figures

List of Tables

Chapter 1

Literature review

1.1 Introduction

Numerical modelling of multiphase flows such as free surface flows and multi-component fluid flows due to continuous change in the location of the boundary. Further challenges are related to flows with high Reynolds numbers (Re) or large density ratios (Tryggvason et al. 2001). Many numerical approaches have been improved to solve Navier–Stokes (NS) equations for multiphase fluid flows (Scardovelli & Zaleski 1999). The most commonly used are Level Set Methods (LSM), Volume of Fluid (VOF) method, Mass-Tracking Method, the Smoothed Particle Hydrodynamics (SPH) method and the Lattice Boltzmann Method (LBM) (Osher & Sethian 1988, Hirt & Nichols 1981, Rüde & Thürey 2004, Rothman & Keller 1988). LBM has become more widespread because of high efficiency computations with free surface flow and its ability to solve complex fluid dynamics problems. An addition, this method is relatively straightforward for coding and parallelisation (Yu et al. 2014). A brief explanation of the common free surface method is presented that can be coupled with LBM approaches in section 1.2.

There are various prevalent LBM approaches for multiphase fluid flows. The Rothman–Keller (RK) multiphase lattice gas model is the oldest one that presented the color-gradient model (Rothman & Keller 1988). The Shan–Chen (SC) model describes the

separation of phases produced by the incorporation of an enticing force for the particles (Shan & Chen 1993). Swift et al. (1995, 1996) introduced the free energy (FE) based model a phase separation for one component and two phases in non ideal fluids. The tracking interface model was described by He et al. (1999). Moreover, some LBM multiphase approaches have been combined with computational fluid dynamics (CFD) methods, for instance Xu (2005) introduced the Finite Difference LBM (FDLBM) for binary fluid which were based on discretization of the Boltzmann equation for velocity distribution according to (Sterling & Chen 1996, Succi 2001). A phase-field based model coupled with the LBM and the Finite Volume Method (FVM) to simulate the motion of droplets by control electrowetting as pointed out by Huang et al. (2012). The Front Tracking Finite Difference Method (FTFDM) was proposed by Sankaranarayanan et al. (2003) to study different cases of rising bubble simulation. Lallemand et al. (2007) proposed coupling LBM with a front tracking (FT) method to model the movement of the interface with surface tension for static bubble and capillary waves simulations. A brief review for each of these models is given and then explained the approach that is used in section 1.3.

In order to update the interface, the multiphase flow is simulated by using a governing Navier-Stokes equation with either an advection-diffusion equation which deals with diffusive interface models or advection equation is used with sharp or diffusive interface models (Banari 2014). The interface is determined by capturing an Eulerian method (e.g. LBM) or surface tracking, a Lagrangian method (e.g. SPH) (Ginzburg & Steiner 2003, Contreras et al. 2013). The capturing methods produce a sharp or diffusive interface representation while the interface tracking methods assume a sharp interface. In order to use the appropriate options, the following points must be taken into account when simulating free surface and multiphase problems by dealing with: (1) a capturing or tracking method for representation of interface; (2) a diffusive or sharp interface method; (3) an advection-diffusion or advection equation for updating

the interface between fluids (Banari 2014).

In the sharp interface, the interface region between two fluids was considered as infinitely thin and is given with properties such as surface tension (Anderson & McFadden 1996). The diffuse interface model uses a technique of modelling interface forces as a continuum force. Many authors preferred to use a diffuse rather than a sharp interface model because the former one can be simply propagated through fixed grids while the sharp interface models need adaptive and fitting grids (Jacqmin 1999).

1.2 LBM with a Free Surface

Several LB approaches have been developed for free surface flows. The simulations must distinguish between the region that contains liquid and the region that contains gas. The interface between two fluids (liquid and gas) in the simulation must be found as part of the computation. In a free surface flow, the gas phase has a negligible effect on the liquid phase, so it can be removed from the computations. There are several major approaches to represent the interface of the free surface which can be coupled with LB techniques.

1.2.1 Level Set (LS) Methods

An implicit function $\phi(x, y, t)$ is used to describe the surface representation. The LS methods represent the movement of the implicit surface, which is a contour in the fluid region (Ω) as introduced by Osher & Sethian (1988). The main idea for LSM was a numerical approach for a Hamilton-Jacobi equation to solve the time dependent equations which describe a moving of $\phi(x, y, t)$ (Osher & Fedkiw 2006). The surface can be evaluated by choosing the set of points in which $\phi(\mathbf{x}, t) = c$. The value of these set is a level set of $\phi(\mathbf{x}, t)$. Usually, the zero level set $(\phi(\mathbf{x}, t) = 0)$ is used to describe the points that are located on the interface region Γ. If the value of $\phi(\mathbf{x}, t) > 0$, it

means that **x** is located outside the interface region Γ, otherwise **x** is located inside the interface region Γ (Johansson 2010).

The distinctive feature this approach is represented by computing the curvature (k) of the interface from the divergence $(\nabla.)$ of the unit normal vector $(\mathbf{n})$ which is related to the gradients (∇) of ϕ. The curvature is used to control the smoothness of the interface. This makes the computation of geometric quantities such as normal $(\mathbf{n})$, gradient (∇) and curvature (k) easy and fast. For these reasons, signed distance functions are best represented by using the Eulerian representation (Johansson 2010). The development of $\phi(x)$ is achieved by the solving of an advection equation. As a result, the development of free surface flows can be simulated. The LSM requires a reinitialization step at every time step because of the level set function $\phi(x)$ does not recover the evolution equation at all time steps. However, the loss of mass is one weakness of LSM which impacts upon the accuracy of the interface development (Rüde & Thürey 2004).

To overcome this weakness, the Particle Level Set Method (PLSM) was presented by Enright et al. (2002) to track water surface for fluid flow simulation. The particle corrects in LSM by adding two sets of massless particles, plus and minus particles, which are located close to the interface at $\phi(x) = 0$ (Yu et al. 2014). This correction step is proposed to recover the evolution equation. Consequently, the mass loss can be reduced for the most part. (Yu et al. 2014) suggested a coupled LB and PLSM (LB-PLSM) which is a correction for LSM. They adopted the LB based single-phase free surface (LB-SP) which was presented by Körner et al. (2005) and Thürey et al. (2005) to simulate breaking dam flow. According to Rüde & Thürey (2004), the LS is advected after applying the streaming and collision steps of LBM. The velocity values can be extrapolated by fast marching pass during each time step because the LBM computes only the velocity of the fluid. The fast marching is used to initialize the level set.

1.2.2 Volume of Fluid (VOF) Method

This method was presented by Hirt & Nichols (1981) and was developed from earlier marker and cell (MAC) methods. The first code was based on the volume fraction of fluid ϵ_f that was introduced for NASA by Torrey et al. (1985). Janssen & Krafczyk (2011) presented the implementation of a VOF based algorithm by adding an advection equation for the VOF fill level. The VOF method is used to track the interface region by introducing ϵ_f for a unit cell to represent the fill level of a control volume Ω_{cell}. A fill level of $\epsilon_f = 0.0$ refers to an empty cell (the gas region), while a fill level of $\epsilon_f = 1.0$ refers to the fill inside the liquid region. Gas cells can be separated from liquid cells by a closed interface layer.

In a weakly compressible LB approach, the VOF fill level ϵ is not conserved so that the finite volume method (FVM) is used to discretize the continuity equation and conservation of mass to derive the advection algorithm. According to Janssen & Krafczyk (2011) the flux term $\phi_i(x,t)$ between neighbouring cells can be found from LBM by use of the particle distribution function $f_i(x,t)$. There are several coupling methods to overcome the difficulties when the interface is represented by using the VOF method. Janssen et al. (2010) suggested a new hybrid Fully Non linear Potential Flow (FNPF) and LB (FNPF-LB) approach to model wave breaking. Also, VOF method implemented with LBM to express the flux term in the free surface (Janssen & Krafczyk 2011).

Janssen et al. (2013) presented an extension of a hybrid LBM-VOF model of free surface problems with a MRT collision operator. The free surface was represented by a VOF method and the extended hybrid algorithm was applied to several problems, such as breaking dam, free filling jet and breaking wave during shoaling problems. Janssen & Krafczyk (2010) proposed a VOF method based on LBM to calculate the free surface motion for breaking dam and breaking wave.

1.2.3 Mass Tracking Method

The mass tracking method links directly into the LBM (Rüde & Thürey 2004). This method can be considered as a surface capturing method and includes three steps: calculation of the interface movement, the boundary condition at the interface region and the reinitialization of the cell types (Thürey et al. 2005). The crucial point is to guarantee conservation of mass, since mass transferred to the liquid or mass coming from the liquid always passes through the interface cells in which the total mass is balanced (Körner et al. 2005).

The interface movement in this method is tracked by computing the mass for each cell from the distribution function $f_i(x,t)$. Similar to the VOF method, the movement of the interface is found from computation of the flux between cells. A new set of $f_i(x,t)$ is presented to evaluate the current cell density, and is computed from the fraction of the fluid value ϵ_f whether the interface cell can be filled $(\epsilon_f > 1.0)$ or emptied $(\epsilon_f < 0.0)$ (Thürey & Rüde 2009). The one advantage of the mass tracking method of free LB is the conservation of mass when tracking the interface, but there are difficulties in obtaining smooth curvature of the simulations for a breaking dam (Rüde & Thürey 2004). By contrast, they found the capability of the LSM to resolve thin fluid layers. Also, the surface normals and curvature are easy to compute with LSM. Although, the interface of LSM and VOF method are needed to reconstruct and re-initialize at each step, this can be complicate to perform (Zheng et al. 2006). The disadvantage of the mass tracking method is often incapability to preform interface break-up or collision (Scardovelli & Zaleski 1999).

1.3 LBM with multiphase methods

It is worth mentioning that the multiphase approach was classified approximately to four main LB techniques as shown below.

1.3.1 Color-gradient model

The original Rothman and Keller (RK) model for two-component lattice gas has been presented by Rothman & Keller (1988). This model consists two distribution functions that represent the two-components by red and blue colour fluid. The collision step of the RK model has been improved by adding the perturbation operator and recoloring step that is proposed by (Gunstensen et al. 1991). Thereby, it contains three steps to represent the two component flow which are collision, recoloring and streaming steps. The recoloring step is used to reduce the mixing at the interface (Huang et al. 2013). (Grunau et al. 1993) developed the RK model for the hexagonal lattice in two dimensions (D2Q7) by adding further two variables to the equilibrium distribution function in order to model the flow with various density ratios. He reported that the simulations become unstable with density ratios more than 10. Also, the recoloring step was included in the two-component model that was proposed by Latva-Kokko & Rothman (2005), A further collision term has been added in this model. The RK model for D2Q9 in LBM has been improved by Reis & Phillips (2007). The two-fluid collision step is corrected and the interfacial tension term satisfy the NS equations in Reis & Phillips (2007) model and the density ratio reaches 18.5 with coalescence of bubbles flow. In this model, a free parameter is used to dominate surface tension (Reis & Phillips 2007).

The RK model has been used to simulate high density ratio flows to test Laplace's law of static bubble and rising bubbles (Grunau et al. 1993, Liu et al. 2012). Tölke (2002) found that simulations of bubble flows were stable only for density ratio up to 30, and computed stable simulations of channel flow for density ratio 1 and viscosity ratio up to 100. Leclaire et al. (2012) proposed more improvement in the recolouring step presented by the Latva-Kokko and Rothman model and coupled with the Reis and Phillips model. In the adopted model, the obstruction of the movement called as lattice

pinning was reduced at the interface. He studied simulations of Poiseuille flow with high viscosity ratio up to 10000 and density ratio of the droplet flow is 85 (Leclaire et al. 2012). Huang et al. (2013) claimed the incapability of the RK model, generally, to deal with high density difference of two phase flows and he used BGK approximation scheme. In last years ago, Ba et al. (2016) investigated the density ratios and Reynolds numbers (Re) of a RK type model with a MRT collision operator. They used the density ratio of 1000 for the droplet flow and further implementation was applied to test density ratio for droplet spreading radius with density ratio of 100 and $Re = 500$ and for the Rayleigh-Taylor Instability density ratio reaches 3 with $Re = 256,\ 2048$. One of the disadvantages of RK models was represented by incapability to extend these model for including the thermodynamic phase movements which leads to not satisfy the Galilean invariant quality and unphysical features of the interface for the fluid flows (Shan & Chen 1993).

1.3.2 Shan–Chen (SC) model

This model is the most common multiphase model, firstly proposed by Shan and Chen in 1993 (Shan & Chen 1993). Many researchers used method based on SC model for its simplicity and rely to non-ideal gas equations of state (EOS). This includes two types of SC model, for single component multiphase that is based on an attractive the force between the molecules for lattice points. The phase separated according to the properties of the non-ideal gas for a one chemical element (Sukop 2006).

In general, the difficulties of the classical SC model are represented by the incapability to deal with high density ratios. It was pointed out that the pseudopotential gradient conveniently can be computed for the intermolecular force in SC model to prevent instabilities of the simulations (Márkus & Házi 2008). Yu et al. (2010) improved the SC model which included the same computation of interaction force for the pseudopotential by adopting new MRT-LBM with high density ratio up to 1000. He studied

buoyant rise of a gas bubble in liquid with a low viscosity $Re = 1000$ and high-surface tension in 3D. Sofonea et al. (2004) imposed a flux limiter approach to minimize spurious currents and developed the stability of the simulations for high Re. Raiskinmäki et al. (2000) studied the spreading droplet on a rough surface in 3D. Sankaranarayanan et al. (2002) simulated the rise bubble for different sizes with the action of buoyancy.

The second type of the SC model is known as the multi component multiphase because it contain more than one chemical component that incorporates interaction forces to create a separation between phases. The fluids of this kind of SC models are of major economic and environmental significance because, for example, petroleum is commonly observed to be a mixed with water and because of the existence petroleum with water often appears as reason of ground water impurity (Sofonea et al. 2004). For example, the index for the first component indicates by 0 and the second by 1 in the system. The equilibrium distribution function is calculated in the loop from the combined macroscopic velocity. The SC multi component model was improved according to Shan & Doolen (1995) (SD) model by introducing the new equilibrium velocity to minimize statistical noise that included in Lattice Gas Automata (LGA) due to the insufficiency of the Galilean invariance and calculation of the velocity from the pressure term. Dong et al. (2010) investigated the numerical simulation for the phenomenon of viscous fingering in two phase fluids that moves in a channel according to gravity, using viscosity ratio from 1 to 5.

The traditional SC model was extended according to Benzi et al. (2006) by introducing an analytic derivation of contact angles simulation in the expression of the energy of surface tension between any pair of the liquid, solid, and gas phases. The wall contact angle was implemented suggested by Huang et al. (2007) using SD model for multi component based on SC model. Huang et al. (2015) studied the applications of two chemical component in the porous media flow in 3D. It was claimed that this model generally has limits with high density ratios and kinematic viscosity ratio.

1.3.3 The Free Energy (FE) based model

Swift et al. (1995, 1996) proposed a free energy (FE) based LB model to define a thermodynamically appropriate representation for the D_2Q_7 model. The key concept of this model is constituted by introducing an appropriate equilibrium distribution function f^{eq} constructed on FE system which is derived from the van der Waals equation to include the thermodynamic pressure tensor $P_{\alpha\,\beta}$. It consists of two types of multiphase models which are single and multi component.

In the single component multiphase model for the non ideal gas, Swift et al. (1996) suggested an appropriate equilibrium distribution function with gradient of density that is structured to satisfy the zero, first and second moments constraints. The first term of the second order moments of f^{eq} is formed by the pressure tensor $P_{\alpha\,\beta}$ that is obtained from the FE density (Swift et al. 1996). By applying a Chapman–Enskog expansion, the FE system and the constraints of the moments of f^{eq} with the velocity of the fluid satisfies the hydrodynamic equations. Guo & Shu (2013) pointed out to the meaning of the gradient of the density when it equal to zero $(\delta_\alpha \rho = 0)$ that the hydrodynamic equations leads to the Navier-Stokes equations. The drawback of this models is represented by unsatisfying the Galilean invariance with high density gradient (Swift et al. 1996).

Holdych et al. (1998) developed this model to D_2Q_9 by extending hydrodynamic terms for density gradient in order to adjust Galilean invariance with second order moment. The second order moment of f^{eq} is one of features of the FE base on LB model by comparing with the SC model that incudes first order that leads to the first order velocity moment with using the interaction force. Also, the computation of the surface tension in the FE is simply calculated than the SC model. Hence, the FE model is considered as a successful technique (Guo & Shu 2013).

In the two component multiphase model according to Swift et al. (1996), the first particle distribution functions was used to recover thermodynamic pressure tensor $P_{\alpha\,\beta}$

in the NS equations and the second particle distribution functions used to satisfy the Cahn-Hilliard equation (CH) for capturing the interface in a D_2Q_7 non-ideal fluid flow model. This model is similar to the single component one, but it required to impose two equilibrium distribution functions that enforced the constrains of the moments except with binary density and velocity (Guo & Shu 2013). These models also demand to enforce the new constraints for the particle distribution functions that define the phases for fluid system. The CH equation described by Swift et al. (1996) for the FE approach consisting of the phase separation will be explained in the next section. The thermodynamic pressure tensor $P_{\alpha\,\beta}$ and the chemical potential difference $\Delta\mu$ were produced in this FE models for binary phase fluid systems.

Takada et al. (2000) improved the models based on Swift et al. (1996) to study the rising two bubble simulation in the 3D duct for a two fluid model and investigated the buoyancy under gravity. The simulation of the rising single bubble compared well with the VOF method in 2D. Fakhari & Rahimian (2010) improved numerically the simple model of the FE which satisfied a Galilean invariance from Zheng et al. (2006) is only effective with density matched for two fluid flows.

Inamuro et al. (2004) developed the FE model by combining it with the projection technique to guarantee the continuity equation for the interface with high density ratio. In this model two particle distribution functions (f_i and g_i) are used, the first one represented the phases by using the order parameters according to the phase field model and the second one computed the velocity by absences density. The density in the advection of the equilibrium distribution functions g_i^{eq} which leads to eliminate the pressure gradient for the binary fluid flow. Then they defined the velocity distribution function (h_i) to correct the pressureless velocity from solving the Poisson equation. The value of the order parameters was cut off to determine the density across the interface for the multiphase fluid flow. The implementations were applied in 3D with density ratios 50 for each capillary wave, two droplet collision and coalescence of rising binary bubbles

simulations. In addition, 24 bubbles were simulated with density ratio 1000 with same radius in a square duct (Inamuro et al. 2004). There are various sides of this approach by comparing with the original LBM on account of the neglecting the density that leads to add the viscosity terms to the g_i^{eq} and stress tensor of viscosity in the collision step (Inamuro et al. 2004, Banari et al. 2014).

Recently, Banari et al. (2014) modified this model by using three equilibrium distribution functions (f_i^{eq}, g_i^{eq} and h_i^{eq}) with SRT for order parameters, pressureless velocity and solving Poisson equation to correct the velocity. This technique is distinguished from the model of (Inamuro et al. 2004) by defining slightly different equilibrium distribution functions. The interpolation values for order parameters were used to define the density at the interface. The applications for different density ratios was simulated reached to 1000 with Poiseuille flow and rising bubble, 100 for static bubble, 3 for single Rayleigh-Taylor Instability and the breaking wave was nicely simulated in 2D. Furthermore, he performed the implementations in 3D for droplet impact on a wet surface with density ratio 1000 and $Re = 2000$, and rising bubble with density ratio 1000 and breaking wave with density ratio 855 by coupling with the Large Eddy Simulation (LES) model with LBM. However, obtaining the pressure by Poisson equation from the work of Inamuro *et al.* increases computational costs (Lee & Lin 2005).

Fakhari & Rahimian (2010) modified the FE model for capturing interface using phase field MRT based LB approach. The investigation was applied for different density ratios 1000, 100, 5 , 5 and 5 which corresponding to the simulations of the Laplace law for stationary bubbles, Capillary wave, rising bubble , splashing of the droplet on a wet surface and falling droplet under gravity, respectively. The Reynolds numbers reach to 1000 with droplet splashing. One of the disadvantage of this model occurs from the computation used to correct the pressure by solving the Poisson equation (Fakhari & Rahimian 2010).

1.3.4 He Chen Zhang (HCZ) model

He et al. (1999) suggested new LB multiphase fluid flows approach for simulating single component by modelling and tracking the interface due to coupling of molecular interactions. The HCZ model introduced two distribution functions, the first one for tracking the velocity and the pressure and second one for the density in the incompressible flow. The interface is tracked by using the index function for the binary fluid flows. The NS equations are recovered from the distribution functions of pressure and the distribution functions for computing the density satisfy the CH equation for tracking the interface. Single mode Rayleigh–Taylor Instability (RTI) was simulated with the range of various density ratio reached to 19 at the high Re was 2048 and the density ratio multi mode RTI results was 3 at $Re = 4096$, so the limitation of this method is represented by incapability with high density ratio (He et al. 1999).

Lee & Lin (2005) introduced an equivalent technique to that presented by He et al. (1999) for computing the pressure and momentum using discretization the Boltzmann equation of multiphase fluid flows. The intermolecular forces for non-ideal gas was separated to hydrodynamic pressure, thermodynamic pressure, and surface tension force to develop the stability of simulations with high density ratios (Lee & Lin 2005). Banari et al. (2014) avoided instabilities due to thermodynamic pressure by adding a stress to the potential term. It was applied various forms for the discretization of derivatives such as first and second order with central, biased or mixed difference approximation in order to obtain smooth variation of the pressure at the interface. This model was validated by comparing the computations result of 1D advection equation with the analytic solution, testing a Laplace law for the stationary droplet and studying the droplet oscillation in D_3Q_{19} lattice model with density ratios 1000 (Lee & Lin 2005). They simulated droplet splashing phenomenon on a thin liquid with various Re in 3D and the largest Re reach to 500. (Banari et al. 2014) used the same concepts of the latter

approach with dividing of the intermolecular forces.

Usually, most of researchers pointed out different sources of the problems and incapability for simulating the high density ratios with multiphase LBM techniques. Proper discretization of density and pressure gradients is required (Inamuro et al. 2004, Guo & Shu 2013). Some of researchers justify to choose the appropriate equation of state to perform the large density ratios of the multiphase flows (He & Doolen 2002, Fakhari & Rahimian 2010). Moreover, d'Humieres (2002) proposed the MRT in the collision step to improve the stability of the computations when used the low viscosity. The MRT leads to simulate the multiphase flows with the high Reynolds numbers (Re) (Yu et al. 2010, Fakhari & Lee 2013).

Chen et al. (2019) proposed virtual lattices layer to realize the no-slip boundary condition for multiphase flow and improved the interface capturing model using the Cahn-Hilliard equation to cope with the problem of the high density ratio between various phases. They studied bubble growth and departure from two orifices is simulated. Furthermore, the various forces effects tested on the deformation and interaction between growing of bubbles from orifices of the same or various sizes (Chen et al. 2019).

(Liang et al. 2019) introduced the model of axisymmetric multiphase LB flows depend on the Allen-Cahn equation by phase-field theory. They used two distribution functions for solving fluid interface and hydrodynamic properties. Moreover, they improved the numerical stability by applying MRT model. The simulations of static droplet with density ratio up to 1000 is studied. In addition, the simulations of oscillation of a viscous droplet, breakup of a liquid thread, and bubble rising in a continuous phase implemented with density ratio up to 100 with axisymmetric Allen-Cahn equation and hydrodynamic equations.

1.4 Objective of the study

The main purpose of this thesis is to develop the multiphase Lattice boltzmann (LB) approach for high density and viscosity ratios with large Reynolds number (Re). In particular, a new Multi Relaxation Time (MRT) is used to develop multiphase LB model, based upon the Single Relaxation Time (SRT) multiphase model of Banari et al. (2014). A unified LBM approach is used with separate formulations for the phase field, the pressureless Naiver-Stokes (NS) equations and the correction of the pressureless velocity field by solving a Poisson equation. To validate the current model, simulations of two dimensional lid driven cavity flow were performed with different Re. The results of the present study are compared with the numerical results from Ghia et al. (1982) in both SRT and MRT models in single phase LB.

Subsequently, the multiphase model in SRT collision operator was verified to study the L_2-norm errors with different density and viscosity ratios for two-fluid Poiseuille flow are compared results in current study with the analytic solutions at different lattice grids. the n static and rising bubbles. Moreover, simulations of static bubble flow with different surface tension coefficient values and various radius are compared with theoretical (Laplace law). The gravitational acceleration force for single rising bubble was studied and compared with Sun & Tao (2010).

In addition, this work is used to test the validation of multiphase LBM with large Re at high density ratio. This method was studied with SRT to simulate two dimensional single and multiple mode Rayleigh-Taylor Instability (RTI). Numerical simulations are compared with those in the literature for large Re and high density ratio in single mode RTI and various values of surface tension coefficient in multiple mode RTI.

The principal contribution of this thesis is the development of multiphase model of Banari et al. (2014) using MRT. This extended the range of values of density ratios and Reynolds numbers (Re) for which successful computations could be completed.

So this work included the extension of the multiphase method using new MRT collision operator to study various breaking dam problems for both dry and wet bed expanding the range of the possible density ratios and Reynolds number which was impossible with SRT.

Finally, the contribution of standing wave simulations with density ratio up to 1000 at large Re was studied using both acoustic and diffusive scaling with various grid resolutions.

1.5 Outline of the study

This thesis describes the LBM and its application for single and multi phase flows. It is organized as follow:

In chapter 2, the derivation of Lattice boltzmann Method (LBM) and the relation to the Navier-Stokes equations according to (Guo & Shu 2013) are introduced. The description of the boundary conditions are presented in this chapter. The algorithm of LBM with Single Relaxation Time (SRT) and Multi Relaxation Time (MRT) are illustrated.

The Lattice Boltzmann (LB) computations for various Reynolds numbers (Re) with different resolutions to simulate 2D lid driven cavity flow with on grid and half way bounce back boundary conditions are performed. The minimum stream function value and the total kinetic energy per unit volume are used for the convergence to the steady state with SRT and MRT. Subsequently, the numerical results for the velocity profiles and streamlines are compared with the numerical results from Ghia et al. (1982) in chapter 3.

In chapter 4, a review of multiphase flows with high density and viscosity ratios for LBM in SRT collision operator is introduced. A similar model to Banari et al. (2014) is used so that the motion of the interface between fluids is modelled by solving the Cahn-Hilliard (CH) equation with LBM. A unified LBM approach with separate for-

mulations for the phase field, the pressureless Navier-Stokes (NS) equations and the correction of the pressureless velocity field by solving a Poisson equation are used. The Chapman-Enskog expansion for multiphase LB approach to recovery the pressureless Navier-Stokes equations, the Cahn-Hilliard equation and solving pressure Poisson equation are introduced.

In chapter 5, the multiphase flows with different density and viscosity ratios at various Reynolds number Re are implemented to simulate two fluid Poiseuille flow. The L_2-norm errors for the simulations in current study are compared with the analytic solutions for different lattice grids. Subsequently, comparison between the theoretical (Laplace law) and current computations for the static bubble flow is made with different surface tension coefficient values and various radius with density ratio 100. In addition, the terminal shapes for three cases of rising bubble with density ratio 100 are formed and comparisons are made with Sun & Tao (2010) results.

In chapter 6, the multiphase LB technique with Single Relaxation Time (SRT) is used to simulate 2D single and multiple mode Rayleigh-Taylor Instability (RTI). The results are compared with those of He et al. (1999) for single mode RTI at various Reynolds number Re with small density ratios. The investigations at high density and viscosity ratios are performed then the results are compared with Ren et al. (2016) and Fakhari et al. (2017) results for the evolution of interface in a multiple mode RTI at different values of surface tension coefficient, Re and various resolutions. Subsequently, the simulations for $\frac{\acute{\rho}_1}{\acute{\rho}_2} = 100$ and 1000 with high $Re = 5000$ are obtained in this study. Moreover, the evolution of interface in a multiple mode RTI with different values of surface tension coefficient (σ_{12}) is examined. The convergence with σ_{12} and grid resolution for the positions of bubble and spike are investigated. The result of He et al. (1999) for the average density profiles across the depth in multiple mode RTI with various σ_{12} at dimensionless time is compared with the result in this work.

In chapter 7, the multiphase of LBM is developed using Multi relaxation Time

(MRT) to simulate breaking dam problems with different of cases. The result of the simulation for both leading edge position and water column height results are compared with Martin et al. (1952). Moreover, the simulation of second case of the dam break problems with Colagrossi & Landrini (2003) is investigated. Furthermore, the investigation of breaking dam problems of this work with wet bed is presented and a comparison with Badarch et al. (2016) is made. The MRT mode is implemented with breaking dam problems especially for density ratio up to 1000 and high Re numbers which was impossible with SRT model.

In chapter 8, the multiphase flows for LBM with different density ratio are developed to study two scaling cases with standing wave simulations firstly, with different density ratios, based on Hodges et al. (1996), Zhao et al. (2013), and secondly, for small density ratio and both high and low viscosity standing waves, Buick & Greated (1998). The results with high density ratio up to 1000 at large $Re = 1000$ was obtained using the MRT model in this study. Finally, the summary of the project and the future work are introduced in chapter 9.

1.6 Summary

In this chapter, various LB approach of free surface and multiphase fluid flows have been introduced. Because of the highly accurate simulations of LBM with free surface flow and its capability to deal with complex fluid dynamics such as the multiphase flow problems, its use has become more prevalent. The most common free surface techniques that are coupled with LBM are methods such as LSM, VOF and the mass tracking method and their applications is mentioned. Furthermore, the development of several significant multiphase LB approaches which are represented by color-gradient model, SC model, FE based model and HCZ model are given. In meantime, on their stable implementation for different application with respect to the values of density ratio, viscosity ratio and Re for each model are focused.

Chapter 2

Lattice Boltzmann Method (LBM)

2.1 Introduction

The Lattice Boltzmann Method (LBM) is a relatively new scheme in computational fluid dynamics (CFD). It has evolved into an alternative numerical technique for simulating fluid flow and modelling physical problems. The fundamental conception of the LBM is based upon the kinetic theory that describes molecular dynamics. In the incompressible limit of the LBM recovers the Navier-Stokes (NS) equations. It can make computations more efficient for fluid flows that contain complex boundaries and interfacial flow phenomena. Consequentially, explicitly of LBM that tend to easy coding and parallelisation (Chen & Doolen 1998). In additional, the most important advantages of the LBM represented by using equation of state to obtain the pressure which is inhibit expensive computations by solving Poisson equation to get pressure. Finally, the LBM is useful approach for modeling single phase and multiphase fluid flows (Shan & Chen 1993, Swift et al. 1995, Chen & Doolen 1998, Rothman et al. 1998, He et al. 1999, Guo & Shu 2013).

This chapter is organized as follows. Section 2.2 give the discretization of Boltzmann equation which is satisfy the Navier-Stokes equations. Section 2.3 describes the boundary conditions is used. Sections 2.4 - 2.5 illustrate the algorithm of LBM with Single Relaxation Time (SRT) and Multiple Relaxation Time (MRT). Finally, summary

of this chapter is given in Section 2.6.

2.2 Discretized Boltzmann equation

Macroscopic variables such as pressure (p) and velocity (**u**) in the CFD method are usually found from solving the Navier-Stokes equations (Mei et al. 1999). There are several techniques from which the Lattice Boltzmann equation (LBE) can be acquired. Historically, LBE originated from Lattice Gas Automata (LGA) (Frisch et al. 1986). On the other hand, it can be shown that using a special discretization of the continuous Boltzmann equation, LBE can also be obtained (He & Luo 1997*b*, Guo & Shu 2013). For simplicity and to preserve generality, the Boltzmann equation with the Bhatnagar–Gross–Krook (BGK) approximation (or Single Relaxation Time) is used (He & Luo 1997*b*). The Boltzmann BGK equation can be written as an ordinary differential equation:

$$D_t f + \frac{1}{\tau_c} f = \frac{1}{\tau_c} f^{(0)}, \tag{2.2.1}$$

where $D_t = \partial_t + \mathbf{c}.\nabla$ is the time derivative along the characteristic line **c**, $f = f(x, \mathbf{c}, t)$ is the single particle probability distribution function, τ_c is the relaxation time and $f^{(0)}$ is the Boltzmann-Maxwellian distribution function in dimension (D) of the space,

$$f^{(0)} = \frac{\rho}{(\,2\pi RT)^{D/2}} \exp\left[\frac{-(\mathbf{c}-\mathbf{u})^2}{2RT}\right], \tag{2.2.2}$$

where R is the ideal gas constant, and $\rho, \mathbf{u}$ and T are the macroscopic density, velocity, and temperature, respectively. The macroscopic variables $\rho, \mathbf{u}$ and T are the moments

of the distribution function f with respect to the velocity $\mathbf{c}$:

$$\rho = \int f \, dc = \int f^{(0)} \, dc, \tag{2.2.3}$$

$$\rho \, \mathbf{u} = \int \mathbf{c} \, f \, dc = \int \mathbf{c} \, f^{(0)} \, dc, \tag{2.2.4}$$

$$\rho \, \epsilon = \frac{1}{2} \int (\mathbf{c} - \mathbf{u})^2 \, f \, dc = \frac{1}{2} \int (\mathbf{c} - \mathbf{u})^2 \, f^{(0)} \, dc, \tag{2.2.5}$$

where $\epsilon = D_o RT/2 = D_o N_A K_B T/2$, and $D_o, N_A,$ and K_B are the number of degrees of a particle, Avogadro's number, and the Boltzmann constant, respectively. An assumption of Chapman-Enskog (Harris 2004) is applied in eqs.(2.2.3, 2.2.4 and 2.2.5). The terms of the integral that are included a $'$ refers to the post collision distributions operator and vice-versa with pre-collision. From eq.(2.2.1)

$$\frac{d}{dt} f + \frac{1}{\tau_c} f = \frac{1}{\tau_c} f^{(0)},$$

$$e^{(t/\tau_c)} \frac{d}{dt} f + \frac{1}{\tau_c} e^{(t/\tau_c)} f = \frac{1}{\tau_c} e^{(t/\tau_c)} f^{(0)},$$

$$\frac{d}{dt} (e^{(t/\tau_c)} \, f) = \frac{1}{\tau_c} e^{(t'/\tau_c)} f^{(0)}(x, \mathbf{c}, t') dt',$$

$$\frac{d}{dt} (e^{(t/\tau_c)} \, f) = \frac{d}{dt} \frac{1}{\tau_c} \int_0^t e^{(t'/\tau_c)} f^{(0)}(x, \mathbf{c}, t') dt'. \tag{2.2.6}$$

by integrating both side of eq.(2.2.6) from t to $t + \Delta t$, yields

$$[\, e^{(t/\tau_c)} \, f \,]_t^{t+\Delta t} = \frac{1}{\tau_c} \int_t^{t+\Delta t} e^{(t'/\tau_c)} f^{(0)}(x, \mathbf{c}, t') dt',$$

$$e^{(t+\Delta t)/\tau_c} f(x+\mathbf{c}\Delta t, \mathbf{c}, t+\Delta t) - e^{(t/\tau_c)}\, f(x,\mathbf{c},t) = \frac{1}{\tau_c}\int_t^{t+\Delta t} e^{(t^{'}/\tau_c)} f^{(0)}(x,\mathbf{c},t^{'})dt^{'},$$

Thus

$$f(x+\mathbf{c}\,\Delta t, \mathbf{c}, t+\Delta t) = \frac{1}{\tau_c} e^{-(\Delta t/\tau_c)} \int_0^{\Delta t} e^{(t^{'}/\tau_c)} f^{(0)}(x+\mathbf{c}t, \mathbf{c}, t+t^{'})\, dt^{'} + e^{-(\Delta t/\tau_c)}\, f(x,\mathbf{c},t)\,. \qquad (2.2.7)$$

By assuming the $f^{(0)}$ is smooth enough on the interval $(0, \Delta t)$ which is made the linear approximation:

$$f^{(0)}(x+\mathbf{c}t, \mathbf{c}, t+t^{'}) = \left[1 - \frac{(t+t^{'})-t}{\Delta t}\right] f^{(0)}(x,\mathbf{c},t) + \left[\frac{(t+t^{'})-t}{\Delta t}\right] f^{(0)}(x+\mathbf{c}\Delta t, \mathbf{c}, t+\Delta t),$$

so

$$f^{(0)}(x+\mathbf{c}t, \mathbf{c}, t+t^{'}) = \left[1 - \frac{t^{'}}{\Delta t}\right] f^{(0)}(x,\mathbf{c},t) + \frac{t^{'}}{\Delta t} f^{(0)}(x+\mathbf{c}\Delta t, \mathbf{c}, t+\Delta t)\,. \quad (2.2.8)$$

Now substitute eq.(2.2.8) in to the first term of the right hand side of eq.(2.2.7) and finding the integration as

$$\frac{1}{\tau_c} e^{-(\Delta t/\tau_c)} \int_0^{\Delta t} e^{(t^{'}/\tau_c)} f^{(0)}(x+\mathbf{c}t, \mathbf{c}, t+t^{'})dt^{'} = \frac{1}{\tau_c} e^{-(\Delta t/\tau_c)} \int_0^{\Delta t} e^{(t^{'}/\tau_c)} \{ f^{(0)}(x,\mathbf{c},t) - \frac{t^{'}}{\Delta t} f^{(0)}(x,\mathbf{c},t) + \frac{t^{'}}{\Delta t} f^{(0)}(x+\mathbf{c}\Delta t, \mathbf{c}, t+\Delta t)\, \} dt^{'}\,.$$

The right hand side of the above equation has three terms these evaluated as follows:
First term:

$$\int_0^{\Delta t} e^{(t^{'}/\tau_c)}\, f^{(0)}(x,\mathbf{c},t)dt^{'} = \tau_c\, (e^{(\Delta t/\tau_c)} - 1)\, f^{(0)}(x,\mathbf{c},t)\,.$$

Second term:

$$\int_0^{\Delta t} -e^{(t^{'}/\tau_c)}\frac{t^{'}}{\Delta t} f^{(0)}(x,\mathbf{c},t)dt^{'} = -\tau_c\, e^{(\Delta t/\tau_c)}\, f^{(0)}(x,\mathbf{c},t) + \frac{\tau_c^2}{\Delta t}\, e^{(\Delta t/\tau_c)}\, f^{(0)}(x,\mathbf{c},t) - \frac{\tau_c^2}{\Delta t}\, f^{(0)}(x,\mathbf{c},t)\,.$$

Third term:

$$\int_0^{\Delta t} e^{(t^{'}/\tau_c)}\frac{t^{'}}{\Delta t} f^{(0)}(x+\mathbf{c}\Delta t,\mathbf{c},t+\Delta t)dt^{'} = \tau_c\, e^{(\Delta t/\tau_c)} f^{(0)}(x+\mathbf{c}\Delta t,\mathbf{c},t+\Delta t) - \frac{\tau_c^2}{\Delta t}\, e^{(\Delta t/\tau_c)}\, f^{(0)}(x+\mathbf{c}\Delta t,\mathbf{c},t+\Delta t) + \frac{\tau_c^2}{\Delta t}\, f^{(0)}(x+\mathbf{c}\Delta t,\mathbf{c},t+\Delta t).$$

Now from these three terms the eq.(2.2.7) was obtained

$$f(x+\mathbf{c}\Delta t,\mathbf{c},t+\Delta t) - f(x,\mathbf{c},t) = (e^{-(\Delta t/\tau_c)} - 1)\, \left[\, f(x,\mathbf{c},t) - f^{(0)}(x,\mathbf{c},t)\right] + (1 + \frac{\tau_c}{\Delta t}(e^{-(\Delta t/\tau_c)} - 1))\, \left[\, f^{(0)}(x+\mathbf{c}\Delta t,\mathbf{c},t+\Delta t) - f^{(0)}(x,\mathbf{c},t)\right]. \quad (2.2.9)$$

Applying Taylor Series to expand $e^{-(\Delta t/\tau_c)}$ on the eq.(2.2.9) and removing terms of second order $O((\Delta t)^2)$ as

$$f(x+\mathbf{c}\Delta t,\mathbf{c},t+\Delta t) - f(x,\mathbf{c},t) = -\frac{1}{\tau}\left[f(x,\mathbf{c},t) - f^{(0)}(x,\mathbf{c},t)\right]\,, \quad (2.2.10)$$

where $\tau = \frac{\tau_c}{\Delta t}$ is the dimensionless relaxation time (in the unit of Δt). Therefore, eq.(2.2.10) is accurate to the first order in Δt and is the evolution equation of the dis-

tribution function f with discrete time. Now to calculate the hydrodynamic moment (ρ, $\rho\mathbf{u}$ and $\rho\epsilon$) in eqs.(2.2.3, 2.2.4 and 2.2.5), the appropriate discretization in momentum space $\mathbf{c}$ needs to be achieved. Then the integration in the momentum space (with weight function $f^{(0)}$) can be approximated by quadrature up to any required degree of accuracy,

$$\int \Psi(\mathbf{c}) f^{(0)}(x, \mathbf{c}, t)\, d\mathbf{c} = \sum_i W_i\, \Psi(\mathbf{c}_i)\, f^{(0)}(x, \mathbf{c}_i, t), \tag{2.2.11}$$

where $\Psi(\mathbf{c})$ is a polynomial in $\mathbf{c}$, W_i is weight coefficient of the quadrature, and $\mathbf{c}_i$ is the discrete velocity set. Then the hydrodynamic moments of eqs.(2.2.3), (2.2.4) and (2.2.5) are computed by

$$\rho = \sum_i f_i = \sum_i f_i^{(0)}, \tag{2.2.12}$$

$$\rho\, \mathbf{u} = \sum_i \mathbf{c}_i\, f_i = \sum_i \mathbf{c}_i\, f_i^{(0)}, \tag{2.2.13}$$

$$\rho\, \epsilon = \frac{1}{2} \sum_i (\mathbf{c}_i - \mathbf{u})^2\, f_i = \frac{1}{2} \sum_i (\mathbf{c}_i - \mathbf{u})^2\, f_i^{(0)}, \tag{2.2.14}$$

where

$$f_i \equiv f_i(x, t) \equiv \sum_i W_i\, f(x, \mathbf{c}_i, t), \tag{2.2.15}$$

$$f_i^{(0)} \equiv f_i^{(0)}(x, t) \equiv \sum_i W_i\, f^{(0)}(x, \mathbf{c}_i, t). \tag{2.2.16}$$

The equilibrium distribution function $f^{(0)}$ can be expanded by using second order Taylor expansion:

$$f^{(0)} = \frac{\rho}{(\,2\pi RT)^{D/2}}\ \exp\left[\frac{-c^2}{2\ RT}\right]\ \exp\left[\frac{(\mathbf{c}.\mathbf{u})}{RT} - \frac{u^2}{2RT}\right]$$

$$= \frac{\rho}{(\,2\pi RT)^{D/2}}\ \exp\left[\frac{-c^2}{2\ RT}\right]\ \left[1 + \frac{(\mathbf{c}.\mathbf{u})}{RT} + \frac{(\mathbf{c}.\mathbf{u})^2}{2\ (RT)^2} - \frac{u^2}{2RT}\right] + O(\mathbf{u}^3),$$

where $u = |\mathbf{u}|$. Finally

$$f^{(eq)} = \frac{\rho}{(\,2\pi RT)^{D/2}}\ \exp\left[\frac{-c^2}{2\ RT}\right]\ \left[1 + \frac{(\mathbf{c}.\mathbf{u})}{RT} + \frac{(\mathbf{c}.\mathbf{u})^2}{2\ (RT)^2} - \frac{u^2}{2RT}\right]. \qquad (2.2.17)$$

To recover the Navier-Stokes equations for low Mach number $\frac{|\mathbf{u}|}{\sqrt{R\,T}} \ll 1$, the following moment integral must be found exactly:

$$\int \mathbf{c}^k\ f_i^{(eq)} d\mathbf{c}\ ,\ 0\ \leq\ k\ \leq\ 3. \qquad (2.2.18)$$

This integral can be obtained by Gaussian-type quadrature (He & Luo 1997*b*, Shan & He 1998):

$$I = \int \exp\left[\frac{-c^2}{2\ RT}\right] \Psi(\mathbf{c})\ d\mathbf{c} = \sum_i\ W_i\ \exp\left[\frac{-c^2}{2\ RT}\right]\ \Psi(\mathbf{c}_i). \qquad (2.2.19)$$

To derive the velocity, here nine-bit (nine direction of the distribution function) in LBE model is used. According to the polynomial function $\Psi(\mathbf{c})$, the system of Cartesian coordinate can be written as

$$\Psi_{m,n}(\mathbf{c}) = c_x^m\ c_y^n, \qquad (2.2.20)$$

where c_x and c_y are the x and y components of $\mathbf{c}$. From the integral of eq.(2.2.19):

$$I = (\sqrt{2R\,T})^{m+n+2}\; I_m\; I_n, \tag{2.2.21}$$

where

$$I_m = \int_{-\infty}^{+\infty} \exp(-C^2)\; C^m\; dC,\; C = \frac{c}{\sqrt{2R\,T}}, \tag{2.2.22}$$

and mth order moment of weight function $\exp(-C^2)$ on the real axis. To find I_m to derive the 9-bit LBE model the third order Hermite formula (Shan et al. 2006) is used:

$$I_m = \sum_{i=1}^{3} \omega_i\; C_i^m. \tag{2.2.23}$$

The three values of (C_i) and the corresponding weights (ω_i) of the quadrature are

$$\begin{aligned} &C_1 = -\sqrt{\frac{3}{2}},\; C_2 = 0,\; C_3 = \sqrt{\frac{3}{2}}, \\ &\omega_1 = \frac{\sqrt{\pi}}{6},\; \omega_2 = \frac{\sqrt{2\,\pi}}{3},\; \omega_3 = \frac{\sqrt{\pi}}{6}. \end{aligned} \tag{2.2.24}$$

Then, eq.(2.2.21) becomes (He & Luo 1997*a*)

$$I = 2R\,T\left[\omega_2^2\;\Psi(0) + \sum_{i=1}^{4}\;\omega_1\;\omega_2\Psi(\mathbf{c}_i) + \;\sum_{i=5}^{8}\omega_1^2\;\;\Psi(\mathbf{c}_i)\right], \tag{2.2.25}$$

where $\mathbf{c}_i$ is zero velocity vector for $i = 0$. Then by discretizing the momentum space with nine-discrete velocities $\mathbf{c}_i,\; i = 0, 1, \cdots, 8$. The nine-bit LBE model is discretized into a square lattice space with lattice constant $\frac{\Delta x}{\Delta t} = \sqrt{3\,R\,T} = c$ or $R\,T = c_s^2 = \frac{c}{3}$, where c_s is the speed of sound of the model. From eqs.(2.2.19) and (2.2.25):

$$W_i = 2\,\pi R\,T\;\exp\left(\frac{c_i^2}{2R\,T}\right)\;\omega_i, \tag{2.2.26}$$

where

$$\omega_i = \begin{cases} \frac{4}{9}, & \text{for } i = 0, \text{the rest vector,} \\ \frac{1}{9}, & \text{for } i = 1, 2, 3, 4, \text{the short vectors,} \\ \frac{1}{36}, & \text{for } i = 5, 6, 7, 8, \text{the long vectors .} \end{cases} \tag{2.2.27}$$

These weights are essential to compute the equilibrium distribution function of the nine-bit LBE model.

$$\begin{aligned} f_i^{eq} &= \rho\, \omega_i\, f_i^{eq}(x, \mathbf{c}_i, t) \\ &= \rho\, \omega_i \left[1 + \frac{3\,(\mathbf{c}_i.\mathbf{u})}{c^2} + \frac{9\,(\mathbf{c}_i.\mathbf{u})^2}{2c^4} - \frac{3\,u^2}{2c^2} \right], \end{aligned} \tag{2.2.28}$$

where the D_2Q_9 model has nine lattice velocities in two dimensions, represented by $c_i(x, y)$ in the x and y directions as shown in next subsection and defined as follows

$$c_i = \begin{cases} (0, 0), & \text{for } i = 0, \\ c(\cos((i-1)\frac{\pi}{4}), \sin((i-1)\frac{\pi}{4})), & \text{for } i = 1, 2, 3, 4, \\ c\sqrt{2}(\cos((i-1)\frac{\pi}{4}), \sin((i-1)\frac{\pi}{4})), & \text{for } i = 5, 6, 7, 8. \end{cases} \tag{2.2.29}$$

Then by Gaussian-type quadrature (He & Luo 1997*b*, Li-shi 2000), the moments can be found in the discretized momentum space. Form the eq.(2.2.10), the Lattice Boltzmann BGK equation is obtained

$$f_i(x + \mathbf{c}_i\Delta t, t + \Delta t) - \ f_i(x, t) = -\frac{1}{\tau}\left[f_i(x, t) - f_i^{(eq)}(x, t) \right]. \tag{2.2.30}$$

2.2.1 Lattice Arrangements

The domain of the simulation in the LB technique must be divided into a lattice arrangement. Each point on the lattice has discretized distribution function in specific directions. The lattice arrangement is represented by D_nQ_m, where n is the number of the physical dimension of the problem and m is the number of the direction on the distribution function. Figure(2.1) illustrates different lattice models as D_1Q_2, D_1Q_3 and D_2Q_9 (Guo & Shu 2013).

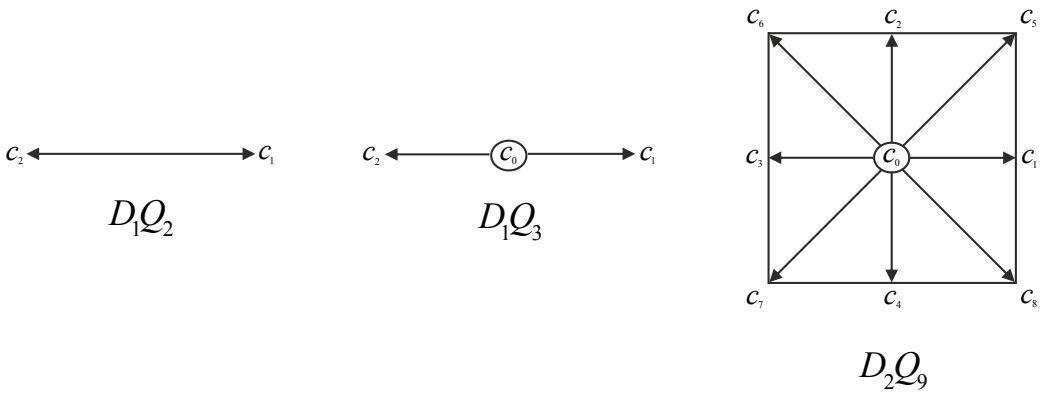

Figure 2.1: Lattice arrangements for 1-D and 2-D.

For simplicity, the D_2Q_9 (two-dimension and nine-velocity) lattice structure which is most practical and is explained in this study. it is successful to simulate two dimensional fluid flow problems.

2.2.2 Streaming and Collision steps

The LBM consists of two steps: collision and streaming. The left hand side of the LBGK eq. (2.2.30) represents streaming step so that after one time step particles move in direction c_i to the nearby of lattice node at $x + c_i\Delta t$, for example the distribution functions (df) $f_1, f_2, f_3, f_4, f_5, f_6, f_7$ and f_8 at (i, j) are moved to $f_1(i+1, j)$, $f_2(i, j+1)$, $f_3(i-1, j)$, $f_4(i, j-1)$, $f_5(i+1, j+1)$, $f_6(i-1, j+1)$, $f_7(i-1, j-1)$ and $f_8(i+1, j-1)$ respectively, but the df at the rest velocity (c_0) stays at the same node as shown in Figure

(2.2). On the other hand, the right hand side of eq. (2.2.30) of LBE represents the collision operator which is updating these particles distribution functions (pdf).

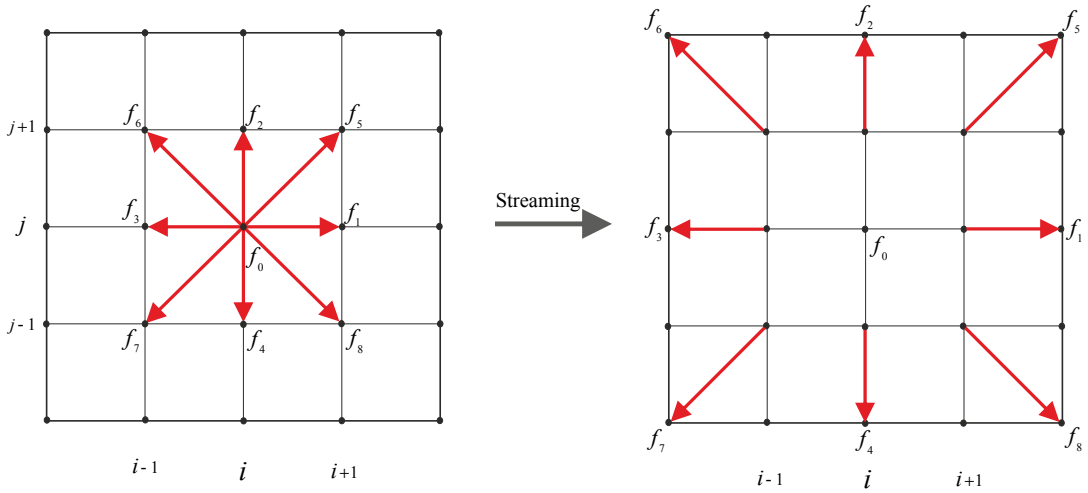

Figure 2.2: The streaming step of LBM

2.2.3 From Lattice Boltzmann Equation to the Navier-Stokes Equations

This section shows that by a multi-scale Chapman-Enskog expansion derivation of the macroscopic Navier-Stokes equations from using the LBGK equation (2.2.30) for the D_2Q_9 model (Guo & Shu 2013, Viggen 2009). Expanding the distribution function $f_i(x,t)$ about the function $f_i^0(x,t)$ as follows

$$f_i = f_i^0 + \varepsilon f_i^1 + \varepsilon^2 f_i^2 + \dots . \tag{2.2.31}$$

For the multi-scale expansion the two time scale and one spatial scale are introduced as

$$\partial_t = \varepsilon \partial_{to} + \varepsilon^2 \partial_{t1}, \tag{2.2.32}$$

$$\partial_\alpha = \varepsilon \partial_{\alpha o}, \tag{2.2.33}$$

where ε is the Knudsen number, which is the ratio between the mean free path and the microscopic length scale, and ∂_t and ∂_α are derivatives with respect to time and space, respectively. ∂_{to} represents the time scale for the fast advection, while ∂_{t1} is the slow diffusive scale. By starting with the second order Taylor series expanding the lattice BGK (LBGK) equation (2.2.30), to get

$$(\partial_t + c_{i\alpha}\partial_\alpha)\, f_i + \frac{\Delta t}{2}(\partial_t^2 + 2\partial_t\, c_{i\alpha}\partial_\alpha + c_{i\alpha}c_{i\alpha}\partial_\alpha\partial_\alpha)\, f_i + O(\partial^3 f_i) = -\frac{1}{\tau\, \Delta t}\left[f_i(x,t) - f_i^{(eq)}(x,t)\right], \tag{2.2.34}$$

where the first and second terms of eq.(2.2.34) represent the first and second order of expansion, respectively. Inserting eqs.(2.2.31), (2.2.32) and (2.2.33) into eq.(2.2.34), yields

$$(\varepsilon\partial_{to}+\varepsilon^2\partial_{t1}+\varepsilon c_{i\alpha}\partial_{\alpha o})(f_i^{(0)}-\varepsilon f_i^{(1)}) + \frac{\Delta t}{2}(\varepsilon^2\partial_t^2+2(\varepsilon\partial_{to}+\varepsilon^2\partial_{t1})\varepsilon c_{i\alpha}\partial_{\alpha o} + \varepsilon^2\, c_{i\alpha}c_{i\alpha}\partial_{\alpha o}\partial_{\alpha o})\,(f_i^{(0)} - \varepsilon f_i^{(1)}) = -\frac{1}{\tau\, \Delta t}((f_i^{(0)} + \varepsilon f_i^{(1)} + \varepsilon^2 f_i^{(2)}) - f_i^{(eq)}).$$

Equating the coefficients of each order ε, at zero order ε^0 is obtained:

$$f_i^{(0)} = f_i^{(eq)}, \tag{2.2.35}$$

at first order ε^1:

$$(\partial_{to} + c_{i\alpha}\partial_{\alpha o})\, f_i^{(0)} = -\frac{1}{\tau\, \Delta t} f_i^{(1)}, \tag{2.2.36}$$

and at second order ε^2:

$$\partial_{t1} f_i^{(0)} + (\partial_{to} + c_{i\alpha}\partial_{\alpha o})\, f_i^{(1)} + \frac{\Delta t}{2}(\partial_{to}^2 + 2\partial_{to} c_{i\alpha}\partial_{\alpha o} + c_{i\alpha}c_{i\alpha}\partial_{\alpha o}\partial_{\alpha o})\, f_i^{(0)} = \frac{-f_i^{(2)}}{\tau\Delta t}. \tag{2.2.37}$$

Eq. (2.2.37) can be written as follows

$$\partial_{t1}\, f_i^{(0)} + (\partial_{to} + c_{i\alpha}\partial_{\alpha o})\, f_i^{(1)} + \frac{\Delta t}{2}(\partial_{to} + c_{i\alpha}\partial_{\alpha o})^2\, f_i^{(0)} = -\frac{1}{\tau\, \Delta t} f_i^{(2)}. \tag{2.2.38}$$

Substituting eq.(2.2.36) into eq.(2.2.38), reads

$$\partial_{t1}\, f_i^{(0)} + (\partial_{to} + c_{i\alpha}\partial_{\alpha o})\, f_i^{(1)} - \frac{\Delta t}{2\,\tau\, \Delta t}(\partial_{to} + c_{i\alpha}\partial_{\alpha o})\, f_i^{(1)} = -\frac{1}{\tau\, \Delta t} f_i^{(2)}. \tag{2.2.39}$$

Rewriting eq. (2.2.39) as follows

$$\partial_{t1}\, f_i^{(0)} + \left[1 - \frac{1}{2\,\tau}\right]\, (\partial_{to} + c_{i\alpha}\partial_{\alpha o})\, f_i^{(1)} = -\frac{1}{\tau\, \Delta t} f_i^{(2)}. \tag{2.2.40}$$

The zeroth and first moments of the distribution function and the zeroth and first moments of the equilibrium distribution function are defined as follow

$$\rho = \sum_i f_i = \sum_i f_i^{(eq)}\ ,\ \rho\mathbf{u} = \sum_i c_i f_i = \sum_i c_i f_i^{(eq)}. \tag{2.2.41}$$

From eq. (2.2.35) and eq. (2.2.41):

$$\sum_i f_i^{(n)} = 0 \quad \text{and} \quad \sum_i c_i f_i^{(n)} = 0 \quad \text{for} \quad n > 0. \tag{2.2.42}$$

Now, by taking the zero order moment of eq. (2.2.36):

$$\sum_i \partial_{to}\, f_i^{(0)} + \sum_i c_{i\alpha}\partial_{\alpha o}\, f_i^{(0)} = \sum_i -\frac{1}{\tau\, \Delta t} f_i^{(1)},$$

so

$$\partial_{to} \sum_i\, f_i^{(0)} + \partial_{\alpha o} \sum_i c_{i\alpha}\, f_i^{(0)} = -\frac{1}{\tau\, \Delta t} \sum_i f_i^{(1)},$$

and

$$\partial_{to}\,\rho + \partial_{\alpha o}\,(\rho u_\alpha) = 0. \tag{2.2.43}$$

The second order moment of eq. (2.2.36) yields

$$\sum_i \partial_{to} c_{i\alpha}\; f_i^{(0)} + \sum_i c_{i\alpha}c_{i\beta}\partial_{\alpha o}\; f_i^{(0)} = \sum_i -\frac{1}{\tau\;\Delta t} c_{i\alpha} f_i^{(1)},$$

so

$$\partial_{to}\sum_i c_{i\alpha}\; f_i^{(0)} + \partial_{\alpha o}\sum_i c_{i\alpha}c_{i\beta}\; f_i^{(0)} = -\frac{1}{\tau\;\Delta t}\sum_i c_{i\alpha} f_i^{(1)},$$

and finally,

$$\partial_{to}\,(\rho u_\alpha) + \partial_{\alpha o}\,\pi^{(0)}_{\alpha\beta} = 0. \tag{2.2.44}$$

Eqs. (2.2.43) and (2.2.44) are mass and momentum conservation equations at order ε. The properties of the generalized lattice tensor (Guo & Shu 2013) for D_2Q_9 are used:

$$\begin{aligned}
&\sum_i w_i c_{i\alpha} = \sum_i w_i c_{i\alpha}c_{i\beta}c_{i\gamma} = \sum_i w_i c_{i\alpha}c_{i\beta}c_{i\gamma}c_{i\delta}c_{i\theta} = 0,\\
&\sum_i w_i c_{i\alpha}c_{i\beta} = c_s^2\delta_{\alpha\beta}\,, \sum_i w_i c_{i\alpha}c_{i\beta}c_{i\gamma}c_{i\delta}c_{i\theta} = c_s^4(\delta_{\alpha\beta}\delta_{\gamma\delta}+\delta_{\alpha\gamma}\delta_{\beta\delta}+\delta_{\alpha\delta}\delta_{\beta\gamma}).
\end{aligned} \tag{2.2.45}$$

Now, by multiplying equation (2.2.35) by $c_{i\alpha}c_{i\beta}$ and taking summation over i to give the zero-order momentum flux tensor $\pi^{(0)}_{\alpha\beta}$:

$$
\begin{aligned}
\pi^{(0)}_{\alpha\beta} &= \sum_i c_{i\alpha} c_{i\beta}\, f^{(0)}_i \\
&= \sum_i c_{i\alpha} c_{i\beta}\, f^{(eq)}_i \\
&= \sum_i c_{i\alpha} c_{i\beta}\, \rho \left[1 + \frac{c_i.\mathbf{u}}{c_s^2} + \frac{(c_i.\mathbf{u})^2}{2\, c_s^4} - \frac{u^2}{2\, c_s^2}\right] \\
&= \sum_i c_{i\alpha} c_{i\beta}\, w_i\, \rho + \frac{\rho}{c_s^2} \sum_i c_{i\alpha} c_{i\beta} c_{i\gamma}\, w_i\, u_\gamma \; + \frac{\rho}{2\, c_s^4} \sum_i c_{i\alpha} c_{i\beta} c_{i\gamma} c_{i\delta}\, w_i\, u_\gamma\, u_\delta \\
&- \frac{\rho}{2\, c_s^2} \sum_i c_{i\alpha} c_{i\beta}\, w_i\, u_\gamma\, u_\gamma \\
&= \rho\, c_s^2\, \delta_{\alpha\beta} + \frac{\rho}{2} \left[\delta_{\alpha\beta}\, \delta_{\gamma\delta}\, u_\gamma\, u_\delta + \delta_{\alpha\gamma}\, \delta_{\beta\delta}\, u_\gamma\, u_\delta + \delta_{\alpha\delta}\, \delta_{\beta\gamma}\, u_\gamma\, u_\delta\right] - \frac{\rho}{2}\, \delta_{\alpha\beta} u_\gamma\, u_\gamma \\
&= \rho\, c_s^2\, \delta_{\alpha\beta} + \rho\, u_\alpha\, u_\beta.
\end{aligned}
$$

Thus

$$
\pi^{(0)}_{\alpha\beta} = p\, \delta_{\alpha\beta} + \rho\, u_\alpha\, u_\beta, \tag{2.2.46}
$$

where $\pi^{(0)}_{\alpha\beta}$ known as second moment of equilibrium function or zero-order momentum flux tensor, with $p = \rho\, c_s^2$ where c_s is speed of sound $c_s = c/\sqrt{3}$ and $c = \Delta x/\Delta t$. The zero and first order moments of eq. (2.2.40) yield the following order moment:

$$
\sum_i \partial_{t1}\, f^{(0)}_i + \sum_i \left[1 - \frac{1}{2\,\tau}\right]\, (\partial_{to} + c_{i\alpha}\partial_{\alpha o})\, f^{(1)}_i = \sum_i -\frac{1}{\tau\, \Delta t} f^{(2)}_i,
$$

$$
\partial_{t1} \sum_i\, f^{(0)}_i + \left[1 - \frac{1}{2\,\tau}\right]\, (\partial_{to} + c_{i\alpha}\partial_{\alpha o}) \sum_i\, f^{(1)}_i = -\frac{1}{\tau\, \Delta t} \sum_i f^{(2)}_i,
$$

thus

$$\partial_{t1}\,\rho = 0, \tag{2.2.47}$$

and the first order moment:

$$\sum_i c_{i\alpha}\partial_{t1}\,f_i^{(0)} + \sum_i c_{i\alpha}\left[1-\frac{1}{2\,\tau}\right]\,(\partial_{to}+c_{i\beta}\partial_{\alpha o})\,f_i^{(1)} = -\sum_i c_{i\alpha}\frac{1}{\tau\,\Delta t}f_i^{(2)},$$

$$\partial_{t1}\sum_i c_{i\alpha}\,f_i^{(0)} + \left[1-\frac{1}{2\,\tau}\right]\,(\partial_{to}\,\sum_i c_{i\alpha}\,f_i^{(1)} + \partial_{\alpha o}\sum_i c_{i\alpha}c_{i\beta}\,f_i^{(1)}) = 0,$$

and

$$\partial_{t1}(\rho u_\alpha) + \left[1-\frac{1}{2\,\tau}\right]\,\partial_{\alpha o}\,\pi_{\alpha\beta}^{(1)} = 0, \tag{2.2.48}$$

where $\pi_{\alpha\beta}^{(1)} = \sum_i c_{i\alpha}c_{i\beta}\,f_i^{(1)}$. Eqs. (2.2.47) and (2.2.48) are the conservation equations at order of ε^2. In order to find $\pi_{\alpha\beta}^{(1)}$, the eq. (2.2.36) multiply by $c_{i\alpha}c_{i\beta}$ and take the summation over i:

$$\begin{aligned}-\frac{1}{\tau\,\Delta t}\sum_i c_{i\alpha}c_{i\beta}\,f_i^{(1)} &= \partial_{to}\sum_i c_{i\alpha}c_{i\beta}\,f_i^{(0)}\;+\partial_{\gamma o}\sum_i c_{i\alpha}c_{i\beta}c_{i\gamma}\,f_i^{(0)}\;,\\ &= \partial_{to}\pi_{\alpha\beta}^{(0)}\;+\partial_{\gamma o}P_{\alpha\beta\gamma}.\end{aligned} \tag{2.2.49}$$

Also, to evaluate $P_{\alpha\beta\gamma}\;=\sum_i c_{i\alpha}c_{i\beta}c_{i\gamma}\,f_i^{(0)}$, the eq. (2.2.36) multiply by $c_{i\alpha}c_{i\beta}c_{i\gamma}$ and take the summation over i:

$$
\begin{aligned}
P_{\alpha\beta\gamma} &= \sum_i c_{i\alpha}c_{i\beta}c_{i\gamma}\ f_i^{(0)} \\
&= \sum_i c_{i\alpha}c_{i\beta}c_{i\gamma}\ \rho\left[1+\frac{c_i.\mathbf{u}}{c_s^2}+\frac{(c_i.\mathbf{u})^2}{2\ c_s^4}-\frac{u^2}{2\ c_s^2}\right] \\
&= \sum_i c_{i\alpha}c_{i\beta}c_{i\gamma}w_i\rho+\frac{\rho}{c_s^2}\sum_i c_{i\alpha}c_{i\beta}c_{i\gamma}c_{i\delta}\ w_i\ u_\delta+\frac{\rho}{2\ c_s^4}\sum_i c_{i\alpha}c_{i\beta}c_{i\gamma}c_{i\delta}c_{i\theta}\ w_i\ u_\delta\ u_\theta \\
&- \frac{\rho}{2\ c_s^2}\sum_i c_{i\alpha}c_{i\beta}c_{i\gamma}\ w_i\ u_\delta\ u_\delta \\
&= \rho\ c_s^2\left[\delta_{\alpha\beta}\ \delta_{\gamma\delta}\ u_\delta+\delta_{\alpha\gamma}\ \delta_{\beta\delta}\ u_\delta+\delta_{\alpha\delta}\ \delta_{\beta\gamma}\ u_\delta\right],
\end{aligned}
$$

then

$$
P_{\alpha\beta\gamma}\ = \rho\ c_s^2\ \left[\ u_\alpha\delta_{\beta\gamma}+u_\beta\delta_{\alpha\gamma}+\ u_\gamma\delta_{\alpha\beta}\ \right]. \tag{2.2.50}
$$

Substituting eqs. (2.2.46) and (2.2.50) into eq. (2.2.49), yields

$$
\begin{aligned}
-\frac{1}{\tau\Delta t}\sum_i c_{i\alpha}c_{i\beta}\ f_i^{(1)} &= \partial_{to}(p\ \delta_{\alpha\beta}+\rho\ u_\alpha\ u_\beta)+\partial_{\gamma o}\left[c_s^2\rho(u_\alpha\delta_{\beta\gamma}+u_\beta\delta_{\alpha\gamma}+u_\gamma\delta_{\alpha\beta})\right] \\
&= \partial_{to}(c_s^2\ \rho)\ \delta_{\alpha\beta}\ +\ \partial_{to}(\rho u_\alpha u_\beta)+\partial_{\beta o}(c_s^2\ \rho\ u_\alpha)+\partial_{\alpha o}(c_s^2\ \rho\ u_\beta) \\
&+ \partial_{\gamma o}(c_s^2\ \rho\ u_\gamma)\delta_{\alpha\beta} \\
&= c_s^2\left[\partial_{to}\ \rho+\partial_{\gamma o}(\rho\ u_\gamma)\right]\ \delta_{\alpha\beta}\ +\rho u_\alpha\partial_{to}\ u_\beta+u_\beta\ \partial_{to}\ (\rho u_\alpha) \\
&+ c_s^2\ \rho\partial_{\beta o}u_\alpha+\ u_\alpha\ \partial_{\beta o}c_s^2\ \rho\ +\ c_s^2\ \rho\partial_{\alpha o}u_\beta+\ u_\beta\ \partial_{\alpha o}\ c_s^2\ \rho\,,
\end{aligned}
$$

thus

$$
\begin{aligned}
-\frac{1}{\tau\Delta t}\sum_i c_{i\alpha}c_{i\beta}\ f_i^{(1)} =& c_s^2\left[\partial_{to}\rho+\partial_{\gamma o}(\rho\ u_\gamma)\right]\delta_{\alpha\beta}+u_\beta\left[\partial_{to}(\rho u_\alpha)+\partial_{\alpha o}p\right] \\
&+ u_\alpha\left[\rho\partial_{to}\ u_\beta+\partial_{\beta o}p\right]+c_s^2\rho\left[\partial_{\alpha o}u_\beta+\partial_{\beta o}u_\alpha\right].
\end{aligned} \tag{2.2.51}
$$

In order to evaluate the time derivatives $\partial_{to}\rho$, $\partial_{to}(\rho u_\alpha)$ and $\rho\partial_{to}\,(u_\beta)$, by rewriting the eqs. (2.2.43) and (2.2.44) on the first order of ε read

$$\partial_{to}\,\rho + \partial_{\gamma o}\,(\rho u_\gamma) = 0, \tag{2.2.52}$$

$$\partial_{to}\,(\rho u_\alpha) + \partial_{\gamma o}\,\pi^{(0)}_{\alpha\gamma} = 0, \tag{2.2.53}$$

from eqs. (2.2.52) and (2.2.53):

$$\partial_{to}\,\rho = -\partial_{\gamma o}\,(\rho u_\gamma)\,, \tag{2.2.54}$$

and

$$\partial_{to}\,(\rho u_\alpha) = -\partial_{\gamma o}\,\pi^{(0)}_{\alpha\gamma} = -\partial_{\gamma o}\,(p\,\delta_{\alpha\gamma} + \rho\,u_\alpha\,u_\gamma),$$

$$\partial_{to}\,(\rho u_\alpha) = -\partial_{\alpha o}\,p - \partial_{\gamma o}(\rho u_\alpha\,u_\gamma)\,, \tag{2.2.55}$$

$$\partial_{to}\,(\rho u_\alpha) = -\partial_{\alpha o}\,p - \rho u_\gamma\,\partial_{\gamma o}\,u_\alpha - \,u_\alpha\,\partial_{\gamma o}(\rho u_\gamma). \tag{2.2.56}$$

The $\partial_{to}\,(\rho u_\alpha)$ can be written as

$$\partial_{to}\,(\rho u_\alpha) = \rho\partial_{to}u_\alpha + u_\alpha\,\partial_{to}\rho, \tag{2.2.57}$$

Substituting eqs. (2.2.54) and (2.2.56) on the second term and the left hand side of equations (2.2.57), read

$$-\partial_{\alpha o}\,p - \rho u_\gamma\,\partial_{\gamma o}\,u_\alpha - \,u_\alpha\,\partial_{\gamma o}(\rho u_\gamma) = \rho\partial_{to}u_\alpha + u_\alpha\,(-\partial_{\gamma o}\,(\rho u_\gamma)),$$

and

$$\rho\partial_{to}u_\alpha = -\partial_{\alpha o}\, p - \rho u_\gamma\, \partial_{\gamma o}\, u_\alpha. \tag{2.2.58}$$

By using the same technique, yields

$$\rho\partial_{to}u_\beta = -\partial_{\beta o}\, p - \rho u_\gamma\, \partial_{\gamma o}\, u_\beta. \tag{2.2.59}$$

Now, by substituting eqs. (2.2.54), (2.2.55) and (2.2.59) into eq. (2.2.51), yield

$$\begin{aligned}-\frac{1}{\tau\Delta t}\sum_i c_{i\alpha}c_{i\beta}f_i^{(1)} = c_s^2\,[-\partial_{\gamma o}(\rho\, u_\gamma)+\partial_{\gamma o}(\rho\, u_\gamma)]\delta_{\alpha\beta}+u_\beta\,[-\partial_{\alpha o}\, p - \partial_{\gamma o}(\rho u_\alpha\, u_\gamma)+\partial_{\alpha o}p]\\ + u_\alpha\,[-\partial_{\beta o}\, p - \rho u_\gamma\, \partial_{\gamma o}\, u_\beta + \partial_{\beta o}p] + c_s^2\rho\,[\partial_{\alpha o}u_\beta + \partial_{\beta o}u_\alpha]\\ = c_s^2\rho\,[\partial_{\alpha o}u_\beta + \partial_{\beta o}u_\alpha] - \partial_{\gamma o}(\rho u_\alpha\, u_\beta\, u_\gamma),\end{aligned}$$

and

$$-\frac{1}{\tau\ \Delta t}\sum_i c_{i\alpha}c_{i\beta}\ f_i^{(1)} = c_s^2\rho\,[\partial_{\alpha o}u_\beta + \partial_{\beta o}u_\alpha] - O(Ma)^3, \tag{2.2.60}$$

where $Ma = \frac{|\mathbf{u}|}{c_s}$ is Mach number. After neglecting the term $O(Ma)^3$ the eq. (2.2.60) become as follow

$$\pi_{\alpha\beta}^{(1)} = -\,\tau\Delta t\, p\, c_s^2\,[\partial_{\alpha o}u_\beta + \partial_{\beta o}u_\alpha]\,, \tag{2.2.61}$$

combining the mass and momentum conservation equations on ε and ε^2 scales, the continuity equation is obtained from eq.(2.2.32) as

$$\begin{aligned}\partial_t\ \rho &= \varepsilon\partial_{to}\ \rho + \varepsilon^2\partial_{t1}\ \rho,\\ &= \varepsilon\partial_{to}\ \rho = -\varepsilon\partial_{\alpha o}(\rho u_\alpha) = -\partial_\alpha(\rho u_\alpha),\end{aligned}$$

so

$$\partial_t\ \rho + \partial_\alpha(\rho u_\alpha) = 0, \tag{2.2.62}$$

and

$$\begin{aligned}\partial_t\ (\rho u_\alpha) &= \varepsilon\partial_{to}\ (\rho u_\alpha) + \varepsilon^2\partial_{t1}\ (\rho u_\alpha),\\ &= -\varepsilon\partial_{\alpha o}\ \pi^{(0)}_{\alpha\beta} - \varepsilon^2\left[1 - \frac{1}{2\,\tau}\right]\ \partial_{\alpha o}\ \pi^{(1)}_{\alpha\beta}.\end{aligned}$$

By using eqs. (2.2.46), (2.2.61) and (2.2.33), yield

$$\partial_t\ (\rho u_\alpha) + \partial_\beta\ p + \partial_\alpha(\rho\ u_\alpha\ u_\beta) = \partial_\alpha\ c_s^2\left[1 - \frac{1}{2\,\tau}\right]\ \tau\Delta t\ \rho(\partial_\alpha u_\beta + \partial_\alpha u_\beta^T),$$

so

$$\partial_t\ (\rho u_\alpha) + \partial_\alpha(\rho\ u_\alpha\ u_\beta) = -\partial_\beta\ p + \partial_\alpha\ \nu\rho\left[(\partial_\alpha u_\beta + \partial_\alpha u_\beta^T)\right]. \tag{2.2.63}$$

By the tensor notation:

$$\partial_t\ \rho + \nabla.(\rho u) = 0, \tag{2.2.64}$$

$$\partial_t\ (\rho u) + \nabla.(\rho\ u\ u) = -\nabla\ p + \nabla.\ \left[\nu\rho(\nabla u_\beta + \nabla u_\beta^T)\right], \tag{2.2.65}$$

where ν is kinematic viscosity given by

$$\nu = c_s^2 \left[\tau - \frac{1}{2}\right] \Delta t, \tag{2.2.66}$$

and $c_s = c/\sqrt{3}$ where $c = \Delta x/\Delta t$ for the D_2Q_9 model. For small Mach number (Ma), the density variation can be removable and assuming incompressibility in order to arrive to the Navier-Stokes (NS) equations as

$$\nabla.\mathbf{u} = 0, \tag{2.2.67}$$

$$\partial_t \, \mathbf{u} + \mathbf{u}.\nabla\mathbf{u} = -\frac{1}{\rho}\nabla \, p + \nu\nabla^2\mathbf{u}. \tag{2.2.68}$$

2.3 Boundary Conditions

Boundary conditions play an important part in describing fluid flow behaviour in LB simulations. There are several types such as periodic, bounce back, pressure or velocity flow boundary condition, open boundary condition, symmetry condition and so on. In this study, the bounce back method is used for moving or stationary boundaries. Also, it is known as no-slip boundary condition which the fluid velocity is zero at the boundary (He et al. 1997, Zhao 2008). Nodes located in the wall are known as solid nodes and otherwise are called fluid nodes. Therefore the solid boundary is located on solid nodes or between solid and the fluid nodes according to the bounce back technique. Here two different types of bounce back conditions will be discussed: on-grid and half-way bounce back.

2.3.1 On-Grid Bounce Back Method

This method is applied when the solid boundary lies exactly on solid nodes and it is easy to implement (Viggen 2009). This bounce back boundary can be explained

using Figure (2.3). After the streaming process the particle distribution function (pdf) move toward to the solid boundary from the fluid nodes. These particles hit the solid boundary and are reflected to the fluid nodes. The particles that stream to the boundary are known distribution functions (dfs) while the other particles which reflect to the fluid node are unknown quantities at these solid boundaries. For example, at the left boundary the known dfs f_3, f_6 and f_7 are found from streaming step. The unknown values f_5, f_1 and f_8 are found from the opposite directions of the known dfs.

$$f_5 = f_7,\ f_1 = f_3 \ \text{ and } \ f_8 = f_6.$$

Some authors such as (He et al. 1997, Succi 2001) claimed that the on-grid method can be compute the unknown dfs at the boundary with second order accuracy.

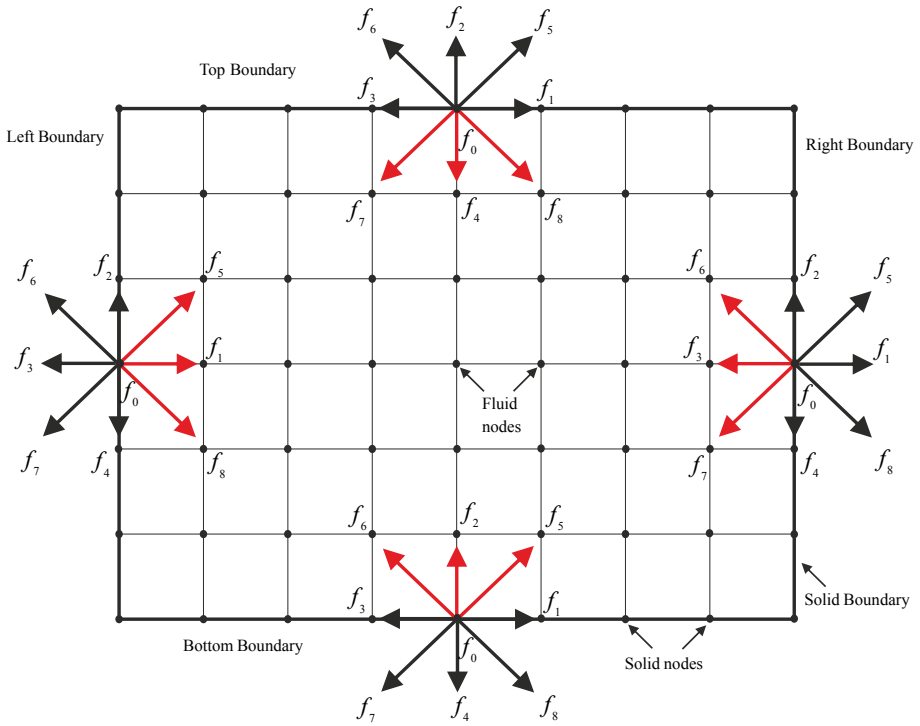

Figure 2.3: The on-grid bounce back method.

2.3.2 Half-way Bounce Back Method

The half-way bounce back requires that the solid boundary is located between fluid and solid nodes. Figure (2.4) shows the half-way method. The collision process is not performed at the solid node and it gives second order accurate according to He et al. (1997), Succi (2001). The bounce back is used to evaluate the three unknown dfs f_2, f_5 and f_6 at bottom boundary. Then,

$$f_2 = f_4,\ f_5 = f_7 \text{ and } f_6 = f_8.$$

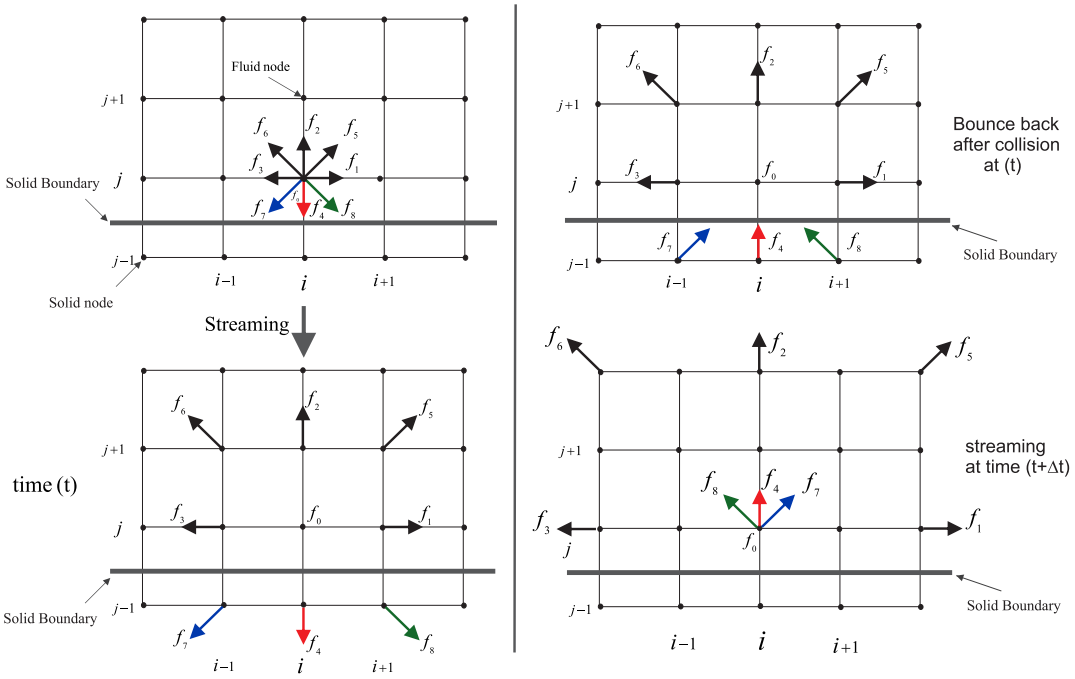

Figure 2.4: The half-way bounce back method.

2.3.3 Specification On-grid of Velocity at Corners

This specific boundary condition is based on a conception of the on-grid bounce back method. By assuming the velocity $\mathbf{u} = (u_x, u_y)$ is given $(u_x = 0, u_y = 0)$ at the corners and density specified (Zou & He 1997). For example, post streaming the dfs f_1, f_2, f_5, f_6 and f_8 are unknown values and ρ is assumed to be a known value at left

bottom corner. the bounce back method is used to evaluate f_1, f_2 and f_5 (those that have red colours in Figure (2.5)). The conservation of mass and momentum are applied for this boundary (Succi 2001).

$$f_1 = f_3, f_2 = f_4 \; and \; f_5 = f_7. \tag{2.3.1}$$

Thereafter, the values of f_6,f_8 (they have blue colours) and ρ pressure (density) need to determine. From the conservation of mass:

$$\rho = \sum_i f_i = f_0 + f_1 + f_2 + f_3 + f_4 + f_5 + f_6 + f_7 + f_8. \tag{2.3.2}$$

By the conservation of momentum, yields

$$\rho u_x = (f_1 + f_5 + f_8) - (f_3 + f_6 + f_7), \tag{2.3.3}$$

$$\rho u_y = (f_2 + f_5 + f_6) - (f_4 + f_7 + f_8), \tag{2.3.4}$$

From eqs.(2.3.1), (2.3.3) and (2.3.4), the value of $f_6 = f_8$ is obtained then by substitution this quantity into eq.(2.3.2) as

$$\rho = f_0 + f_1 + f_2 + f_3 + f_4 + f_5 + f_7 + 2f_8.$$

Thus

$$f_8 = \frac{1}{2}(\rho - f_0 - f_1 - f_2 - f_3 - f_4 - f_5 - f_7),$$

similar procedure can be used in the other corners.

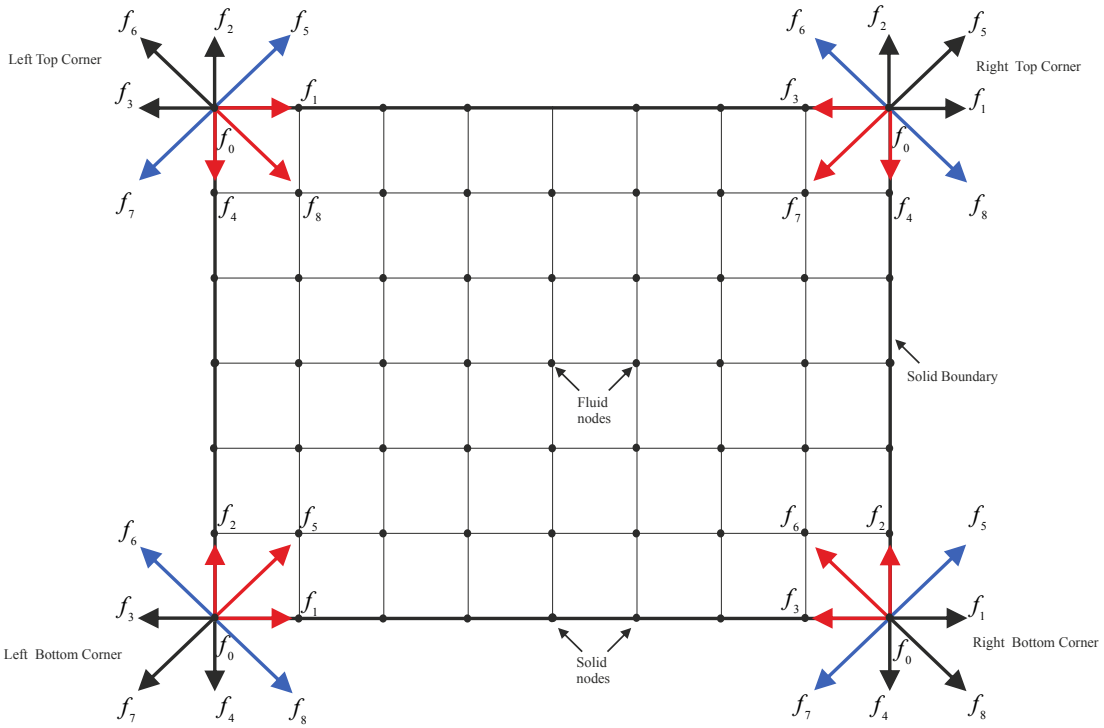

Figure 2.5: Specification on-grid of Velocity at Corners.

2.3.4 Periodic boundary conditions

Periodic boundary conditions are the simplest boundary conditions. It is useful for modeling bulk system because it tend to reduce finite size edge effects, such as flow in along channel driven by a pressure or an external force density (body force) in the x-direction. In the D_2Q_9 model, the periodic boundary is applied in the left and right boundaries as illustrated in Figure (2.6). For example, the known particles $f_6,\ f_3$ and f_7 leaving the left boundary (at $i = 0$) then they re-entered to the unknown particles $f_6,\ f_3$ and f_7 in the right boundary (at $i = lx$) and vice-versa. It can be

written as

$$f_k(0, j, t) = f_k(lx, j, t)\,, \quad k = 1, 5, 8, \;\; j = 0,\, 1,\, 2, \ldots,\, ly.$$

$$f_k(lx, j, t) = f_k(0, j, t)\,, \quad k = 3, 6, 7, \;\; j = 0,\, 1,\, 2, \ldots,\, ly.$$

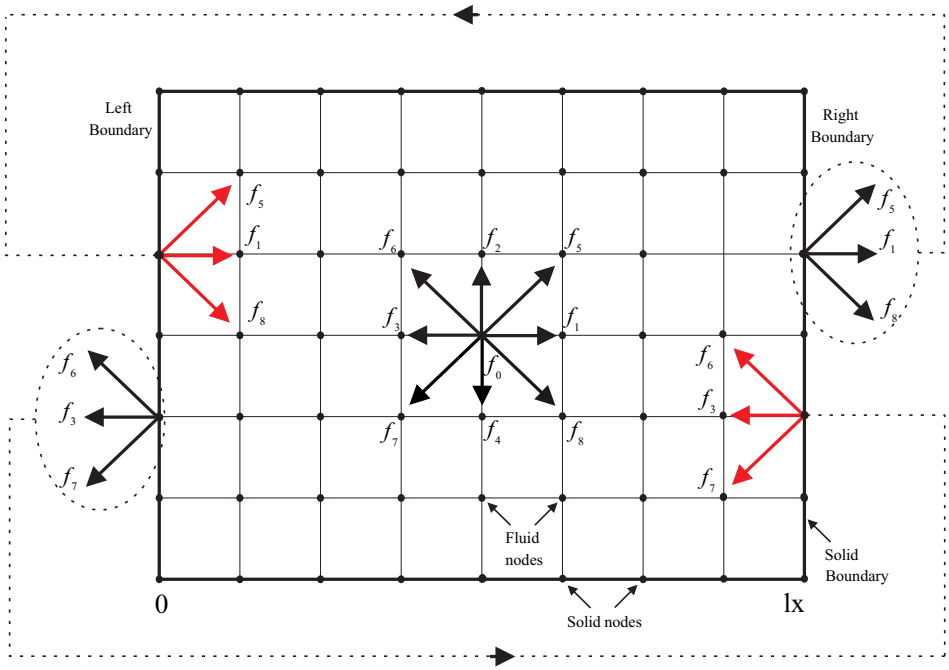

Figure 2.6: Periodic boundary conditions.

2.4 The Algorithm for Lattice Boltzmann Method

A simple implementation of LBM is illustrated in Figure (2.7). The collision and streaming steps are performed for each time iteration. The arrangement of the collision and streaming can be changed according to the process of LBM, either collide-stream or stream-collide (Bao & Meskas 2011, Zhao 2008). This algorithm of the LBM with the SRT stops by obtaining the steady state simulations or controls by choosing the proper time (maxt) for the loop.

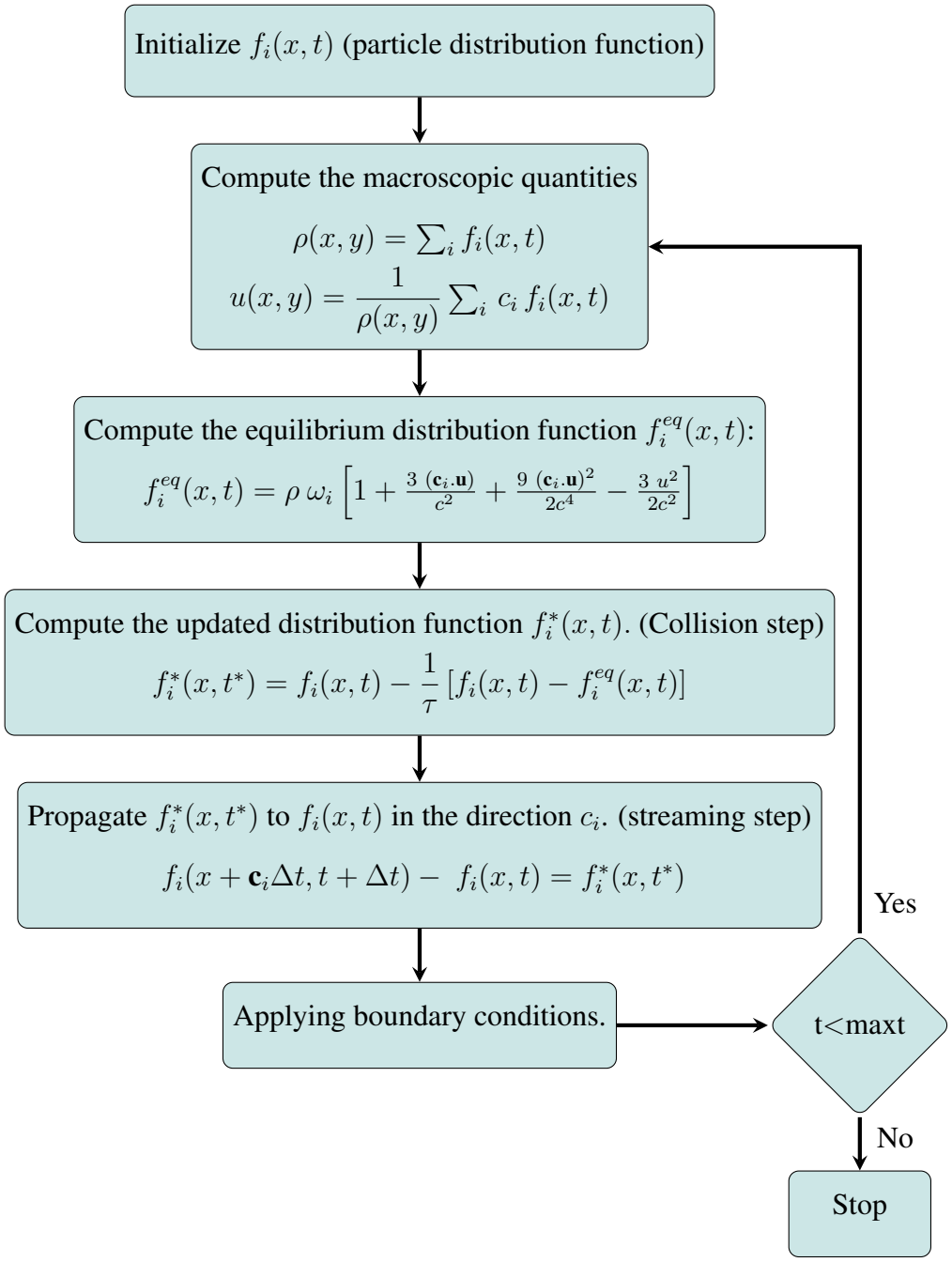

Figure 2.7: General algorithm for LBM with SRT.

2.5 LBM with Multiple Relaxation Time (MRT)

The Lattice Boltzmann Bhatnagar–Gross–Krook (BGK) model, a single relaxation time (SRT) is used in order to describe the collision effect. This means the pdfs relax

to their local equilibrium with the same rate determined by a single parameter. Physically, however, the relaxation rates at the collision step may be different. Wherefore, a collision matrix with different relaxation times can be used to eliminate this limitation (Guo & Shu 2013). d'Humieres (1994) presented a 2D MRT LB model for D_2Q_9. The collision operator in the LBE with a MRT can be define as

$$f_i(x + c_i\Delta t, t + \Delta t) - \ f_i(x,t) = -\sum_i \ \Lambda_{ij} \ (\ f_j(x,t) - f_j^{(eq)}(x,t) \ ), \qquad (2.5.1)$$

or

$$\mathbf{f}(x + c_i\Delta t, t + \Delta t) - \ \mathbf{f}(x,t) = -\Lambda \ (\ \mathbf{f}(x,t) - \mathbf{f}^{(eq)} j(x,t) \ ), \qquad (2.5.2)$$

where Λ is collision matrix. Eq.(2.5.2) characterize the evolution of $\mathbf{f} = (f_0, \ f_1, \ f_2, \ f_3, \ f_4, \ f_5, \ \ f_6, \ f_7, \ f_8)^T$ in the velocity space which is represented in a moment space (Lallemand & Luo 2000). The relation between the distribution function and the moments vector can be defined by

$$\mathbf{m} = \mathbf{M}\,\mathbf{f} = (\rho, e, \epsilon, j_x, q_x, j_y, q_y, p_{xx}, p_{xy})^T, \qquad (2.5.3)$$

and

$$\mathbf{f} = \mathbf{M}^{-1}\,\mathbf{m}, \qquad (2.5.4)$$

where $\mathbf{M}$ is the 9×9 matrix transforming $\mathbf{f}$ in the velocity space to $\mathbf{m}$ in the moment space. In the vector $\mathbf{m}$, ρ is the density mode, e is the energy mode, ϵ is related to the energy squared, j_x and j_y correspond to the momentum density (or mass flux), q_x and q_y correspond to the energy flux, and p_{xx} and p_{xy} correspond to the diagonal and

off-diagonal component of the viscous stress tensor (Lallemand & Luo 2000).

$$j_x = \rho\, \mathbf{u}_x = \sum_i \mathbf{c}_{ix}\, f_i^{(eq)} \;\; and \;\; j_y = \rho\, \mathbf{u}_y = \sum_i \mathbf{c}_{iy}\, f_i^{(eq)}, \tag{2.5.5}$$

and the transformation matrix $\mathbf{M}$ is

$$\mathbf{M} = \begin{bmatrix} 1 & 1 & 1 & 1 & 1 & 1 & 1 & 1 & 1 \\ -4 & -1 & -1 & -1 & -1 & 2 & 2 & 2 & 2 \\ 4 & -2 & -2 & -2 & -2 & 1 & 1 & 1 & 1 \\ 0 & 1 & 0 & -1 & 0 & 1 & -1 & -1 & 1 \\ 0 & -2 & 0 & 2 & 0 & 1 & -1 & -1 & 1 \\ 0 & 0 & 1 & 0 & -1 & 1 & 1 & -1 & -1 \\ 0 & 0 & -2 & 0 & 2 & 1 & 1 & -1 & -1 \\ 0 & 1 & -1 & 1 & -1 & 0 & 0 & 0 & 0 \\ 0 & 0 & 0 & 0 & 0 & 1 & -1 & 1 & -1 \end{bmatrix}, \tag{2.5.6}$$

and the inverse of M is

$$\mathbf{M}^{-1} = a \begin{bmatrix} 4 & -4 & 4 & 0 & 0 & 0 & 0 & 0 & 0 \\ 4 & -1 & -2 & 6 & -6 & 0 & 0 & 9 & 0 \\ 4 & -1 & -2 & 0 & 0 & 6 & -6 & -9 & 0 \\ 4 & -1 & -2 & -6 & 6 & 0 & 0 & 9 & 0 \\ 4 & -1 & -2 & 0 & 0 & -6 & 6 & -9 & 0 \\ 4 & 2 & 1 & 6 & 3 & 6 & 3 & 0 & -1 \\ 4 & 2 & 1 & -6 & -3 & 6 & 3 & 0 & -1 \\ 4 & 2 & 1 & -6 & -3 & -6 & -3 & 0 & 0 \\ 4 & 2 & 1 & 6 & 3 & -6 & -3 & 0 & -1 \end{bmatrix}, \tag{2.5.7}$$

where $a = 1/36$. From eq.(2.5.4), the eq.(2.5.2) is rewritten as follows

$$\begin{aligned} \mathbf{M}^{-1}\, \mathbf{m}(x + c_i\Delta t, t + \Delta t) - \; \mathbf{M}^{-1}\, \mathbf{m}(x,t) &= -\Lambda\, (\, \mathbf{M}^{-1}\, \mathbf{m} - \mathbf{M}^{-1}\, \mathbf{m}^{(eq)}\,), \\ &= -\Lambda\, \mathbf{M}^{-1} (\, \mathbf{m} - \mathbf{m}^{(eq)}\,), \end{aligned} \tag{2.5.8}$$

by using the left multiplication to **M**, yield

$$\mathbf{M}\,\mathbf{M}^{-1}\,\mathbf{m}(x + c_i\Delta t, t + \Delta t) - \mathbf{M}\,\mathbf{M}^{-1}\,\mathbf{m}(x,t) = -\mathbf{M}\,\Lambda\,\mathbf{M}^{-1}(\,\mathbf{m} - \mathbf{m}^{(eq)}\,),$$

so

$$\mathbf{m}(x + c_i\Delta t, t + \Delta t) - \mathbf{m}(x,t) = -\mathbf{M}\,\Lambda\,\mathbf{M}^{-1}(\,\mathbf{m} - \mathbf{m}^{(eq)}\,), \quad ,$$

thus

$$\mathbf{m}(x + c_i\Delta t, t + \Delta t) - \mathbf{m}(x,t) = -\mathbf{S}\,(\,\mathbf{m} - \mathbf{m}^{(eq)}\,), \tag{2.5.9}$$

where $\mathbf{S} = \mathbf{M}\,\Lambda\,\mathbf{M}^{-1}$ is diagonal matrix can be expressed as follows

$$\mathbf{S} = \begin{bmatrix} s_0 & 0 & 0 & 0 & 0 & 0 & 0 & 0 & 0 \\ 0 & s_1 & 0 & 0 & 0 & 0 & 0 & 0 & 0 \\ 0 & 0 & s_2 & 0 & 0 & 0 & 0 & 0 & 0 \\ 0 & 0 & 0 & s_3 & 0 & 0 & 0 & 0 & 0 \\ 0 & 0 & 0 & 0 & s_4 & 0 & 0 & 0 & 0 \\ 0 & 0 & 0 & 0 & 0 & s_5 & 0 & 0 & 0 \\ 0 & 0 & 0 & 0 & 0 & 0 & s_6 & 0 & 0 \\ 0 & 0 & 0 & 0 & 0 & 0 & 0 & s_7 & 0 \\ 0 & 0 & 0 & 0 & 0 & 0 & 0 & 0 & s_8 \end{bmatrix}.$$

It is more flexible to make the remaining the relaxation parameters (Yu et al. 2003). $\mathbf{S} = (1.0,\ 1.4,\ 1.4,\ s_3,\ 1.2,\ s_5,\ 1.2,\ s_7,\ s_8)$, where $s_7 = s_8 = \omega = \frac{1}{(3\nu+0.5)}$, s_3 and s_5 are arbitrary, can be set to 1.0 (Sidik et al. 2013). The the equilibrium in the moment space is $\mathbf{m}^{eq} = \mathbf{M}\,\mathbf{f}^{(eq)}$ which can be defined as

$$\mathbf{m}^{eq} = \begin{bmatrix} \rho \\ -2\,\rho + 3\,\rho(u_x^2 + u_y^2) \\ \rho - 3\,\rho(u_x^2 + u_y^2) \\ \rho\,u_x \\ -\rho\,u_x \\ \rho\,u_y \\ -\rho\,u_y \\ \rho\,(u_x^2 - u_y^2) \\ \rho\,u_x\,u_y \end{bmatrix} = \mathbf{M}\,\mathbf{f}^{(eq)}. \tag{2.5.10}$$

In the practical applications, the MRT combines the evolutions in the moment space and the velocity space. The collision process is performed in the moment space, but the streaming step is implemented in the velocity space such as the Lattice Boltzmann BGK approximation (SRT model). The MRT collision operator is used to obtain more stable simulations specially for high Re numbers as shown in chapter 3. In addition, a new MRT model is derived in chapter 7 to simulated breaking dams problems with high density ratio and high Re numbers which is impossible with SRT model. Therefore, a numerical comparison is made between SRT and MRT models in chapter 3. This algorithm with MRT model has same terminate that explained in the SRT model. The basic algorithm of a MRT can be represented as follows

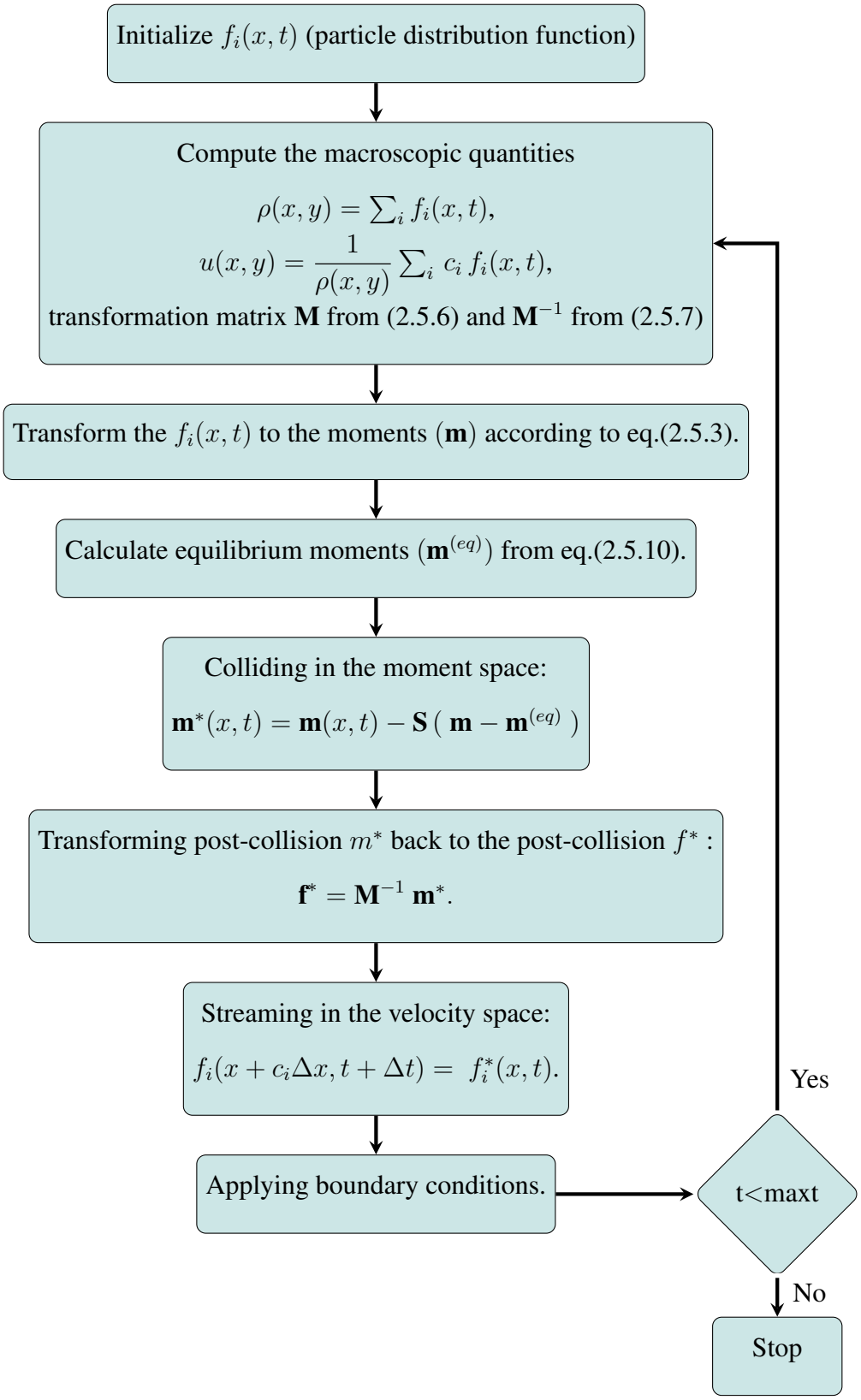

Figure 2.8: General algorithm for LBM with MRT.

2.6 Summary

In this chapter, a LBM is presented because of the accurate ability to deal and couple with various numerical techniques to simulate multiphase fluid flows with single and multi components, and capability for treating with complex fluid dynamics problems. Advantages include its ease for coding and parallelisation because of the lattice arrangement from the discretization of lattice Boltzmann equation. The derivation LBE from the continuous Boltzmann equation is explained with discrete time, velocity and lattice space. Also, the Navier-Stokes equation is recovered from LBE by using multi-scale Chapman-Enskog expansion. Several type of boundary condition has been explained such as bounce back (on-grid and half-way) and periodic boundary conditions. Finally, the algorithms for LBGK (or SRT) and MRT collision operator are illustrated.

Chapter 3

Simulation of Lid-Driven Cavity Flow Using LBM with SRT and MRT

3.1 Introduction

In this chapter, the LB computations in this study are performed for various Reynolds numbers (Re) with different number of grids to simulate 2D lid driven cavity flow. In order to study the stability and the accuracy, the numerical results between SRT (with on-grid and half-way bounce back boundary conditions) and MRT with on-grid bounce back boundary conditions are implemented. The minimum stream function value and the total kinetic energy per unit volume are used for the convergence to the steady state with a fine grid in LBM with SRT and MRT. Also, the numerical results for the velocity profiles and streamlines are compared with the numerical results from Ghia et al. (1982). This chapter is organized as follows: Section 3.2 describes the two dimensional nine velocity lid-driven square cavity flow. In sections 3.3 - 3.4, two functions are used as a measure to test the steady state of the convergence. Section 3.5 provides numerical result and discusses the results. Finally, summary of this chapter is given in Section 3.6.

3.2 Lid-Driven Cavity Flow

Lid driven cavity flow is a benchmark problem for computational fluid dynamics. It consists of a two dimensional viscous flow inside a cavity that is driven by a lid at the top of the cavity which moves to the right side (Ghia et al. 1982). In LBM a lid velocity U_{lid} taken to be 0.1 (in lattice units) to guarantee low Mach number ($Ma = U_{\text{lid}}/c_s$), where $c_s = \frac{c}{\sqrt{3}}$,$c = \frac{\Delta x}{\Delta t}$ and $\Delta x = \Delta t = 1$ lattice unit leads Ma equal to 0.1732 (Hou et al. 1995, Dabbaghitehrani 2013). The other boundaries have no slip boundary conditions for velocity $\mathbf{u} = (u_x, u_y) = (0, 0)$; see Figure (3.1) (Bao & Meskas 2011).

The results obtained from SRT and MRT simulations of the cavity will be compared with numerical results of Ghia et al. (1982). The computations are performed for the same (Re) from 100 to 10000 with various number of grids $lx = ly = [33, 65, 129, 257, 513]$. The results of the simulation need to be scaled. The scaling parameters are:

$$X = \frac{x}{lx}, \qquad Y = \frac{y}{ly},$$

where lx and ly are the number of grids in LBM. The velocity and the time as follow:

$$U = \frac{u}{U_{\text{lid}}},\ T = \frac{t * U_{\text{lid}}}{lx},$$

with

$$Re = \frac{U_{\text{lid}}\, lx}{\nu},$$

where

$$\nu = {c_s}^2 \left[\tau - \frac{1}{2}\right] \Delta t,$$

is the kinematic viscosity and it is related to the relaxation frequency (ω) of the collision operator in the LBE (Qian et al. 1992), as follows

$$\omega = \frac{1}{\tau} = \frac{1}{(3v + 0.5)}.$$

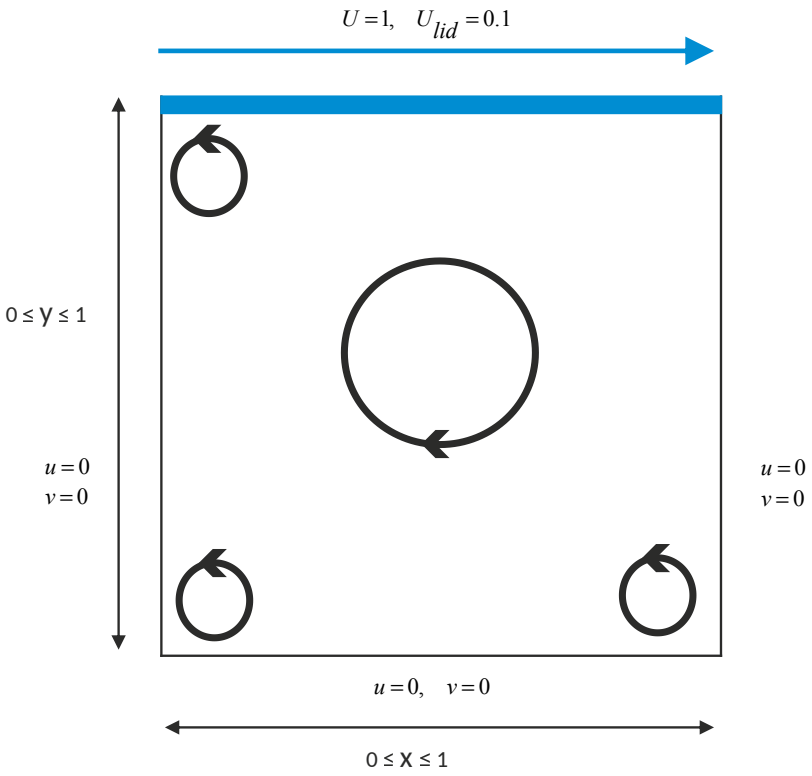

Figure 3.1: Lid driven cavity flow.

3.3 Stream Function

The stream function is important theoretically for visualising two-dimensional incompressible flow problems. The stream function can be used to examine the steady-state of the problems (Hou et al. 1995). It consists of solving the following equation

$$d\psi = \frac{\partial \psi}{\partial x} dx + \frac{\partial \psi}{\partial y} dy, \tag{3.3.1}$$

where ψ is the stream function and the velocity component can be define from the stream function as:

$$u = \frac{\partial \psi}{\partial y}, v = -\frac{\partial \psi}{\partial x}. \tag{3.3.2}$$

In the current study, the stream function is calculated at lattice points as follows:

$$\Delta\psi(i,j) = \frac{1}{2}[u(i,j+1) + u(i,j)]\, dy - \frac{1}{2}[v(i+1,j) + v(i,j)]\, dx, \tag{3.3.3}$$

and

$$\psi(i+1,j+1) = \psi(i,j) + \Delta\psi(i,j). \tag{3.3.4}$$

3.4 Kinetic Energy

Kinetic energy is the energy of motion. It is essential for the fluid motion as a measure when the steady state involves no change in the fluid motion. The kinetic energy per unit volume is given by (Chen et al. 1992) as:

$$\frac{Kinetic\ Energy}{Volume} = \frac{1}{2}\,\rho\,\mathbf{u}^2, \tag{3.4.1}$$

where **u** is the velocity and ρ is density then the total kinetic energy is given by:

$$E = \sum_{i,j} \frac{1}{2}\,\rho(i,j)\,[u(i,j)^2 + v(i,j)^2]dx\,dy. \tag{3.4.2}$$

3.5 Results and Discussion

In this section, the measures of the total kinetic energy per unit volume and the minimum stream function value are used for testing the convergence to the steady state of the cavity flow for SRT (on-grid and half-way bounce back boundary conditions) and MRT. The iterative process is used to examine the convergence by kinetic energy and stream function. On the other hand, the same Re with number of grids $lx,\ ly\ =\ [33, 65, 129, 257, 513]$ are performed by SRT and MRT. The $\psi_{min}(Re, 513)$ which represents the errors ψ_{min} at the best lattice region (513×513) is used to define the $error_1$ in the simulations. It can be defined as follows

$$error_1 = |\, \psi_{min}(Re, lx) - \psi_{min}(Re, 513)\,|, \tag{3.5.1}$$

with a similar definition for the energy error ($error_2$):

$$error_2 = |\, energy(Re, lx) - energy(Re, 513)\,|. \tag{3.5.2}$$

Furthermore, the results obtained from Lattice Boltzmann simulation of the cavity will be compared with numerical results of finite difference method (FDM) by Ghia et al. (1982) for the velocity component and the streamlines.

3.5.1 Convergence of Iterative process

In order to study the convergence of iterative process, different Re and number of lattice grids are performed for the current simulations with two dimensional lid driven cavity flow. The measure of convergence of stream function with iterative process (e_1)

can be written as:

$$e_1 = \left| \frac{\psi_{min}^{(n+1)} - \psi_{min}^{(n)}}{\psi_{min}^{(n+1)}} \right| \leq \ tol_1, \tag{3.5.3}$$

where n refers to iteration number and the measure of convergence of energy with iterative process (e_2) can be define as follow:

$$e_2 = \left| \frac{E^{(n+1)} - E^{(n)}}{E^{(n+1)}} \right| \leq \ tol_2. \tag{3.5.4}$$

In the calculations, for each Re that convergence to the steady state was achieved when both $e_1 \leq \ tol_1$ and $e_2 \leq \ tol_2$ was considered. The low value of $tol_1 = 10^{-7}$ and $tol_2 = 10^{-7}$ was chosen with $Re = 100, 400, 1000, 3200, 5000$ and 7500 to guarantee that the current solutions are accurate and with $Re = 10000$ the $tol_1 = tol_2 = 10^{-6}$ was taken. The convergence of ψ_{min} with iterative process is illustrated in Figure (3.2). It shows the relation between dimensionless time (T) and the grid sizes. The (T) from number of iteration can be found as follows

$$T = \frac{t * U_{lid}}{lx}, \tag{3.5.5}$$

t is the number of iterations. From the results, it found that the level of convergence of ψ_{min} with SRT using half-way bounce back boundary conditions at $Re = 100$ stay the same for lx, $ly = [33, 65, 129, 257, 513]$. At $Re = 400$, the convergence has become flatten after (65×65), for $Re = 1000$ and 3200 the line of convergence stays in the same level after (129×129) and (257×257), respectively. A large number of the lattice grid required to obtain the convergence flat behaviour for high Re for $Re = 5000, 7500$ and 10000. Also, the half-way bounce back that obtained is more convergent than on-grid bounce back boundary conditions by SRT as shown in Figure (3.2).

On the other hand, the results from MRT with $Re = 100, 400$ and 1000 are found

that the level of convergence stays the same at all number of the grids. For $Re = 3200$ and 5000 are convergent at the grids $lx,\ ly = [65, 129, 257, 513]$, with $Re = 7500$ is convergent at $lx,\ ly = [129, 257, 513]$, and with $Re = 10000$ is stable at $lx,\ ly = [257, 513]$ as shown in Figure (3.3).

Furthermore, It was observed that the level of convergences of energy at $Re = 100$ and 400 stay the same for $lx,\ ly = [33, 65, 129, 257, 513]$ with half-way bounce back boundary in SRT. At $Re = 1000$ the convergence has approximately become flattened after (65×65) and to see the flatten the convergence for Reynolds number from 3200 to 10000 need a large grid as illustrated in Figure (3.4). The convergences of the energy with half-way bounce back more convergence to the steady state than on-grid bounce back boundary conditions.

In the MRT, the same results obtained with convergences of energy except for $Re = 1000$ the level of convergence stays the same at the grids $lx,\ ly = [65, 129, 257, 513]$ by comparing with SRT as illustrated in Figure (3.5). Therefore, for high Re numbers the result that are found from MRT is more stable than SRT.

In addition, from these results the number of iterations required for large grids can be estimated. For example, $(t = 130000)$ is required to obtain the steady state of ψ_{min} for $Re = 400$ with (513×513) in the MRT. That corresponds to the dimensionless time $(T = 25.09551)$ by using eq.(3.5.5). Since the level of convergence stays the same at $Re = 400$ and from eq.(3.5.5) the dimensionless time $(T = 25.09551)$ with (1025×1025) can be guessed. Therefore, the double number of iterations $(t = 260000)$ is required to get the steady state.

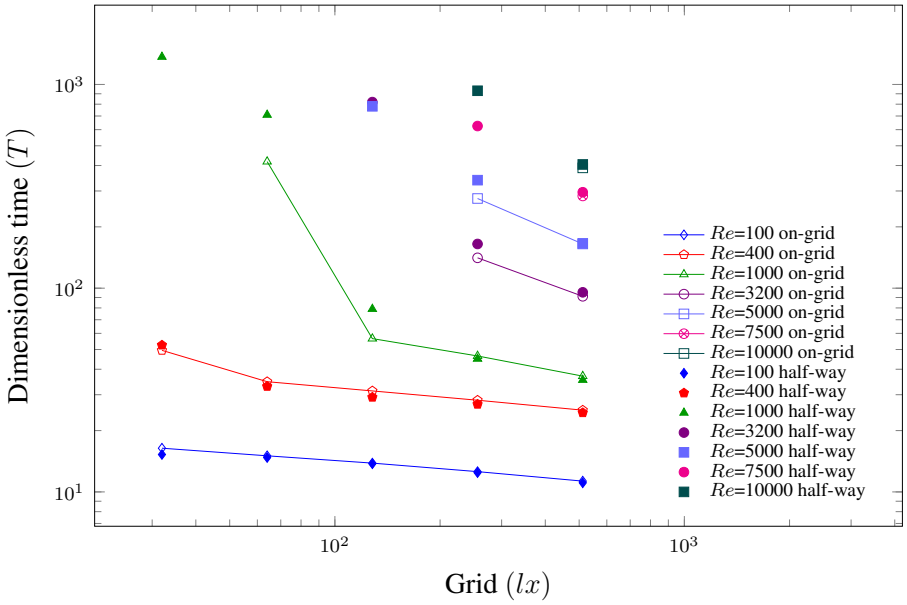

Figure 3.2: Convergence of ψ_{min} for cavity flow with iterative process.

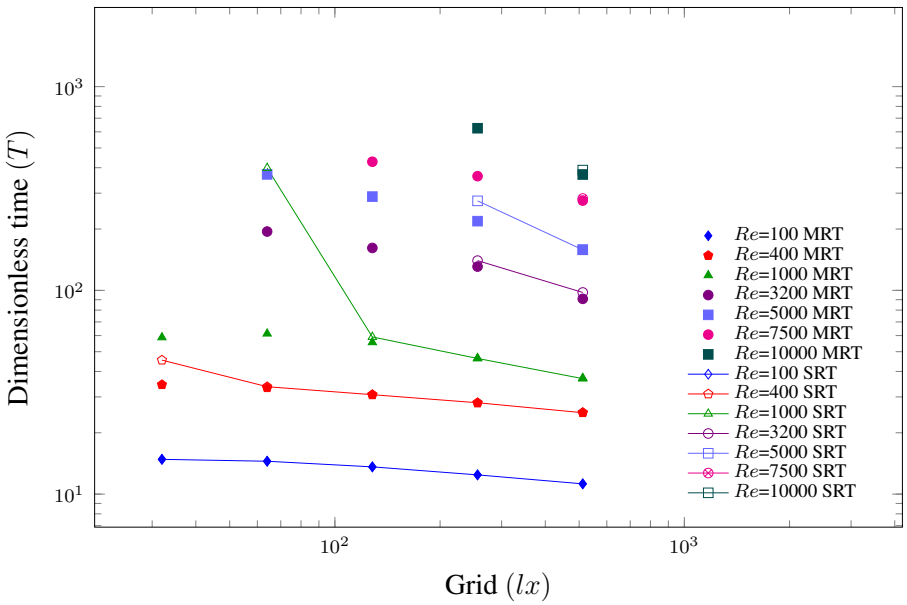

Figure 3.3: Convergence of ψ_{min} for SRT and MRT simulation of cavity flow with iterative process.

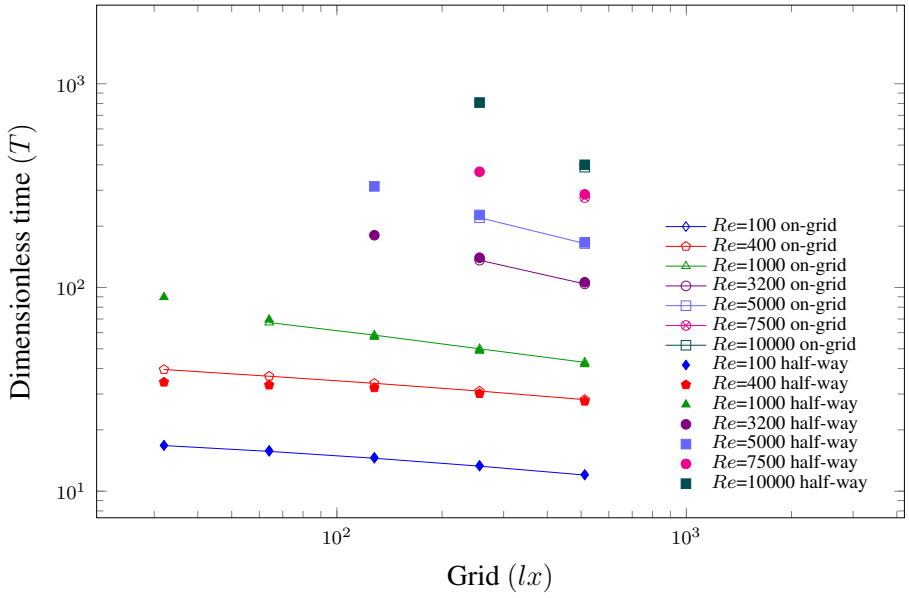

Figure 3.4: Convergence of energy for cavity flow with iterative process.

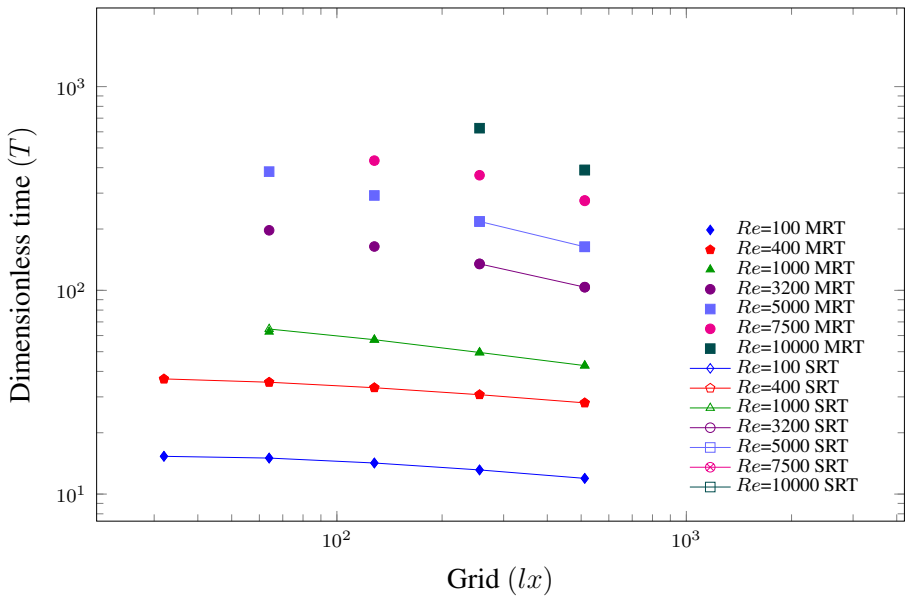

Figure 3.5: Convergence of energy for SRT and MRT simulation of cavity flow with iterative process.

3.5.2 Convergence with Grid

The energy and stream function for finding the error are used as a function of grid. For SRT (on-grid and half-way bounce back), Figures (3.6-3.9) illustrate the errors of

ψ_{min} and energy become very small when increasing the grids and they have several order of accuracy. This means that the accuracy of these functions for SRT (on-grid and half-way bounce back) with $Re = 100, 400$ and 1000 have 1st order at the grids from $(lx = 33)$ to $(lx = 129)$ and 2nd order at the grids from $(lx = 129)$ to $(lx = 257)$. The SRT does not convergent at small grids with $Re = 3200, 5000, 7500$ and 10000. On the other hand, the errors of ψ_{min} and energy for MRT that illustrate in Figures (3.7-3.9) with $Re = 100, 400, 1000, 3200$ and 5000 have 2nd order after the grids (65×65) and less than 2nd order with the grids (65×65). In general, It observed that MRT does not need a large numbers of grids to estimate the accuracy of these functions as SRT because the MRT more convergence than SRT.

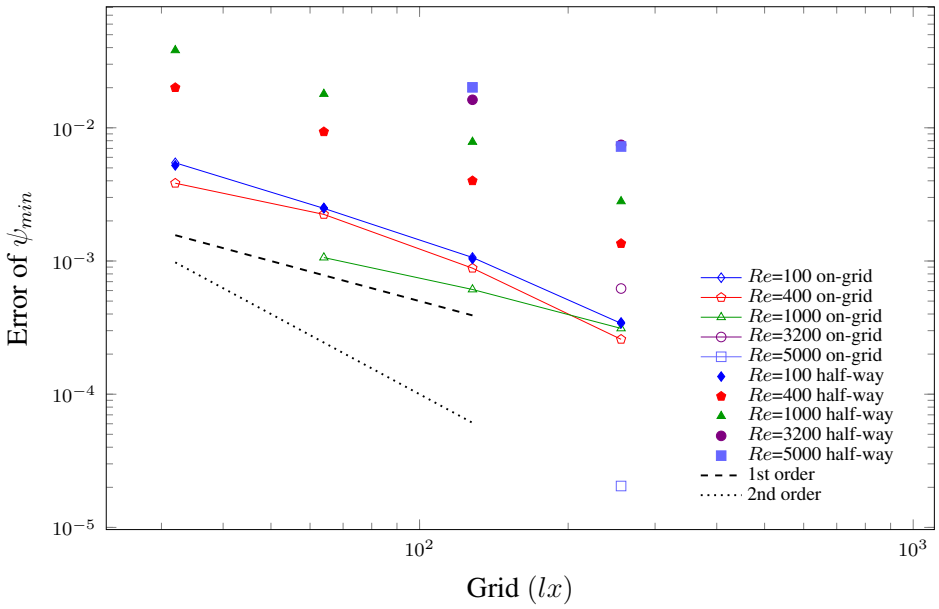

Figure 3.6: Error of ψ_{min} with grid for on-grid and half-way bounce back boundaries.

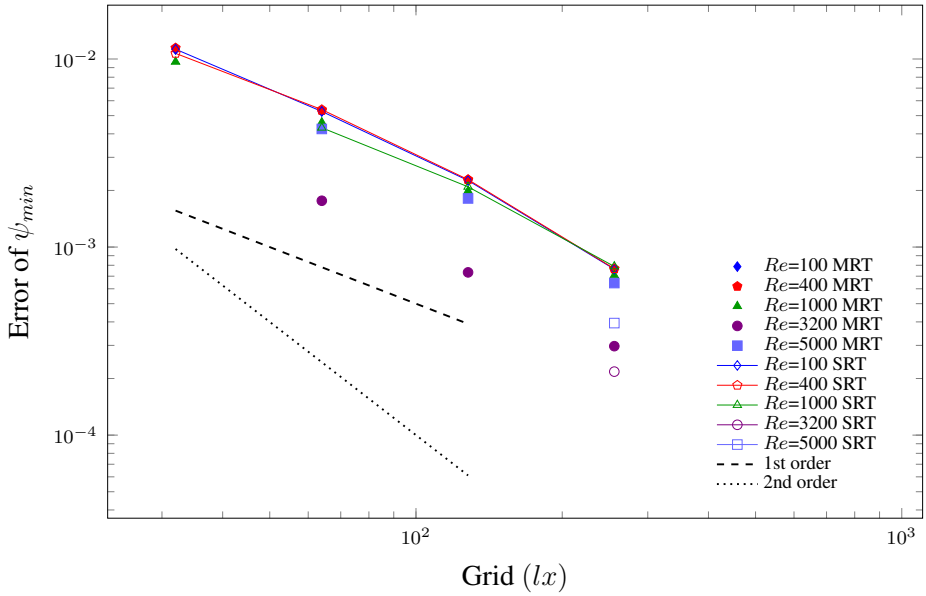

Figure 3.7: Error of ψ_{min} with grid for SRT and MRT.

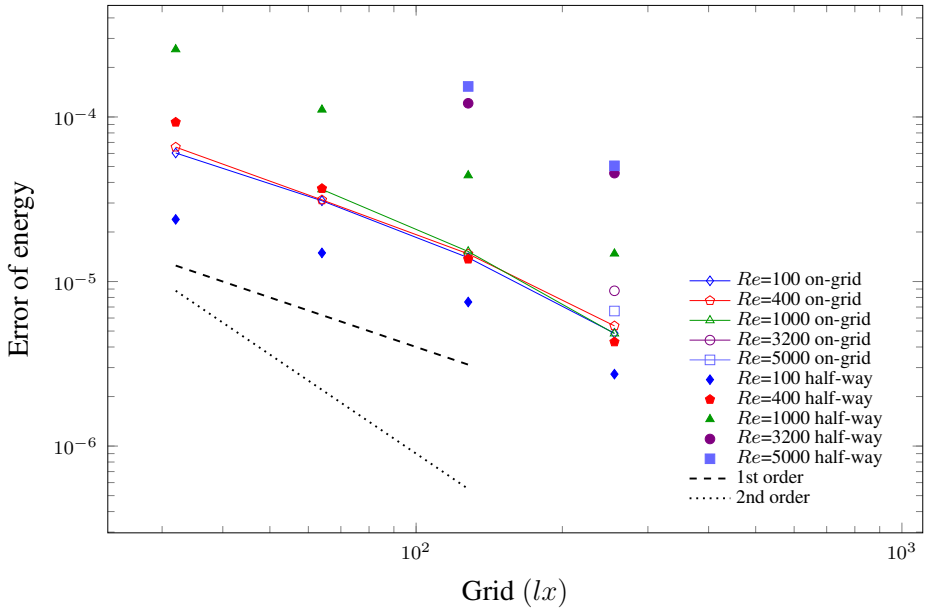

Figure 3.8: Error of energy with grid for on-grid and half-way bounce back boundaries.

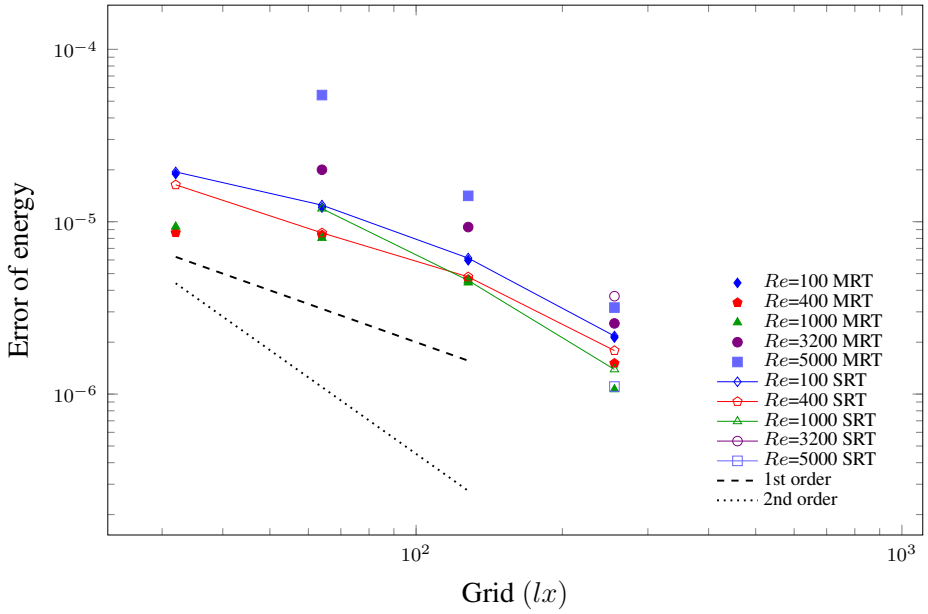

Figure 3.9: Error of energy with grid for SRT and MRT.

3.5.3 Comparison Velocity profiles and Stream functions

The lid driven cavity flow does not have an analytic solution. There are several studies of cavity flow that proposed by (Bruneau & Jouron 1990), (Botella & Peyret 1998), (Sahin & Owens 2003, Deng et al. 1994) and (Luo et al. 2011, Hou et al. 1995) using FDM, a Chebyshev collocation method, Finite Volume Method (FVM) and LBM, respectively which are compared their result with Ghia et al. (1982). So the results that obtained from SRT and MRT simulations of the cavity will be compared with the numerical results by Ghia et al. (1982) for the velocity component and the streamlines.

The Figures (3.10-3.13) show the velocity profiles along vertical and horizontal lines passing through the centre of cavity flow at $(x = 0.5)$ with various Re from 100 to 10000 at different grids in SRT (on-grid and half-way bounce back boundary) and MRT. A comparison of the results for u_x-velocity and u_y-velocity along these centre lines are made. The relative errors (RE_1), (RE_2) and (RE_3) are referred to for u_x-velocity and u_y-velocity between Ghia et al. (1982) and SRT (on-grid and half-way bounce back boundary) as well as MRT for $Re = 100, 400, 1000, 3200, 5000, 7500$ and

10000 with (513×513) as shown in Tables (3.1 - 3.2). It observed that the results of velocities for high Reynolds number with on-grid bounce back are closer to the results of Ghia et al. (1982) than half-way bounce back as shown in Tables (3.3 - 3.4), but the half-way bounce back is more convergent than on-grid bounce back as illustrated in Figures 3.10 (e,f) and 3.11 (e,f).

Also, the results that are found with velocities of MRT are more convergent at higher Re than SRT as illustrated in Table (3.5 - 3.8) and Figures (3.12-3.13). In general, the comparisons of the present work with Ghia et al.(1982) are good. RE_1, RE_2 and RE_3 are defined in which u_{min} is either u_xmin velocity or u_ymin the velocity as follows

$$RE_1 = \frac{\left| \, u_{min}^{\text{Ghia}} \; - \; u_{min}^{\text{SRT(on-grid)}} \, \right|}{\left| \, u_{min}^{\text{Ghia}} \, \right|} \, , \tag{3.5.6}$$

$$RE_2 = \frac{\left| \, u_{min}^{\text{Ghia}} \; - \; u_{min}^{\text{SRT(half-way)}} \, \right|}{\left| \, u_{min}^{\text{Ghia}} \, \right|} \, , \tag{3.5.7}$$

$$RE_3 = \frac{\left| \, u_{min}^{\text{Ghia}} \; - \; u_{min}^{\text{MRT}} \, \right|}{\left| \, u_{min}^{\text{Ghia}} \, \right|} \, . \tag{3.5.8}$$

Table 3.1: Comparison of the results for u_x-velocity along vertical centre line of the cavity between Ghia et al. (1982) and SRT (on-grid and half-way) as well as MRT with Re from 100 to 10000.

Re	Ghia et al. (1982)		SRT (on-grid)		SRT (half-way)		MRT	
	y	u_xmin	y	u_xmin	y	u_xmin	y	u_xmin
100	0.4531	-0.21090	0.45313	-0.19767	0.46086	-0.20516	0.45695	-0.19772
400	0.2813	-0.32726	0.28516	-0.31129	0.28278	-0.32483	0.28474	-0.31137
1000	0.1719	-0.38289	0.17578	-0.37214	0.17123	-0.38972	0.17515	-0.37205
3200	0.1016	-0.41933	0.0957	-0.41869	0.09295	-0.44523	0.09491	-0.41898
5000	0.0703	-0.43643	0.07617	-0.4303	0.07339	-0.46308	0.0773	-0.42949
7500	0.0625	-0.43590	0.06055	-0.43541	0.05969	-0.47467	0.06164	-0.43535
10000	0.0547	-0.42735	0.05469	-0.44404	0.05186	-0.48395	0.05382	-0.43542

Table 3.2: Comparison of the results for u_y-velocity along vertical centre line of the cavity between Ghia et al. (1982) and SRT (on-grid and half-way) as well as MRT with Re from 100 to 10000.

Re	Ghia et al. (1982)		SRT (on-grid)		SRT (half-way)		MRT	
	x	$u_y min$	x	$u_y min$	x	$u_y min$	x	$u_y min$
100	0.8047	-0.24533	0.8125	-0.23743	0.81115	-0.24297	0.81115	-0.23729
400	0.8594	-0.44993	0.86133	-0.43173	0.86204	-0.44825	0.86008	-0.43192
1000	0.9063	-0.51550	0.9082	-0.50534	0.909	-0.52801	0.90705	-0.50523
3200	0.9453	-0.54053	0.94727	-0.54564	0.94814	-0.5795	0.94618	-0.54600
5000	0.9531	-0.55408	0.95703	-0.55329	0.95793	-0.59462	0.95597	-0.55238
7500	0.9609	-0.55216	0.96289	-0.55375	0.9638	-0.6024	0.96184	-0.55364
10000	0.9688	-0.54302	0.9668	-0.55391	0.9697	-0.60512	0.96771	-0.55124

Table 3.3: Comparison of RE for u_x-velocity between Ghia et al. (1982) and SRT as well as MRT with Re from 100 to 10000.

RE of u_x-velocity	Re=100	Re=400	Re=1000	Re=3200	Re=5000	Re=7500	Re=10000
RE_1	0.0627	0.0488	0.0281	0.00153	0.0141	0.0011	0.0391
RE_2	0.0272	0.0074	0.01784	0.06177	0.06106	0.0889	0.13244
RE_3	0.06249	0.04855	0.02831	0.00083	0.01581	0.00126	0.0189

Table 3.4: Comparison of RE for u_y-velocity between Ghia et al. (1982) and SRT as well as MRT with Re from 100 to 10000.

RE u_y-velocity	Re=100	Re=400	Re=1000	Re=3200	Re=5000	Re=7500	Re=10000
RE_1	0.03220	0.04045	0.01971	0.0095	0.0014	0.0029	0.02
RE_2	0.00962	0.00373	0.0247	0.0721	0.07317	0.0919	0.1144
RE_3	0.03277	0.04001	0.01992	0.01012	0.00307	0.00268	0.01514

Table 3.5: Comparison of the results for u_x-velocity along vertical centre line of the cavity between Ghia et al. (1982) and SRT as well as MRT with Re from 100 to 7500 at $lx = 129$.

Re	Ghia et al. (1982)		SRT		MRT	
	y	$u_x min$	y	$u_x min$	y	$u_x min$
100	0.4531	-0.21090	0.45276	-0.19811	0.45276	-0.19811
400	0.2813	-0.32726	0.2874	-0.31228	0.2874	-0.31228
1000	0.1719	-0.38289	0.17717	-0.374175	0.17717	-0.374241
3200	0.1016	-0.41933	—	—	0.09843	-0.42364
5000	0.0703	-0.43643	—	—	0.0748	-0.43281
7500	0.0625	-0.43590	—	—	0.06693	-0.44416

Table 3.6: Comparison of the results for u_y-velocity along horizontal centre line of the cavity between Ghia et al. (1982) and SRT as well as MRT with Re from 100 to 7500 at $lx = 129$.

Re	Ghia et al. (1982)		SRT		MRT	
	x	u_ymin	x	u_ymin	x	u_ymin
100	0.8047	-0.24533	0.80709	-0.23931	0.80709	-0.23929
400	0.8594	-0.44993	0.8622	-0.43393	0.8622	-0.43391
1000	0.9063	-0.51550	0.90157	-0.50749	0.90157	-0.50756
3200	0.9453	-0.54053	—	—	0.94094	-0.55079
5000	0.9531	-0.55408	—	—	0.94882	-0.55584
7500	0.9609	-0.55216	—	—	0.95669	-0.56253

Table 3.7: Comparison of RE for u_x-velocity between Ghia et al. (1982) and SRT as well as MRT with Re from 100 to 7500 at $lx = 129$.

RE of u_x-velocity	Re=100	Re=400	Re=1000	Re=3200	Re=5000	Re=7500
RE_1	0.06065	0.04577	0.02276	—	—	—
RE_2	0.06065	0.04577	0.02259	0.01028	0.00830	0.01895

Table 3.8: Comparison of RE for u_y-velocity between Ghia et al. (1982) and SRT as well as MRT with Re from 100 to 7500 at $lx = 129$.

RE of u_y-velocity	Re=100	Re=400	Re=1000	Re=3200	Re=5000	Re=7500
RE_1	0.02454	0.03556	0.01554	—	—	—
RE_2	0.02462	0.03556	0.01540	0.01898	0.00318	0.18781

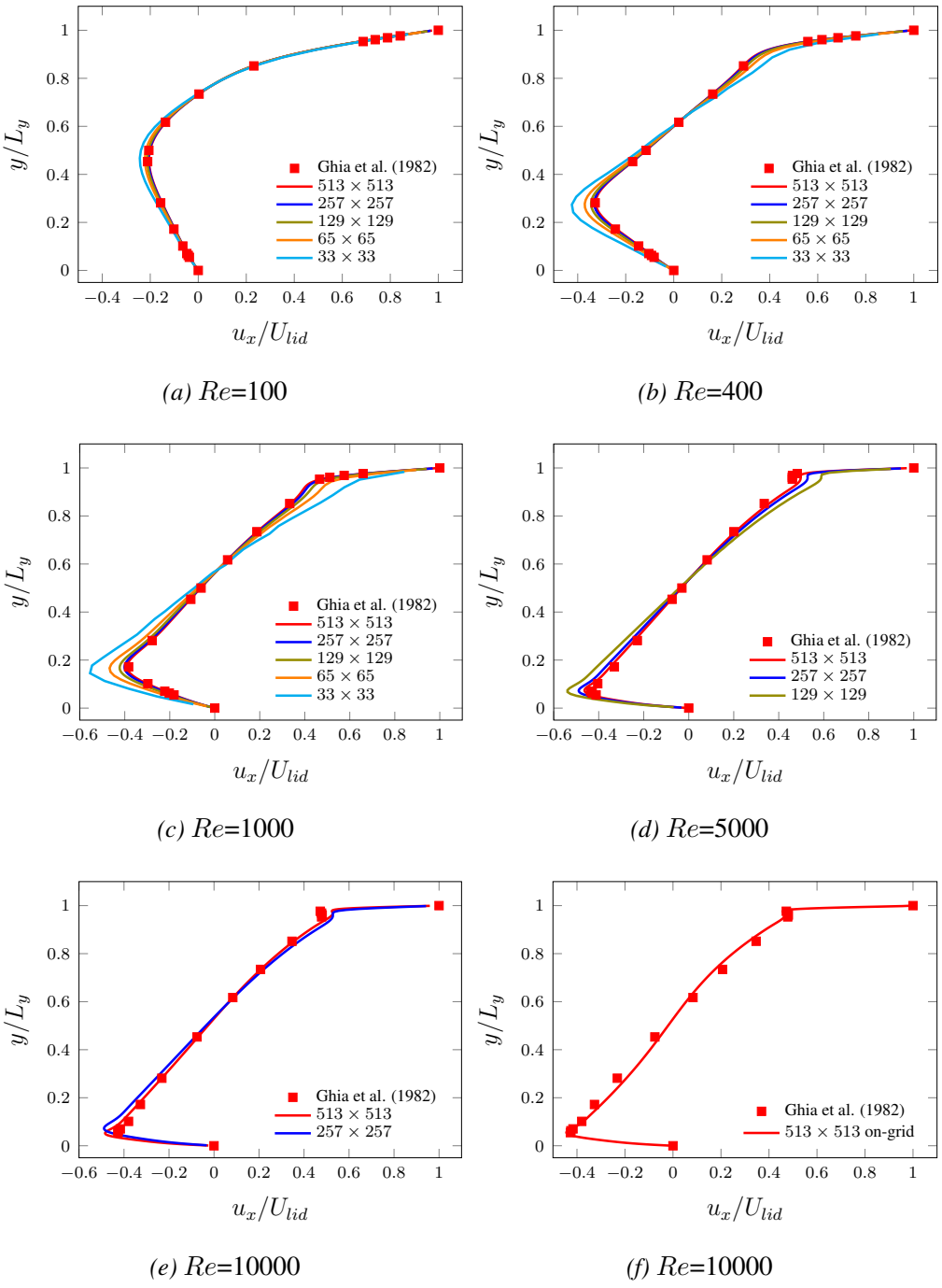

(a) Re=100 *(b)* Re=400

(c) Re=1000 *(d)* Re=5000

(e) Re=10000 *(f)* Re=10000

Figure 3.10: Velocity profiles show the u_x-velocity distribution along a vertical line passing through the centre of cavity $(x = 0.5)$ at different Re for bounce back boundary by SRT are compared with Ghia et al. (1982).

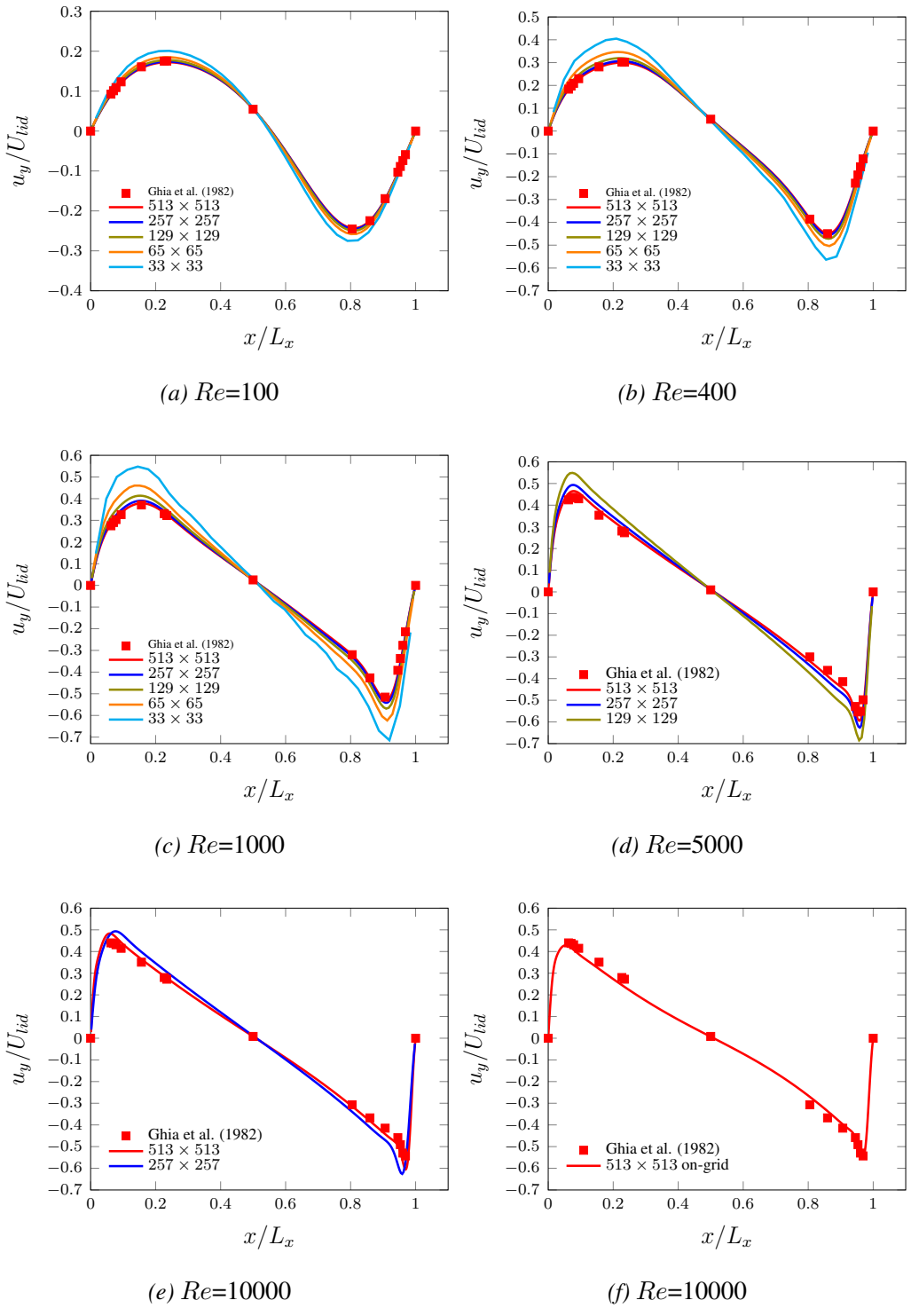

(a) Re=100 *(b)* Re=400

(c) Re=1000 *(d)* Re=5000

(e) Re=10000 *(f)* Re=10000

Figure 3.11: Velocity profiles show the u_y-velocity distribution along a horizontal line passing through the centre of cavity (y=0.5) at different Re for bounce back boundary by SRT are compared with Ghia et al. (1982).

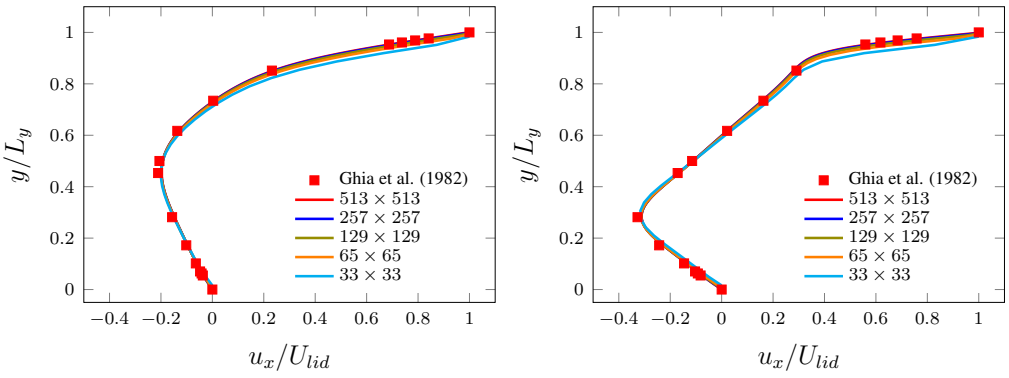

(a) Re=100 *(b)* Re=400

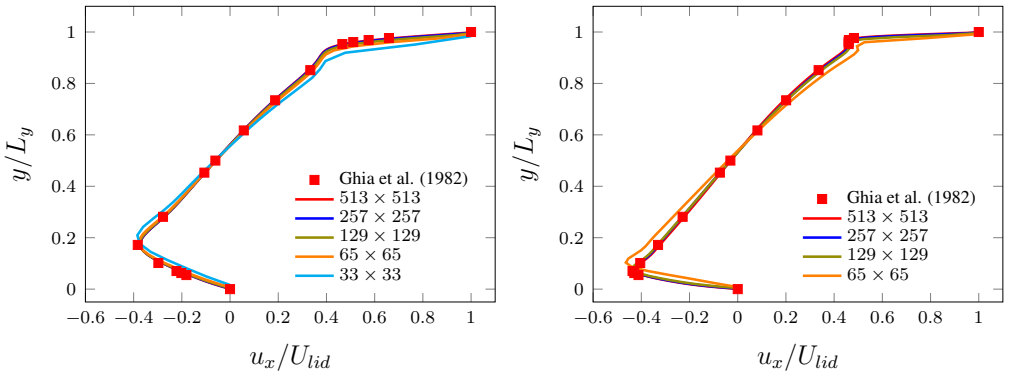

(c) Re=1000 *(d)* Re=5000

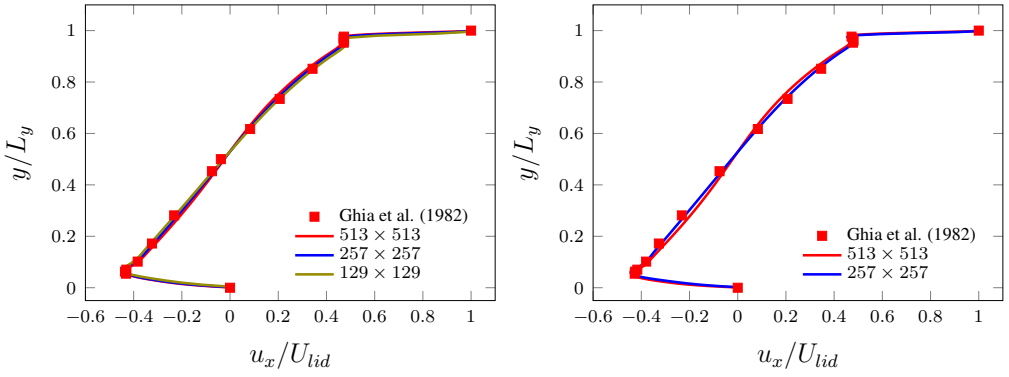

(e) Re=7500 *(f)* Re=10000

Figure 3.12: Velocity profiles show the u_x-velocity distribution along a vertical line passing through the centre of cavity $(x = 0.5)$ at different Re for MRT are compared with Ghia et al. (1982).

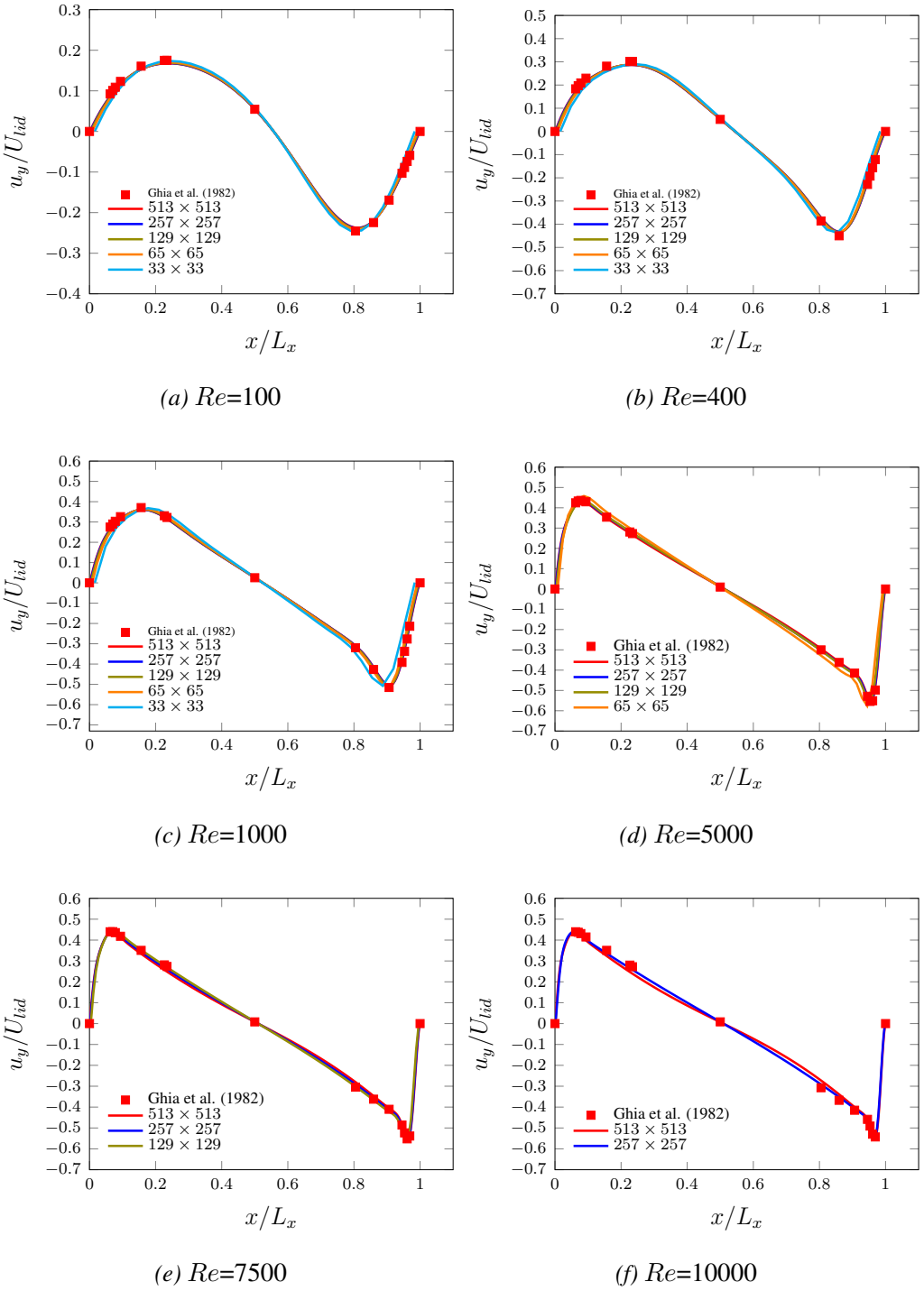

(a) Re=100 *(b)* Re=400

(c) Re=1000 *(d)* Re=5000

(e) Re=7500 *(f)* Re=10000

Figure 3.13: Velocity profiles show the u_y-velocity distribution along a vertical line passing through the centre of cavity $(x = 0.5)$ at different Re for MRT are compared with Ghia et al. (1982).

In Figure (3.14), a comparison of the streamline contours for cavity flow between the present work (SRT and MRT) and Ghia et al. (1982) was made with various Reynolds number from 100 to 10000 at (129×129), (257×257) and (513×513) grids. The stream function value ψ for Ghia et al. (1982) along the contours are listed in Table (3.9). The range of streamline values are taken from the minimum value -0.11 to the maximum value 0.01 with the number of contours 12 for $Re = 100$ at (129×129), from the minimum value -0.12 to the maximum value 0.01 with the number of contours 13 for $Re = 400$ at (129×129), $Re = 400, 1000$ and 3200 at (257×257) and $Re = 5000, 7500$ and 10000 at (513×513).

It observed that the streamline patterns agree with Ghia et al. (1982) as shown in Figure (3.14), when increasing Reynolds number leads to that the vortex for streamlines trend toward to the centre and created three vortices at bottom right corner, bottom left corner and top left corner, respectively.

Also, the result of the simulation at $Re = 10000$ is created a second small vortex in the bottom right corner. In addition, the minimum stream function value is predicted a slightly better with half-way compared than on-grid bounce back boundary in SRT as well as MRT which shown in Table (3.10) that have a good match with Ghia et al. (1982).

Table 3.9: Streamlines value of Ghia et al. (1982).

Contour letter	b	c	d	e	f	g	h	i	j	k	l	m
Value of ψ	-1×10^{-7}	-1×10^{-5}	-1×10^{-4}	-0.01	-0.03	-0.05	-0.07	-0.09	-0.1	-0.11	-0.115	-0.1175
Contour number	0	1	2	3	4	5	6	7	8	9	10	
Value of ψ	1×10^{-8}	1×10^{-7}	1×10^{-6}	1×10^{-5}	5×10^{-5}	1×10^{-4}	2.5×10^{-4}	5×10^{-4}	1×10^{-3}	1.5×10^{-3}	3×10^{-3}	

Table 3.10: Comparison of cavity flow of the centre of streamline for Re from 100 to 10000 between Ghia et al. (1982) and SRT as well as MRT.

Re	Ghia et al. (1982)			SRT(on-grid)			SRT(half-way)			MRT		
	ψ_{min}	x	y	ψ_{min}	x	y	ψ_{min}	x	y	ψ_{min}	x	y
100	-0.10342	0.6172	0.7344	-0.09594	0.61133	0.73242	-0.0992	0.61328	0.73632	-0.09557	0.61133	0.73242
400	-0.11391	0.5547	0.6055	-0.10823	0.55469	0.60352	-0.11223	0.55273	0.60352	-0.10786	0.55469	0.60563
1000	-0.11793	0.5313	0.5625	-0.11377	0.52930	0.5625	-0.11864	0.52734	0.5625	-0.11332	0.52930	0.5625
3200	-0.12038	0.5165	0.5469	-0.11587	0.51563	0.53711	-0.1220	0.51563	0.53906	-0.11583	0.51563	0.53711
5000	-0.11897	0.5117	0.5352	-0.11686	0.51367	0.53320	-0.12509	0.51172	0.53320	-0.11501	0.51367	0.53320
7500	-0.11998	0.5117	0.5322	-0.11154	0.51172	0.52930	-0.12195	0.50977	0.53125	-0.11113	0.51172	0.52930
10000	-0.11973	0.5117	0.5333	-0.10894	0.56977	0.52539	-0.12029	0.50977	0.52734	-0.10898	0.50977	0.52734

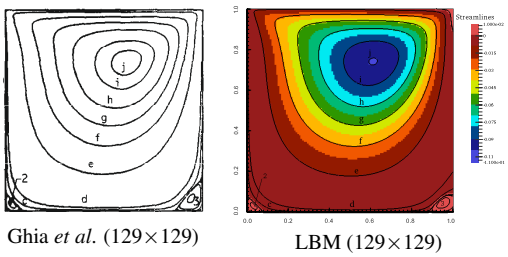

(a) Re=100

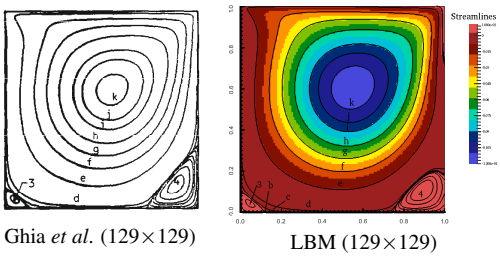

(b) Re=400

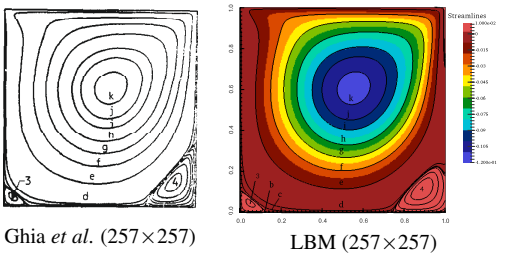

(c) Re=400

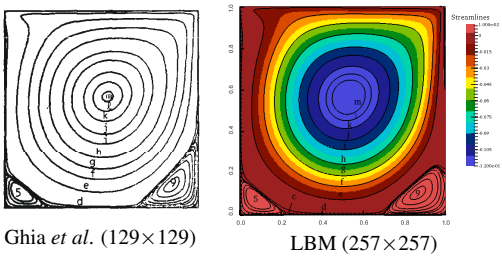

(d) Re=1000

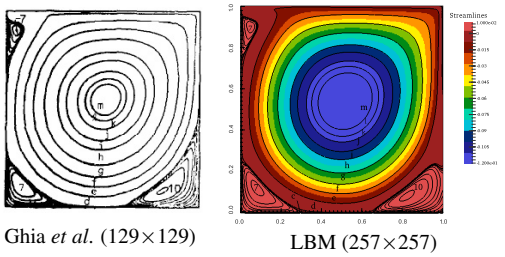

(e) Re=3200

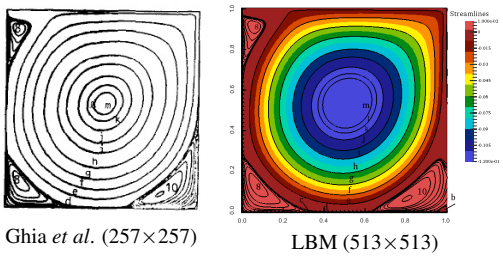

(f) Re=5000

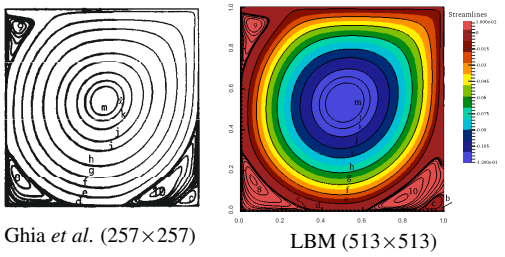

(g) Re=7500

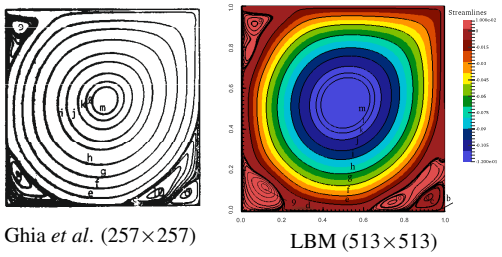

(h) Re=10000

Figure 3.14: Streamlines for $Re = 100, 400, 1000, 3200, 5000, 7500$ and 10000.

3.6 Summary

In this chapter, two cases of relaxation times the SRT (on-grid and half-way) bounce back boundary conditions and the MRT with on-grid bounce back boundary condition for LBM were tested to simulate 2D cavity flow. In the computations, the stream function and energy were used as measures to study the convergence to steady state and estimate the error for Re from 100 to 10000 at $lx, ly = [33, 65, 129, 257, 513]$ as shown in Figures (3.2 - 3.9). For these Re, the convergence to steady state was achieved when both $e_1 \leq \ tol_1$ and $e_2 \leq \ tol_2$. The low value of $tol_1 = tol_2 = 10^{-7}$ was chosen at $Re = 100, 400, 1000, 3200, 5000$ and 7500 to guarantee the accurate solutions and for $Re = 10000$ the $tol_1 = tol_2 = 10^{-6}$ was chosen with SRT and MRT. In general, MRT is more stable than SRT especially with ψ_{min} at $Re = 1000$.

The behaviours of the current simulation has 1st order for small grids and 2nd order for large grids of accuracy in SRT while MRT with $Re = 3200$ and 5000 has 2nd order as shown in Figures (3.6 - 3.9). On the other hand, The comparisons are made between current numerical results (for the velocity profiles and streamlines) and the numerical results from Ghia et al. (1982). In SRT with half-way bounce back is more convergent than on-grid bounce back as illustrated in cases e and f as shown in Figures (3.10-3.11) and they are close to the results of Ghia et al. (1982) as illustrated in Figures (3.10-3.13). From the obtained results, it found that here is not much difference between SRT and MRT and they are close to the results of Ghia et al. (1982) for velocity profiles except MRT is more stable than SRT as illustrated in Tables (3.7 - 3.8). Also, the minima of the stream function using SRT agree slightly better with Ghia et al. (1982) than MRT. Figure (3.14) and Tables (3.10) shows the streamlines have a good match with Ghia et al. (1982).

Chapter 4

Multiphase for LBM with high density ratios

4.1 Introduction

Modelling of multiphase fluid flows has been studied and researched with various LB techniques as reviewed in chapter 1. The multiphase flows LB approach with high density ratios is presented in this chapter. The model suggested by Banari et al. (2014) will be introduced by defining three particle distribution functions. The interface moving between fluids is captured by the Cahn-Hilliard (CH) equation which is related to free energy model as shown in chapter 1. A unified LBM approach is used with separate formulations for the phase field, the pressureless velocity of Navier-Stokes (NS) equations and the corrected velocity field (found by solving a Poisson equation).

In this chapter, Section 4.2 introduces the phase separation using the order parameters with the phase-field model. Section 4.3, describes the three three particle distribution functions of the two fluid flows that represent the CH equation, pressureless NS equation and Poisson equation for correction of the velocity. Section 4.4, illustrates the algorithm of multiphase LBM with SRT. Section 4.5, The Chapman-Enskog expansion is presented for Solving multiphase flow. Finally, a summary of this chapter is given in Section 4.6.

4.2 Phase-field models

The main difficulties of multiphase simulations occur when modelling the interfacial dynamics between various phases. The phase-field models are the best of several models that represent the diffuse-interface models for multiphase flows. The key concept of the diffuse-interface models is to approximate the sharp-interfaces with non-zero thickness at the interface which guarantee smooth density, viscosity, and the physical properties for the multiphase (Fakhari et al. 2017).

The features of the phase-field methods constitute an easy technique to implement for the interface and can be easily applied to three spatial dimensions according to Jacqmin (1999). On the contrary, with tracking force models (Tryggvason et al. 2001), it needs the obligation to deal with topological variations, it does not maintain mass or volume and it demands the use of moving grids which might cause computational difficulties in tracking interfaces in three dimensions (Jacqmin 1999).

In phase-field model, following Banari et al. (2014), the total FE function can be written as a function of the order parameter $\phi(\zeta)$ to separate two phases of the fluid and the ζ is refer to the coordinate (Cahn & Hilliard 1958, Penrose & Fife 1990):

$$\mathcal{F} = \int_{\Omega} e_f(\phi, \nabla\phi)\, d\Omega, \tag{4.2.1}$$

where Ω is the domain occupied by the system and the free energy density (e_f) for two-phase an isothermal system proposed by Cahn & Hilliard (1958) as,

$$e_f = \frac{k}{2} |\nabla\phi|^2 + \beta\, \Psi(\phi)\,, \tag{4.2.2}$$

where $\frac{k}{2} |\nabla\phi|^2$ represents the gradient of FE which defines the surface energy at the interface region, β and k are parameters which depend on the surface tension coefficient $\sigma_{1\,2}$ and thickness of the interface D , and $\Psi(\phi)$ is bulk FE density which has a double-

well form (Jacqmin 1999),

$$\Psi(\phi) = (\phi - \phi_1)^2 \, (\phi - \phi_2)^2 \,, \tag{4.2.3}$$

with ϕ_1 and ϕ_2 are constant minima value that refer to fluid A and fluid B, respectively. The rate of the variation of the FE $\mathcal{F}$ with respect of the order parameter Ψ introduces the chemical potential μ_ϕ (Cahn & Hilliard 1958, Jacqmin 1999, Badalassi et al. 2003), and then ϕ satisfied Euler-Lagrange equation (Penrose & Fife 1990) as follows:

$$\mu_\phi = \frac{\delta \, \mathcal{F}}{\delta \, \phi} = \beta \, \acute{\Psi} - k \, \nabla^2 \phi = 4 \, \beta \, (\phi - \phi_0)(\phi - \phi_1) \, (\phi - \phi_2) - k \, \nabla^2 \phi \,, \tag{4.2.4}$$

where $\phi_0 = \dfrac{(\phi_1 + \phi_2)}{2}$. The interface profile at the equilibrium state (along the ζ coordinate) obtained by minimizing $\mathcal{F}$, which means $\mu_\phi = 0$, yields

$$k \, \frac{d^2 \phi}{d \zeta^2} = \beta \, \frac{d \Psi}{d \phi} \,, \tag{4.2.5}$$

by integrating both side with respect to ζ, yields

$$k \left(\frac{\partial \phi}{\partial \zeta} \right)^2 = 2 \, \beta \, \Psi \,, \tag{4.2.6}$$

which can be solved for ϕ as

$$\phi(\zeta) = \frac{(\phi_1 + \phi_2)}{2} + \frac{(\phi_1 - \phi_2)}{2} \tanh \left(\frac{2 \, \zeta}{W} \right) , \tag{4.2.7}$$

where

$$W = \frac{4}{(\phi_1 - \phi_2)} \sqrt{\frac{k}{2 \, \beta}} \,, \tag{4.2.8}$$

is the thickness of the interface (Rowlinson & Widom 1982, Jacqmin 1999, Badalassi et al. 2003) and they estimated the surface tension coefficient in a plane interface as,

$$\sigma_{1\,2} = k \int_{-\infty}^{\infty} \left(\frac{\partial \phi}{\partial \zeta}\right)^2 d\zeta \,. \tag{4.2.9}$$

By integrating eq. (4.2.9) for ϕ with respect to ζ:

$$\sigma_{1\,2} = \frac{2\,k}{3}\frac{(\phi_1 - \phi_2)^2}{W} = \frac{(\phi_1 - \phi_2)^3}{6}\sqrt{2\,k\,\beta}. \tag{4.2.10}$$

The diffusive interface motion can be represented by solving the CH equation as following the strategy of Jacqmin (1999), Banari et al. (2014)

$$\frac{\partial \phi}{\partial t} + \nabla .(\phi\,\mathbf{u}) = M\,\nabla^2\,\mu_\phi \,, \tag{4.2.11}$$

where M is a diffusion parameter named as mobility coefficient. The advection and diffusion of the interface movement appear in the left and right hand side of eq.(4.2.11), respectively. The β and k parameters can be computed from eqs. (4.2.8) and (4.2.10) which are determined by the interface thickness W and the coefficient of surface tension ($\sigma_{1\,2}$) (Banari et al. 2014). Three parameters were introduced to determine W and $\sigma_{1\,2}$ which is one considerable difference with respect to Inamuro et al.'s approach (Inamuro et al. 2004). Furthermore, the CH equation in their model included the pressure tensor $P_{\alpha\,\beta}$ term which is different than that suggested from (Banari et al. 2014). In the next section, the probability distribution functions with multiphase LBM in SRT will be presented to recover the CH equation.

4.3 Two phase LBM

In this section, the two phase LBM with SRT collision step will be introduced for three different probability distribution functions according to Banari et al. (2014) and then extending that to MRT collision step and using in chapters (7 - 8).

4.3.1 LBM for phase separation by Cahn-Hilliard equation

In order to solve the CH equation in eq.(4.2.11), the probability distribution functions $(f_i(\mathbf{x},t))$ is proposed for phase parameter (ϕ) according to the classical LBM approach as follows (Swift et al. 1996, Inamuro et al. 2004, Fakhari & Rahimian 2010, Banari et al. 2014).

$$f_i(\mathbf{x}+c_i\Delta t, t+\Delta t) - \ f_i(\mathbf{x},t) = -\frac{\Delta t}{\tau_f}\Big(f_i(\mathbf{x},t) - f_i^{(eq)}(\mathbf{x},t)\Big)\,, \tag{4.3.1}$$

where $\acute{\tau_f} = \tau_f/\Delta t$ is the dimensionless relaxation time and the equilibrium distribution functions $(f_i^{(eq)})$ can be written as

$$f_i^{(eq)} = H_i\,\phi + v_i\,\frac{M}{\tau_f - \frac{1}{2}\Delta t}\,\mu_\phi + \phi\,\omega_i\left[\frac{(c_{i\alpha}.\mathbf{u})}{c_s^2} + \frac{(c_{i\alpha}.\mathbf{u})^2}{2c_s^4} - \frac{u^2}{2c_s^2}\right], \tag{4.3.2}$$

where $c_{i\alpha}$ is the velocity with index $\alpha = (x,y) = (1,2)$, the weight function (ω_i) is defined in eq.(2.2.27) and

$$v_i = \begin{cases} \frac{-5}{3\,c^2}, & \text{for } \ i=0, \\ \frac{3\,w_i}{c^2}, & \text{for } \ i=1,2,\cdots,8\,, \end{cases} \tag{4.3.3}$$

with

$$H_i = \begin{cases} 1, & \text{for } i = 0, \\ 0, & \text{for } i = 1, 2, 3, \cdots, 8\,, \end{cases} \tag{4.3.4}$$

are weight functions defined according to (Swift et al. 1996, Inamuro et al. 2004, Banari et al. 2014). The zero, first and second order moments of f_i for the Phase-field models can be written as

$$\sum_i f_i = \phi\,, \tag{4.3.5}$$

$$\sum_i c_{i\alpha}\, f_i = \phi\, u_\alpha\,, \tag{4.3.6}$$

$$\sum_i c_{i\alpha}\, c_{i\beta}\, f_i = \frac{M}{\tau_f - \frac{1}{2}\Delta t}\, M_\phi\, \delta_{\alpha\beta} + \phi\, u_\alpha\, u_\beta\,. \tag{4.3.7}$$

The density ρ can be computed as function for ϕ values according to cut-off at the interface as defined below by Inamuro et al. (2004):

$$\rho(\phi) = \begin{cases} \rho_2, & \phi < \phi_2 \\ \frac{(\rho_1 - \rho_2)}{2}\left[\sin(\frac{\phi - \phi_0}{\phi_1 - \phi_2}\pi) + 1\right], & \phi_2 \leqslant \phi \leqslant \phi_1 \\ \rho_1, & \phi > \phi_1, \end{cases} \tag{4.3.8}$$

or use the linear interpolation to differ smoothly across the interface as pointed out from Banari et al. (2014):

$$\rho(\phi) = \begin{cases} \rho_2, & \phi \leqslant \phi_2 \\ \frac{(\phi-\phi_2)}{(\phi_1-\phi_2)}(\rho_1-\rho_2)+\rho_2, & \phi_2 < \phi < \phi_1 \\ \rho_1, & \phi \geqslant \phi_1, \end{cases} \tag{4.3.9}$$

where ρ_1 and ρ_2 are represent the densities of the two phase.

Same technique is used to compute the kinematic viscosity as a function of density, hence in the current multiphase LB study the dynamic viscosity or vice versa is determined as

$$\nu(\rho) = \frac{(\rho-\rho_2)}{(\rho_1-\rho_2)}(\nu_1-\nu_2)+\nu_2 \quad \text{and} \quad \mu(\rho) = \rho(\phi)\,\nu(\rho). \tag{4.3.10}$$

4.3.2 LBM for Pressure-less Navier-Stokes equation

Nadiga & Zaleski (1995) pointed out that the mass and momentum conservation equations for ideal gases such as the Navier–Stokes equations with absence of force terms can be written as

$$\frac{\partial \rho}{\partial_t} + \frac{\partial \rho u_\alpha}{\partial x_\alpha} = 0, \tag{4.3.11}$$

$$\rho\Big\{\frac{\partial u_\alpha}{\partial_t} + u_\beta \frac{\partial u_\alpha}{\partial x_\beta}\Big\} = \frac{\partial \sigma^{(ig)}_{\alpha\beta}}{\partial x_\beta}\,, \tag{4.3.12}$$

where ρ is a function of ϕ in two phase model and $\sigma^{(ig)}_{\alpha\beta}$ is the stress of ideal-gas (Lee & Lin 2005)

$$\sigma^{(ig)}_{\alpha\,\beta} = -P\,\delta_{\alpha\beta} + \mu\Big(\frac{\partial u_\alpha}{\partial x_\beta} + \frac{\partial u_\beta}{\partial x_\alpha}\Big)\,, \tag{4.3.13}$$

where the first term is the thermodynamic pressure and the second term is the viscous stress tensor $\sigma_{\alpha\,\beta}^{visc}$ which includes the dynamic viscosity μ of the two fluid system.

In this model, the essential concept is represented by adding the force term to the NS equation which is obtained thermodynamically from the CH equation free energy (Nadiga & Zaleski 1995). That means the eq. (4.3.12) changes to non-ideal form after adding the surface tension force

$$\rho\Big\{\frac{\partial u_\alpha}{\partial_t} + u_\beta \frac{\partial u_\alpha}{\partial x_\beta}\Big\} = \frac{\partial \sigma_{\alpha\beta}}{\partial x_\beta}\,, \tag{4.3.14}$$

where $\sigma_{\alpha\beta}$ contains three terms (Lee & Lin 2005)

$$\sigma_{\alpha\,\beta} = -P\,\delta_{\alpha\beta} + \sigma_{\alpha\,\beta}^{visc} + \sigma_{\alpha\,\beta}^{st}\,, \tag{4.3.15}$$

and with the gradient of the order parameter of $\sigma_{\alpha\,\beta}^{st}$ takes the form

$$\sigma_{\alpha\,\beta}^{st} = k\,\Big\{\Big(\frac{1}{2}\frac{\partial\phi}{\partial x_\gamma}\frac{\partial\phi}{\partial x_\gamma} + \phi\frac{\partial^2\phi}{x_\gamma\,x_\gamma}\Big)\delta_{\alpha\beta} - \Big(\frac{\partial\phi}{\partial x_\alpha}\frac{\partial\phi}{\partial x_\beta}\Big)\Big\}\,, \tag{4.3.16}$$

Lee & Lin (2005) developed the pressure P effect by adding new terms P^{new} to preserve the equipoise between the pressure and the $\sigma_{\alpha\,\beta}^{st}$ term which leads to improve the stability of the numerical computations (Banari et al. 2014) as

$$P^{new}\delta_{\alpha\beta} = P\delta_{\alpha\beta} + k\,\Big(\frac{1}{2}\frac{\partial\phi}{\partial x_\gamma}\frac{\partial\phi}{\partial x_\gamma} - \phi\frac{\partial^2\phi}{x_\gamma\,x_\gamma}\Big)\delta_{\alpha\beta}\,, \tag{4.3.17}$$

by substitution of eq.(4.3.17) in eq.(4.3.15), the new form of $\sigma_{\alpha\,\beta}$ is obtained (Banari et al. 2014)

$$\sigma_{\alpha\,\beta} = -P^{new}\delta_{\alpha\beta} + \mu\Big(\frac{\partial u_\alpha}{\partial x_\beta} + \frac{\partial u_\beta}{\partial x_\alpha}\Big) + k\,\Big\{\frac{\partial\phi}{\partial x_\gamma}\frac{\partial\phi}{\partial x_\gamma}\delta_{\alpha\beta} - \frac{\partial\phi}{\partial x_\alpha}\frac{\partial\phi}{\partial x_\beta}\Big\}\,, \tag{4.3.18}$$

which can deal with large force of surface tension and also obtain smooth differ at interfaces for two fluid flows.

The mass and momentum in eqs. (4.3.11) and (4.3.14) with the simplest form of the force term ($B_i = \omega_i c_{i\alpha} B_\alpha / c_s^2$) as suggested by (He et al. 1997, Buick & Greated 2000) can be recovered from the particle distribution function ($g_i(\mathbf{x}, t)$) as

$$g_i(\mathbf{x} + c_i\Delta t, t + \Delta t) - g_i(\mathbf{x}, t) = -\frac{\Delta t}{\tau_g}(g_i(\mathbf{x}, t) - g_i^{(eq)}(\mathbf{x}, t)) + \Delta t\, B_i, \tag{4.3.19}$$

where $\acute{\tau}_g = \tau_g/\Delta t$ is the dimensionless relaxation time. Banari et al. (2014) claimed that the classical LBM for the multiphase model is limited to low density ratios. The equilibrium distribution function ($g_i^{(eq)}$), can be defined as

$$g_i^{(eq)} = \omega_i \left[1 + \frac{(c_{i\alpha}.\mathbf{u})}{c_s^2} + \frac{(c_{i\alpha}.\mathbf{u})^2}{2c_s^4} - \frac{u^2}{2c_s^2}\right] + \omega_i\, k\, G_{\alpha\beta} c_{i\alpha} c_{i\beta} - v_i \frac{k}{2} |\nabla\phi|^2, \tag{4.3.20}$$

where

$$G_{\alpha\beta} = \frac{9}{2\,c^4}\left(\frac{\partial\phi}{\partial x_\alpha}\frac{\partial\phi}{\partial x_\beta}\right) - \frac{9}{4\,c^4}\left(\frac{\partial\phi}{\partial x_\gamma}\frac{\partial\phi}{\partial x_\gamma}\right)\delta_{\alpha\beta}, \tag{4.3.21}$$

is the same formula presented by Swift et al. (1996), Inamuro et al. (2004) and Banari et al. (2014) that can be written as

$$G = \frac{9}{2c^4}\begin{bmatrix} G_{11} & G_{12} \\ G_{21} & G_{22} \end{bmatrix}, \tag{4.3.22}$$

where

$$G_{11} = -G_{22} = \frac{1}{2}\left[(\frac{\partial\phi}{\partial x_1})^2 - (\frac{\partial\phi}{\partial x_2})^2\right] \text{ and } G_{12} = G_{21} = \frac{\partial\phi}{\partial x_1}\frac{\partial\phi}{\partial x_2}.$$

The particle distribution function $(g_i(\mathbf{x}, t))$ should satisfy the following constraints:

$$\sum_i g_i^{(eq)} = \rho \,, \tag{4.3.23}$$

$$\sum_i c_{i\alpha} g_i^{(eq)} = \rho \, u_\alpha \,, \tag{4.3.24}$$

$$\sum_i c_{i\alpha} \, c_{i\beta} \, g_i^{(eq)} = \rho \, u_\alpha \, u_\beta + k \left(\frac{\partial \phi}{\partial x_\alpha} \frac{\partial \phi}{\partial x_\beta} \right) + \left(\rho \, c_s^2 - k \, \frac{\partial \phi}{\partial x_\gamma} \frac{\partial \phi}{\partial x_\gamma} \right) \delta_{\alpha\beta} \,, \tag{4.3.25}$$

In order to improve the multiphase LB simulations for high density ratios, the bulk density is removed from eqs. (4.3.23), (4.3.23) and (4.3.25) as suggested by Inamuro et al. (2004) and based on Banari et al. (2014) model. This leads to absence of the gradient of the pressure which known as pressureless NS equations. The equilibrium distribution function proposed by Banari et al. (2014) is

$$g_i^{(eq)} = \omega_i \left[\frac{(c_{i\alpha}.\mathbf{u}^*)}{c_s^2} + \frac{(c_{i\alpha}.\mathbf{u}^*)^2}{2c_s^4} - \frac{u^{*2}}{2c_s^2} \right] + \omega_i \frac{k}{\rho} \, G_{\alpha\beta} c_{i\alpha} c_{i\beta} - v_i \frac{k}{2\rho} \, |\nabla \phi|^2, \tag{4.3.26}$$

The new constraints for the zero, first and second order moments of $(g_i^{(eq)})$ with absence the pressure can be define as

$$\sum_i g_i^{(eq)} = 0 \,, \tag{4.3.27}$$

$$\sum_i c_{i\alpha} g_i^{(eq)} = u_\alpha^* \,, \tag{4.3.28}$$

$$\sum_i c_{i\alpha}\, c_{i\beta}\, g_i^{(eq)} = u_\alpha^*\, u_\beta^* + \frac{k}{\rho}\left(\frac{\partial\phi}{\partial x_\alpha}\frac{\partial\phi}{\partial x_\beta}\right) - \frac{k}{\rho}\left(\frac{\partial\phi}{\partial x_\gamma}\frac{\partial\phi}{\partial x_\gamma}\right)\delta_{\alpha\beta}\,, \tag{4.3.29}$$

where u_α^* refers to the pressureless velocity. In general, the pressure value in classical LBM is computed from zero order moment of $g_i^{(eq)}$ in (4.3.23) and because this constraint is changed in the improved multiphase LBM models leads to the absence of density in (4.3.27). The second order moment of $g_i^{(eq)}$ in eqs.(4.3.29) is different than Banari et al. (2014) equation which is without c_s^2 as shown by details in the appendix B.1.

Chapman & Cowling (1970) proposed the Chapman-Enskog expansion for LBE to recover the NS equation. This expansion is used for LBE with a suitable equilibrium distribution function as defined in eq.(4.3.19) and eqs.(4.3.26), respectively. So the resulting (pressureless) equation can be written as

$$\begin{aligned}\frac{\partial u_\alpha^*}{\partial_t} + u_\beta^*\frac{\partial u_\alpha^*}{\partial x_\beta} = \frac{k}{\rho}\frac{\partial}{\partial x_\beta}\Big\{\Big(\frac{\partial\phi}{\partial x_\gamma}\frac{\partial\phi}{\partial x_\gamma}\Big)\delta_{\alpha\beta} - \Big(\frac{\partial\phi}{\partial x_\alpha}\frac{\partial\phi}{\partial x_\beta}\Big)\Big\} \\ + \frac{\partial}{\partial x_\beta}\Big\{\frac{\mu}{\rho}\Big(\frac{\partial u_\alpha^*}{\partial x_\beta} + \frac{\partial u_\beta^*}{\partial x_\alpha}\Big)\Big\} - \mu\Big(\frac{\partial u_\alpha^*}{\partial x_\beta} + \frac{\partial u_\beta^*}{\partial x_\alpha}\Big)\frac{\partial}{\partial x_\beta}\frac{1}{\rho} + \frac{B_\alpha}{\rho},\end{aligned} \tag{4.3.30}$$

From the definition of pressureless surface tension $(\sigma_{\alpha\,\beta}^*)$, yields

$$\sigma_{\alpha\,\beta}^* = \frac{k}{\rho}\Big\{\Big(\frac{\partial\phi}{\partial x_\gamma}\frac{\partial\phi}{\partial x_\gamma}\Big)\delta_{\alpha\beta} - \Big(\frac{\partial\phi}{\partial x_\alpha}\frac{\partial\phi}{\partial x_\beta}\Big)\Big\} + \Big\{\frac{\mu}{\rho}\Big(\frac{\partial u_\alpha^*}{\partial x_\beta} + \frac{\partial u_\beta^*}{\partial x_\alpha}\Big)\Big\}\,. \tag{4.3.31}$$

According to Banari et al. (2014), the previous equation and eq.(4.3.19) with the sim-

ple body force (B_α) which was defined from (Buick & Greated 2000) the LBM for multiphase for the pressureless velocity takes the follow form,

$$g_i(\mathbf{x}+c_i\Delta t, t+\Delta t) - g_i(\mathbf{x},t) = -\frac{\Delta t}{\tau_g}(g_i(\mathbf{x},t) - g_i^{(eq)}(\mathbf{x},t)) + \frac{3}{c^2}\omega_i\, c_{i\alpha}\,\Delta t\left\{\frac{B_\alpha}{\rho} - \sigma^{visc,*}_{\alpha\,\beta}\frac{\partial}{\partial x_\beta}\left(\frac{1}{\rho}\right)\right\}, \quad (4.3.32)$$

where

$$\sigma^{visc,*}_{\alpha\,\beta} = \mu\Big(\frac{\partial u^*_\alpha}{\partial x_\beta} + \frac{\partial u^*_\beta}{\partial x_\alpha}\Big)\,, \quad (4.3.33)$$

is viscous stress tensor with $\mathbf{u}^*$ and body force $B_\alpha = \rho\, g_\alpha$.

4.3.3 Correction of velocity field based on a Poisson equation.

As in Inamuro et al. (2004), Banari et al. (2014) presented the diffusive Poisson equation to correct the pressureless velocity $\mathbf{u}^*$ which is computed from first order moment of $g_i(\mathbf{x},t)$ at each time step in the pressureless NS eq.(4.3.30). For fully solving the NS equation, a new particle distribution function $h_i(\mathbf{x},t)$ is presented to calculate the pressure term and obtain the proper velocity field $\mathbf{u}$ by adding $(\Delta\mathbf{u})$ term to pressureless velocity $\mathbf{u}^*$ (Banari et al. 2014). The Poisson equation according to (Inamuro et al. 2004) defined as,

$$\nabla.\,(\frac{\Delta t\,\nabla p}{\rho}) = \nabla.\mathbf{u}^*\,, \quad (4.3.34)$$

which is recovered from pressureless velocity $\mathbf{u}^*$ in order to satisfy the continuity equation

$$\nabla.\,\mathbf{u} = 0\,. \quad (4.3.35)$$

The pressure term in the Poisson eq.(4.3.34) equivalents to the correction part of the pressureless velocity $\mathbf{u}^*$ as

$$\Delta\mathbf{u} \cong -\frac{\Delta t\,\nabla p}{\rho}\,, \tag{4.3.36}$$

and

$$\mathbf{u} = \mathbf{u}^* + \Delta\mathbf{u}. \tag{4.3.37}$$

Many different method are available for discretization of the Poisson equation such as Finite Element and Finite Difference Methods (Golberg 1995). Here in the current study follow Banari et al. (2014), who solved the equation by using LBM. So the third particle distribution function $h_i(\mathbf{x}, t)$ presented for Poisson equation as

$$h_i^n(\mathbf{x} + c_i\Delta t, t + \Delta t) - h_i^n(\mathbf{x}, t) = -\frac{\Delta t}{\tau_h}\Big(h_i^n(\mathbf{x}, t) - h_i^{(eq,n)}(\mathbf{x}, t)\Big) - \Delta t\,\omega_i\left(\nabla.\mathbf{u}^*(t)\right), \tag{4.3.38}$$

with suitable equilibrium distribution function

$$h_i^{(eq,n)} = \omega_i\,\frac{p^n(\mathbf{x}, \mathbf{t})}{\rho_o\,c^2}\,, \tag{4.3.39}$$

where n refer to the iteration which obtain the stable solution, ρ_o the reference density and

$$\tau_h = \Delta t\left(\frac{1}{2} + \frac{\rho_o\,c^2}{\rho\,c_s^2}\right), \tag{4.3.40}$$

is the relaxation time. According to Banari et al. (2014) definition of LBM parameters for the length scale (λ_x) and mass scale (λ_m) with of $\acute{\rho} = \rho\,\lambda_x^3/\lambda_m$ and $\acute{\rho}_0 = \rho_0\,\lambda_x^3/\lambda_m$. It observed that in the current study different form of the dimensionless relation time $\acute{\tau}_h = \tau_h/\Delta t$ than Banari et al. (2014) form which define as

$$\acute{\tau}_h = \frac{1}{2} + \frac{\rho_0\,c^2}{\rho\,c_s^2} = \frac{1}{2} + \frac{3\,\acute{\rho}_0}{\acute{\rho}}\,, \tag{4.3.41}$$

where ρ_0 is the reference density, the non-dimensional form of ρ_0 which is $(\acute{\rho}_0)$ equal to 1 for simplicity.

The zero order moments of the particle distribution function $h_i^{(n)}$ is used to compute the pressure as defined below

$$\sum_i h_i^{(n)} = \frac{p^{n+1}}{\rho_0\,c^2}\,, \tag{4.3.42}$$

where $\rho_0 = 1$ (in lattice unit), $\acute{\rho}_1 = \rho_1/\rho_0$ and $\acute{\rho}_2 = \rho_2/\rho_0$. The iterative process is used until stable computation is achieved. Then use the accurate value of pressure which leads to the obtain the pressure gradient and correct the velocity.

4.4 The Algorithm of Multiphase LBM

The algorithm of multiphase LBM with high density ratio is illustrated in Figure (4.1). In general, the definitions and scale the parameters is used in each simulation according the domain and geometry. After the boundary of the fluid flow is known, the particle distribution functions $f_i(\mathbf{x}, t)$, $g_i(\mathbf{x}, t)$ and $h_i^n(\mathbf{x}, t)$ at the boundary is specified such as bounce back or a periodic boundary condition. The boundary with respect to $h_i(\mathbf{x}, t)$ that represented by a correction of velocity with pressure Poisson equation and

according to NS equation, as supposed from Banari et al. (2014), can be defined as

$$\frac{\partial p}{\partial y} = -\rho\, g + \mu\Big(\frac{\partial^2 u_y}{\partial x^2} + \frac{\partial^2 u_y}{\partial y^2}\Big)\,, \tag{4.4.1}$$

the Taylor expansion for FDM used to define the pressure at the top boundary $(x = x_n)$, as follow

$$\frac{\partial p(x_n, y_n, t)}{\partial y}\,\Delta x = p(x_n, y_n, t) - p(x_n, y_n - \Delta x, t)\,, \tag{4.4.2}$$

which is simplified from eq.(4.4.1) to

$$p(x_n, y_n, t) = p(x_n, y_n - \Delta x, t) - \rho\, g + \mu\Big(\frac{\partial^2 u_y}{\partial x^2} + \frac{\partial^2 u_y}{\partial y^2}\Big)\,. \tag{4.4.3}$$

Thus the unknown $h_i(\mathbf{x}_n, t)$ can be computed from their equilibrium distribution function $h_i^{(eq)}(\mathbf{x}_n, t)$ as

$$h_i(\mathbf{x}_n, t) = h_i^{(eq)}(p(\mathbf{x}_n, t))\,. \tag{4.4.4}$$

When initialize all values such as time, phases, densities, radius, domain, length, velocity, viscosity and etc. From the zero order moment of distribution function $f_i(\mathbf{x}, t)$, the phases that represented by the order parameter is computed from eq.(4.3.5). By defining the order parameter, the densities of the fluid can be computed smoothly across interface according to the linear interpolation of the order parameters in eq.(4.3.8) or (4.3.9).

In the meantime from the first order moment of the equilibrium distribution function $g_i^{eq}(\mathbf{x}, t)$, the pressureless velocity (u^*) is computed according to eq.(4.3.28). In order to correct this velocity (u^*), the third particle distribution function is defined $h_i(\mathbf{x}, t)$ for

pressure Poisson equation which is the pressure computed from (4.3.42) by an iterative process as

$$\left| \frac{p^{(n+1)} - p^{(n)}}{p^{(n)}} \right| \leq \ tol, \tag{4.4.5}$$

where the tolerance $tol = 10^{-5}$.

The central finite difference approximations of first and second order are used according to Lee & Lin (2005) and Banari et al. (2014) to calculate the first and second derivatives with respect to space (x_α) for eqs.(4.2.4), (4.3.21), (4.3.26), (4.3.32), (4.3.33) and (4.3.36), as shown below

$$\frac{\partial \phi}{\partial x_\alpha} = \sum_{i=0}^{8} \omega_i \, c_i \, \frac{\phi(\mathbf{x} + c_i \Delta t) - \phi(\mathbf{x} - c_i \Delta t)}{2 c_s^2 \, \Delta t} \,, \tag{4.4.6}$$

and

$$\frac{\partial^2 \phi}{\partial x_\alpha^2} = \sum_{i=0}^{8} \omega_i \, \frac{\phi(\mathbf{x} + c_i \Delta t) - 2\,\phi(\mathbf{x}) + \phi(\mathbf{x} - c_i \Delta t)}{c_s^2 \, \Delta t^2} \,, \tag{4.4.7}$$

where α refer to 1, 2 -coordinate (in the x or y-directions) in the D_2Q_9 lattice model and these derivatives can be used for any related variables. For more details for the computation see appendix C.

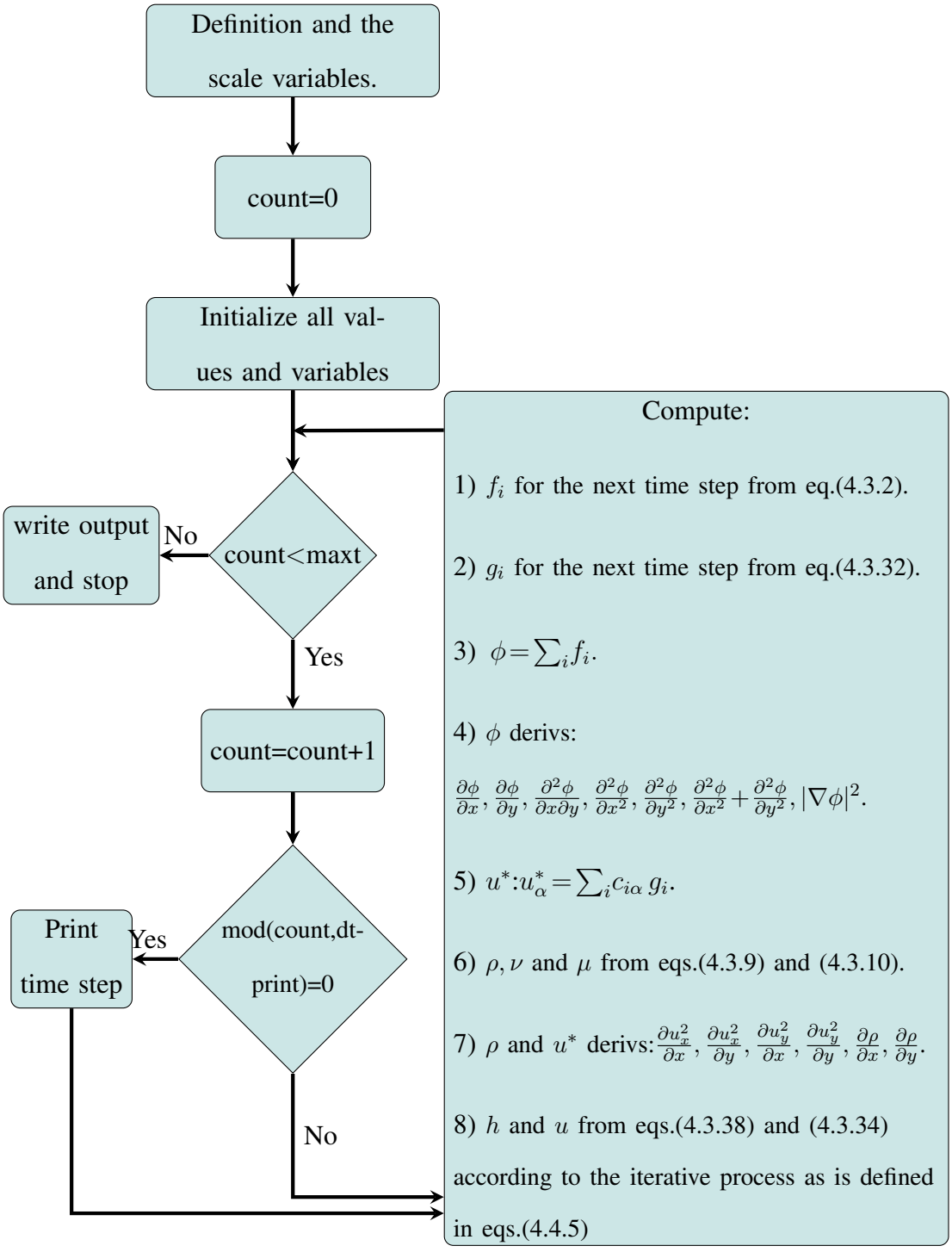

Figure 4.1: The Algorithm for Multiphase LBM.

4.5 Chapman-Enskog Expansion for Solving Multiphase Flow

4.5.1 Chapman-Enskog expansion for recovery pressure-less Navier-Stokes equations

In this section, It observed that the LBGK equation

$$g_i(\mathbf{x}+c_i\Delta t, t+\Delta t) - \ g_i(\mathbf{x},t) = -\frac{\Delta t}{\tau_g}(g_i(\mathbf{x},t) - g_i^{(eq)}(\mathbf{x},t)) + \Delta t\ B_i, \tag{4.5.1}$$

with the equilibrium distribution function of D_2Q_9

$$g_i^{(eq)} = \ \omega_i \left[\frac{(c_{i\alpha}.\mathbf{u}^*)}{c_s^2} + \frac{(c_{i\alpha}.\mathbf{u}^*)^2}{2c_s^4} - \frac{u^{*2}}{2c_s^2}\right] + \omega_i \frac{k}{\rho}\, G_{\alpha\beta}c_{i\alpha}c_{i\beta} - v_i\frac{k}{2\rho}\,|\nabla\phi|^2, \tag{4.5.2}$$

leads to the macroscopic (pressureless) Navier-Stokes equations

$$\frac{\partial u_\alpha^*}{\partial_t} + u_\beta^*\,\frac{\partial u_\alpha^*}{\partial x_\beta} = \frac{k}{\rho}\,\frac{\partial}{\partial x_\beta}\left\{\left(\frac{\partial\phi}{\partial x_\gamma}\frac{\partial\phi}{\partial x_\gamma}\right)\delta_{\alpha\beta} - \left(\frac{\partial\phi}{\partial x_\alpha}\frac{\partial\phi}{\partial x_\beta}\right)\right\} + \frac{\partial}{\partial x_\beta}\left\{\frac{\mu}{\rho}\left(\frac{\partial u_\alpha^*}{\partial x_\beta} + \frac{\partial u_\beta^*}{\partial x_\alpha}\right)\right\}$$
$$- \mu\,\left(\frac{\partial u_\alpha^*}{\partial x_\beta} + \frac{\partial u_\beta^*}{\partial x_\alpha}\right)\,\frac{\partial}{\partial x_\beta}\,\frac{1}{\rho} + \frac{B_\alpha}{\rho}, \tag{4.5.3}$$

where

$$\frac{\mu}{\rho} = \nu = c_s^2\left(\acute{\tau}_g - \frac{1}{2}\,\Delta t\right). \tag{4.5.4}$$

Full details are given in appendix B.1.

4.5.2 Chapman-Enskog expansion for satisfying the Cahn-Hilliard equation

Here the LBGK equation

$$f_i(\mathbf{x} + c_i\Delta t, t + \Delta t) - \ f_i(\mathbf{x}, t) = -\frac{\Delta t}{\tau_f}\Big(f_i(\mathbf{x}, t) - f_i^{(eq)}(\mathbf{x}, t)\Big)\,, \tag{4.5.5}$$

with the equilibrium distribution function of $D_2\,Q_9$

$$f_i^{(eq)} = H_i\,\phi + v_i\,\frac{M}{\tau_f - \frac{1}{2}\Delta t}\,M_\phi + \phi\,\omega_i\left[\frac{(c_{i\alpha}.\mathbf{u})}{c_s^2} + \frac{(c_{i\alpha}.\mathbf{u})^2}{2c_s^4} - \frac{u^2}{2c_s^2}\right]\,, \tag{4.5.6}$$

recovers the diffusive interface motion modeled by the Cahn-Hilliard (CH) equation,

$$\frac{\partial\phi}{\partial_t} + \nabla.(\phi\,\mathbf{u}) = M\,\nabla^2\,M_\phi\,, \tag{4.5.7}$$

where M diffusive is the coefficient (Mobility) and

$$M_\phi = \beta\,\acute{\Psi} - k\,\nabla^2\,\phi\,, \tag{4.5.8}$$

is the chemical potential, where β and k are parameters which depend on the surface tension coefficient $\sigma_{1\,2}$ and thickness of the interface D, Ψ is related to bulk FE density and $\nabla\,\phi$ is the energy gradient. Full details are given in appendix B.2.

4.5.3 Chapman-Enskog expansion for solving pressure Poisson equation

The Chapman-Enskog expansion is applied to the LB equation for solving pressure Poisson equation

$$h_i^n(\mathbf{x}+c_i\Delta t, t+\Delta t) - h_i^n(\mathbf{x},t) = -\frac{\Delta t}{\tau_h}\left(h_i^n(\mathbf{x},t) - h_i^{(eq,n)}(\mathbf{x},t)\right) - \Delta t\,\omega_i\left(\nabla.\mathbf{u}^*(t)\right), \tag{4.5.9}$$

where n is $n-$ th iteration for the pressure, with the equilibrium distribution function of the $D_2\,Q_9$ lattice model

$$h_i^{(eq,n)} = \omega_i\,\frac{p^n(\mathbf{x},\mathbf{t})}{\rho_o\,c^2}\,, \tag{4.5.10}$$

where

$$\tau_h = \Delta t\left(\frac{1}{2} + \frac{\rho_o\,c^2}{\rho\,c_s^2}\right). \tag{4.5.11}$$

This leads to

$$\nabla.\,(\frac{\Delta t\,\nabla p}{\rho}) = \nabla.\mathbf{u}^*\,, \tag{4.5.12}$$

the Poisson equation. For more details see appendix B.3.

4.6 Summary

In this chapter, a single relaxation time multiphase LBM model was introduced. Following the Banari et al. (2014) model, the motion of the interface between fluids is modelled by solving the Cahn-Hilliard equation based on free energy density with LBM. Incompressibility of the velocity fields in each phase is imposed by using a pressure correction scheme. A unified LBM approach is used with separate formulations for the phase field, the pressure-less Navier-Stokes (NS) equations and the pressure Poisson equation required for correction of the velocity field. Also, the implementation of the algorithm for multiphase in SRT LBM is illustrated. Finally, the Chapman-Enskog expansion for solving multiphase LBM is derived.

Chapter 5

Verifications of Multiphase LBM

5.1 Introduction

In order to improve the multiphase LB approach proposed by Banari et al. (2014) is extended from SRT to the MRT. This development improves the stability of the computations with high Re. In this chapter, it should be apply the simulations that is used in the literature with SRT such as two fluid Poiseuille flow, static and a rising bubble flows in order to investigate the codes of the current work for multiphase LBM.

This chapter consists of the following sections. Sections 5.2 - 5.3 include the analytic solution and the convergence of implementations of two fluid Poiseuille flow with different lattice grids. Section 5.4 investigates the pressure jump by the Laplace law for two static initial square and circular droplets. Section 5.5 presents the study of non-dimensional velocity profile for the terminal shapes of the rising bubble. Finally, the summary of this chapter is given in Section 5.6.

5.2 Implementations

In the simulations, the lattice variables are given as: $\Delta\acute{x} = \Delta\acute{t} = \acute{c} = 1$. For the stability of LB simulations require that the non-dimensional relaxation time $(\acute{\tau}_g)$ to satisfy $0.5 < \acute{\tau}_g \leqslant 1$ for solving Navier-Stokes equation (Yu et al. 2003). The non-dimensional relaxation time $(\acute{\tau}_f)$ is recovered from a Cahn-Hilliard equation by

satisfying $\acute{\tau_f} = 1$ (Inamuro et al. 2004, Banari et al. 2014). The order parameters are chosen to be $\phi_1 = 0.4,\ \phi_2 = 0.1$ or $\phi_1 = 1,\ \phi_2 = 0$ with the interface thickness $\acute{W} = 4$ and for more stable simulations the mobility is chosen to be $\acute{M} = \frac{0.02}{\beta}$ according to Banari et al. (2014). Using the interface thickness (W) and the coefficient of surface tension $(\sigma_{1\,2})$, the parameters of interface $\acute{k}$ and $\acute{\beta}$ can be defined as follow

$$\acute{k} = \frac{6\,\acute{\sigma}_{1\,2}}{(\phi_1 - \phi_2)^2}, \tag{5.2.1}$$

and

$$\acute{\beta} = \frac{3\,\acute{\sigma}_{1\,2}}{(\phi_A - \phi_2)^4}, \tag{5.2.2}$$

where

$$\acute{\sigma}_{1\,2} = \frac{\sigma_{1\,2}}{\rho_0\, c^2\, \Delta x},\ \text{with}\ \acute{k} = \frac{k}{\rho_0\, c^2\, \Delta x^2},\ \text{with}\ \acute{\beta} = \frac{\beta}{\rho_0\, c^2}\,. \tag{5.2.3}$$

The non-dimensional relaxation time $(\acute{\tau_h})$ satisfying Poisson equation as suggested by Grunau et al. (1993), Banari et al. (2014) should be defined as
$0.5 < \acute{\tau_h} \leqslant 1$ where $\acute{\tau_h} = \tau_h/\Delta t$ in eq.(4.3.38). This leads to determine the minimum density values $(6 \leqslant \acute{\rho_1}$ or $\acute{\rho_2})$.

5.3 Two fluid Poiseuille flow

5.3.1 Analytic solution of Two fluid Poiseuille flow

The Poiseuille flow consists of two immiscible fluid between two horizontally parallel plates with the angle (α) is equal to $\frac{\pi}{2}$ as illustrated in Figure (5.1). The flow has

different phase (ϕ_i), dynamic viscosities (μ_i), velocities(u_i) and densities (ρ_i) where $i = 1, 2$. The surface tension is taken to be zero. The two fluids are driven by a body force $(\rho\, g)$ in the $x-$direction (Zu & He 2013, Huang et al. 2015).

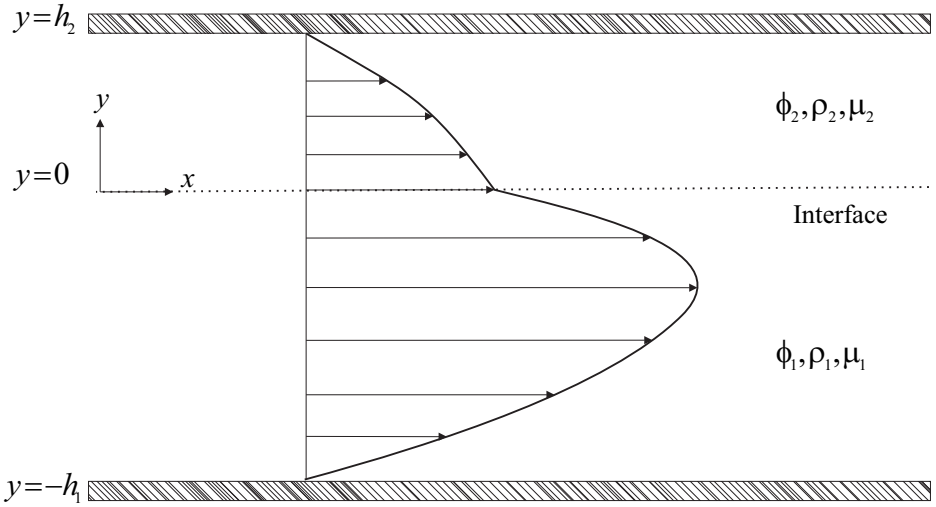

Figure 5.1: The two fluid flow configuration for Poiseuille flow between two parallel plates.

An analytical solution for Poiseuille flow is considered as a perfect technique to investigate the high density ratio (ρ_1/ρ_2) and high kinematic viscosity ratio (ν_1/ν_2). The fully developed of the velocity of Poiseuille flow, so the NS equations can be written as

$$\mu \frac{d^2u}{d\,y^2} = G = -\rho\, g\,, \tag{5.3.1}$$

so

$$u(y) = \frac{G}{2\,\mu}\, y^2 + B\, y + C\,, \tag{5.3.2}$$

the velocity components in the two fluid flow, reads

$$u_1(y) = \frac{-\rho_1\, g}{2\,\mu_1}\, y^2 + B_1\, y + C_1\,, \tag{5.3.3}$$

and

$$u_2(y) = \frac{-\rho_2\, g}{2\,\mu_2}\, y^2 + B_2\, y + C_2\,. \tag{5.3.4}$$

Applying the boundary conditions at the interface the constant values B_1, B_2, C_1 and C_2 can be evaluated. At the upper and lower boundaries, the no-slip condition is used $(u_1(-h_1) = u_2(h_2) = 0)$ where h_1 and h_2 are the depths of the two fluid Poiseuille flow. The continuity of fluid velocity $(u_1(0) = u_2(0))$ and stresses $(\mu_1 \frac{du_1(0)}{dy} = \mu_2 \frac{du_2(0)}{dy})$ have to be satisfied at the interface of two the fluid. From the continuity of fluid velocity, $C_1 = C_2$ and from the continuity of fluid stresses, the $B_2 = \dfrac{\mu_1}{\mu_2}\, B_1$ is obtained. By applying the upper and lower no- slip boundary conditions, yields

$$u_1(-h_1) = \frac{-\rho_1\, g}{2\,\mu_1}\, h_1^2 - B_1\, h_1 + C_1 = 0\,, \tag{5.3.5}$$

and

$$u_2(h_2) = \frac{-\rho_2\, g}{2\,\mu_2}\, h_2^2 + \frac{\mu_1}{\mu_2}\, B_1\, h_2 + C_2 = 0\,. \tag{5.3.6}$$

From the eqs. (5.3.5) and (5.3.6), yield

$$B_1 = \frac{-g}{2}\, \frac{\left(\mu_2\, \rho_1\, h_1^2 - \mu_1\, \rho_2\, h_2^2\right)}{\mu_1\left(h_1\, \mu_2 + h_2\, \mu_1\right)}\,. \quad \text{and} \quad B_2 = \frac{-g}{2}\, \frac{\left(\mu_2\, \rho_1\, h_1^2 - \mu_1\, \rho_2\, h_2^2\right)}{\mu_2\left(h_1\, \mu_2 + h_2\, \mu_1\right)}\,,$$

By substituting B_1 and B_1 in eqs. (5.3.5) and (5.3.6):

$$u_1(-h_1) = \frac{-\rho_1\, g}{2\,\mu_1}\, h_1^2 + \frac{g}{2}\, \frac{\left(\mu_2\, \rho_1\, h_1^2 - \mu_1\, \rho_2\, h_2^2\right)}{\mu_1\left(h_1\, \mu_2 + h_2\, \mu_1\right)}\, h_1 + C_1 = 0\,, \tag{5.3.7}$$

and

$$u_2(h_2) = \frac{-\rho_2\, g}{2\,\mu_2}\, h_2^2 - \frac{g}{2}\, \frac{\left(\mu_2\, \rho_1\, h_1^2 - \mu_1\, \rho_2\, h_2^2\right)}{\mu_2\left(h_1\, \mu_2 + h_2\, \mu_1\right)}\, h_2 + C_1 = 0\,. \tag{5.3.8}$$

The eqs. (5.3.7) and (5.3.8) can be simplified to,

$$-\left(\frac{\mu_1}{h_1} + \frac{\mu_2}{h_2}\right) C_1 = \frac{-g}{2}\left(\rho_1\, h_1 + \rho_2\, h_2\right),$$

then,

$$C_1 = C_2 = \frac{g}{2}\, \frac{\left(\rho_1\, h_1 + \rho_2\, h_2\right) h_1\, h_2}{\left(h_1\, \mu_2 + h_2\, \mu_1\right)}\,,$$

By substituting $B_1,\, B_2,\, C_1$ and C_2 into eqs. (5.3.3) and (5.3.4), the velocities of two phases is obtained as

$$u_1(y) = \frac{g}{2}\left[\frac{-\rho_1}{\mu_1} y^2 - \frac{\left(\mu_2\, \rho_1\, h_1^2 - \mu_1\, \rho_2\, h_2^2\right)}{\mu_1\left(h_1\, \mu_2 + h_2\, \mu_1\right)}\, y + \frac{\left(\rho_1\, h_1 + \rho_2\, h_2\right) h_1\, h_2}{\left(h_1\, \mu_2 + h_2\, \mu_1\right)}\right], \tag{5.3.9}$$

and

$$u_2(y) = \frac{g}{2}\left[\frac{-\rho_2}{\mu_2} y^2 - \frac{\left(\mu_2\, \rho_1\, h_1^2 - \mu_1\, \rho_2\, h_2^2\right)}{\mu_2\left(h_1\, \mu_2 + h_2\, \mu_1\right)}\, y + \frac{\left(\rho_1\, h_1 + \rho_2\, h_2\right) h_1\, h_2}{\left(h_1\, \mu_2 + h_2\, \mu_1\right)}\right]. \tag{5.3.10}$$

5.3.2 The Convergence results of Poiseuille flow with grid in a two fluid system

In this study, the convergence of LB simulations with the grids will be investigated for different cases of density and viscosity ratios. The number of grid cells in the horizontal x-direction is $lx = 2$ and the vertical y-direction is $ly = 2\acute{h} = 16,\ 32,\ 64,\ 128,\ 256$ and 512, where h is the depth of the flow and equals to 1. In the simulation, the order parameters $\phi_1 = 1$, $\phi_2 = 0$ is used with no slip bounce back boundary condition at the top and bottom boundaries and periodic at the left and right side walls. The interface parameters $\acute{k} = 0.01$ and $\acute{\beta} = 0.02$ are defined as in Banari et al. (2014). The convergent of LB simulation is considered as a function of ly which performs by fixing

$$Re = \frac{u_{1,\text{scale}}\, ly}{\nu_1} = 100 \ \text{ or } \ 1000\,,$$

where ν_1 is kinematic viscosity of fluid 1 with constant

$$Ma = \frac{u_{1,\text{scale}}}{c_s} = 0.01 \ \text{ or } \ 0.005\,,$$

where $u_{1,\text{scale}}$ is the scale velocity of fluid 1.

In the equilibrium state, the two phases is setted from the order parameters and the density of the fluid 2 $(\acute{\rho_2})$ and density ratio (ρ_{ratio}) are specified, respectively. According to the value of low density $\acute{\rho_2}$ which is 6 as mentioned in section 5.2, the value of high density $\acute{\rho_1}$ is determined with given the proper density ratio from $\acute{\rho_1} = \acute{\rho_2}\, \rho_{\text{ratio}}$. For a constant Ma value, the $u_{1,\text{scale}}$ can be found as 0.005774 or 0.002887. In the computations, the ratios of μ and ν are defined as $\mu_{\text{ratio}} = \acute{\mu_1}/\acute{\mu_2}$ and $\nu_{\text{ratio}} = \acute{\nu_1}/\acute{\nu_2}$,

respectively. By fixing Re, μ_1 is determined as

$$\acute{\mu_1} = \frac{\acute{\rho_1}\, u_{1,\text{scale}}\, ly}{Re}\,. \tag{5.3.11}$$

From the value of μ_1, the μ_2 can be read as follows:

$$\acute{\mu_2} = \frac{\acute{\mu_1}\, \acute{\rho_2}}{\nu_{\text{ratio}}\, \acute{\rho_1}}\,. \tag{5.3.12}$$

The initial values of $\acute{\nu_1}$ and $\acute{\nu_2}$ are given by $\acute{\mu_1}/\acute{\rho_1}$ and $\acute{\mu_2}/\acute{\rho_2}$, respectively.

Velocity profiles $u_1(y)$ and $u_2(y)$ in eqs. (5.3.9 and 5.3.10) correspond to:

$$u_1(y) = a_1 + b_1\, y + c_1\, y^2\,, \tag{5.3.13}$$

and

$$u_2(y) = a_2 + b_2\, y + c_2\, y^2\,. \tag{5.3.14}$$

In order to find the maximum velocity value (u_{max}) for fluid 1 or 2:

$$\frac{du_1}{d\,y} = b_1 + 2\,c_1\, y = 0 \quad \text{and} \quad \frac{du_2}{d\,y} = b_2 + 2\,c_2\, y = 0\,,$$

which gives either

$$y = \frac{-b_1}{2\,c_1} \quad \text{or} \quad y = \frac{-b_2}{2\,c_2}\,,$$

by substituting y-values in eqs. (5.3.13) and (5.3.14), yields

$$u_{1,max} = a_1 - \frac{b_1^2}{4\,c_1^2} \quad \text{and} \quad u_{2,max} = a_2 - \frac{b_2^2}{4\,c_2^2}\,.$$

Then the coefficient values of $u_{1,max}$ and $u_{2,max}$ can be defined by eqs. (5.3.9) and (5.3.10) as

$$a_1 = \frac{g\left(\rho_1 h_1 + \rho_2 h_2\right) h_1 h_2}{2\left(h_1 \mu_2 + h_2 \mu_1\right)}, b_1 = \frac{-g\left(\mu_2 \rho_1 h_1^2 - \mu_1 \rho_2 h_2^2\right)}{2\mu_1\left(h_1 \mu_2 + h_2 \mu_1\right)}, c_1 = \frac{-g\rho_1}{2\mu_1}, \quad (5.3.15)$$

and

$$a_2 = \frac{g\left(\rho_1 h_1 + \rho_2 h_2\right) h_1 h_2}{2\left(h_1 \mu_2 + h_2 \mu_1\right)}, b_2 = \frac{-g\left(\mu_2 \rho_1 h_1^2 - \mu_1 \rho_2 h_2^2\right)}{2\mu_2\left(h_1 \mu_2 + h_2 \mu_1\right)}, c_2 = \frac{-g\rho_2}{2\mu_2}. \quad (5.3.16)$$

Therefore, the values of $u_{1,max}$ and $u_{2,max}$ after substitution the coefficient values can be read as

$$u_{1,max} = \frac{g\left(\rho_1 h_1 + \rho_2 h_2\right) h_1 h_2}{2\left(h_1 \mu_2 + h_2 \mu_1\right)} - \frac{\left(\mu_2 \rho_1 h_1^2 - \mu_1 \rho_2 h_2^2\right)^2}{4\rho_1^2\left(h_1 \mu_2 + h_2 \mu_1\right)^2}, \quad (5.3.17)$$

and

$$u_{2,max} = \frac{g\left(\rho_1 h_1 + \rho_2 h_2\right) h_1 h_2}{2\left(h_1 \mu_2 + h_2 \mu_1\right)} - \frac{\left(\mu_2 \rho_1 h_1^2 - \mu_1 \rho_2 h_2^2\right)^2}{4\rho_1^2\left(h_1 \mu_2 + h_2 \mu_1\right)^2}. \quad (5.3.18)$$

There are two cases to normalize the maximum velocity u_{max} for fluid 1 or fluid 2, from the relation if $\mu_2 \rho_1 h_1^2 > \mu_1 \rho_2 h_2^2$ which

$$g = \frac{2\left(h_1 \mu_2 + h_2 \mu_1\right)}{\left(\rho_1 h_1 + \rho_2 h_2\right) h_1 h_2} + \frac{\left(\mu_2 \rho_1 h_1^2 - \mu_1 \rho_2 h_2^2\right)^2}{2\rho_1^2\left(h_1 \mu_2 + h_2 \mu_1\right)\left(\rho_1 h_1 + \rho_2 h_2\right) h_1 h_2}, \quad (5.3.19)$$

else, It can be obtained that

$$g = \frac{2\left(h_1 \mu_2 + h_2 \mu_1\right)}{\left(\rho_1 h_1 + \rho_2 h_2\right) h_1 h_2} + \frac{\left(\mu_2 \rho_1 h_1^2 - \mu_1 \rho_2 h_2^2\right)^2}{2\rho_2^2\left(h_1 \mu_2 + h_2 \mu_1\right)\left(\rho_1 h_1 + \rho_2 h_2\right) h_1 h_2}. \quad (5.3.20)$$

In order to scale the parameters in the simulations of the current study, the length scale (λ_l) is computed as $\lambda_l = ly/(h_1 + h_1)$, where $h_1 = h_1 = 1$. From the veloc-

ity scale u_{scale}, μ and ν scales are calculated as $\mu_{\text{scale}} = u_{\text{scale}}\,\lambda_l$ and $\nu_{\text{scale}} = u_{\text{scale}}\,\lambda_l$, respectively. So g is scaled according to $g_{\text{scale}} = u^2_{\text{scale}}/\lambda_l$ and the force is driven in the x-axis. Normalizing g requires to divide by maximum velocity value $u_{1,max}$ of the two fluid in the system. Similarly, the numerical and the analytical (exact) velocity are normalized by division by the $u_{1,max}$ value.

In this study, the simulations of Poiseuille flow with various density and viscosity ratios is checked and then the convergence with different grids tested. Figure (5.2), shows the simulation of the two fluid flow with $Ma = 0.005$ for $Re = 100$ and 1000 at $\acute{\rho_1}/\acute{\rho_2} = 1$ and $\acute{\nu_1}/\acute{\nu_2} = 0.1$. The numerical velocity profile is convergent to the exact solution by increasing the grid number. It can be observed that the steady state solution for the non dimensional parabolic velocity profiles with $\acute{\rho_1}/\acute{\rho_2} = 100$ and $\acute{\nu_1}/\acute{\nu_2} = 1$ for $Re = 100$ and 1000 as illustrated in Figure (5.3). By changing the $\acute{\rho_1}/\acute{\rho_2} = 1000$ and $\acute{\nu_1}/\acute{\nu_2} = 1/15$ which represents the air and water phases shows the accurate LB result by increasing the grid resolutions in Figure (5.4). Furthermore, the Ma fixed by choosing 0.01 with $Re = 100$ for $\acute{\rho_1}/\acute{\rho_2} = 100$ and $\acute{\nu_1}/\acute{\nu_2} = 1/10$ as shown in Figure (5.5).

In addition, a comparison between the exact solution and the numerical solution for the velocity profiles is given by the L_2-norm error

$$L_2 = \sqrt{\frac{\sum_i \sum_j \left(u_{LBM}(x,y) - u_{exact}(x,y)\right)^2}{\sum_i \sum_j u_{exact}(x,y)^2}}\,, \tag{5.3.21}$$

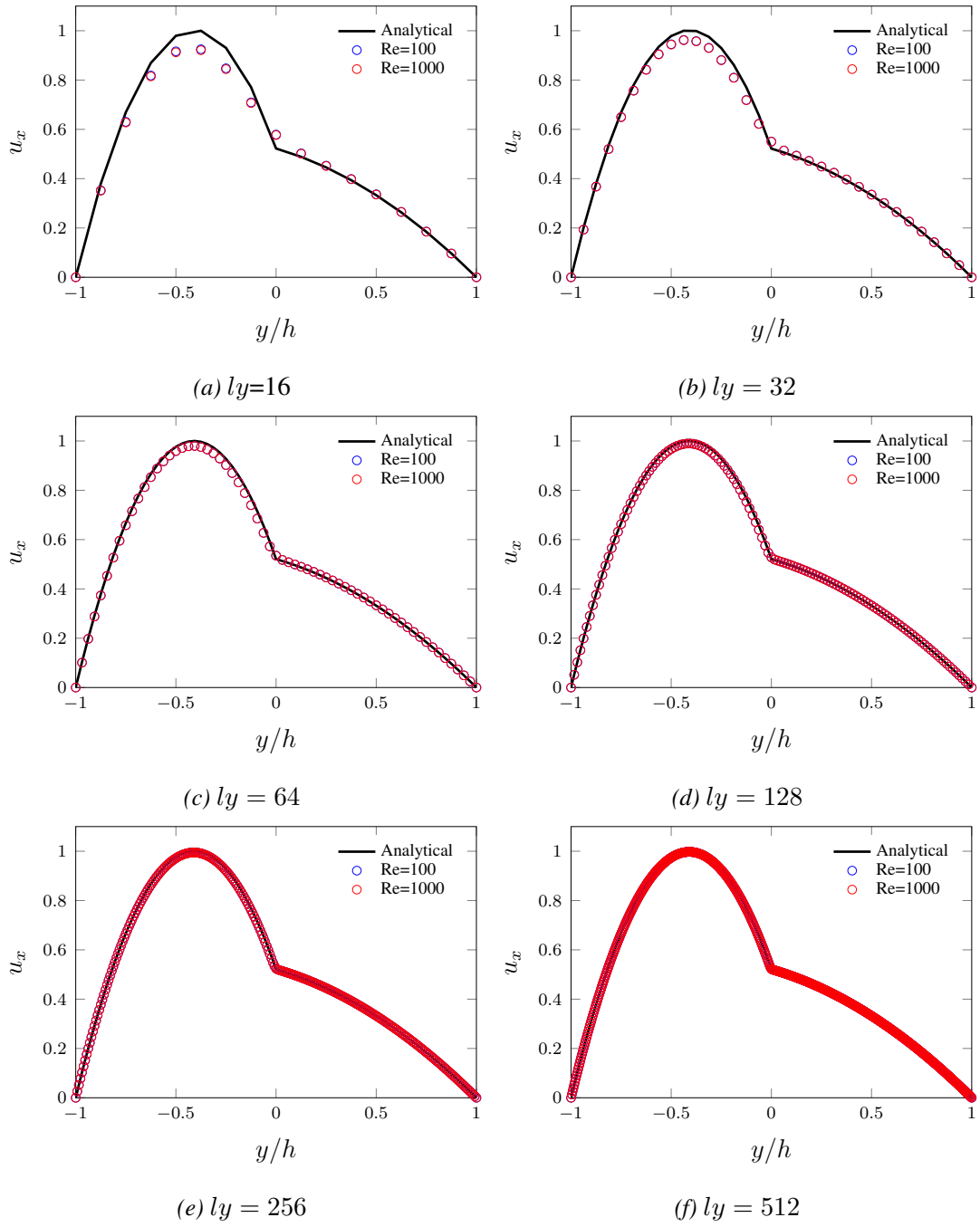

(a) ly=16 *(b)* $ly = 32$

(c) $ly = 64$ *(d)* $ly = 128$

(e) $ly = 256$ *(f)* $ly = 512$

Figure 5.2: Non dimensional velocity profiles of two fluid Poiseuille flow, for $Ma = 0.005$, $\acute{\rho_1}/\acute{\rho_2} = 1$ and $\acute{\nu_1}/\acute{\nu_2} = 0.1$ with various lattice grids ly.

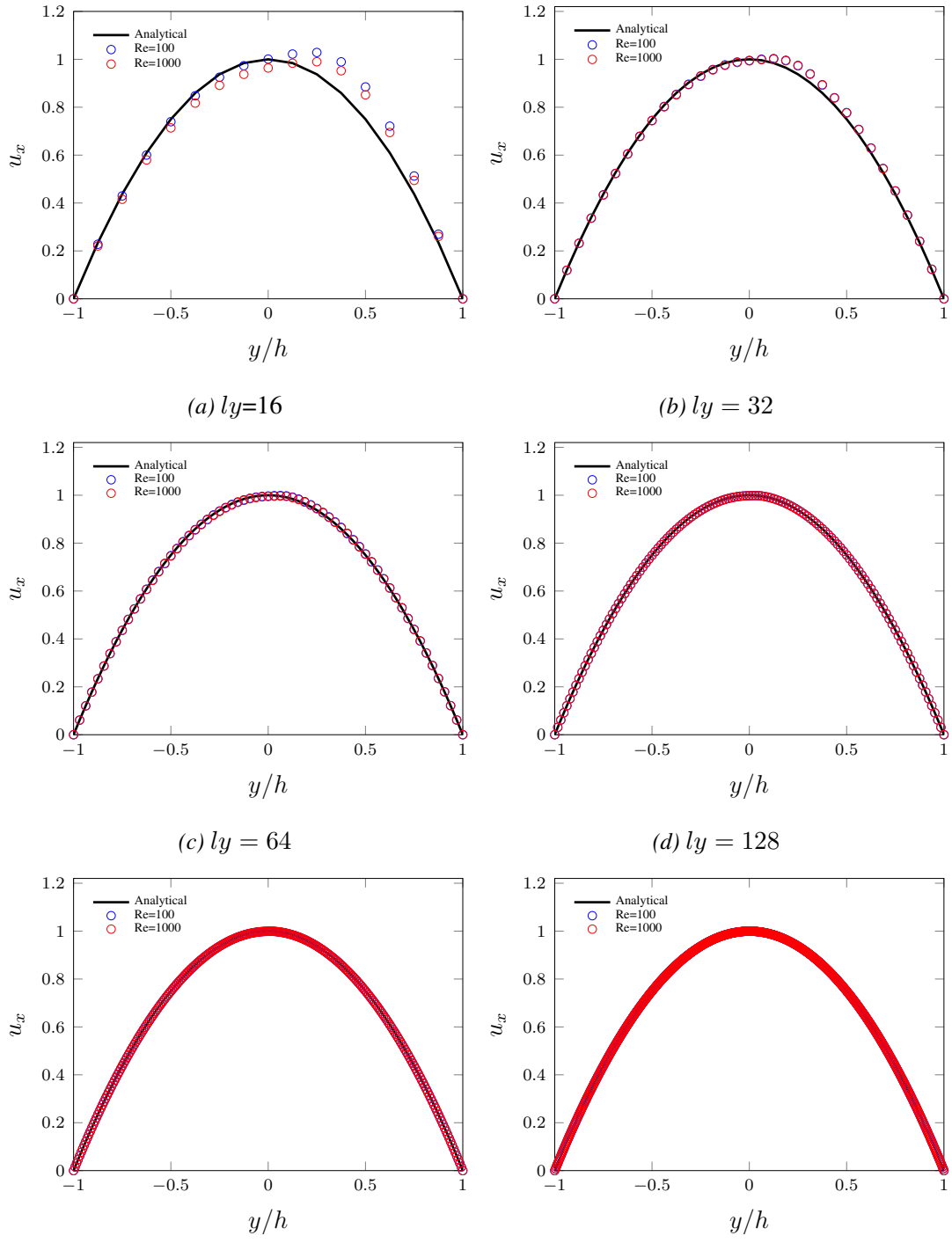

(a) ly=16 *(b)* $ly = 32$

(c) $ly = 64$ *(d)* $ly = 128$

(e) $ly = 256$ *(f)* $ly = 512$

Figure 5.3: Non dimensional velocity profiles in two fluid Poiseuille flow, for $Ma = 0.005$, $\acute{\rho_1}/\acute{\rho_2} = 100$ and $\acute{\nu_1}/\acute{\nu_2} = 1$ with various lattice grids ly.

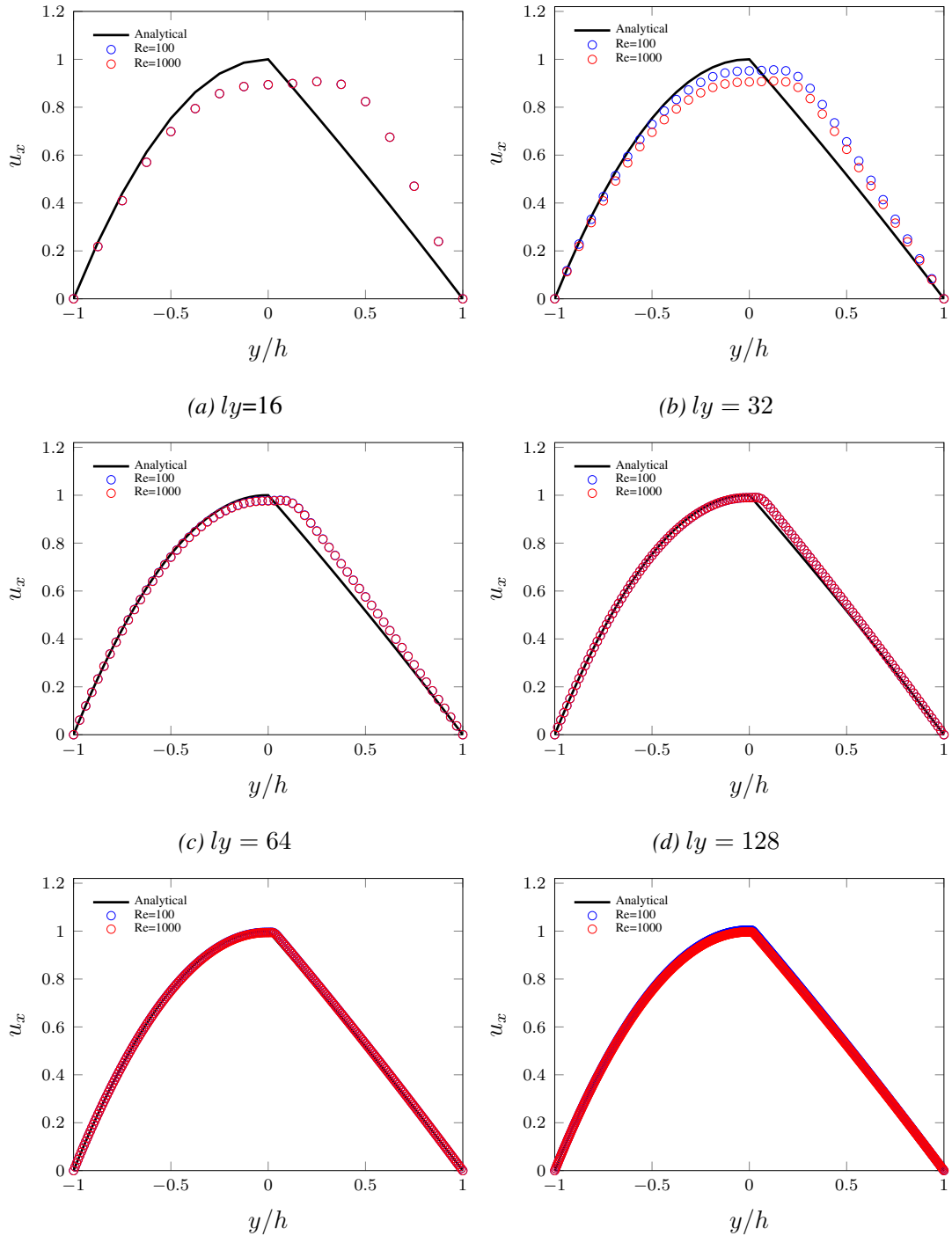

(a) ly=16 *(b)* $ly = 32$

(c) $ly = 64$ *(d)* $ly = 128$

(e) $ly = 256$ *(f)* $ly = 512$

Figure 5.4: Non dimensional velocity profiles in two fluid Poiseuille flow, for $Ma = 0.005$, $\acute{\rho_1}/\acute{\rho_2} = 1000$ and $\acute{\nu_1}/\acute{\nu_2} = 1/15$ with various lattice grids ly.

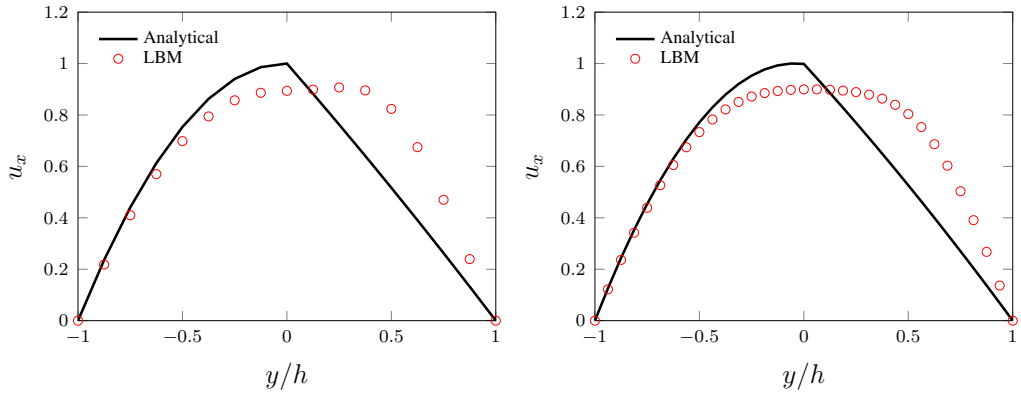

(a) ly=16 *(b)* $ly = 32$

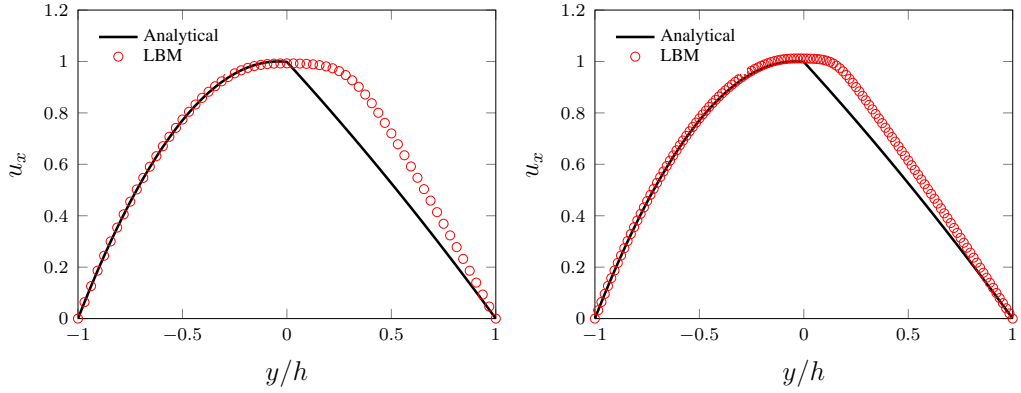

(c) $ly = 64$ *(d)* $ly = 128$

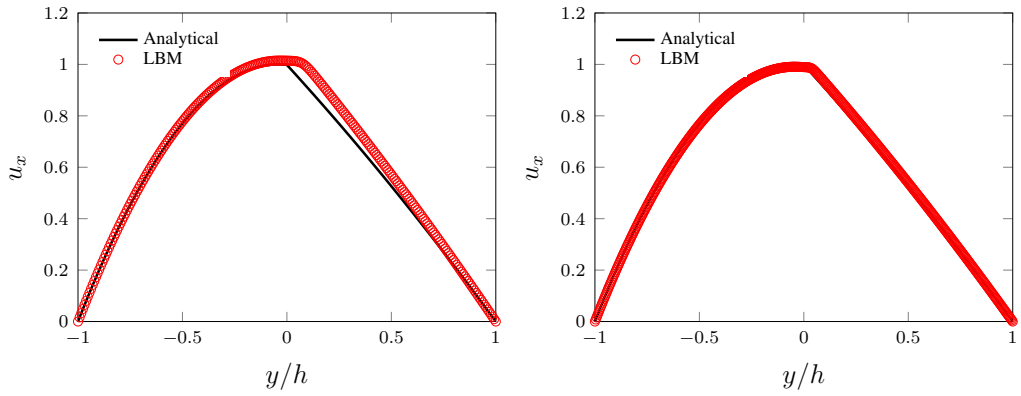

(e) $ly = 256$ *(f)* $ly = 512$

Figure 5.5: Non dimensional velocity profiles in two fluid Poiseuille flow, for $Ma = 0.01$, $\acute{\rho_1}/\acute{\rho_2} = 100$ and $\nu_1/\nu_2 = 0.1$ with various lattice grids ly.

The L_2-norm error of Figures (5.2-5.5) for various number of grid sizes are illustrate in Figures (5.6 - 5.9), respectively. From the results of L_2-norm error test are found that all are convergent with accurate resolutions have first order error except the case of $\acute{\rho_1}/\acute{\rho_2} = 100$ and $\acute{\nu_1}/\acute{\nu_2} = 1$ for $Re = 100$ and 1000 has second order accuracy because the kinematic viscosity ratio for each phase has the same value as shown in Figure (5.7). It has the same behaviour of the error with single phase component as obtain from using bounce back boundary. It also found that the flow is not affected with changing the Re.

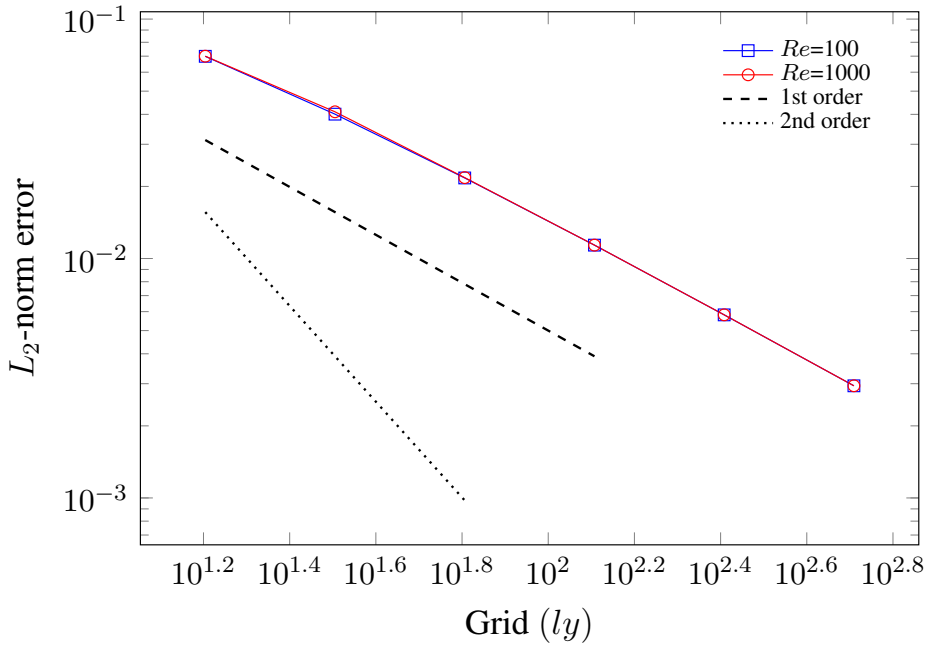

Figure 5.6: L_2-norm error with grid (ly) between Analytical and LBM result for the two fluid Poiseuille flow when $Ma = 0.005$, density ratio 1 and kinematic ratio 0.1.

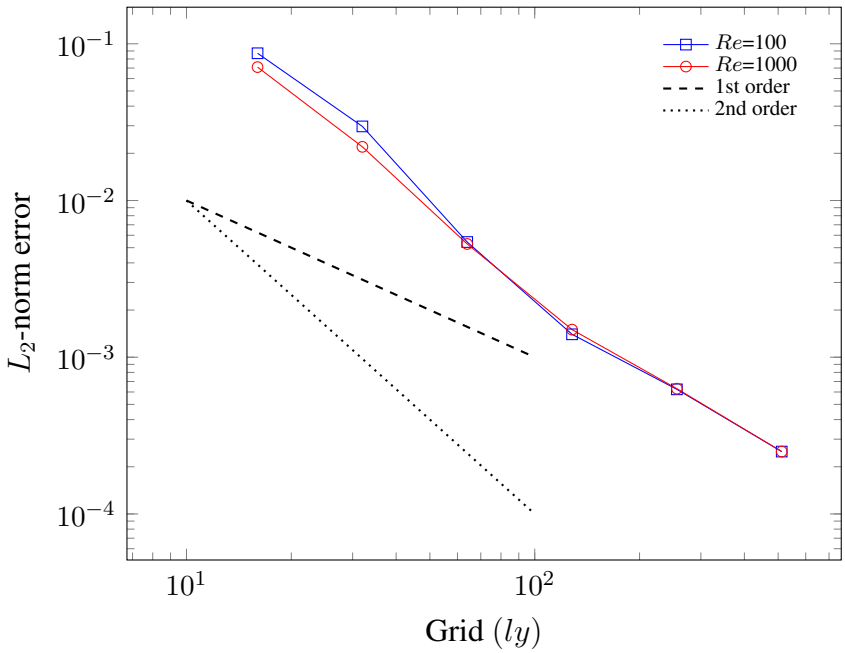

Figure 5.7: L_2-norm error with grid (ly) between Analytical and LBM result for the two fluid Poiseuille flow when $Ma = 0.005$, density ratio 100 and kinematic ratio 1.

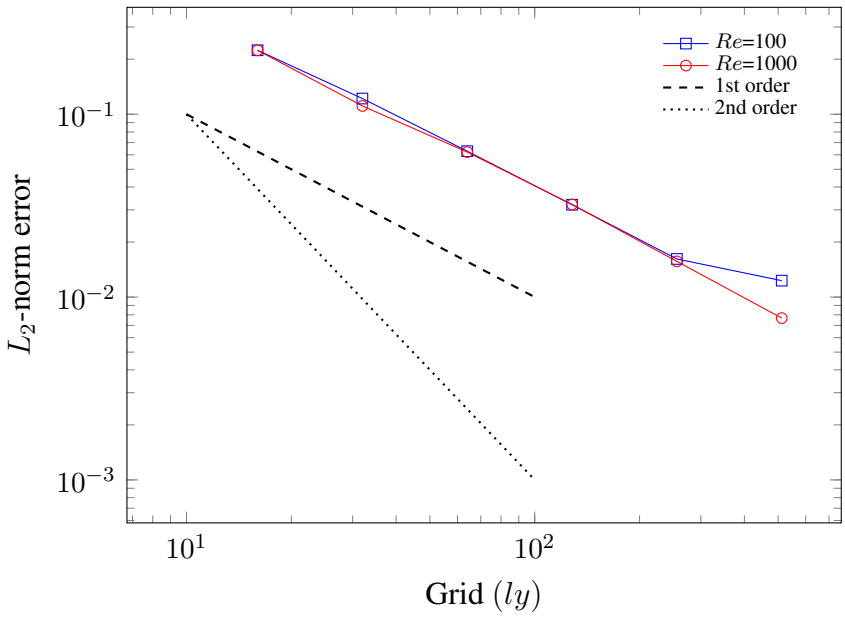

Figure 5.8: L_2-norm error with grid (ly) between Analytical and LBM result for the two fluid Poiseuille flow when $Ma = 0.005$, density ratio 1000 and kinematic ratio 0.0667.

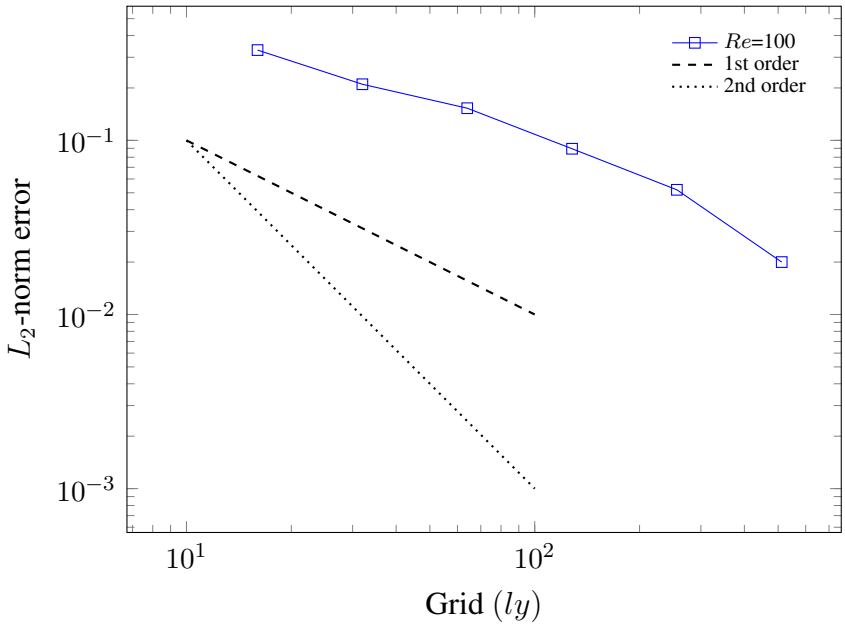

Figure 5.9: L_2-norm error with grid (ly) between Analytical and LBM result for the two fluid Poiseuille flow when $Ma = 0.01$, density ratio 100 and kinematic ratio 0.1.

In addition, from the result that is obtained in Figure (5.9) had first order accuracy as is noted in work of Banari et al. (2014). In general, It observed that the results from the current study had excellent comparisons with the analytic solutions at different density and viscosity ratios.

5.4 Static bubble

As a further test of the code of the current study for the multiphase LB approach, the verification for Laplace's law is performed. It is represented by the pressure difference or the pressure jump (ΔP) between the outside and the inside of the static bubble (see Figure (5.10)). It can be observed that the high density is sited in outside the bubble and low density is lied inside the bubble. The pressure jump (ΔP) for a two dimension

circular bubble with radius R is given by:

$$\Delta P = \frac{\sigma_{1\,2}}{R}, \tag{5.4.1}$$

where $\sigma_{1\,2}$ is the surface tension coefficient. The pressure jump (ΔP) is computed after the bubble reaches the steady state. The periodic boundary condition is used at all four sides of the domain with zero gravity. The parameters to distinguish the phases are defined as $\phi_1 = 0.4$, and $\phi_2 = 0.1$, and density ratio 100 with $R = 0.005m$ and $d = 0.02m$ according to Banari et al. (2014).

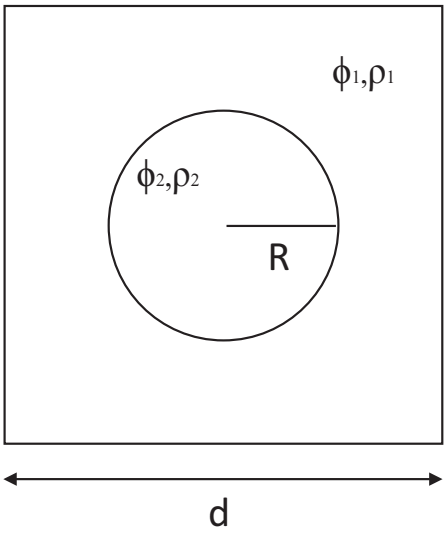

Figure 5.10: Two dimensional circular bubble.

In simulations of the current study, two initial static (square and circular) droplets implemented for various surface tension coefficient $\sigma_{1\,2} = 0.01,\ 0.004,\ 0.001$ and radius with lattice (128×128) grid. The physical kinematic viscosity for each phase have the same values $\nu_1 = \nu_2 = 0.002m^2/s$ and the surface tension coefficient $\sigma_{1\,2} = 0.004\ N/m$, so according to Laplace law the pressure jump equation is equal to $0.753\ N/m$. It can be illustrated in Figure (5.11) the density, order parameter and velocity of each

phase in the simulation. From the definition of kinematic viscosity which relates to the relaxation time reads

$$\nu = (\tau_g - \frac{1}{2})\, c_s^2\, \Delta t$$

corresponding to $\acute{\nu} = \frac{1}{6}$ in the LB computation by choosing $\acute{\tau}_g = 1$ and the relation between the physical and LB kinematic viscosity can be written as

$$\acute{\nu} = \nu \frac{\Delta t}{\Delta x^2}\,. \tag{5.4.2}$$

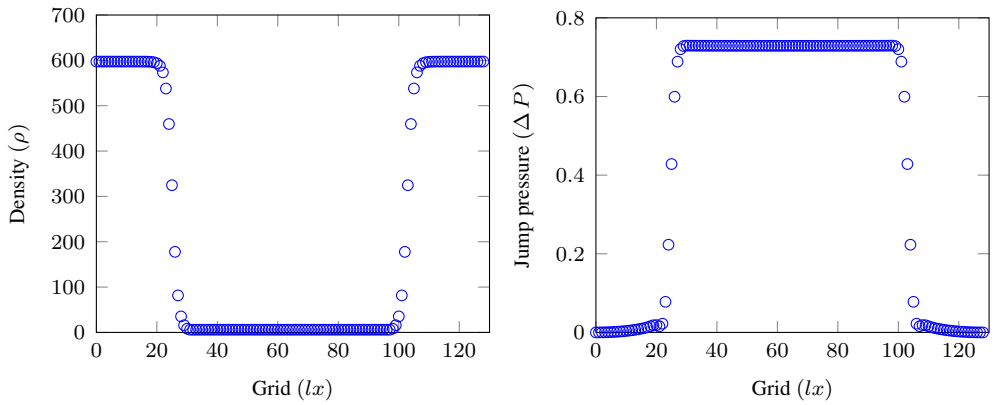

(a) Density *(b)* Jump pressure

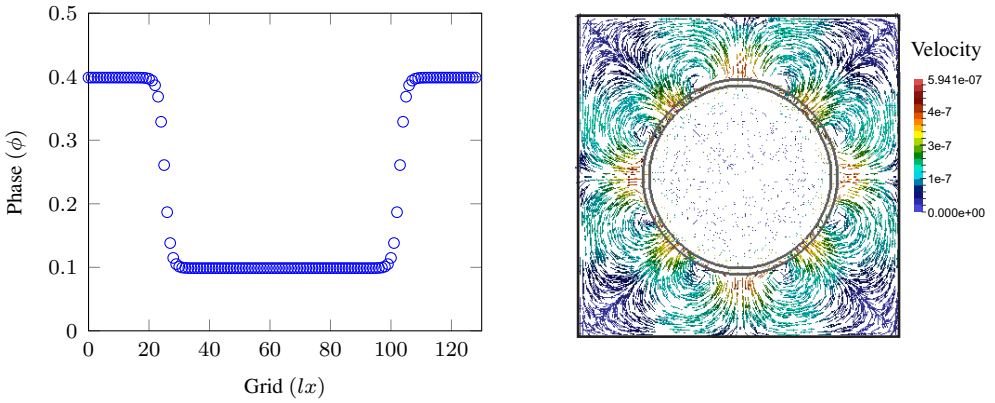

(c) Order parameters *(d)* Velocity

Figure 5.11: The initially square droplet with $lx = 128$ for two phases.

Then lattice surface tension coefficient is defined as

$$\acute{\sigma}_{1\,2} = \frac{\sigma_{1\,2}}{c^2\,\Delta x}, \text{ where the step size is } \Delta x = \frac{d}{lx}\,. \tag{5.4.3}$$

For more details of scaling the parameters see appendix A. In the current work, the dynamic viscosity is defined after specifying the density ratios then the kinematic viscosity values is computed as $\mu(\rho) = \rho(\phi)\,\nu(\rho)$.

For a (128×128) lattice grid, $\Delta x = 0.0001563\,m$ and $\Delta t = 2.03 \times 10^{-6}\,s$ which leads to $c^2 = 5899.42\,m^2/s^2$. The lattice surface tension coefficient $(\acute{\sigma}_{1\,2})$ is equal to 4.34×10^{-3} from eq. (5.4.3).

Therefore, the parameters

$$\acute{k} = \frac{6\,\acute{\sigma}_{1\,2}}{(\phi_1 - \phi_2)^2} \quad \text{and} \quad \acute{\beta} = \frac{3\,\acute{\sigma}_{1\,2}}{(\phi_1 - \phi_2)^4}\,,$$

are computed as $\acute{k} = 0.289$ and $\acute{\beta} = 1.607$. The lattice radius $(\acute{R} = 34)$ which corresponding to the physical radii $R = 0.005313\,m$ can be calculated as

$$\acute{R} = \frac{R\,lx}{d}\,. \tag{5.4.4}$$

For the physical jump pressure (ΔP), the lattice jump pressure $(\Delta \acute{P})$ is defined as follows

$$\Delta \acute{P} = \frac{\Delta P}{c^2}\,, \tag{5.4.5}$$

In Figure (5.12), from the results a good comparison is obtained between the theoretical and the LB results of the two initial droplet cases with various surface tension coefficient $\sigma_{1\,2}$. The four lattice radius of the static bubble flow started from 12 to 34 lattice units.

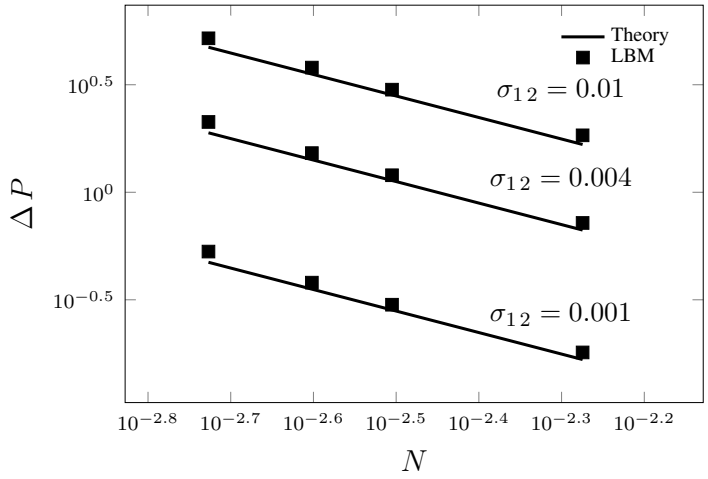

(a) Stationary square droplet

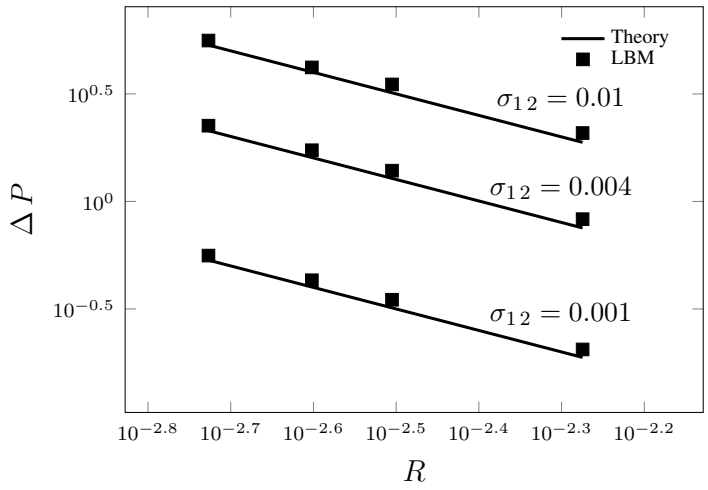

(b) Stationary circular bubble

Figure 5.12: Pressure difference across the interface for different $\sigma_{1\,2}$ and bubble radii between LBM simulation and theoretical solution.

5.5 Rising bubble

In this section, the rising bubble flow is implemented to check the properties of a single bubble movement under the gravitational acceleration (g). The low-density fluid $(\acute{\rho}_2)$ of bubble rising in the denser fluid $(\acute{\rho}_1)$ according to g is simulated with different cases. The terminal shape of the bubble is related to the non-dimensional parameters; for instance Eotvos number (Eo) (or Bond number) , Morton number (Mo) and Re

which are defined as follows

$$Eo = \frac{(\acute{\rho}_1 - \acute{\rho}_2)\, g\, D^2}{\sigma_{1\,2}}\,,$$

$$Mo = \frac{g\, \mu_1^4}{\sigma_{1\,2}^3\, \acute{\rho}_1}\,(1 - \frac{\acute{\rho}_2}{\acute{\rho}_2})\,,$$

and

$$Re = \frac{\acute{\rho}_1\, g^{1/2}\, D^{3/2}}{\acute{\mu}_1}\,.$$

where D is the diameter of the bubble and g is the gravitational acceleration force. The bubble rising is based on the fundamental properties of the drops as introduced by Clift et al. (2005). According to Banari et al. (2014) study, the high Re and Eo diminishes the effect of the surface tension on the terminal shape of the bubble.

In simulation of the current work, periodic boundary conditions are used with the left and right walls and no slip bounce back boundary is imposed at the top and bottom boundary conditions. Three cases of rising bubble with density ratio 100 at (128×512) lattice grid have a good comparison with Sun & Tao (2010) simulations as illustrated in Figure (5.13). It found that the spherical, oblate ellipsoidal and oblate ellipsoidal cap terminal shapes are formed by using $Eo = 0.1$, $Mo = 1 \times 10^{-3}$, $Eo = 10$, $Mo = 1 \times 10^{-1}$ and $Eo = 100$, $Mo = 1 \times 10^{3}$,respectively. For the (128×512) lattice grid with initial diameter $D = 30$ for the oblate ellipsoidal terminal shape, the parameters in lattice units are defined as $\acute{k} = 0.532$ and $\acute{\beta} = 2.962$ which correspond to the lattice surface tension coefficient $\acute{\sigma}_{1\,2} = 0.008$.

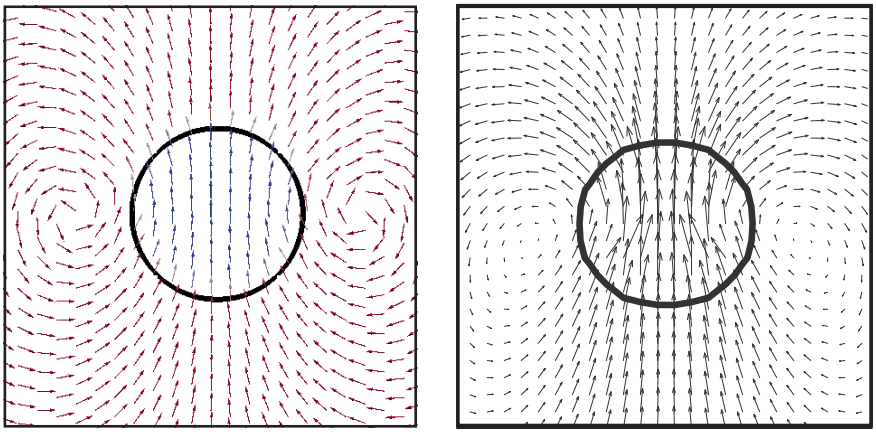

(a) $Eo = 0.1,\ Mo = 1 \times 10^{-3}$

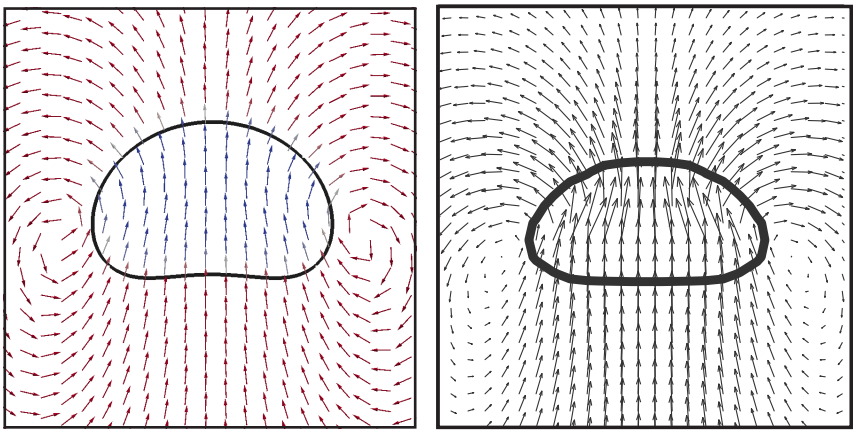

(b) $Eo = 10,\ Mo = 1 \times 10^{-1}$

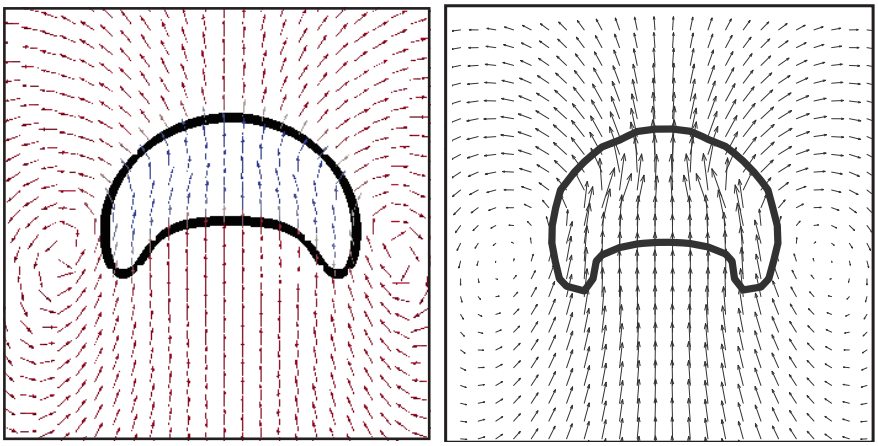

(c) $Eo = 100,\ Mo = 1 \times 10^{3}$

Figure 5.13: The terminal shape with the velocity vectors for rising bubble between the present results at (128×512) lattice grid and Sun & Tao (2010) results.

The parameters of terminal shapes for each cases for lattice unit of rising bubble simulations are defined in Table (5.1)

Table 5.1: The parameters of terminal shapes in lattice unit for rising bubble simulations.

Terminal shapes	$\nu_1^{'} = \nu_1^{'}$	g	Eo	Mo
Spherical	0.002	1.496×10^{-9}	1×10^{-1}	1×10^{-3}
Oblate ellipsoidal	0.002	1.493×10^{-7}	10	1×10^{-1}
Oblate ellipsoidal cap	0.012	5.892×10^{-7}	100	1×10^{3}

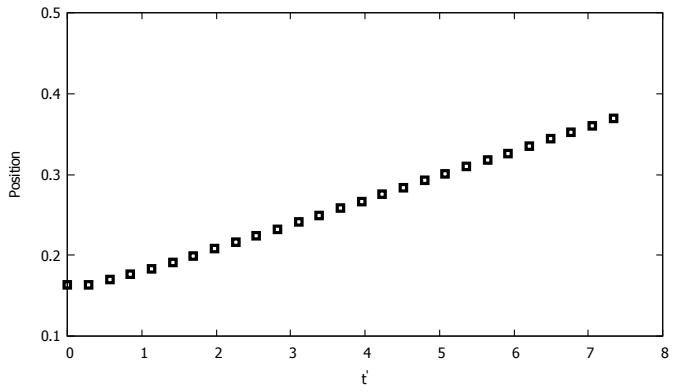

(a) Position

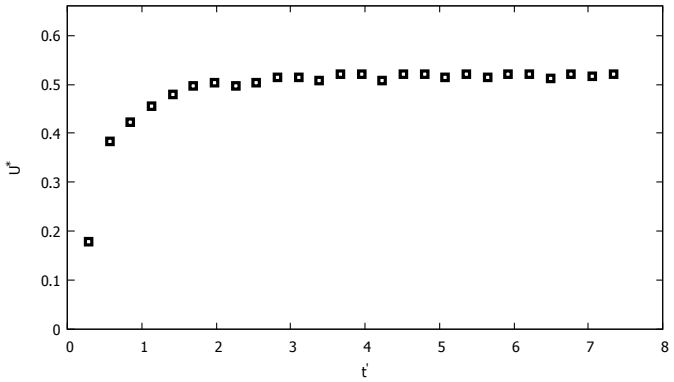

(b) non-dimensional velocity

Figure 5.14: The position and the non-dimensional rising velocity (U^*) as a function of non-dimensional time (t^*) at (128×512) lattice grid.

The position and the non-dimensional rising velocity ($U^* = u/\sqrt{g\,D}$) can be defined as a function of non-dimensional time ($t^* = t\,\sqrt{g\,/D}$) for oblate ellipsoidal cap bubble shape as illustrated in Figure (5.14). The value of bubble rising velocity (U^*) agree well with predicted result that obtained from Hua & Lou (2007). It found by computing Re for the oblate ellipsoidal cap that $10 < Re < 20$ as expected by the relation between the Eo and Re according to Hua & Lou (2007).

5.6 Summary

In this chapter a single relaxation time multiphase LBM model is used to simulate two fluid Poiseuille flow, static and rising bubble flows. The L_2-norm errors for the results shown in Figures (5.2-5.5) for different number of grids are shown in Figures (5.6 - 5.9), respectively. From the results, the first order error convergence are obtained except the case of $\acute{\rho_1}/\acute{\rho_2} = 100$ and $\acute{\nu_1}/\acute{\nu_2} = 1$ which has second order accuracy as illustrated in Figure (5.7). For the static bubble flow, a good comparison is made between the theoretical (Laplace law) and current computations with different surface tension coefficient values and various radius with density ratio 100 (see Figure (5.12)). Finally, when comparing the terminal shapes and the non-dimensional rising velocity profile as shown in Figures (5.13) and (5.14), respectively, the simulations for a rising bubble agree well with those in the literature.

Chapter 6

Single and Multiple Rayleigh-Taylor Instability

6.1 Introduction

The Rayleigh–Taylor instability (RTI) appears when the denser phase of the fluid at the start lies above a lighter phase with influence of a gravity. It was proposed from Taylor (1950) and then implemented with whole fluid flows according to Lord (1900). Sharp (1983) was the first to suggested the terms of a bubble and spikes due to the instability of the tiny perturbations for a initial state which is increased by development of the complexity of the fluid with time. The implementation has been verified for various test cases: single Rayleigh-Taylor Instability with different Re (256, 600, 614.4, 2048, 3000 and 5000), density ratios (3, 19, 100 and 1000) at various number of lattice grids. The multiple mode Rayleigh-Taylor Instability is studied with various surface tension coefficients and values of initial perturbations functions at density ratio 3 and $Re = 4096$.

The organization of this chapter is as follows: Section 6.2, details the convergence of implementations of single mode Rayleigh-Taylor Instability (RTI) fluid flow with number of the grid and various Re and density ratios. In section 6.3, The effect of changing the surface tension coefficient is investigated in the multiple mode RTI with

different grid resolutions. Finally, summary of this chapter is given in Section 6.4.

6.2 Single Rayleigh-Taylor Instability

Rayleigh-Taylor instability (RTI) appears when a low density fluid (blue colour in Figure (6.1)) sits below the more dense fluid (red). The low density fluid (ρ_2) rises when the denser fluid (ρ_1) drops under the effect of the gravitational acceleration (g). Here, an initial interface location in the 1×4 domain is specified as

$$y(x) = 2 + A\, \cos(2\pi\, x)\,, \tag{6.2.1}$$

with disturbance amplitude $A = 0.1$. The periodic boundary condition is used at left and right side boundaries and the no slip bounce back boundary is applied at top and bottom boundaries.

In the current multiphase study, the time evolution of the two fluid interface from a single mode perturbation of RTI is presented with different density ratios ($\frac{\acute{\rho}_1}{\acute{\rho}_2}$). The gravitational acceleration (g) value is chosen to achieve the characteristic velocity (U_c) as

$$U_c = \sqrt{lx\, g} = 0.04 \tag{6.2.2}$$

in lattice units, where lx and ly are the numbers of lattice grids in the x, y-directions, respectively.

The comparison between He et al. (1999) and the present results of the time evolution of the two fluid interface from a single mode perturbation illustrated in Figure (6.1) for 10 dimensionless times $(\acute{t})$ which reads as follow

$$\acute{t} = \frac{t}{\sqrt{lx/g}}\,. \tag{6.2.3}$$

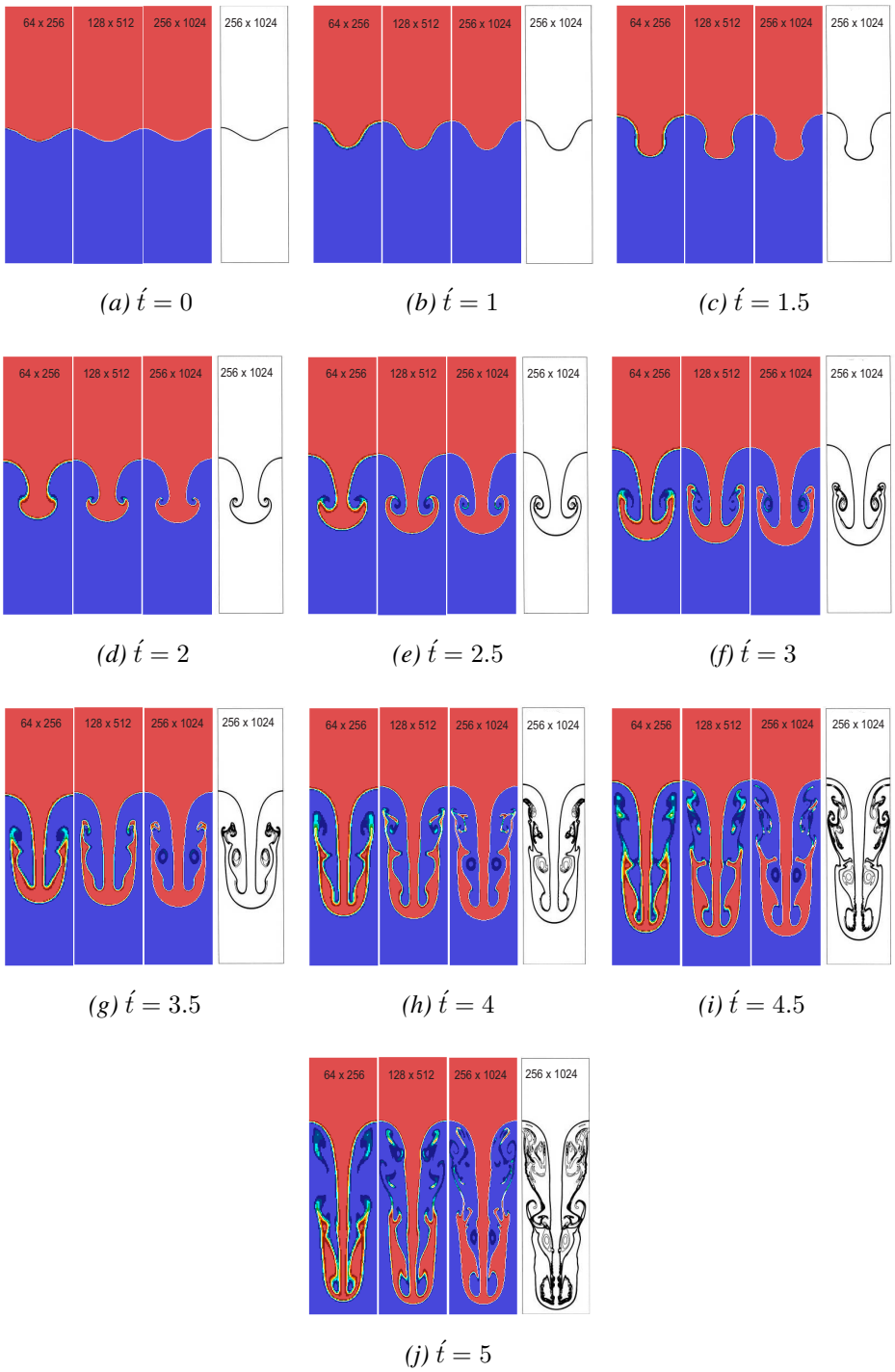

(a) $\acute{t} = 0$ *(b)* $\acute{t} = 1$ *(c)* $\acute{t} = 1.5$

(d) $\acute{t} = 2$ *(e)* $\acute{t} = 2.5$ *(f)* $\acute{t} = 3$

(g) $\acute{t} = 3.5$ *(h)* $\acute{t} = 4$ *(i)* $\acute{t} = 4.5$

(j) $\acute{t} = 5$

Figure 6.1: The comparison of the time evolution of the two fluid interface from a single mode perturbation for 10 dimensionless times $(\acute{t})$ between He et al. (1999) and the present results with different grids $lx = 64,\ 128$ and 256.

The non dimensional parameters such as Reynolds number (Re) is read as

$$Re = \frac{\sqrt{lx\, g}\, lx}{\nu}\,, \tag{6.2.4}$$

where ν is the kinematic viscosity and the Atwood number (At) is defined as

$$At = \frac{(\rho_1 - \rho_2)}{(\rho_1 + \rho_2)}\,. \tag{6.2.5}$$

The density ratio is equal to 3, $At = 0.5$ and $Re = 2048$ with different number of the grids $lx = 64$, 128 and 256 with order parameters $\phi_1 = 0.4$ and $\phi_2 = 0.1$. It observed that the simulations converged by using further investigation with different $\phi_1 = 0.5$, $\phi_2 = -0.5$ and $\phi_1 = 1$, $\phi_2 = 0$.

The evolution of the fluid interface appears identical with top and bottom at the initial state $(\acute{t} = 0)$. With developing the interface under effect of g the denser fluid drops like a spike which starts to roll up and the low density fluid rises to bubbles shape. Then the vortices grow unstable with second vortices appearing at the ends of the roll ups with time evolution. The results show a good comparison with He et al. (1999) results by obtaining the complicated form with time evolution at $\acute{t} = 5$. In the meantime, the interface along the central line of the fluid stays symmetric and comparatively smooth which is significant with combining the high and low density fluids.

The grid convergence of numerical solution between He et al. (1999) and the present results with the contour of $(\rho_1+\rho_2)/2$ is investigated. In the work of He et al. (1999), the molecular interactions is incorporated to model the interfacial dynamics. It observed that they are used two distribution functions in their simulations. The density ratio is equal to 3, $At = 0.5$ with the number of grids $lx = 128$ and 256 for $Re = 256$ and 2048 are illustrated in Figure (6.2).

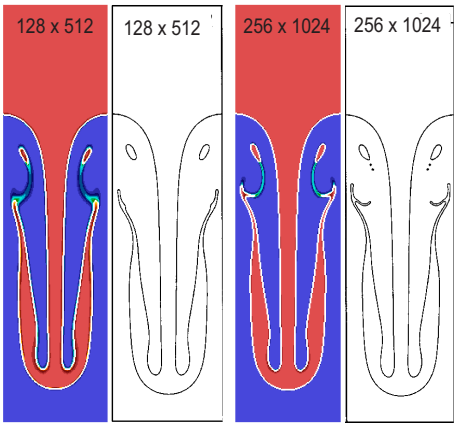

(a) $Re = 256$, $\acute{t} = 5$

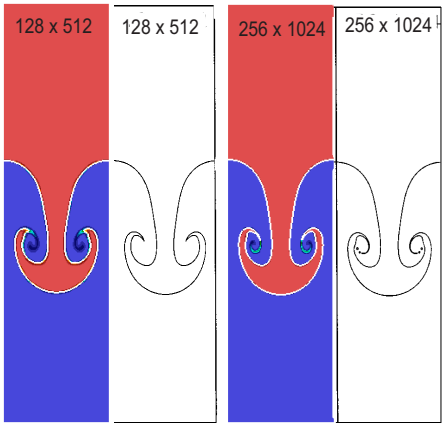

(b) $Re = 2048$, $\acute{t} = 2.5$

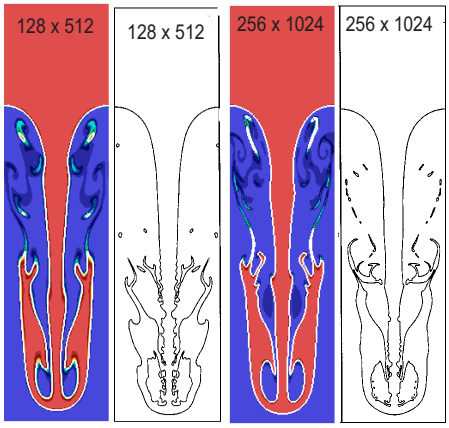

(c) $Re = 2048$, $\acute{t} = 5$

Figure 6.2: The comparison of grid convergence of numerical solution between He et al. (1999) and the present results. The contour of $(\rho_1 + \rho_2)/2$ is plotted with different Re.

Figure (6.3) shows an excellent agreement of the position and velocities results of the bubble and spike fronts versus time with various Re at $At = 0.5$ which implemented in Figures (6.1) and (6.2).

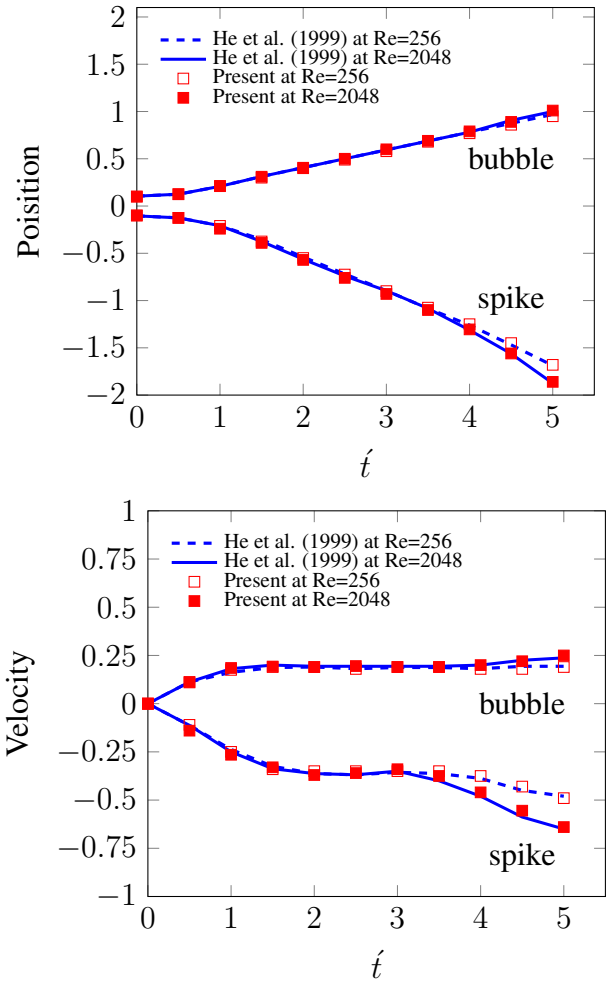

Figure 6.3: Position and velocities of the bubble and spike fronts versus time with $Re = 2048$ and 256 at $At = 0.5$.

The behaviour of convergence with grid resolution of single RTI for $\frac{\acute{\rho}_1}{\acute{\rho}_2} = 19$, $At = 0.9$, $Re = 614.4$ and the order parameters $\phi_1 = 0.4, \phi_2 = 0.1$ has been studied and compared with the results of He et al. (1999) as shown in Figure (6.4) is agree well with those in the literature. In addition, various cases of the order parameters such as $\phi_1 = 0.5$, $\phi_2 = -0.5$ and $\phi_1 = 1$, $\phi_2 = 0$ have been tested and the results obtained a good agreements with He et al. (1999).

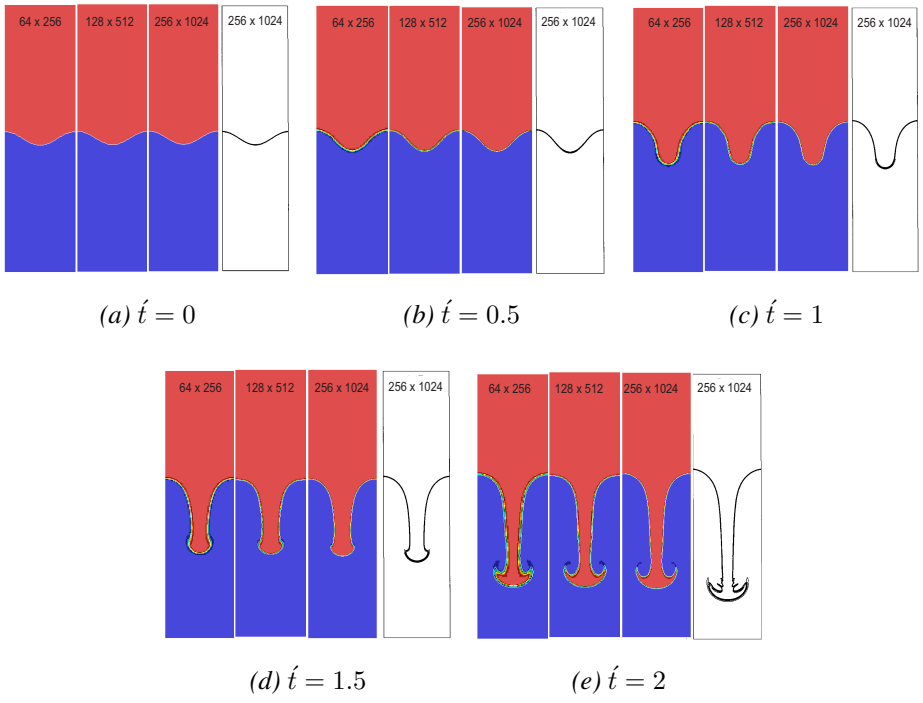

(a) $\acute{t} = 0$ (b) $\acute{t} = 0.5$ (c) $\acute{t} = 1$

(d) $\acute{t} = 1.5$ (e) $\acute{t} = 2$

Figure 6.4: The comparison of 5 dimensionless time evolution of single mode perturbation between He et al. (1999) and the present results for $\frac{\acute{\rho}_1}{\acute{\rho}_2} = 19$ and $\phi_1 = 0.4, \phi_2 = 0.1$.

The simulations in the current study were improved by increasing the values of Re and density ratios to 5000 and 1000, respectively rather than $Re = 256, 614, 2048$ and density ratio$= 3, 19$ that were applied in work of He et al. (1999). So an addition tests made for single RTI with two different density ratios $\frac{\acute{\rho}_1}{\acute{\rho}_2} = 100$ and $\frac{\acute{\rho}_1}{\acute{\rho}_2} = 1000$ for 5 different $Re = 600, 3000, 4000$ and 5000 to study the time evolution of the two fluid interface, relative mass and the kinetic energy.

Ren et al. (2016) investigated the single mode RTI simulation by modifying the conservative from Allen-Cahn equation (ACE) Allen & Cahn (1976) for tracking the interface with $\frac{\acute{\rho}_1}{\acute{\rho}_2} = 99$ and $Re = 600$ and high $Re = 3000$. From the present results for the $\frac{\acute{\rho}_1}{\acute{\rho}_2} = 100$ with $Re = 600$ and $Re = 3000$ is illustrated in Figures (6.5) and (6.6), respectively. As well as, the results with $\frac{\acute{\rho}_1}{\acute{\rho}_2} = 100$ has been improved for $Re = 5000$ as shown in Figure (6.7).

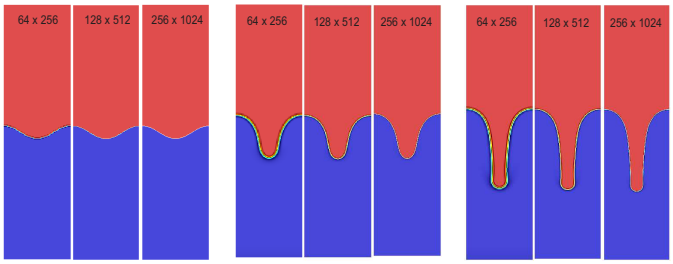

(a) $\acute{t}$=0 *(b)* $\acute{t}$=1 *(c)* $\acute{t}$=1.5

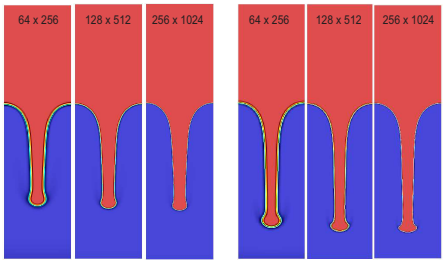

(d) $\acute{t}$=1.75 *(e)* $\acute{t}$=2

Figure 6.5: The time evolution of single mode perturbation for $\frac{\acute{\rho}_1}{\acute{\rho}_2} = 100$, $At = 0.98$ and $Re = 600$ with $\phi_1 = 0.5, \phi_2 = 0.5$.

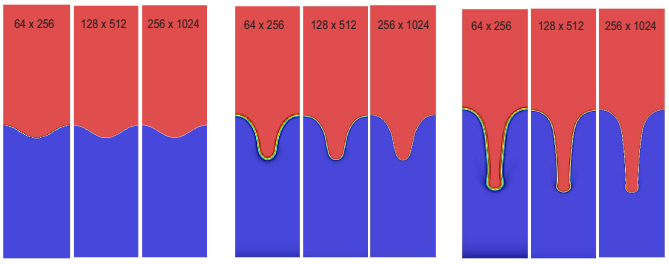

(a) $\acute{t}$=0 *(b)* $\acute{t}$=1 *(c)* $\acute{t}$=1.5

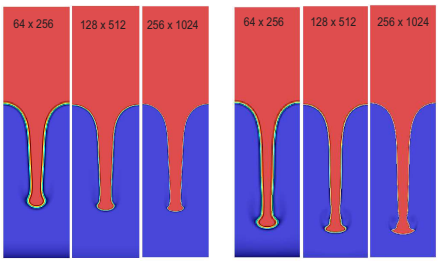

(d) $\acute{t}$=1.75 *(e)* $\acute{t}$=2

Figure 6.6: The time evolution of a single mode perturbation for $\frac{\acute{\rho}_1}{\acute{\rho}_2} = 100$, $At = 0.98$ and $Re = 3000$ with $\phi_1 = 0.5, \phi_2 = 0.5$.

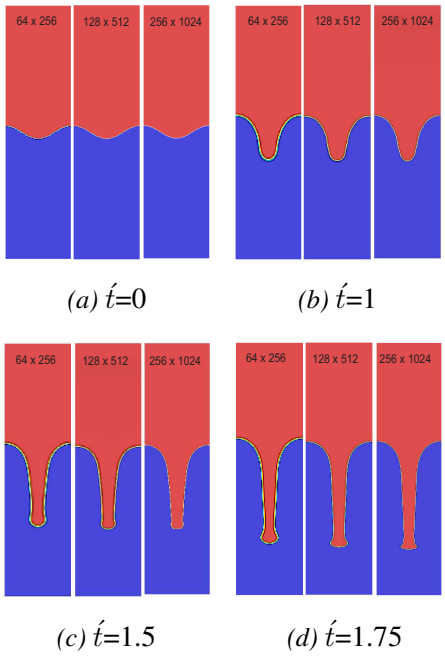

(a) $\acute{t}$=0 *(b)* $\acute{t}$=1

(c) $\acute{t}$=1.5 *(d)* $\acute{t}$=1.75

Figure 6.7: The time evolution of single mode perturbation for $\frac{\acute{\rho}_1}{\acute{\rho}_2} = 100$, $At = 0.98$ and $Re = 5000$ with $\phi_1 = 0.5, \phi_2 = 0.5$.

Fakhari et al. (2017) developed the model of the multiphase that suggested by Zu & He (2013) for conservative phase field model to present the result for high density ratio ($\frac{\acute{\rho}_1}{\acute{\rho}_2} = 1000$) with $Re = 3000$ while Shao & Shu (2015) employed for $\frac{\acute{\rho}_1}{\acute{\rho}_2} = 1000$ with $Re = 200$.

The simulations in the current study of the multiphase is presented for $\frac{\acute{\rho}_1}{\acute{\rho}_2} = 1000$ with $Re = 600$ and 3000. Stable results of single RTI with $Re = 600$ and 3000 for high density ratio up to 1000 has been simulated in Figures (6.8) and (6.9), respectively as pointed out by Fakhari et al. (2017). In addition, the simulations of the high density ratios with $Re = 5000$ has been implemented well as shown in Figure (6.10). It worth mention that the results performed by using single relaxation times (SRT) collision operator for both $\frac{\acute{\rho}_1}{\acute{\rho}_2} = 100$ and 1000. Furthermore, it observed from the results in Figures for $\frac{\acute{\rho}_1}{\acute{\rho}_2} = 1000$ that the high density fluid is dropped as column without complexity of the ends of roll up when it compared with low density ratios.

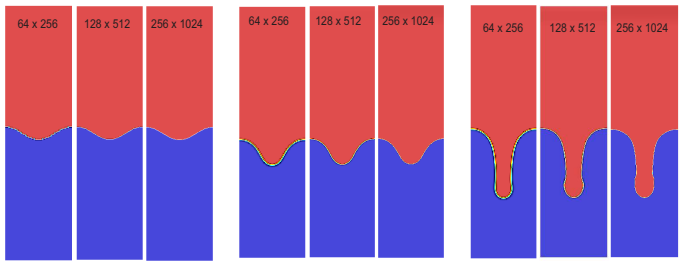

(a) $\acute{t}$=0 *(b)* $\acute{t}$=1 *(c)* $\acute{t}$=1.5

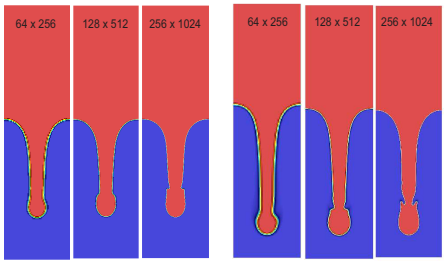

(d) $\acute{t}$=1.75 *(e)* $\acute{t}$=2

Figure 6.8: The time evolution of single mode perturbation for $\frac{\acute{\rho}_1}{\acute{\rho}_2} = 1000$, $At = 0.998$ and $Re = 600$ with $\phi_1 = 0.5, \phi_2 = 0.5$.

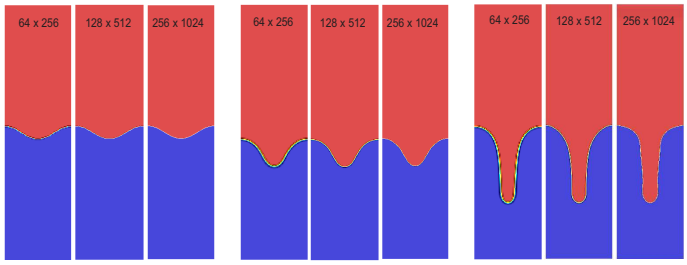

(a) $\acute{t}$=0 *(b)* $\acute{t}$=1 *(c)* $\acute{t}$=1.5

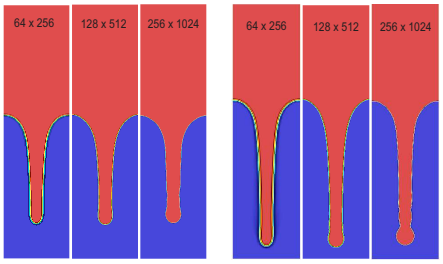

(d) $\acute{t}$=1.75 *(e)* $\acute{t}$=2

Figure 6.9: The time evolution of single mode perturbation for $\frac{\acute{\rho}_1}{\acute{\rho}_2} = 1000$, $At = 0.998$ and $Re = 3000$ with $\phi_1 = 0.5, \phi_2 = 0.5$.

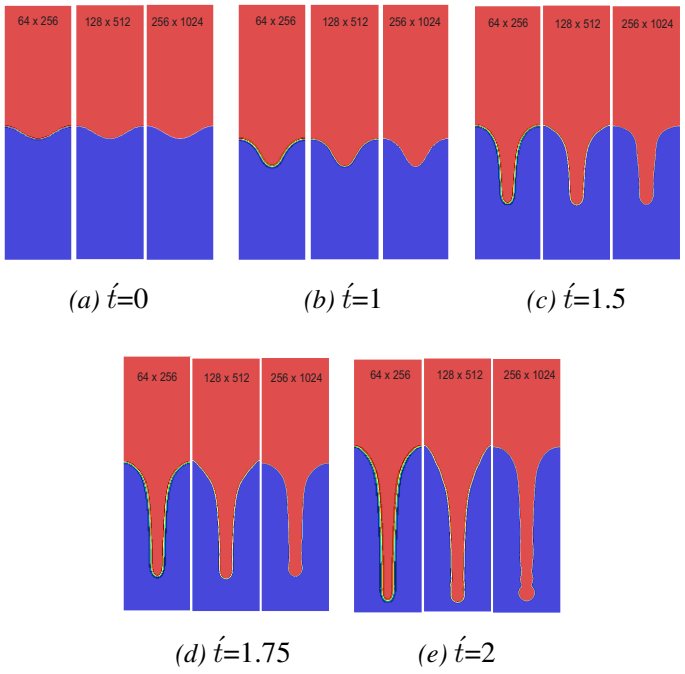

(a) $\acute{t}$=0 *(b)* $\acute{t}$=1 *(c)* $\acute{t}$=1.5

(d) $\acute{t}$=1.75 *(e)* $\acute{t}$=2

Figure 6.10: The time evolution of single mode perturbation for $\frac{\acute{\rho}_1}{\acute{\rho}_2}=1000$, $At=0.998$ and $Re = 5000$ with $\phi_1 = 0.5, \phi_2 = 0.5$.

The kinetic energy of the RTI is computed according to density and the velocity values. A made a comparison is made to test the kinetic energy for various density ratios with Re as illustrated in Figure (6.11). The energy of the flow is increased according to time evolution of the simulation for $\frac{\acute{\rho}_1}{\acute{\rho}_2} = 100$ and 1000. The values of the kinetic energy with high density ratio is larger than the low one because of it depend on the given density ratio value. The result with the number of grid resolution at (64×256), (128×512) and (256×1024) is convergence. From the results, it found that the value of kinetic energy are increased with increasing the density ratios and Re values as shown in Figure (6.11). In addition, the relative mass is studied for the different density, Re and number of grids as illustrated in Figure (6.12). It found that with low density ratios the mass conserved better than the large density ratios.

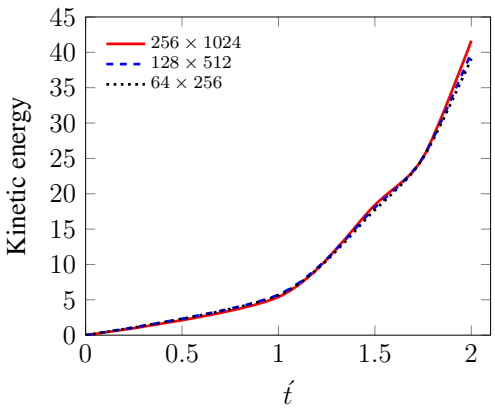

(a) $\frac{\acute{\rho_1}}{\acute{\rho_2}} = 100, Re = 600$

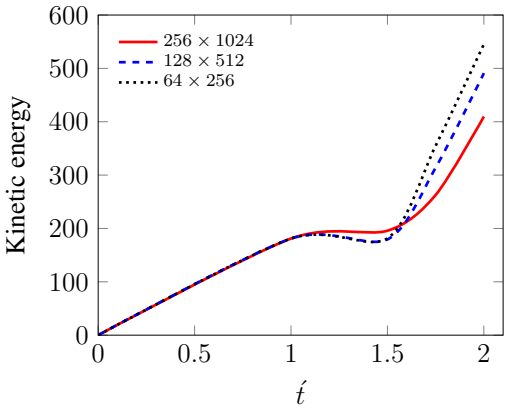

(b) $\frac{\acute{\rho_1}}{\acute{\rho_2}} = 1000, Re = 600$

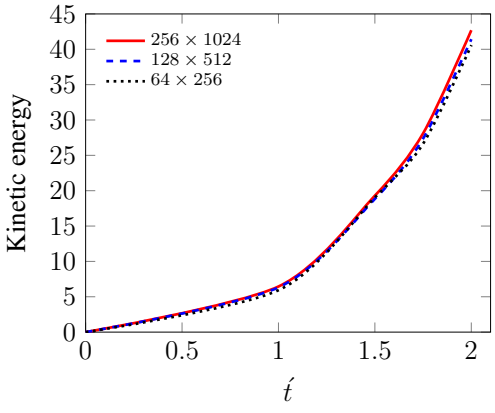

(c) $\frac{\acute{\rho_1}}{\acute{\rho_2}} = 100, Re = 3000$

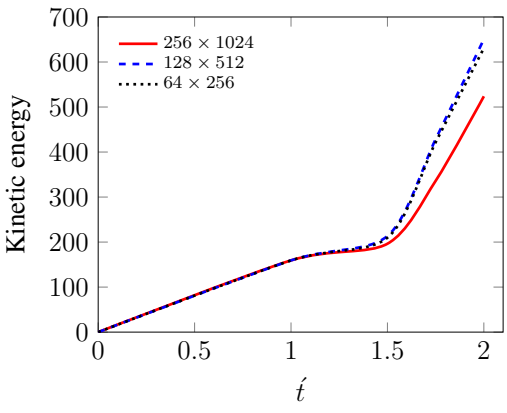

(d) $\frac{\acute{\rho_1}}{\acute{\rho_2}} = 1000, Re = 3000$

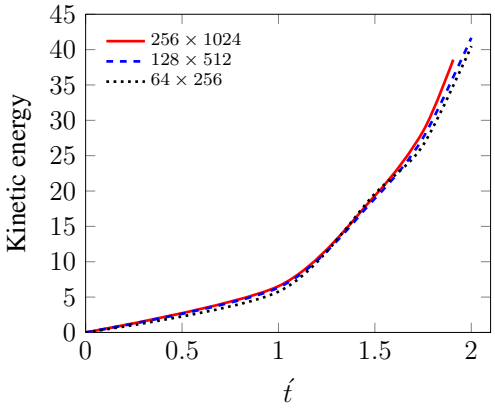

(e) $\frac{\acute{\rho_1}}{\acute{\rho_2}} = 100, Re = 5000$

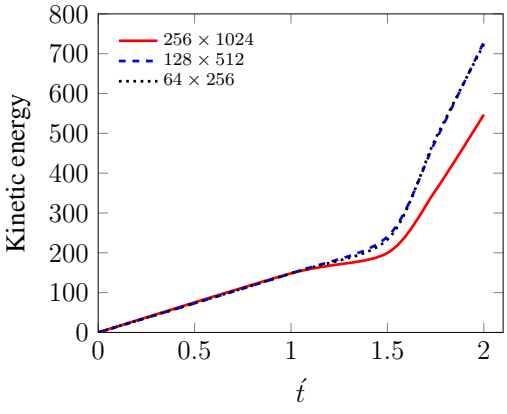

(f) $\frac{\acute{\rho_1}}{\acute{\rho_2}} = 1000, Re = 5000$

Figure 6.11: The time evolution of the kinetic energy for $\frac{\acute{\rho_1}}{\acute{\rho_2}}$=100 and 1000 with different Re .

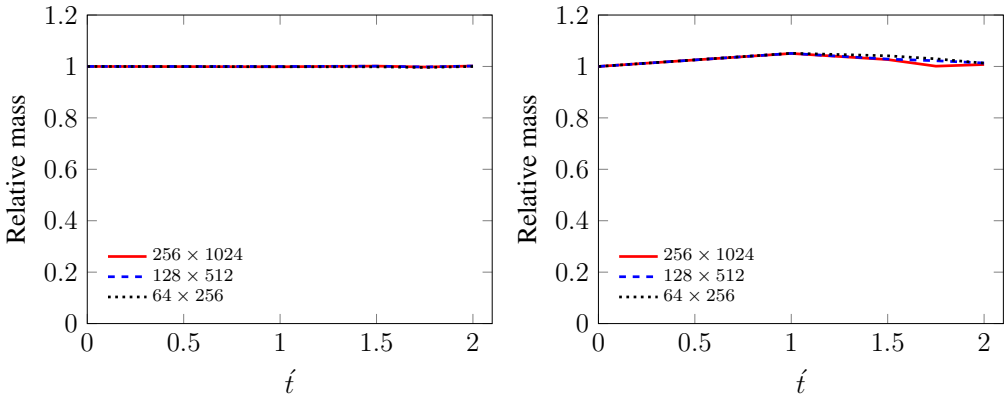

(a) $\frac{\acute{\rho_1}}{\acute{\rho_2}} = 100, Re = 600$

(b) $\frac{\acute{\rho_1}}{\acute{\rho_2}} = 1000, Re = 600$

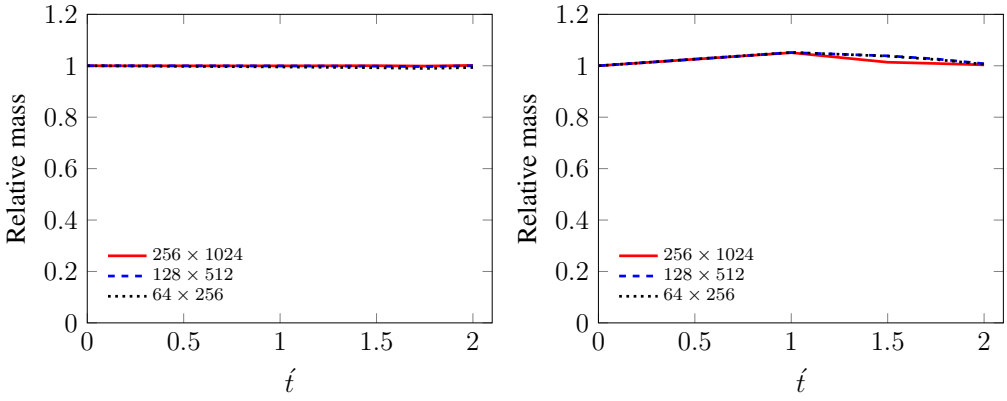

(c) $\frac{\acute{\rho_1}}{\acute{\rho_2}} = 100, Re = 3000$

(d) $\frac{\acute{\rho_1}}{\acute{\rho_2}} = 1000, Re = 3000$

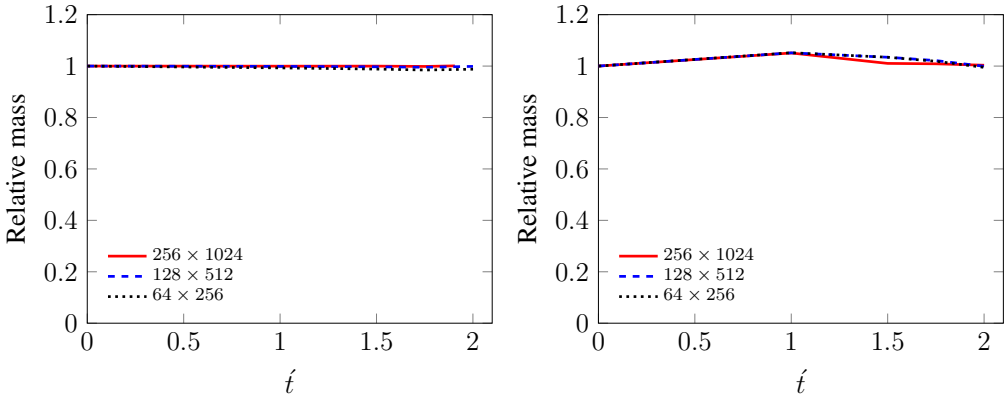

(e) $\frac{\acute{\rho_1}}{\acute{\rho_2}} = 100, Re = 5000$

(f) $\frac{\acute{\rho_1}}{\acute{\rho_2}} = 1000, Re = 5000$

Figure 6.12: The time evolution of the relative mass for $\frac{\acute{\rho_1}}{\acute{\rho_2}}$=100 and 1000 with different Re .

6.3 Multiple mode Rayleigh-Taylor Instability

This kind of Rayleigh-Taylor Instability (RTI) is represented by the development of the interface into turbulent fluid flow. For the multiple mode RTI, the characteristic velocity is $U_c = \sqrt{lx\, g} = 0.08$ and the initial interface function is defined as a random combination of frequency modes

$$y(x) = \frac{1}{2} + \sum_n (a_n \cos(k_n\, x) + b_n \sin(k_n\, x))\,, \tag{6.3.1}$$

with amplitudes a_n and b_n chosen randomly from a Gaussian distribution and $k_n = 2\, n\pi$ is the wave number.

The effect of the surface tension coefficient (σ_{12}) is investigated in the current study. The no slip bounce back boundary is applied in the top and bottom walls and the periodic boundary condition is imposed at left and right side walls of the square domain.

In Figures (6.13)-(6.16), the evolution of two fluid interfaces for different values of the surface tension coefficient (σ_{12}) are illustrated at 6 dimensionless times $\acute{t} = t/\sqrt{lx/g}$ with 512×512 grid and $Re = 4096$.

The results has been demonstrated the expected in increasing complexity of the interface as surface tension coefficient decreases. As shown in Figures (6.13)-(6.16), the small bubbles occur from the small perturbations in the interface move slowly and combine with the big bubbles with the fast motion.

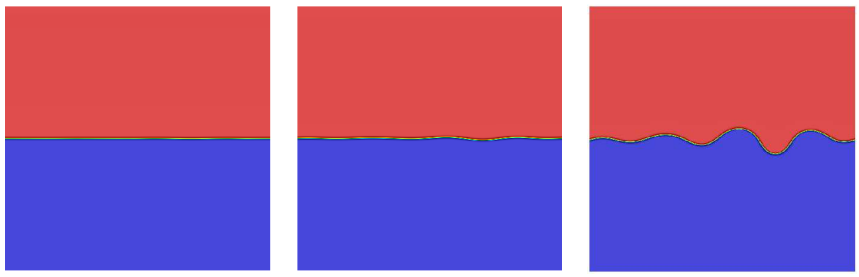

(a) $\acute{t} = 1$ (b) $\acute{t} = 2$ (c) $\acute{t} = 3$

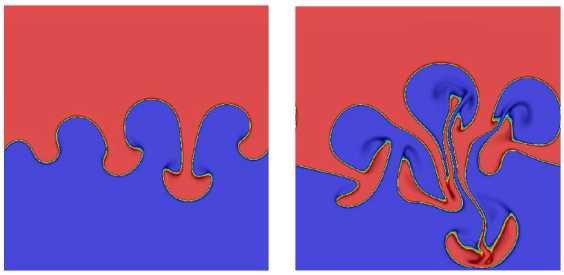

(d) $\acute{t} = 4$ (e) $\acute{t} = 5$

Figure 6.13: The time evolution of Rayleigh-Taylor instability from a multiple mode perturbation at 5 $\acute{t}$ with $\sigma_{12} = 0.1$.

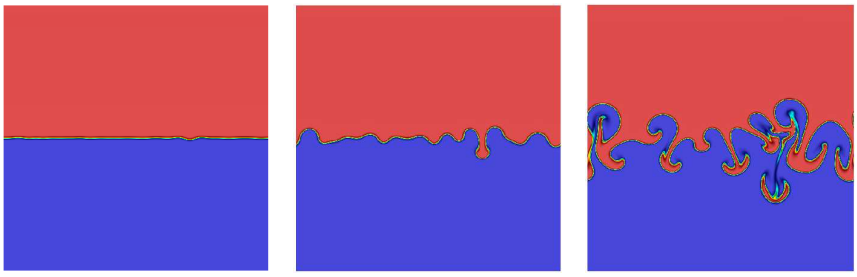

(a) $\acute{t} = 1$ (b) $\acute{t} = 2$ (c) $\acute{t} = 3$

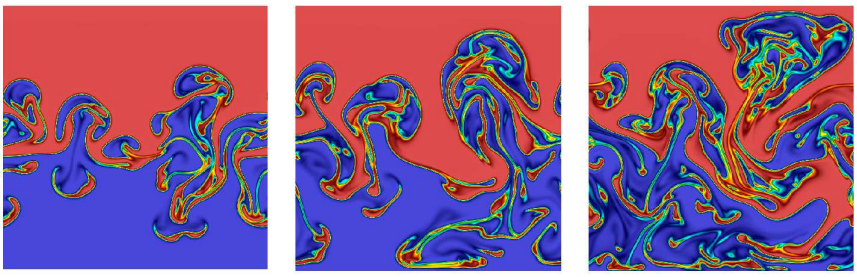

(d) $\acute{t} = 4$ (e) $\acute{t} = 5$ (f) $\acute{t} = 6$

Figure 6.14: The time evolution of Rayleigh-Taylor instability from a multiple mode perturbation at 6 $\acute{t}$ with $\sigma_{12} = 0.01$.

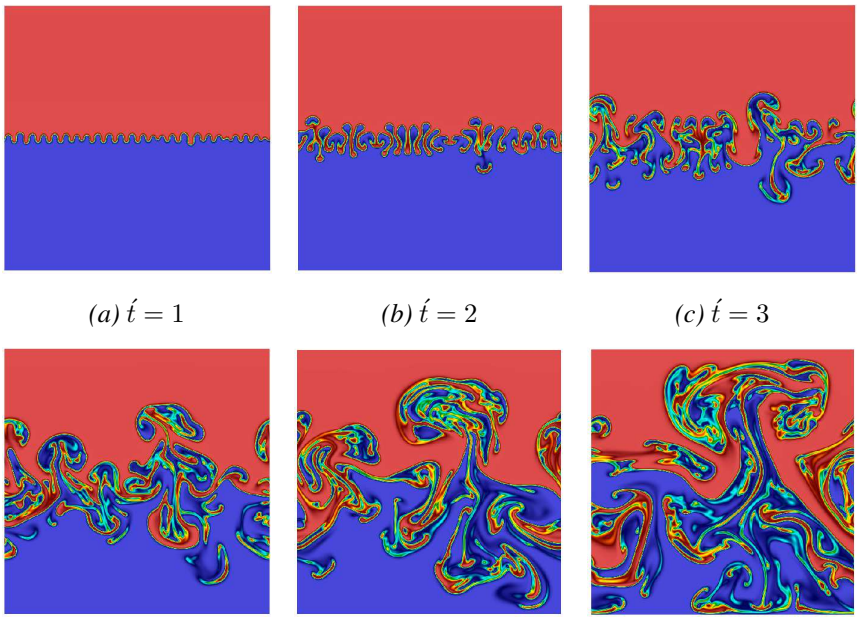

(a) $\acute{t} = 1$ (b) $\acute{t} = 2$ (c) $\acute{t} = 3$

(d) $\acute{t} = 4$ (e) $\acute{t} = 5$ (f) $\acute{t} = 6$

Figure 6.15: The time evolution of Rayleigh-Taylor instability from a multiple mode perturbation at 6 $\acute{t}$ with $\sigma_{12} = 0.001$.

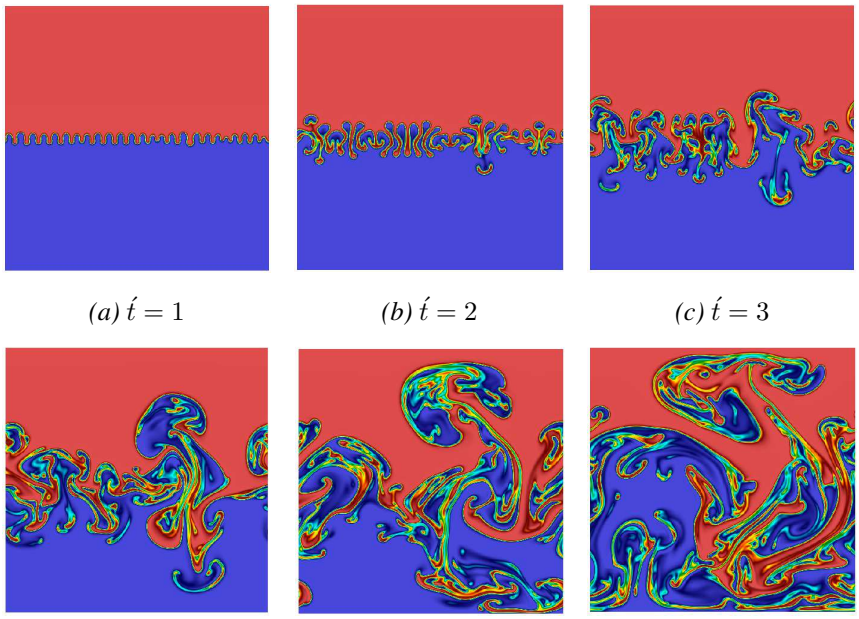

(a) $\acute{t} = 1$ (b) $\acute{t} = 2$ (c) $\acute{t} = 3$

(d) $\acute{t} = 4$ (e) $\acute{t} = 5$ (f) $\acute{t} = 6$

Figure 6.16: The time evolution of Rayleigh-Taylor instability from a multiple mode perturbation at 6 $\acute{t}$ with $\sigma_{12} = 0.000001$.

In Figure (6.17), the time evolution of the relative mass difference is shown for $lx = ly = [64, 128, 256, 512, 1024]$ and $\sigma_{12} = 0.1, 0.01, 0.001, 0.0001, 0.00001$ and 0.000001 with density ratio$= 3$, $At = 0.5$, $Re = 4096$.

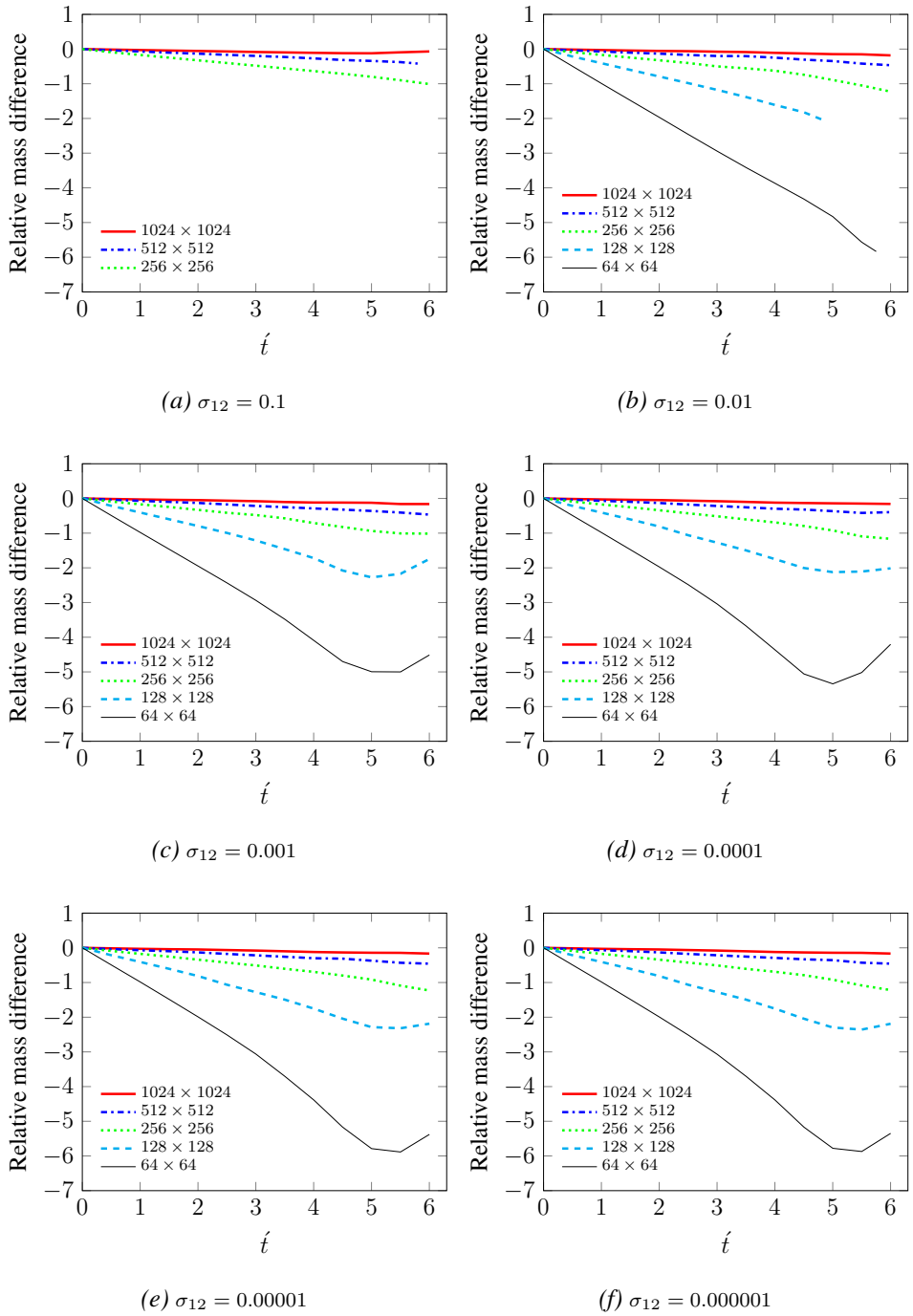

(a) $\sigma_{12} = 0.1$ *(b)* $\sigma_{12} = 0.01$

(c) $\sigma_{12} = 0.001$ *(d)* $\sigma_{12} = 0.0001$

(e) $\sigma_{12} = 0.00001$ *(f)* $\sigma_{12} = 0.000001$

Figure 6.17: The time evolution of the relative mass difference for various σ_{12} and number of grids.

It observed that the mass is conserved with increasing the resolution of the number of grids. The kinetic energy increased according to combine the small bubble with the large one and hit the walls of the simulation as illustrated in Figure (6.18).

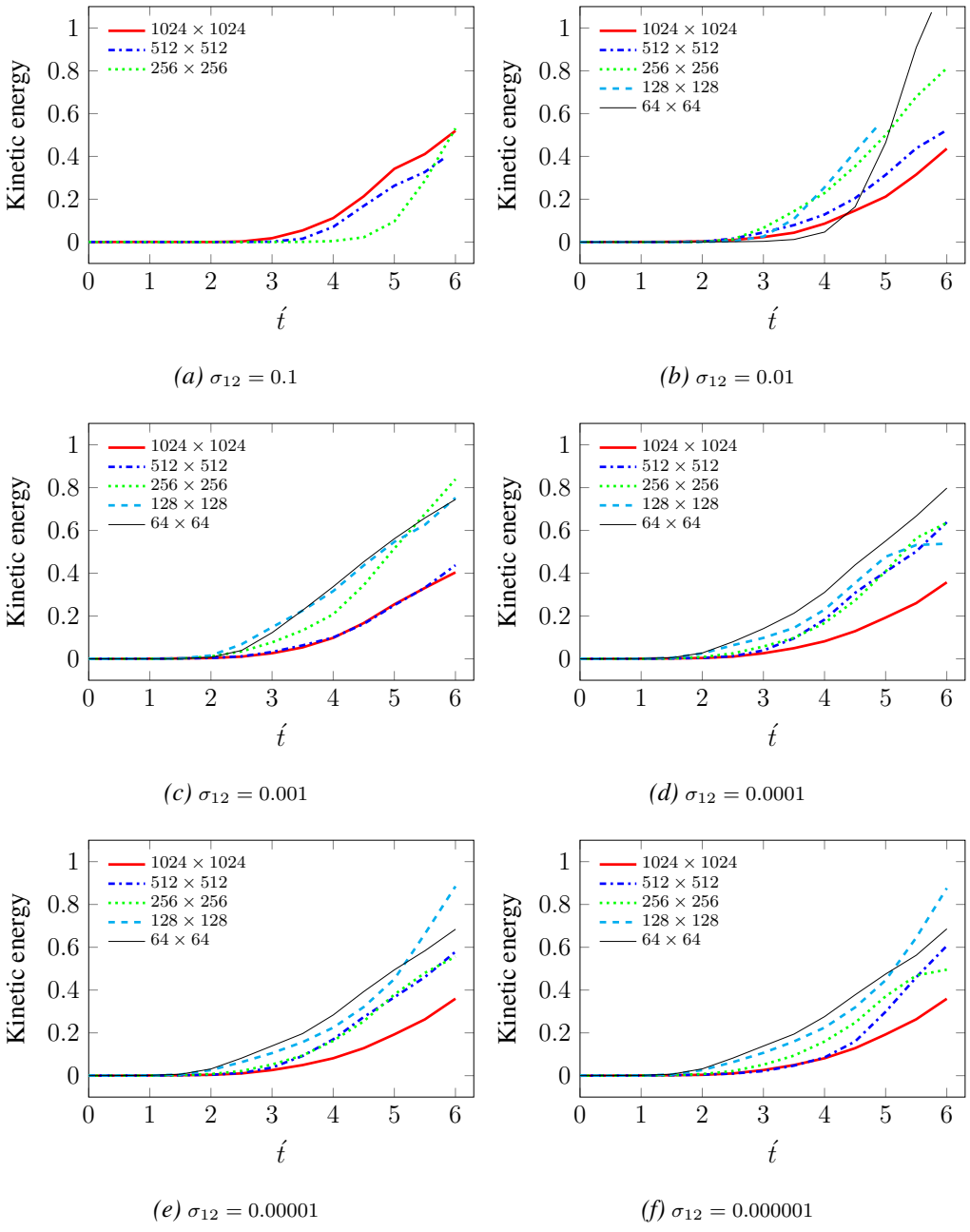

(a) $\sigma_{12} = 0.1$ *(b)* $\sigma_{12} = 0.01$

(c) $\sigma_{12} = 0.001$ *(d)* $\sigma_{12} = 0.0001$

(e) $\sigma_{12} = 0.00001$ *(f)* $\sigma_{12} = 0.000001$

Figure 6.18: The time evolution of the kinetic energy for various σ_{12} and number of grids.

Figure (6.19) are illustrated the convergence of the results for kinetic energy between one initial and average of four initial distribution functions across the interface with the effect of various values of σ_{12} at (512×512) lattice grid. The results show the effect of the σ_{12} which occurred after non dimensional time $\acute{t} = 3$. The small values of σ_{12} slightly different than the large one might be because of the small perturbations that generates the complexity of the flow with time evolution.

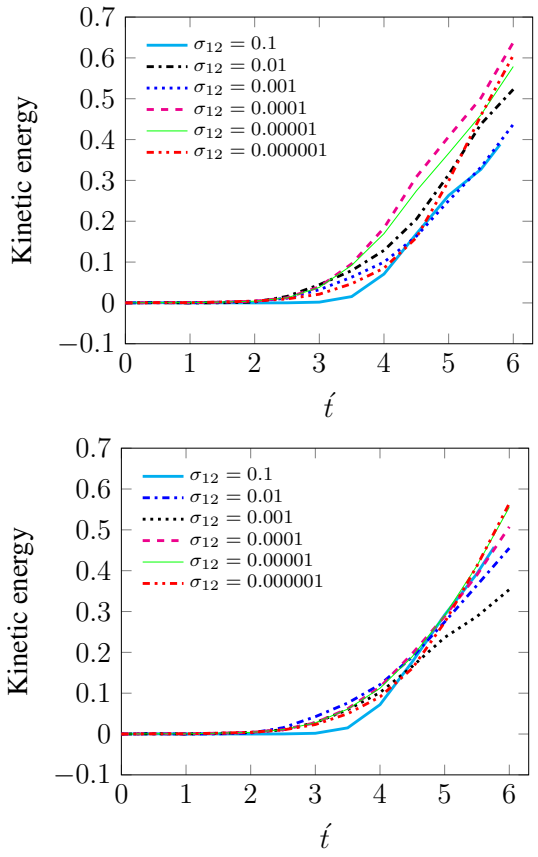

Figure 6.19: The time evolution of the kinetic energy for two distributions initial function with various σ_{12} at (512×512) grid.

The results in Figures (6.20) - (6.23), agree well with those in He et al. (1999) when the comparison made for the average density profiles across the depth in multiple mode RTI with various σ_{12} at four dimensionless time. The results with small value of σ_{12} give excellent agreement with those in the literature.

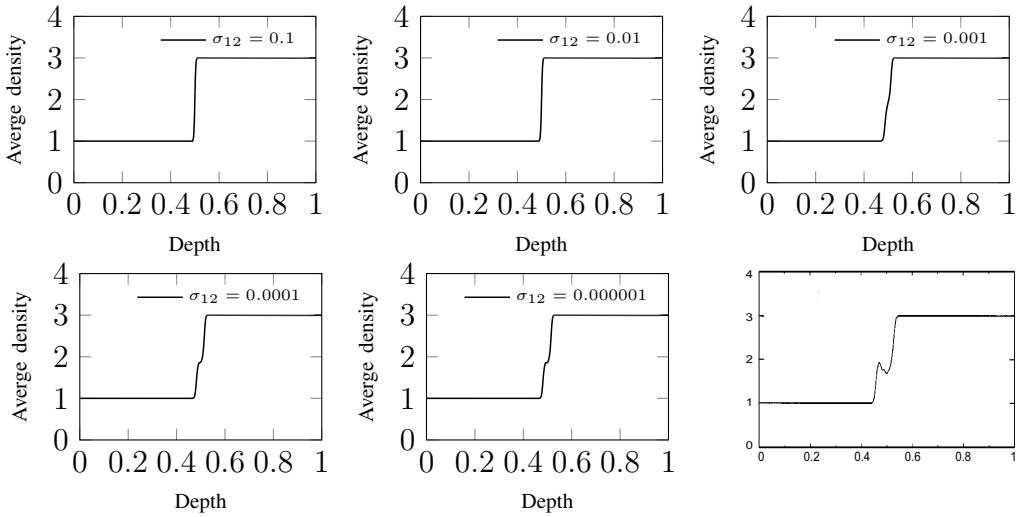

Figure 6.20: The comparison of the average density profiles across the depth in the multiple mode RTI at $\acute{t} = 1$ between He et al. (1999) and the present results with various σ_{12} at (512×512) grid.

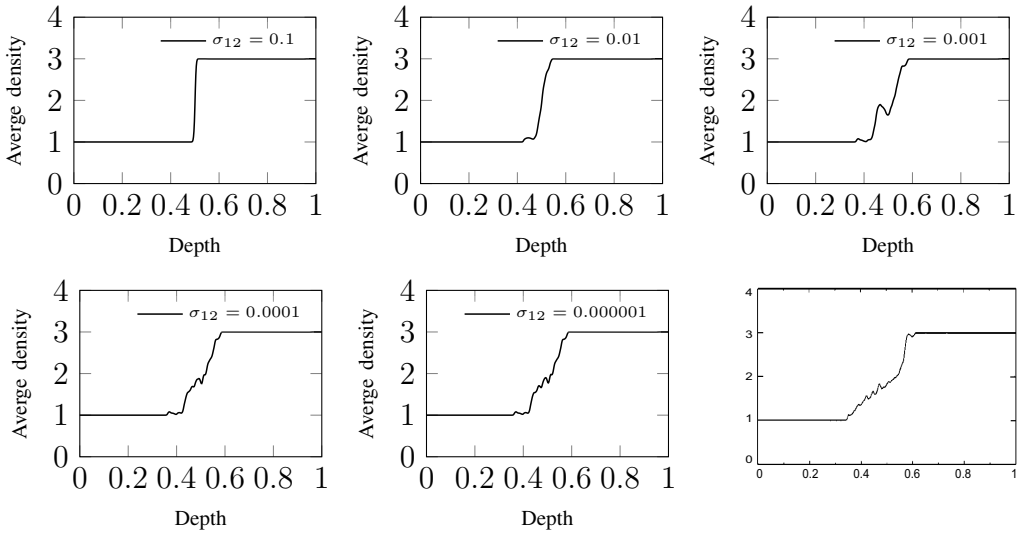

Figure 6.21: The comparison of the average density profiles across the depth in the multiple mode RTI at $\acute{t} = 2$ between He et al. (1999) and the present results with various σ_{12} at (512×512) grid.

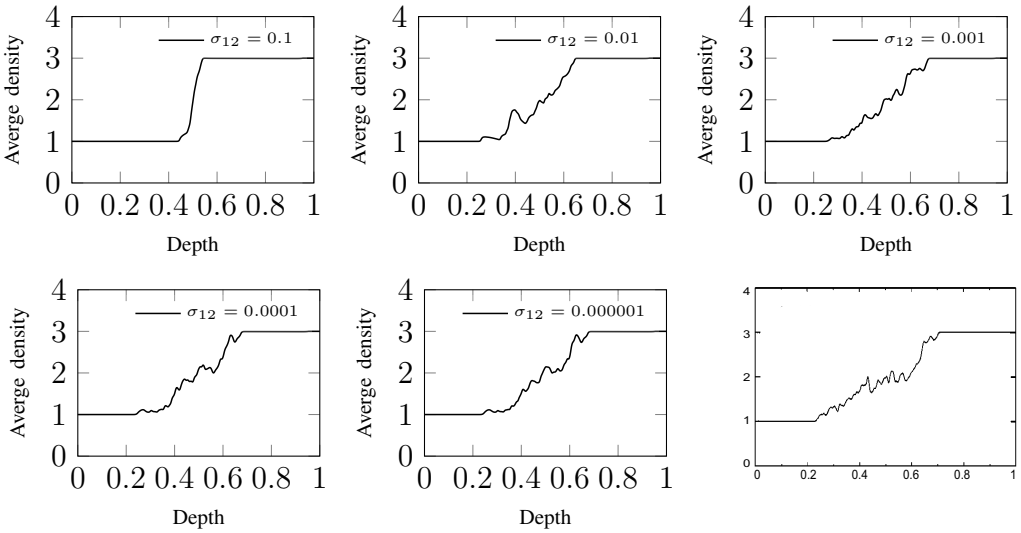

Figure 6.22: The comparison of the average density profiles across the depth in the multiple mode RTI at $\acute{t} = 3$ between He et al. (1999) and the present results with various σ_{12} at (512×512) grid.

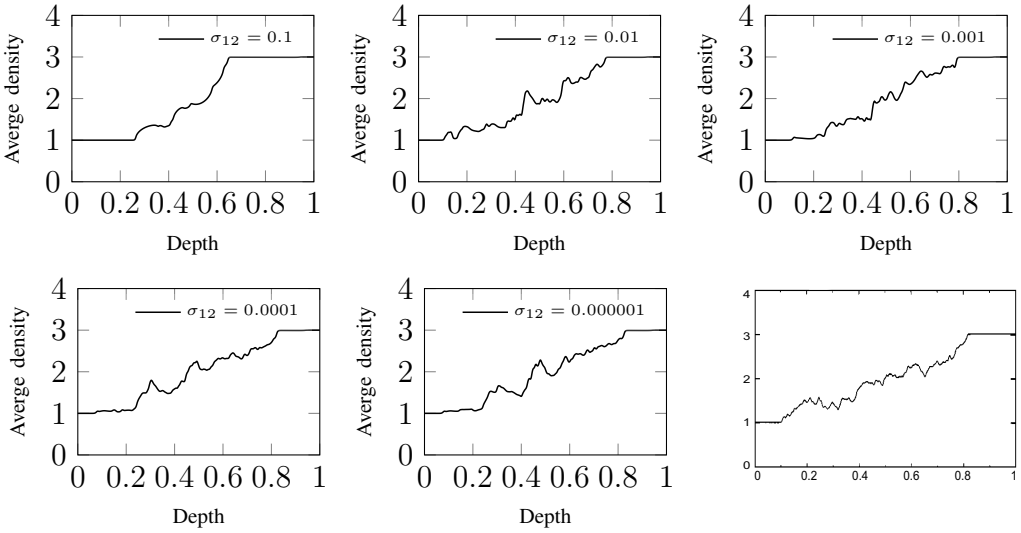

Figure 6.23: The comparison of the average density profiles across the depth in the multiple mode RTI at $\acute{t} = 4$ between He et al. (1999) and the present results with various σ_{12} at (512×512) grid.

The investigation of the position of the bubble and spike fronts versus time for multiple mode RTI has been made as shown in Figure (6.24). As well as, the convergent the grid numbers are tested or each suggestion of σ_{12} at dimensionless time $\acute{t} = 6$. The

results of the position for $lx = 128$ are not stable at $\sigma_{12} = 0.1$ and do not converge with respect to the grid resolutions.

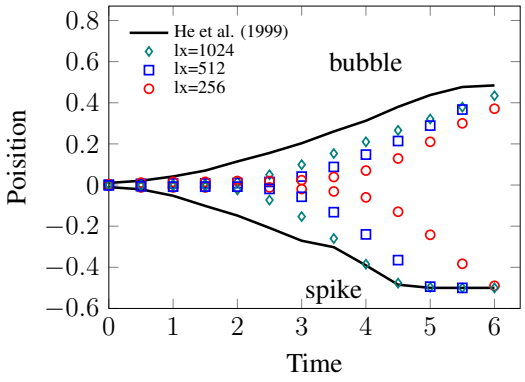

(a) $\sigma_{12} = 0.1$

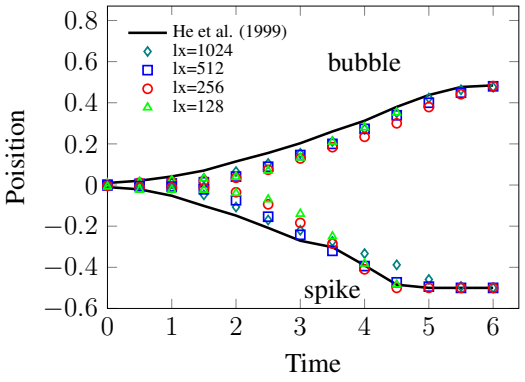

(b) $\sigma_{12} = 0.01$

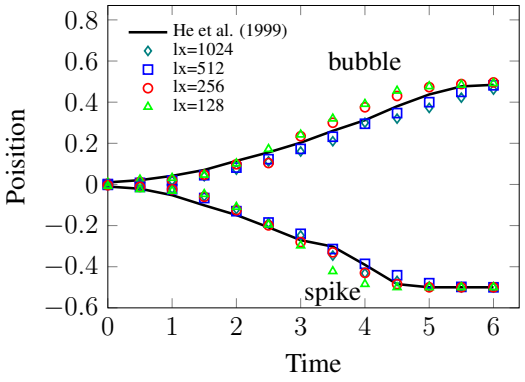

(c) $\sigma_{12} = 0.001$

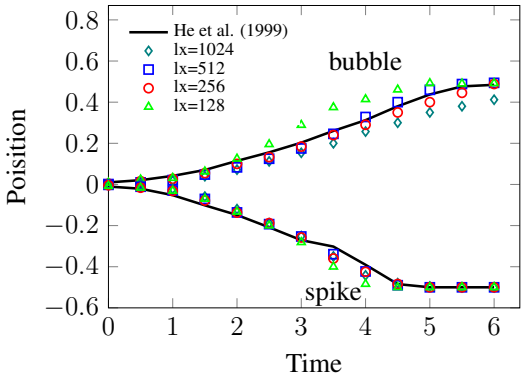

(d) $\sigma_{12} = 0.0001$

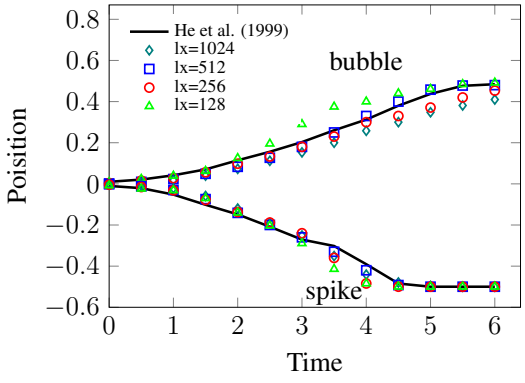

(e) $\sigma_{12} = 0.000001$

Figure 6.24: The Position of the bubble and spike fronts versus time for multiple mode Rayleigh-Taylor instability at Re=4096, At=0.5, different σ_{12} with number of grid lx =1024, 512, 256 and 128.

Large numbers of grid points are necessary to obtain a satisfactory comparison with the results of He et al. (1999). In the meantime, the results for the positions of the bubble and spike agree well at very small values of σ_{12} such as 1×10^{-6} with all grid numbers in the simulations. Further, the convergence with σ_{12} for two different initial distribution function of the positions of the bubble and spike at (512×512) lattice grid in Figures (6.25). From the results, It observed that small values of σ_{12} give an excellent comparison with reference results.

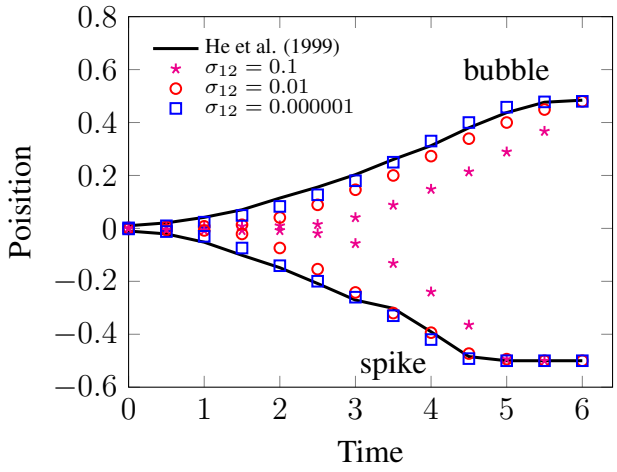

(a) one initial distributions

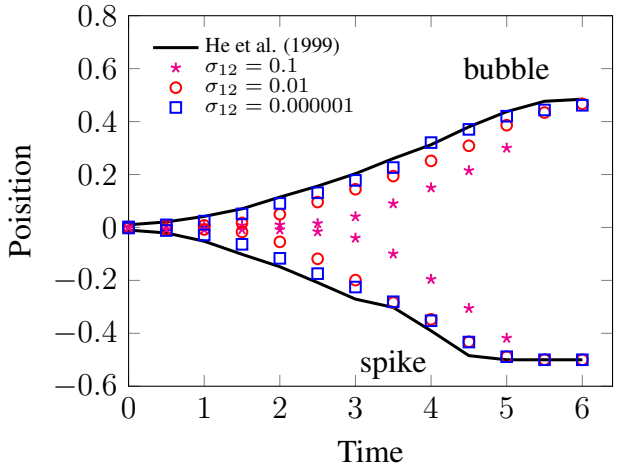

(b) The average of four initial distribution

Figure 6.25: The Position of the bubble and spike fronts versus time for two cases of multiple mode RTI with 3 different σ_{12} at number of grid $lx = 512$ with $\acute{t} = 6$.

6.4 Summary

In this chapter, the LBM for multiphase flows with high density and viscosity ratios have been used to simulate 2D single and multiple mode Rayleigh Taylor instability (RTI). The results agree well with those of He et al. (1999) for single-mode RTI at moderate with small density ratios up to 3 and $Re = 256,\ 614,\ 2048$. Also, the investigations are performed at high density up to 100 and 1000 at $Re = 600,\ 3000$ as mentioned by Fakhari et al. (2017). A good simulations are obtained with $\frac{\acute{\rho}_1}{\acute{\rho}_2} = 100$ and 1000 and high $Re = 5000$. The evolution of interface in a multiple mode RTI with different values of surface tension coefficient (σ_{12}) is examined. Further, the convergence with σ_{12} and grid resolution for the positions of bubble and spike has been investigated. A good result compared with those in He et al. (1999) for the average density profiles across the depth in multiple mode RTI with various σ_{12} at dimensionless time $\acute{t} = 4$. Finally, the results followed the expected pattern of increased interface complexity with decreasing surface tension coefficient (σ_{12}).

Chapter 7

MRT extension of multiphase LBM: Simulation of a Breaking Dam

7.1 Introduction

Nonlinear free surface flows represent a significant problem for studying the application of ocean engineering that can be included the dam breaking problems, breaking wave flow, wave impact and tsunami problems (Janssen & Krafczyk 2011). This type of applications demand large Reynolds number (Re) with high density ratios which can be performed in three dimension simulations. Janssen & Krafczyk (2010) introduced a Volume of fluid (VOF) method based on the Lattice Boltzmann Method (LBM) to implement free surface motion for breaking waves and breaking dams.

Rüde & Thürey (2004) pointed out the advantage of using the mass tracking method of free LB to conserve the mass with tracking the interface, but lack of this approach represent with the difficulties with obtaining the smooth curvature of the simulations for a breaking dam. Janssen et al. (2013) suggested an extension of a hybrid LBM-VOF model of free surface flows with a MRT collision operator. It was applied to several free surface problems, such as breaking dams, free filling jets and breaking waves during shoaling problems. LBM is applied by combining it with different methods to model the physical phenomena such as VOF, LSM and FEM.

In this chapter, the multiphase method has been extended by using MRT to study different cases of breaking dam problems with LBM. The range of the possible density ratios and Reynolds numbers (Re) are explained beyond what was possible with SRT. The convergence with grid resolutions have been investigated in the current study.

This chapter is organized as follows: Section 7.2 presents the Multiple Relaxation Time (MRT) for multiphase with LBM. In section 7.3, different cases of breaking dam simulations are implemented. Section 7.4 provides results for numerical simulations of a two dimensional physical model of a breaking dam on a wet bed. Finally, summary of this chapter is given in Section 7.5.

7.2 Multiple Relaxation Time (MRT) for multiphase with LBM

In the single relaxation time process used in LBGK, the particle distributions functions relax to their local equilibrium with the same rate determined by a single parameter. However, the relaxation rates at the collision step may be different. Wherefore, a collision matrix approach with different relaxation times can be used to eliminate this limitation (Guo & Shu 2013). d'Humieres (1994) presented a 2D MRT lattice Boltzmann model for D_2Q_9. In the current study a new multi relaxation time collision operator with equilibrium distribution function is applied to deal with two-phase flows at high density ratios and high Re number. The collision operator in the multiphase LBM with a MRT for pressureless Navier-Stokes equation, can be defined as

$$g_i(x + c_i\Delta t, t + \Delta t) - \ g_i(x,t) = -\sum_i \ \Lambda_{ij} \ (\ g_j(x,t) - g_j^{(eq)}(x,t) \ ), \qquad (7.2.1)$$

or

$$\mathbf{g}(x + c_i\Delta t, t + \Delta t) - \ \mathbf{g}(x,t) = -\Lambda \ (\ \mathbf{g}(x,t) - \mathbf{g}^{(eq)} j(x,t) \ ), \qquad (7.2.2)$$

where Λ is the collision matrix. Eq.(7.2.2) characterizes the evolution of

$$\mathbf{g} = (g_0,\ g_1,\ g_2,\ g_3,\ g_4,\ g_5,\ g_6,\ g_7,\ g_8)^T\ , \tag{7.2.3}$$

in the velocity space. Also, **g** is represented in a moment space (Lallemand & Luo 2000). The relation between the distribution function and moment can be defined by

$$\mathbf{m} = \mathbf{M}\,\mathbf{g} = (\rho, e, \epsilon, j_x, q_x, j_y, q_y, p_{xx}, p_{xy})^T, \tag{7.2.4}$$

and

$$\mathbf{g} = \mathbf{M}^{-1}\,\mathbf{m}, \tag{7.2.5}$$

where **m** is the moments vector and **M** is a 9×9 matrix transforming **g** in the velocity space to **m** in moment space. In the vector **m**, ρ is the density mode, e is the energy mode, ϵ is related to the energy squared, j_x and j_y correspond to the momentum density (or mass flux), q_x and q_y correspond to the energy flux, and p_{xx} and p_{xy} correspond to the diagonal and off-diagonal component of the viscous stress tensor (Lallemand & Luo 2000).

$$j_x = \rho\,\mathbf{u}_x = \sum_i \mathbf{c}_{ix}\,g_i^{(eq)}\ \ and\ \ j_y = \rho\,\mathbf{u}_y = \sum_i \mathbf{c}_{iy}\,g_i^{(eq)}, \tag{7.2.6}$$

with

$$g_i^{(eq)} = w_i \left[\frac{(c_{i\alpha}.\mathbf{u}^*)}{c_s^2} + \frac{(c_{i\alpha}.\mathbf{u}^*)^2}{2c_s^4} - \frac{u^{*2}}{2c_s^2} \right] + w_i \frac{k}{\rho} G_{\alpha\beta} c_{i\alpha} c_{i\beta} - v_i \frac{k}{2\rho} |\nabla\phi|^2, \quad (7.2.7)$$

where

$$G_{\alpha\beta} = \frac{9}{2\,c^4} \left(\frac{\partial\phi}{\partial x_\alpha} \frac{\partial\phi}{\partial x_\beta} \right) - \frac{9}{4\,c^4} \left(\frac{\partial\phi}{\partial x_\gamma} \frac{\partial\phi}{\partial x_\gamma} \right) \delta_{\alpha\beta}, \quad (7.2.8)$$

and the transformation matrix **M** is

$$\mathbf{M} = \begin{bmatrix} 1 & 1 & 1 & 1 & 1 & 1 & 1 & 1 & 1 \\ -4 & -1 & -1 & -1 & -1 & 2 & 2 & 2 & 2 \\ 4 & -2 & -2 & -2 & -2 & 1 & 1 & 1 & 1 \\ 0 & 1 & 0 & -1 & 0 & 1 & -1 & -1 & 1 \\ 0 & -2 & 0 & 2 & 0 & 1 & -1 & -1 & 1 \\ 0 & 0 & 1 & 0 & -1 & 1 & 1 & -1 & -1 \\ 0 & 0 & -2 & 0 & 2 & 1 & 1 & -1 & -1 \\ 0 & 1 & -1 & 1 & -1 & 0 & 0 & 0 & 0 \\ 0 & 0 & 0 & 0 & 0 & 1 & -1 & 1 & -1 \end{bmatrix},$$

and the inverse of transformation matrix M is M^{-1}

$$\mathbf{M}^{-1} = a \begin{bmatrix} 4 & -4 & 4 & 0 & 0 & 0 & 0 & 0 & 0 \\ 4 & -1 & -2 & 6 & -6 & 0 & 0 & 9 & 0 \\ 4 & -1 & -2 & 0 & 0 & 6 & -6 & -9 & 0 \\ 4 & -1 & -2 & -6 & 6 & 0 & 0 & 9 & 0 \\ 4 & -1 & -2 & 0 & 0 & -6 & 6 & -9 & 0 \\ 4 & 2 & 1 & 6 & 3 & 6 & 3 & 0 & -1 \\ 4 & 2 & 1 & -6 & -3 & 6 & 3 & 0 & -1 \\ 4 & 2 & 1 & -6 & -3 & -6 & -3 & 0 & 0 \\ 4 & 2 & 1 & 6 & 3 & -6 & -3 & 0 & -1 \end{bmatrix},$$

where $a = \frac{1}{36}$. From eq.(7.2.5), the eq.(7.2.2) can be rewritten as follows

$$\mathbf{M}^{-1}\,\mathbf{m}(x + c_i\Delta t, t + \Delta t) - \mathbf{M}^{-1}\,\mathbf{m}(x,t) = -\Lambda\,\mathbf{M}^{-1}(\,\mathbf{m} - \mathbf{m}^{(eq)}\,), \qquad (7.2.9)$$

by using the left multiplication to **M**, yields

$$\mathbf{M}\,\mathbf{M}^{-1}\,\mathbf{m}(x + c_i\Delta t, t + \Delta t) - \mathbf{M}\,\mathbf{M}^{-1}\,\mathbf{m}(x,t) = -\mathbf{M}\,\Lambda\,\mathbf{M}^{-1}(\,\mathbf{m} - \mathbf{m}^{(eq)}\,),$$

so

$$\mathbf{m}(x + c_i\Delta t, t + \Delta t) - \mathbf{m}(x,t) = -\mathbf{M}\,\Lambda\,\mathbf{M}^{-1}(\,\mathbf{m} - \mathbf{m}^{(eq)}\,),$$

$$= -\mathbf{S}\,(\,\mathbf{m} - \mathbf{m}^{(eq)}\,),$$

where $\mathbf{S} = \mathbf{M}\ \Lambda\ \mathbf{M}^{-1}$ is diagonal matrix can be expressed as follows

$$\mathbf{S} = \begin{bmatrix} s_0 & 0 & 0 & 0 & 0 & 0 & 0 & 0 & 0 \\ 0 & s_1 & 0 & 0 & 0 & 0 & 0 & 0 & 0 \\ 0 & 0 & s_2 & 0 & 0 & 0 & 0 & 0 & 0 \\ 0 & 0 & 0 & s_3 & 0 & 0 & 0 & 0 & 0 \\ 0 & 0 & 0 & 0 & s_4 & 0 & 0 & 0 & 0 \\ 0 & 0 & 0 & 0 & 0 & s_5 & 0 & 0 & 0 \\ 0 & 0 & 0 & 0 & 0 & 0 & s_6 & 0 & 0 \\ 0 & 0 & 0 & 0 & 0 & 0 & 0 & s_7 & 0 \\ 0 & 0 & 0 & 0 & 0 & 0 & 0 & 0 & s_8 \end{bmatrix},$$

It is more flexible to make the rest of the relaxation parameters (Yu et al. 2003).
$\mathbf{S} = (1.0,\ 1.4,\ 1.4,\ s_3,\ 1.2,\ s_5,\ 1.2,\ s_7,\ s_8)$, where $s_7 = s_8 = \omega = \frac{1}{(3\nu+0.5)}$, s_3 and s_5 are arbitrary, can be set to 1.0 (Sidik et al. 2013). thus

$$\mathbf{m}(x + c_i\Delta t, t + \Delta t) - \mathbf{m}(x,t) = -\mathbf{S}\ (\ \mathbf{m} - \mathbf{m}^{(eq)}\ ), \tag{7.2.10}$$

The equilibrium in the moment space of the multiphase approach is $\mathbf{m}^{eq} = \mathbf{M}\ \mathbf{g}^{(eq)}$ which can defined as

$$\mathbf{m}^{eq} = \begin{bmatrix} \frac{k\,(G_{xx}+G_{yy})}{3\,\rho} \\ \frac{3\,(u_x^2+u_y^2)\,\rho - 3\,k\left((\frac{\partial\phi}{\partial x})^2+(\frac{\partial\phi}{\partial y})^2\right)}{3\,\rho} \\ \frac{27\,k\left((\frac{\partial\phi}{\partial x})^2+(\frac{\partial\phi}{\partial y})^2\right) - 2\,k(G_{xx}+G_{yy}) - 18\,\rho(u_x^2+u_y^2)}{3\,\rho} \\ u_x \\ -u_x \\ u_y \\ -u_y \\ \frac{9\,(u_x^2+u_y^2)\,\rho + 2\,k(G_{xx}-G_{yy})}{9\,\rho} \\ \frac{3\,\rho\,u_x\,u_y + 2\,k\,G_{xy}}{9\,\rho} \end{bmatrix} = \mathbf{M}\,\mathbf{g}^{(eq)}. \tag{7.2.11}$$

7.3 Numerical results and analysis of the Simulation of Breaking Dam problem

In this section, the dam break problems by multi phase LBM method with high density and viscosity ratios are simulated for different cases and physical geometry. In this study, the MRT mode is applied with breaking dam problems especially for density ratio up to 1000 and high Re numbers which was imposable with SRT mode. Succi (2001) introduced various kind of boundary conditions such as the no-slip, free-slip and partial slip boundary conditions as illustrated in Figure (7.1). It observed that

these boundaries are used with breaking waves and breaking dams as are mentioned in literature review of chapter 1. In the current simulations, the free-slip at bottom boundary has been employed as shown in Figure (7.1). For the no-slip bounce back boundary condition, the distribution function with normal and tangential direction is reversed at the boundary. The unknown distribution function at boundary is obtained from $f_5 = f_7$, $f_2 = f_4$ and $f_6 = f_8$ at bottom boundary. Free-slip boundary condition is implemented for the smooth boundary with little contact spend when the fluid flowing and the momentum in tangential direction is not modified at the boundary. In this case, the unknown distribution function at boundary found from $f_5 = f_8$, $f_2 = f_4$ and $f_6 = f_7$ at bottom boundary. The partial slip boundary conditions is combine between no-slip and free-slip boundary condition and the unknown distribution function at boundary estimates from

$$f_i^{unknown} = \alpha\, f_{i\,no-slip} + (1-\alpha)\, f_{i\,free-slip} \quad 0 \le \alpha \le 1, \tag{7.3.1}$$

where α is partial slip coefficient.

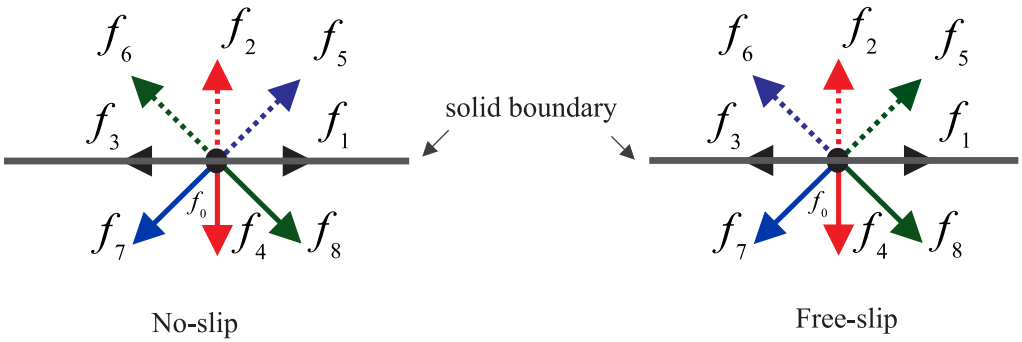

Figure 7.1: Schematic boundary condition.

7.3.1 H=2W and D=2H

The two dimensional physical model of breaking dam problem illustrated in Figure (7.2). The simulation of breaking dam is adopted to investigate the MRT of multiphase LBM by comparing the numerical result with Martin et al. (1952). The same setup of breaking dam in Sun & Tao (2010) which coupled volume of fluid and level set (VOSET) method are is used.

The height of initial water column $(H = 2W)$ is $0.292m$ and width (W) equals to $0.146m$ and $D = 0.584m$. The density of water column is $1 \times 10^3 kg/m^2$, viscosity equals to $1 \times 10^{-6} m^2/s$ and gravity is $9.8m/s^2$. The parameters of the dam breaking is obtained by applying the scaling parameters among the physical (dimensional), non dimensional and the computational (LBM), for more details see appendix A. The free-slip boundary conditions are applied for four walls in Figure (7.2).

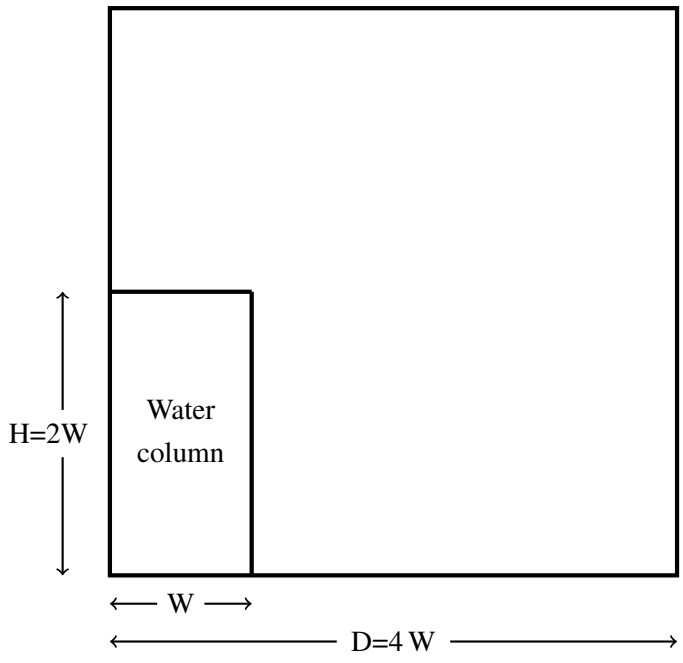

Figure 7.2: Schematic illustration of dam break problem.

In the current simulations, the dimensionless parameters of LB are $\Delta x = \Delta t = 1$, the number of grid points $(200 \times 200,\ 300 \times 300,\ 400 \times 400,\ 500 \times 500)$ with corresponding gravity (g) $(2.817 \times 10^{-6},\ 8.346 \times 10^{-7},\ 3.521 \times 10^{-7},\ 1.803 \times 10^{-7})$, which is represented as a body force according to Guo et al. (2002). The comparison of the position of the surge front and water column height between the numerical results and experimental result from Martin et al. (1952) with square domain of the tank is illustrated in Figure (7.3) and Figure (7.4). From the result for leading edge position have shown a good comparison with Martin et al. (1952) by increasing the grid resolution. In addition, the perfect result obtained for water column height with those in the literature. Further, simulation is applied with a rectangular domain.

The results of Figure (7.5) and Figure (7.6) illustrated the convergence with grid numbers of the domain of the breaking dam to Martin et al. (1952) results for both leading edge position and water column height results. For the results of square domain is slightly more convergent than the rectangular one to Martin et al. (1952) results might be increasing the gird numbers agree well with the those in the literature.

In addition, the comparison between the numerical (LBM) and experimental simulation of Koshizuka & Oka (1996) at four times is shown in Figure (7.7). It observed that the results of the LBM simulations showing agreement with Koshizuka & Oka (1996) results.

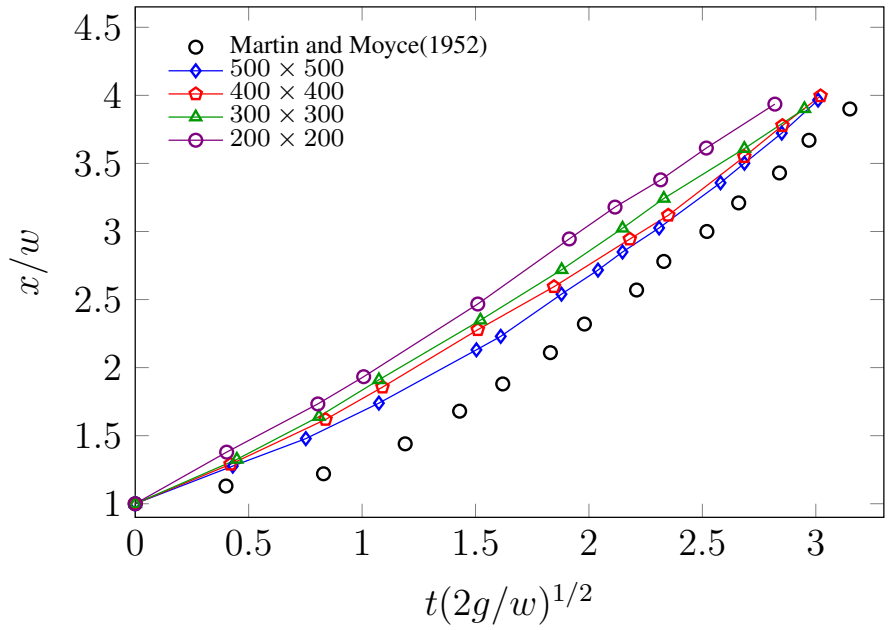

Figure 7.3: The comparison between the numerical and experimental results for leading edge location.

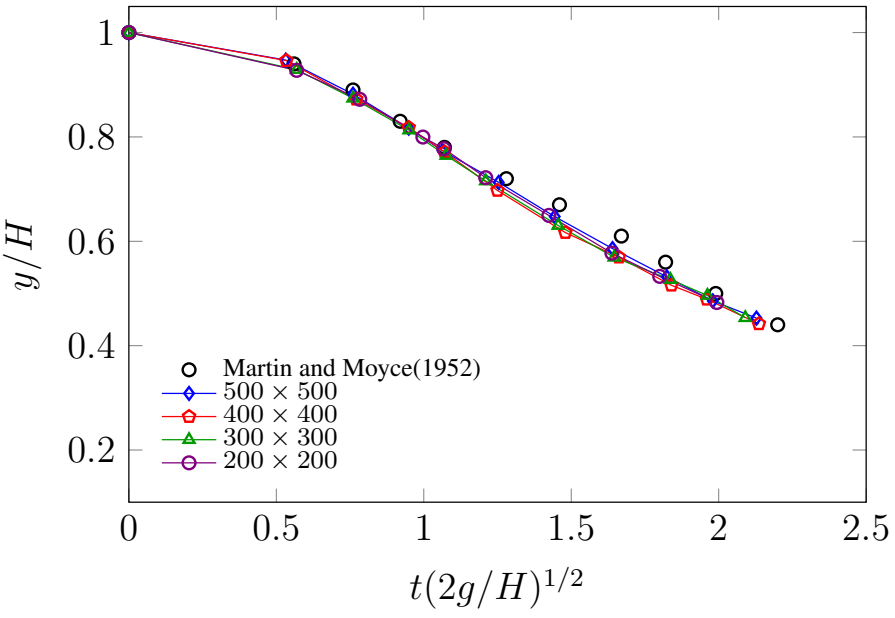

Figure 7.4: The comparison between the numerical and experimental results for water column height.

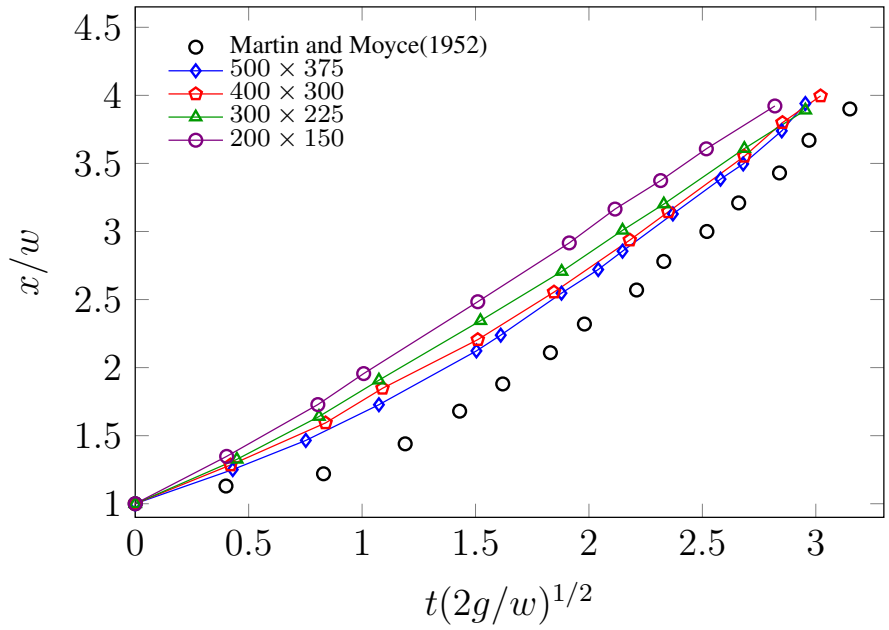

Figure 7.5: The comparison between the numerical and experimental results for leading edge location.

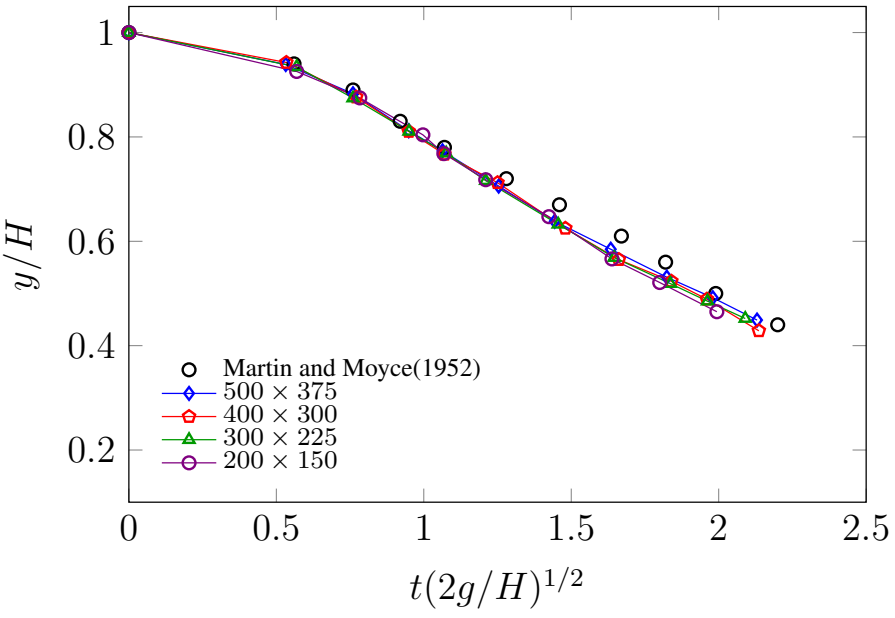

Figure 7.6: The comparison between the numerical and experimental results for water column height.

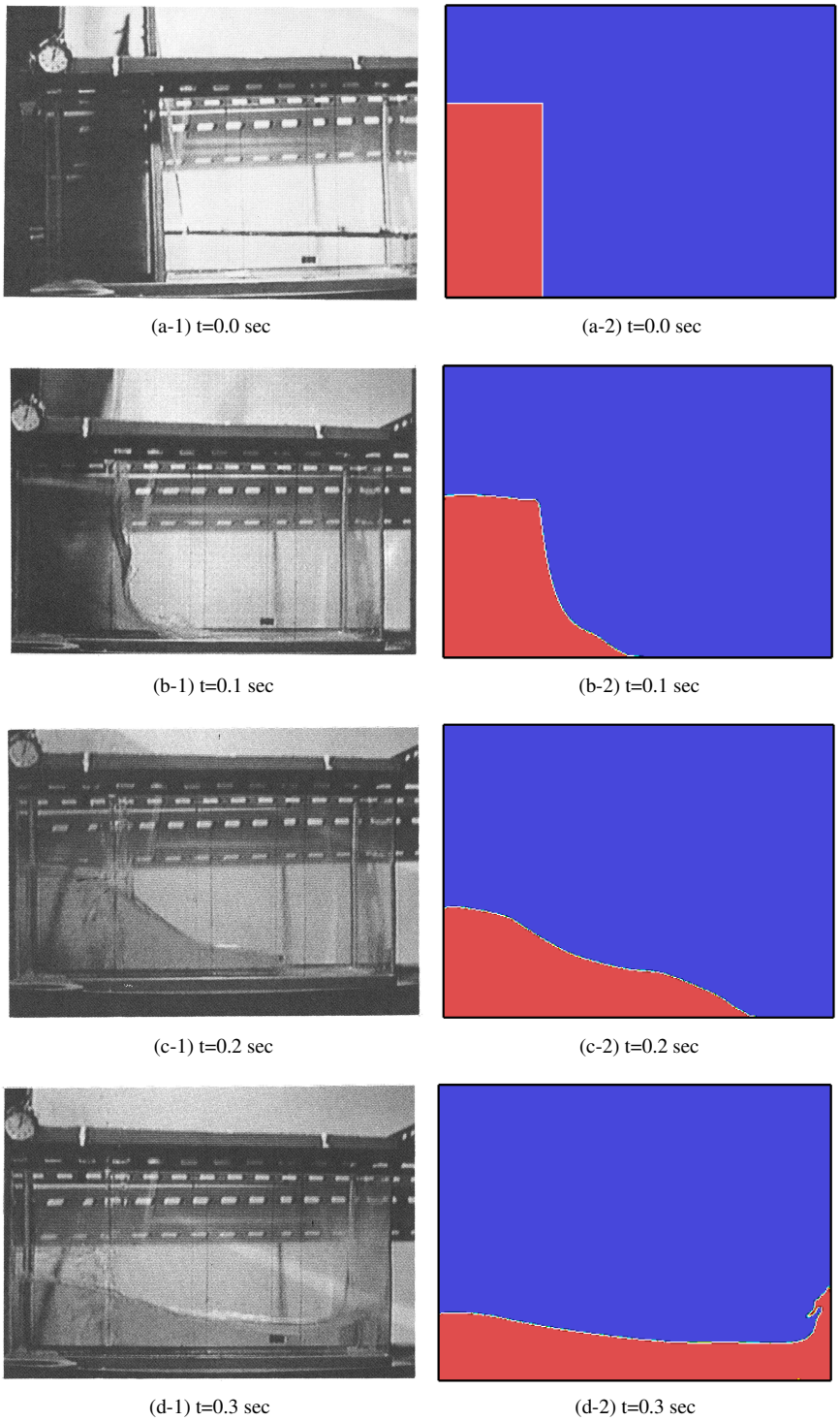

(a-1) t=0.0 sec (a-2) t=0.0 sec

(b-1) t=0.1 sec (b-2) t=0.1 sec

(c-1) t=0.2 sec (c-2) t=0.2 sec

(d-1) t=0.3 sec (d-2) t=0.3 sec

Figure 7.7: Comparison of the evolution of leading edge between the experimental data of Koshizuka & Oka (1996) and the present breaking dam problem.

7.3.2 H=0.5W and D=5.366H

The two dimensional physical model of breaking dam problem proposed by Colagrossi & Landrini (2003) as illustrated in the Figure (7.8). The simulation of breaking dam is adopted to investigate the MRT of multiphase LBM by comparing the numerical result with Colagrossi & Landrini (2003). The height of initial water column is H=0.5W and width is W and $D = 5.366H$. The density of water column is $1 \times 10^3\, kg/m^2$, viscosity is $1 \times 10^{-6}\, m^2/s$ and gravity is $9.8\, m/s^2$. The slip boundary conditions for four walls are applied. In the simulations the dimensionless parameters of LB are $\Delta x = \Delta t = 1$, number of grid points $(lx \times ly = 268 \times 100,\ 536 \times 200,\ 804 \times 300)$ with $(W \times H = 100 \times 50,\ 200 \times 100,\ 300 \times 150)$ at different $Ma = 0.08,\ 0.04,\ 0.027$ with corresponding gravity $(1.459 \times 10^{-5},\ 1.8239 \times 10^{-6},\ 5.4042 \times 10^{-7})$, respectively. The $Re = H * U_{\max}/\nu$ is 169367 and Froude number $(Fr = U_{\max}/\sqrt{g\,H} = 1.71)$, where $U_{\max} = \mathrm{Ma}\, c_s$ is maximum non dimensional velocity.

Figure 7.8: Sketch of dam break problem in a rectangular tank.

A good agreement is obtained see (Figure (7.10)) by comparing with Colagrossi & Landrini (2003) when fixing $Ma = 0.02$ and increase the number of grid points $(lx \times ly = 268 \times 100,\ 536 \times 200,\ 804 \times 300)$ with corresponding g $(9.1196 \times 10^{-7},\ 4.5598 \times 10^{-7},\ 3.0399 \times 10^{-7})$ and relaxation time coefficient τ $(0.50001,\ 0.500025,\ 0.500031)$.

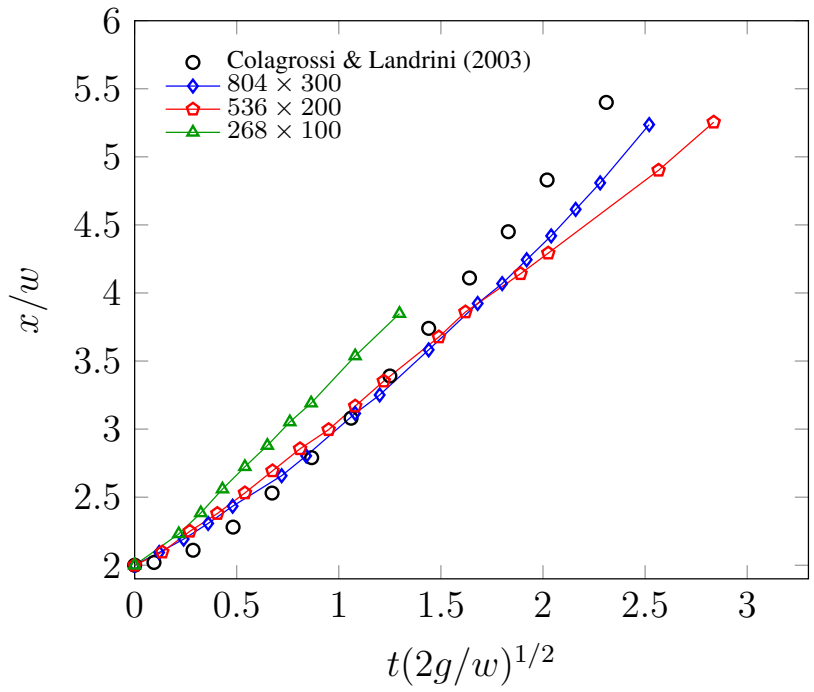

Figure 7.9: The comparison between the numerical and experimental results for leading edge location with different Ma.

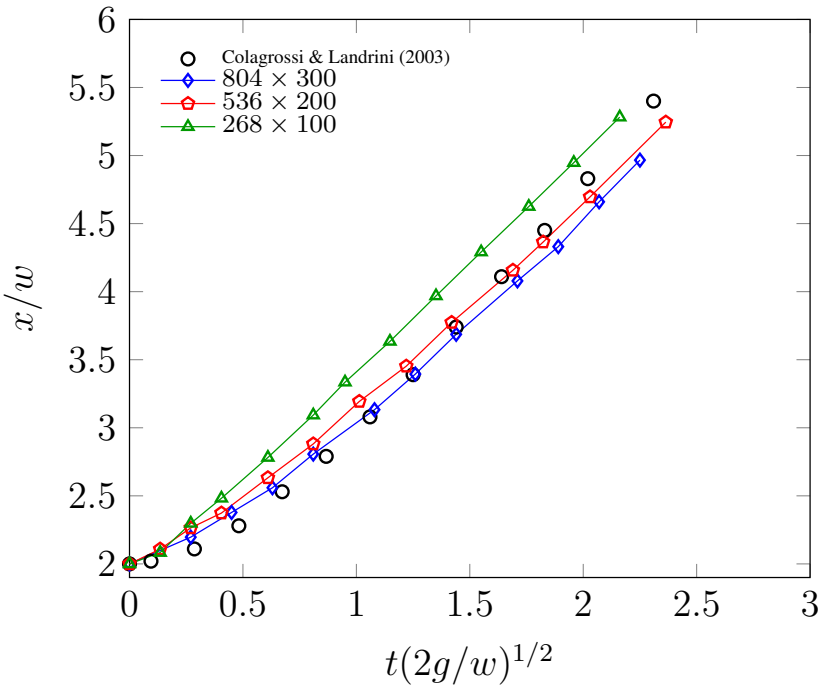

Figure 7.10: The comparison between the numerical and experimental results for leading edge location with $Ma = 0.02$.

7.4 Dam breaking with a wet bed

The two dimensional physical model of breaking dam on a wet bed simulation proposed by Badarch et al. (2016) is illustrated in Figure (7.11). The simulation of wet bed for breaking dam is adopted to investigate the MRT of multiphase LBM by comparing the numerical result with both results (experiment and numerical) of Badarch et al. (2016). Badarch et al. (2016) used free-surface algorithm for LBM adopted from Thürey et al. (2005). The height of initial water depth is H=0.27m with width $W = 0.1m$, length of downstream domain $D = 0.8m$ and water depth of the wet bed is $d = 0.04m$ as followed the configuration of Badarch et al. (2016). The density of water column is $1 \times 10^3 kg/m^2$, viscosity is $1 \times 10^{-6} m^2/s$ and gravity is $9.8m/s^2$. The free slip boundary conditions is used for the walls.

In order to investigate the simulation, the non dimensional scale can be written for the position of the water front $\acute{X}$ at time $\acute{T}$ as

$$\acute{X} = \frac{x}{W}, \quad \text{and} \quad \acute{T} = t\sqrt{\frac{n\,g}{W}}, \tag{7.4.1}$$

where $n = \frac{H}{W}$, the first point P_1 is defined at position $\frac{D}{4}$ and the second point P_2 at $\frac{3D}{4}$. In the simulations the dimensionless parameters of LB are $\Delta x = \Delta t = 1$, number of grid points $(lx \times ly = 320 \times 160,\, 400 \times 200)$ with corresponding $(W \times H = 40 \times 108,\, 50 \times 135)$ and gravity $(8.3333 \times 10^{-7},\, 6.6667 \times 10^{-7})$, respectively. The $Re = H * U_{\max}/\nu$ equals to 439420, where $U_{\max} = \text{Ma}\, c_s$ is maximum non dimensional velocity. It observed that the result becomes more accurate by increasing the number of grid point to (400×200) as shown in Figure (7.12) which illustrated a comparison of the position of the surge front and water column height between the numerical results and both experimental and numerical results from Badarch et al. (2016). A good agreement obtained from Figure (7.12) by comparing when with fix Ma $= 0.01$ and in-

crease the number of grid points $(lx \times ly = 320 \times 160,\ 400 \times 200)$ with corresponding relaxation time coefficient τ $(0.5000043,\ 0.5000053)$ and d $(16,\ 20)$, respectively. Further, the comparison between the numerical and experimental simulation at four time is illustrated in Figure (7.13) shows agreement with Badarch et al. (2016) results.

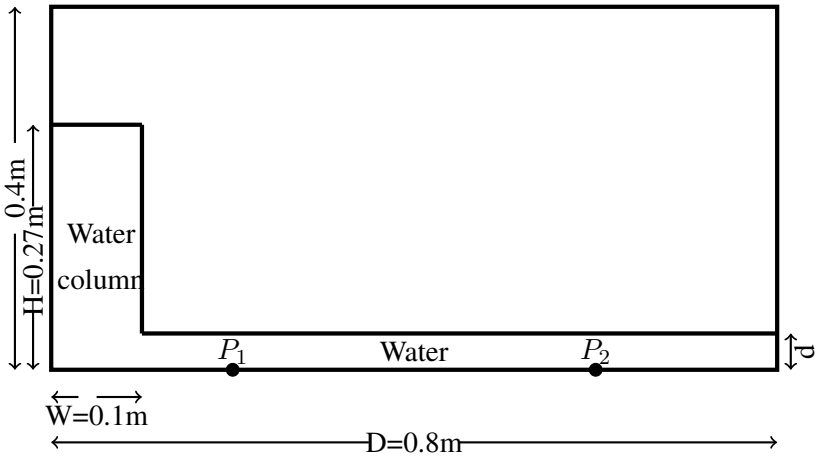

Figure 7.11: Sketch of dam break problem on a wet bed in a rectangular tank.

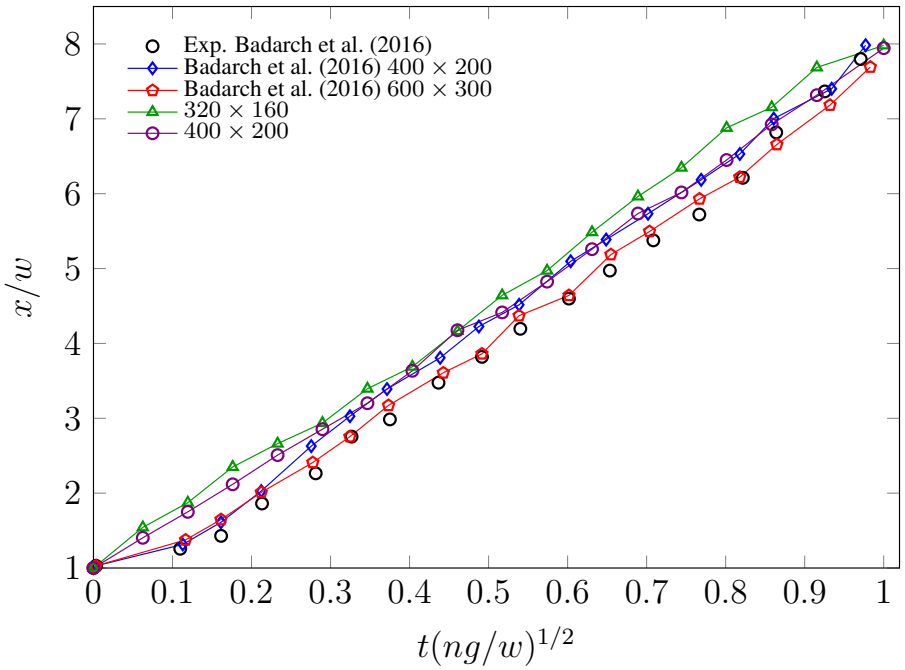

Figure 7.12: The comparison between the numerical and experimental results for leading edge location with different number of grid point.

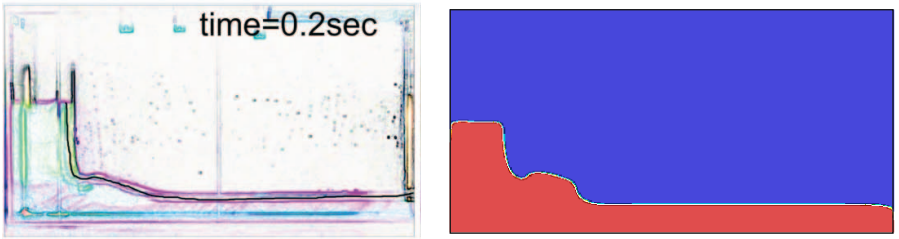

(a-1) t=0.2sec (a-2) t=0.2sec

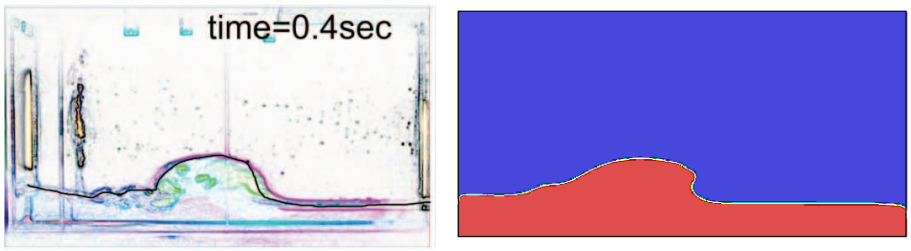

(b-1) t=0.4sec (b-2) t=0.4sec

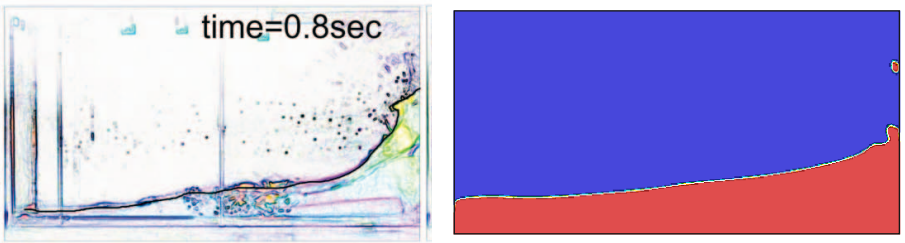

(d-1) t=0.8sec (d-2) t=0.8sec

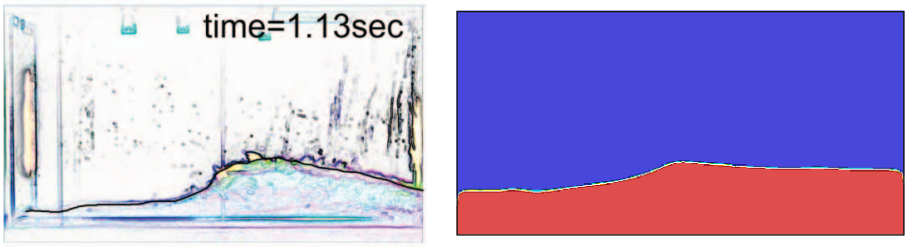

(d-1) t=1.13sec (d-2) t=1.13sec

Figure 7.13: Comparison of the evolution of leading edge between the experimental data of Badarch et al. (2016) and the present breaking wet bed of dam problem.

7.5 Summary

In this chapter, the multiphase LB approach has been improved by using MRT to study different cases of breaking dam problems. The range of the possible density ratios and Reynolds number (Re) are explained beyond what was possible with SRT. The results has been illustrated for teasing the convergence with grid numbers of the square and rectangular domain of the breaking dam. The result of the simulation for both leading edge position and water column height results for grid resolutions is give a good comparison with Martin et al. (1952). In addition, A good agreement is obtained when investigated the second case of the Dam break problems with Colagrossi & Landrini (2003). In addition, the wet bed of the dam break problems have been tested and show a fine results of the simulation by comparing with Badarch et al. (2016). Finally, the MRT mode is implemented with breaking dam problems especially for density ratio up to 1000 and high Re numbers which was impossible with SRT mode.

Chapter 8

Standing Wave Simulations

8.1 Introduction

The first movement of the internal wave was registered by Nansen in the 17th century. For the density variation, waves the interface gravity might appear in coastal waters (Buick & Greated 1998). The authors simulated the interfacial gravity waves numerically for binary fluid lattice Boltzmann Method (LBM) by incorporating a gravitational interaction for viscous fluids with various density ratio in a sharp interface. Grid convergence was investigated by using both acoustic and diffusive scaling for standing wave simulations with density ratios up to 1000. Using MRT was found to improve the stability for high density ratios. This method has been developed to study two scaling cases with standing wave simulations: firstly, with difference density ratios which parameters based on Hodges et al. (1996) and Zhao et al. (2013). Secondly, for small density ratio and both high and low viscosity standing waves that depends on Buick & Greated (1998).

This chapter is organized as follows: Section 8.2 introduces the simulations of the standing wave with Single Relaxation Time (SRT). In section 8.3, different cases of standing wave simulations was implemented using the Multiple Relaxation Time (MRT) for multiphase with LBM. Section 8.4 provides numerical results for the standing wave with high and low viscosity values at small density ratios. Finally, summary

of this chapter is given in Section 8.5.

8.2 Standing Wave with SRT

In the first instance, the standing wave with SRT is simulated at Re effect to investigate the codes of the current study for multiphase method. According to Hodges et al. (1996) and Zhao et al. (2013), two dimensional standing wave is implemented with length $2m$, depth $2m$, wavelength $2m$, the wave number k equals to 3.1 and wave period $1.1339s$. For the non dimensional parameters, the wavelength L equal to 1, depth d is 0.5, wave amplitude a is 0.1 and Froude number Fr is 0.13 at Reynolds number (Re)

$$Re = \frac{L\,U_c}{\nu}\,,$$

where ν is the kinematic viscosity and U_c is the Characteristic velocity defined as

$$U_c = a\,\omega\,,$$

where ω is the frequency of wave.

In the simulations, different $Re = 10, 100$ and 1000 are performed with various Mach numbers $Ma = 0.015, 0.0075, 0.00375, 0.001875, 0.00009375$ and 0.00004875 at various number of grid points. In the implementation for the standing wave of the $l_x \times l_y$ square domain, U_c can be found from Ma number as

$$U_c = Ma\,c_s\,,$$

where $c_s = \frac{c}{\sqrt{3}}$ is speed of sound, $a = 0.1\,\frac{l_x}{2}$ and the frequency ω is obtained as

$$\omega = \frac{U_c}{a}\,.$$

The kinematic viscosity ν and the gravitational acceleration g are taken, respectively as

$$\nu = \frac{a\,\omega\,L_x}{Re}\,,$$

and

$$g = \frac{(a\,\omega)^2}{Fr^2\,L_x}\,.$$

Thus, the period of the wave p is defined as

$$p = \frac{L_x}{\sqrt{\frac{g}{k}\,tanh(k\,d)}} = \sqrt{\frac{2\,\pi\,L_x}{g\;tanh(\frac{2\,\pi}{L_x}\,d)}}\,,$$

where wave number $k = \dfrac{2\,\pi}{L_x}$, and the celerity of the wave C_w is

$$C_w = \frac{L_x}{p}\,,$$

So, the number of the iteration for time in the simulation is computed according to the non dimensional time per period.

8.2.1 Density ratio 2 and different Reynolds number

The implementation of acoustic scaling, consider as fixing the values of Ma numbers and different grid number while the diffusive scaling is defined by taking the double grid numbers when half the value of Ma numbers. The results with density ratio 2 at $Re = 100$ are illustrated in Figure (8.1) and (8.2). It observed that the results show convergence with grid number less than time $= 1$ for a acoustic scaling and less than

time $= 2$ for the diffusive scaling.

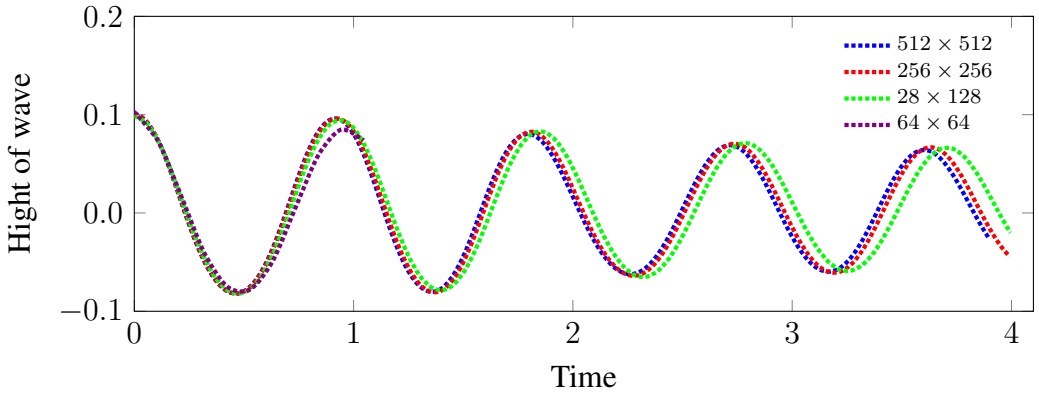

Figure 8.1: The evolution of the height of wave at the centreline for standing wave against time with density ratio$=$ 2, $Re = 100$, number of lattice grids $lx = 64, 128, 256$ and 512 and fixing $Ma = 0.00375$ using acoustic scaling.

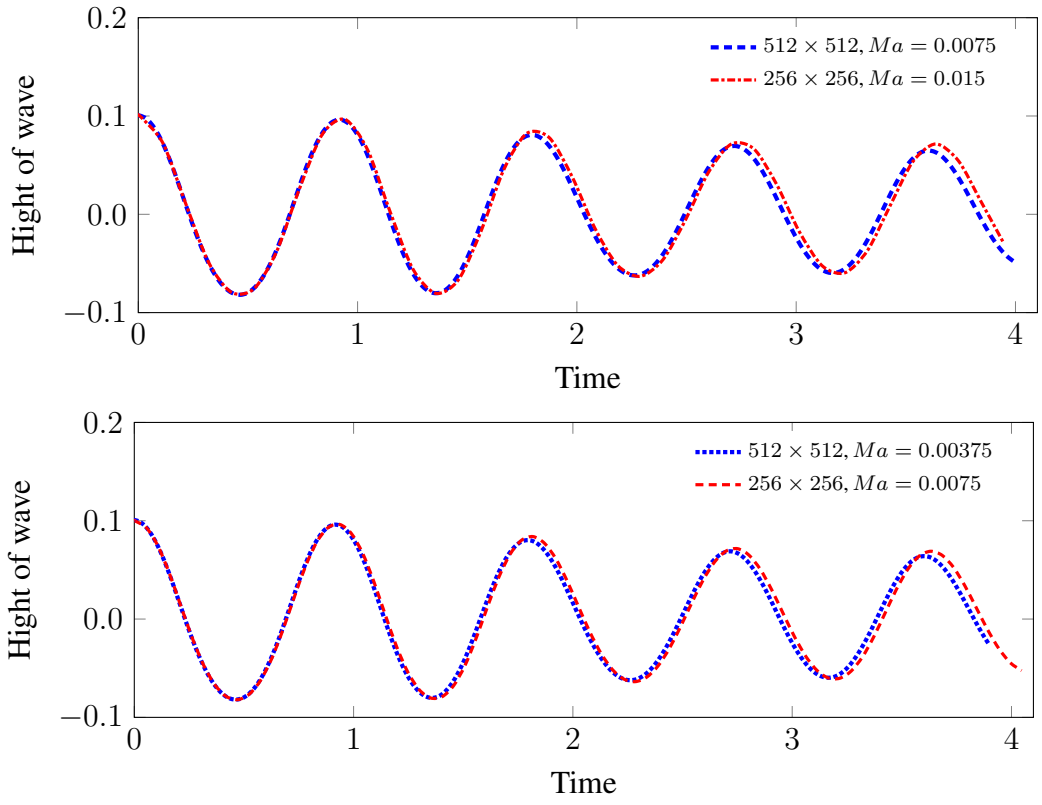

Figure 8.2: The evolution of the height of wave at the centreline for standing wave against time with density ratio$=$ 2, $Re = 100$, number of lattice grids $lx = 256$ and 512 and different Ma numbers using diffusive scaling.

8.2.2 Density ratio 100 and different Reynolds number

The results with density ratio 100 at $Re = 10$ are illustrated in Figure (8.3) and (8.4). The Figure (8.3) illustrated more convergence results with accurate Ma numbers at grid number for acoustic scaling. In the meantime in Figure (8.4), the convergence with lattice grid such as 64×64 improved by halving the Ma numbers according to the diffusive scaling.

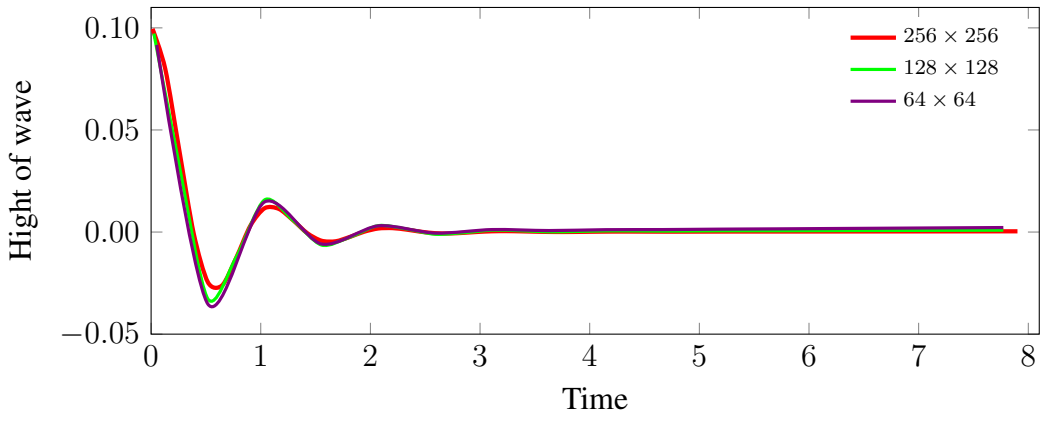

(a) $Ma = 0.0009375$

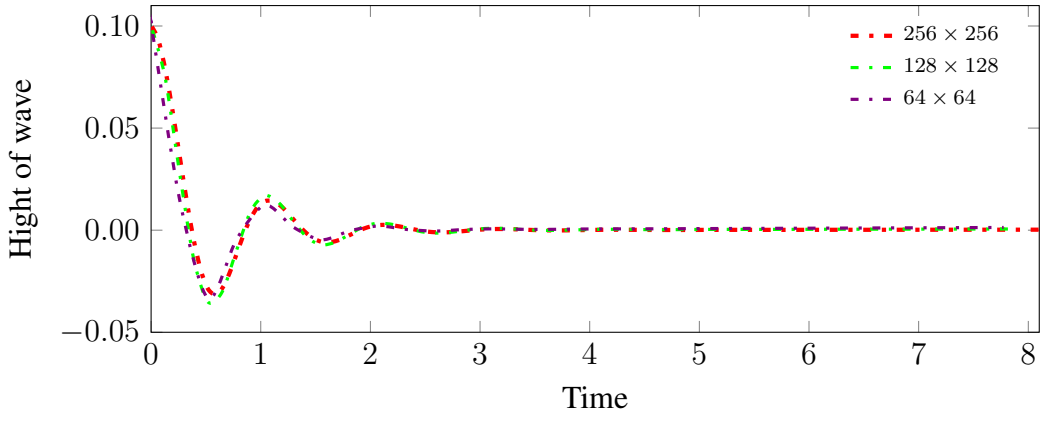

(b) $Ma = 0.00046875$

Figure 8.3: The evolution of the height of wave at the centreline for standing wave against time with density ratio= 100, $Re = 10$, number of lattice grids $lx = 64,\ 128$ and 256 and different Ma numbers using acoustic scaling.

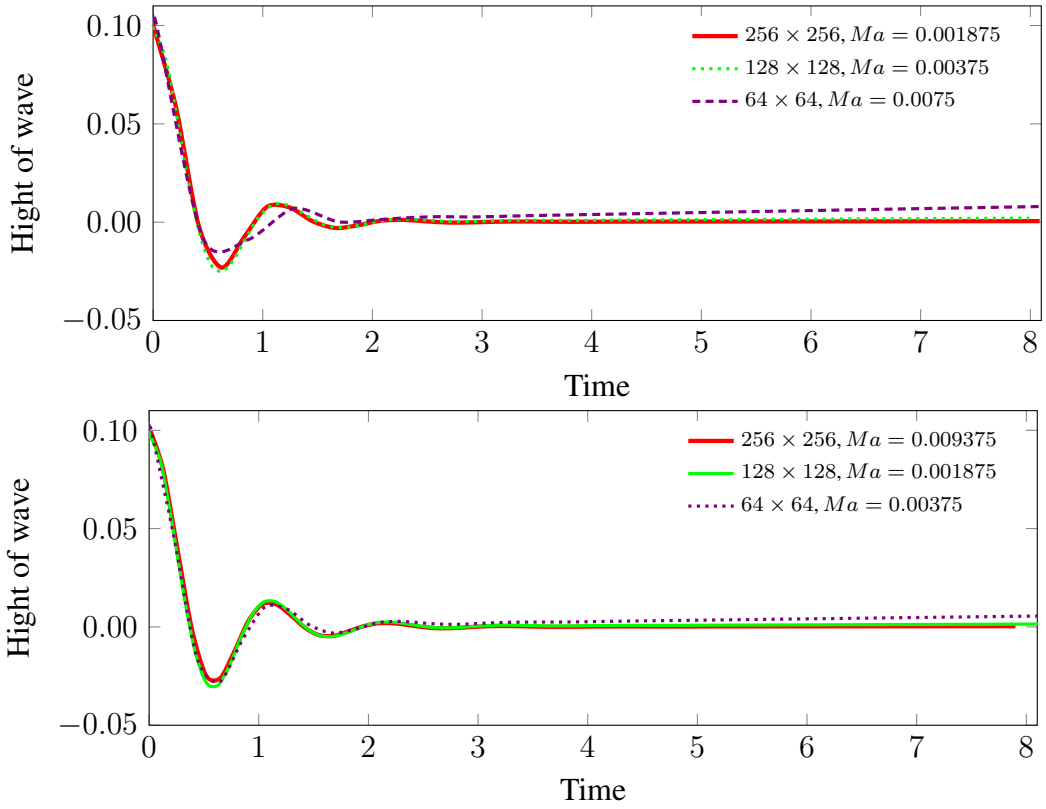

Figure 8.4: The evolution of the height of wave at the centreline for standing wave against time with density ratio= 100, $Re = 10$, different number of lattice grids and various Ma numbers using diffusive scaling.

It observed that the results of density ratio 100 and $Re = 100$ gives a good and accurate convergence with using diffusive scaling than the acoustic scaling specially for small Ma number at grid numbers as shown in Figures (8.5) and (8.6).

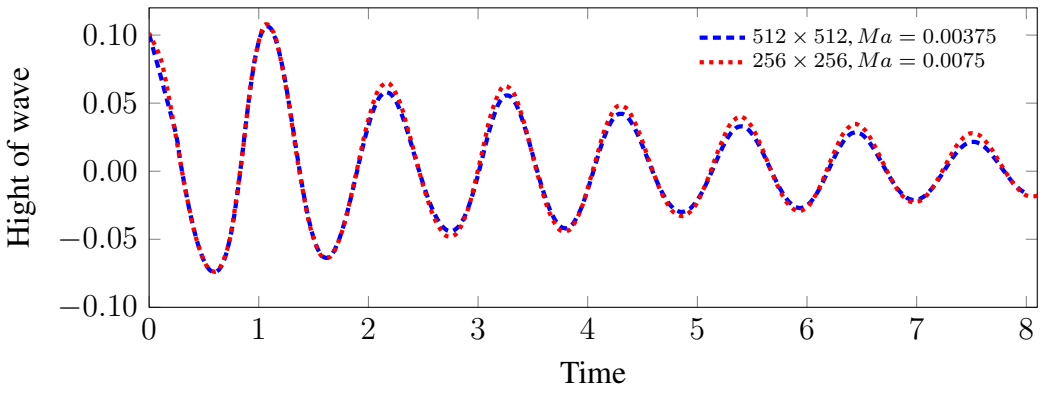

Figure 8.5: The evolution of the height of wave at the centreline for standing wave against time with density ratio= 100, $Re = 100$, number of lattice grids $lx = 256$ and 512 and different Ma numbers using diffusive scaling.

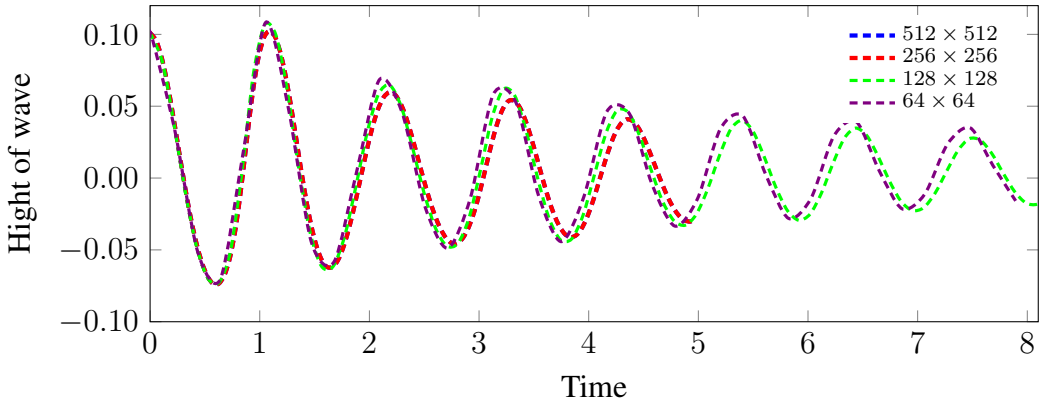

(a) $Ma = 0.0075$

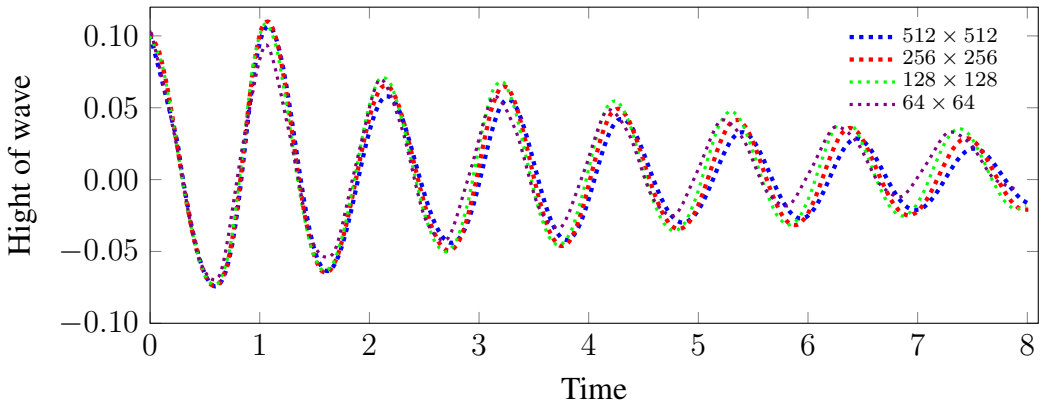

(b) $Ma = 0.00375$

Figure 8.6: The evolution of the height of wave at the centreline for standing wave against time with density ratio= 100, $Re = 100$, number of lattice grids $lx = 64, 128, 256$ and 512 and different Ma numbers using acoustic scaling.

8.2.3 Density ratio 1000 and different Reynolds number

The density ratio up to 1000 with small $Re = 10$ gives a reasonable convergence with grid numbers as shown in Figures (8.7) and (8.8). The results with diffusive scale is more convergent with lattice grid than the acoustic scale. The simulations for SRT with high density ratio at large Re numbers are not stable. So the MRT model is used in the next section.

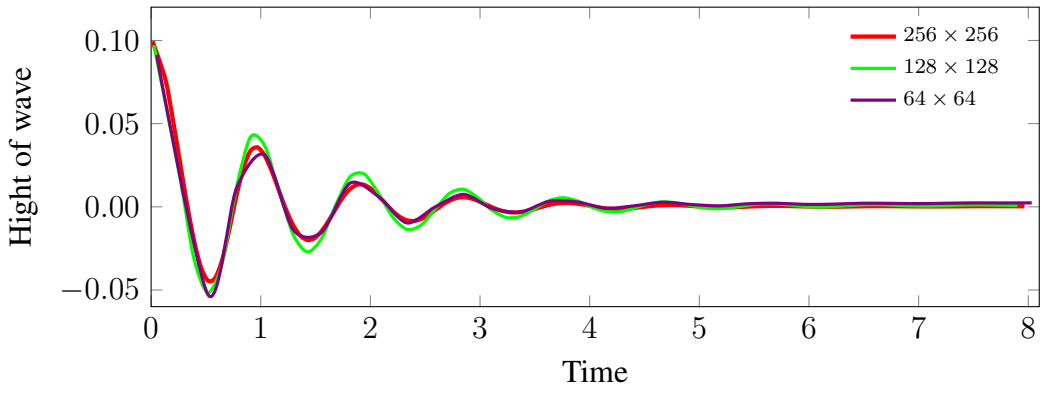

(a) $Ma = 0.0009375$

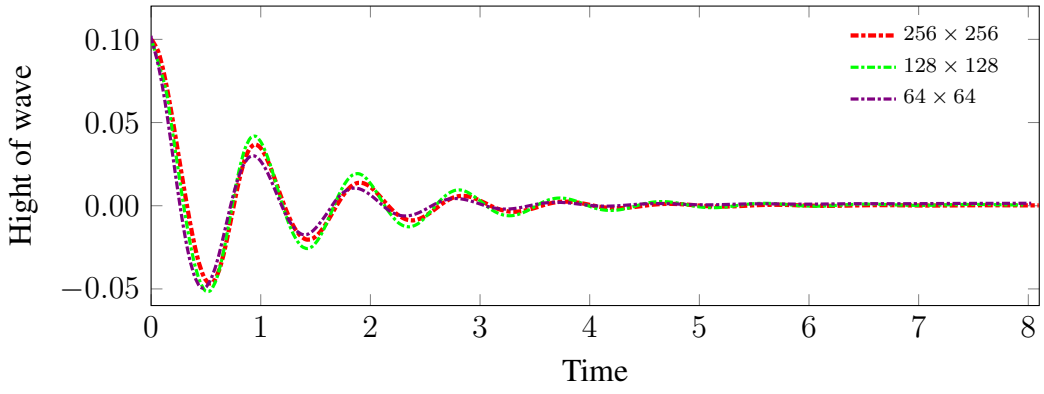

(b) $Ma = 0.00046875$

Figure 8.7: The evolution of the height of wave at the centreline for standing wave against time with density ratio= 1000, $Re = 10$, number of lattice grids $lx = 64,\ 128,$ and 256 and different Ma numbers using acoustic scaling.

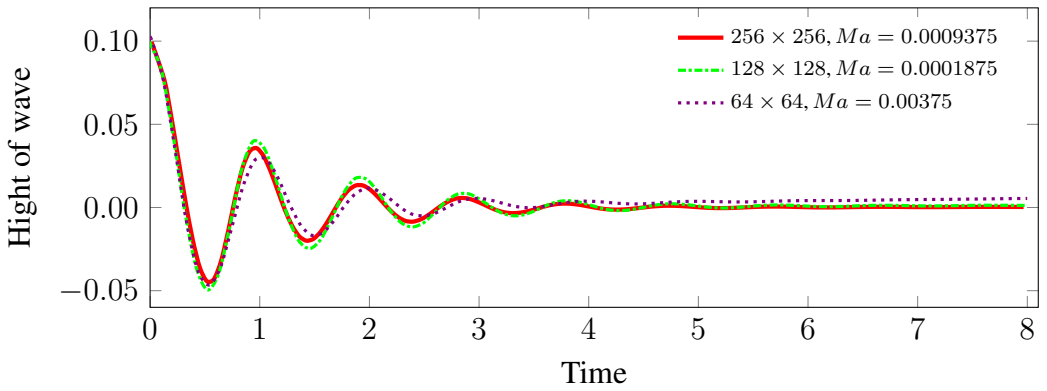

Figure 8.8: The evolution of the height of wave at the centreline for standing wave against time with density ratio= 1000, $Re = 10$, number of lattice grids $lx = 64,\ 128$ and 256 and different Ma numbers using diffusive scaling.

8.3 Standing Wave with MRT

The results with MRT model is applied for high density ratio up to 1000 at $Re = 100$ and 1000. Thus the MRT is improved the results for the standing wave simulations as shown in Figures (8.9), (8.10) and (8.11). It observed that the results become more stable with increasing the accuracy of Ma number with doubling the lattice grids. In addition, the results that is obtained from the diffusive scale is more convergent than the acoustic scale for $Re = 100$ and 1000.

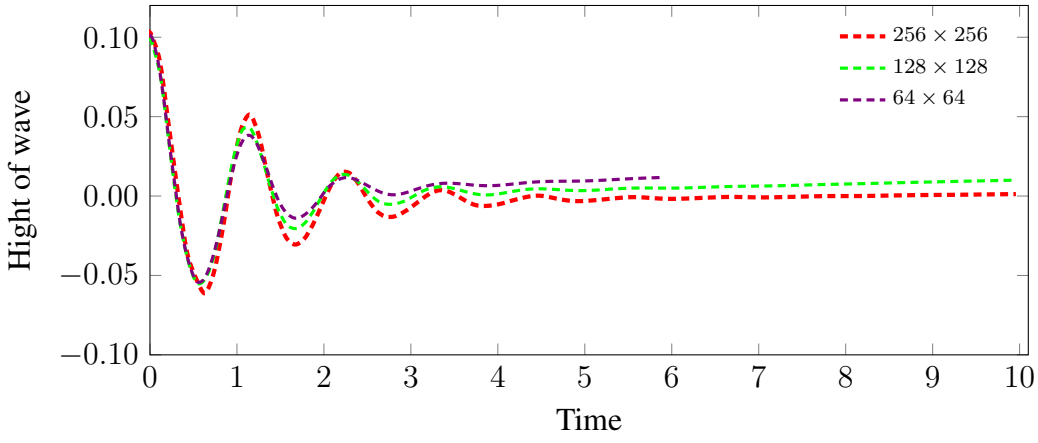

(a) $Ma = 0.0075$

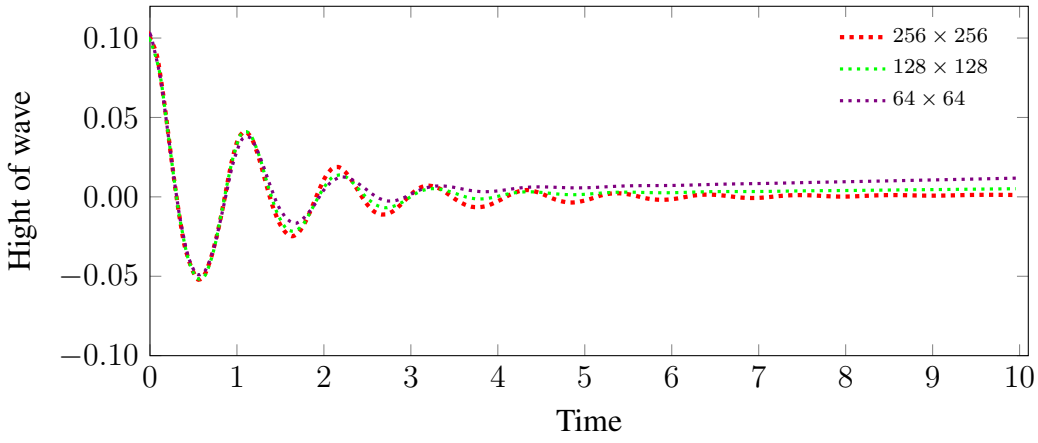

(b) $Ma = 0.00375$

Figure 8.9: The evolution of the height of wave at the centreline for standing wave against time with density ratio= 1000, $Re = 100$, number of lattice grids $lx = 64,\ 128,$ and 256 and different Ma numbers using acoustic scaling in MRT.

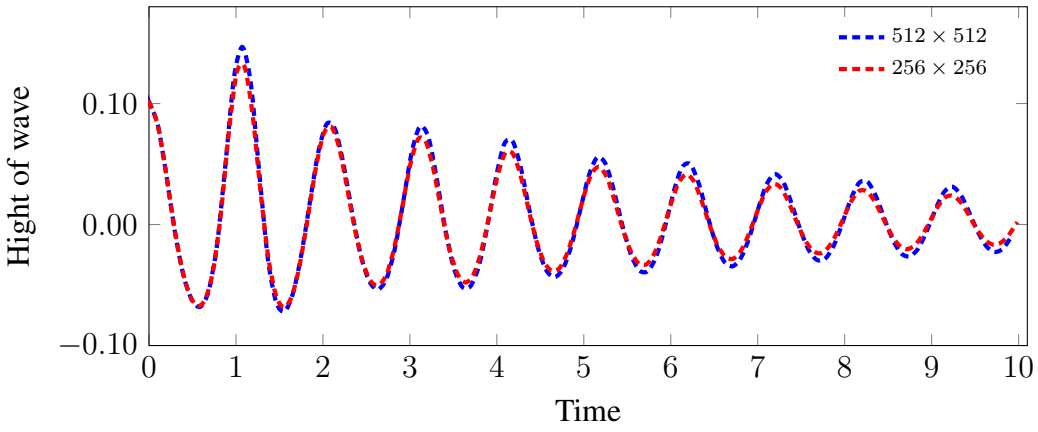

Figure 8.10: The evolution of the height of wave at the centreline for standing wave against time with density ratio= 1000, $Re = 1000$, number of lattice grids $lx = 256$ and 512 and different Ma numbers using acoustic scaling in MRT.

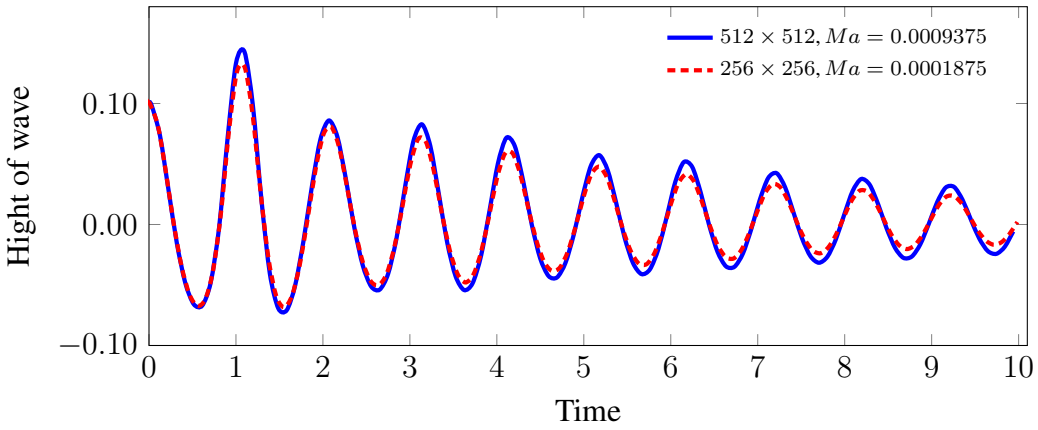

Figure 8.11: The evolution of the height of wave at the centreline for standing wave against time with density ratio= 1000, $Re = 1000$, number of lattice grids $lx = 256$ and 512 and different Ma numbers using diffusive scaling in MRT.

The results that are obtained from MRT model for the multiphase LB are more stable than the SRT collision operator especially for large Re with high density ratio. It observed that from the implementations of standing wave with the MRT model for

density ratio up 1000 and $Re = 100, 1000$ which are not obtainable with SRT model.

8.4 The second case of the standing wave simulations

In the second case, The results are presented for a standing wave with Buick & Greated (1998) for $\frac{\acute{\rho_1}}{\acute{\rho_2}} = 2$ and initial interface at $y(x) = \frac{1}{2} + A\cos(2\pi\, x)$ in a 1×1 domain for both low and high viscosity as shown in Figures (8.12) and (8.13), respectively. Figure (8.12) shows the evolution of wave height at the centreline ($x = 1/2$) against dimensionless time $\acute{t} = t/\sqrt{lx/g}$ using $A = 0.07$ on a 256×256 lattice. The predicted period $p = 3.66$ and decay rate $\alpha = 1.679 \times 10^{-1}$ agree well with results from Buick & Greated (1998). Figure 8.13 illustrates the standing wave for low viscosity ($Re = 10000$), $A = 0.077$ for a 512×512 lattice, with predicted period $p = 2$ and decay rate $\alpha = 2.71 \times 10^{-2}$.

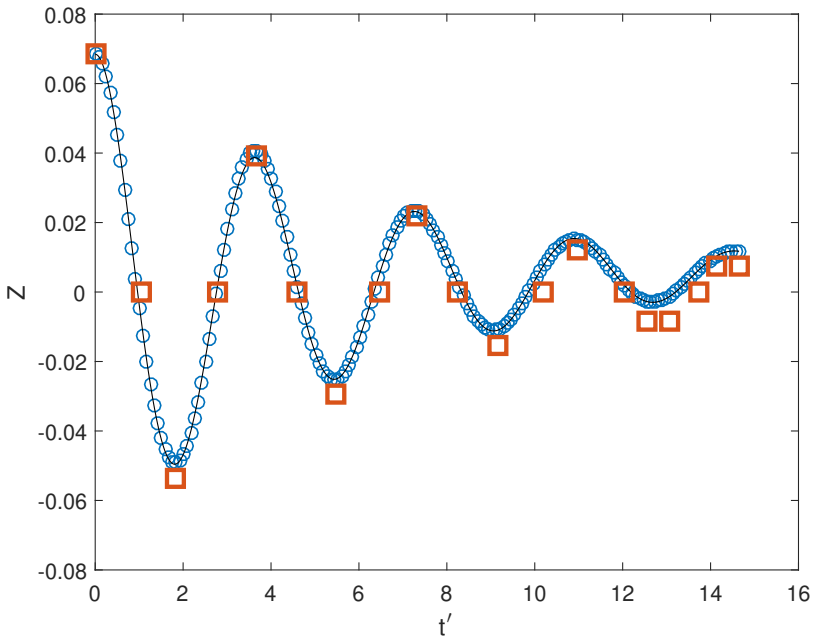

Figure 8.12: The evolution of the height of wave at the centreline for standing wave against $\acute{t}$ with $Re = 400$. The circle marker is the present result, the line is the best fitting curve and the square is for Buick et al. (1998).

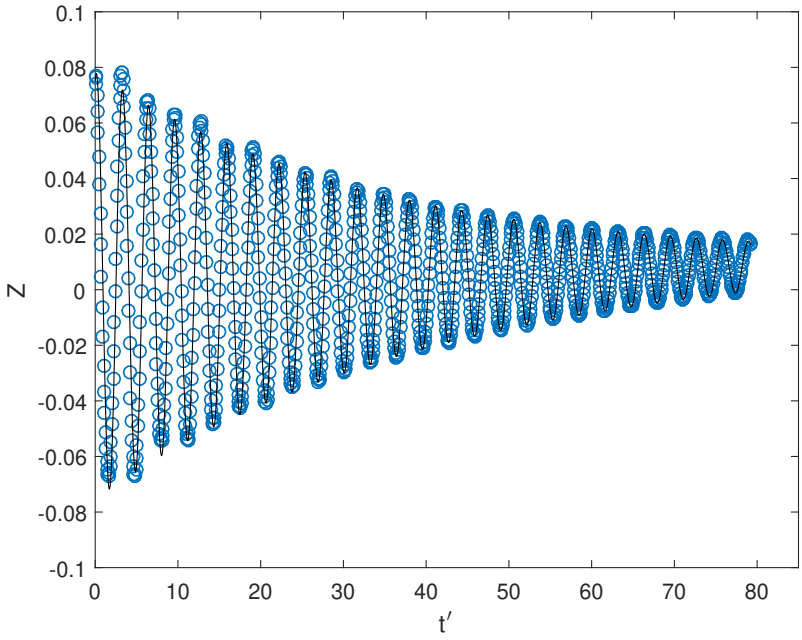

Figure 8.13: The evolution of the height of wave at the centreline for standing wave against $\acute{t}$ with $Re = 10000$. The circle marker is the present result and the line is the best fitting curve.

8.5 Summary

In this work, the implementations of multiphase LB flows is applied for different density and viscosity ratios with various Re numbers to simulate two different scaling for 2D standing waves. The first scale is given with different density and viscosity ratios which based on Hodges et al. (1996) and Zhao et al. (2013). The results with high density ratio up to 1000 at large $Re = 1000$ was obtained using the MRT model in the current study. The results that are given from MRT model are more stable than the SRT mode especially for large Re with high density ratio. In the second scale, the evolution of the height of a standing wave was presented for both high and low viscosity. The high viscosity result agrees well with results of Buick & Greated (1998). As expected the decay rate was reduced for low viscosity $(Re = 10000)$ standing wave.

Chapter 9

Summary and Future work

9.1 Summary

The overall aim of this thesis was to simulate multiphase Lattice Boltzmann flows with high density and viscosity ratios at large Reynolds numbers (Re). In order to overcome the numerical instabilities which occurred with high Re or high density ratio a Multi Relaxation Time (MRT) model was developed by using LBM. A brief review of the free surface with different approaches that have been coupled with LBM is given to simulate wave structure interaction, wave and dam breaking. In meantime, the development of main significant multiphase LB approaches was presented such as Color-Gradient model, SC model, FE based model and HCZ model. It observed that in their stable implementations was focused for various applications with respect to the values of density ratio, viscosity ratio and Re for each model. Eventually, the unified approach of Banari et al. (2014) for high density ratio with Single Relaxation Time (SRT) was chosen. So for that reason the multiphase LB method was developed by using MRT to apply with large Re and high density ratio.

So the basic outline of LBM and the relation with the Navier-Stokes (NS) equations was presented according to Guo & Shu (2013). Also, the boundary conditions was described then the algorithms of the classical LBM with Single Relaxation Time (SRT) and Multi Relaxation Time (MRT) were illustrated.

In the classical LBM, two cases of relaxation Time SRT (on grid and half way) bounce back boundary conditions and MRT with on grid bounce back boundary condition for LBM have been used to simulate 2D cavity flow. In the computations, the stream function and energy were used as measures to study the convergence to steady state and estimate the error for Re from 100 to 10000 at $lx, ly = [33, 65, 129, 257, 513]$ as shown in Figures (3.2 - 3.9). In general, MRT model is more stable than SRT especially with high Re as shown in Tables (3.5 - 3.6). It observed that the behaviours of the simulations have 1st order accuracy for small lattice grids and 2nd order accuracy for large lattice grids of in SRT while MRT with $Re = 3200$ and 5000 has 2nd order accuracy as illustrated in Figures (3.10-3.13). On the other hand, A comparisons between the numerical results of the current study (for the velocity profiles and streamlines) and the numerical results from Ghia et al. (1982) were made. The results of minima of the stream function have excellent match with Ghia et al. (1982) results.

The methodology of multiphase flows with unified LB approach for high density and viscosity ratios was presented. The movement of interface was modelled as follow Banari et al. (2014) by the Cahn-Hilliard (CH) equation then the values of order parameter were used to specify the densities of each phases. The pressureless NS equations and the correction of the pressureless velocity field was found by the Poisson equation. Also, the Chapman-Enskog expansion for solving multiphase LBM was derived.

The implementations of LBM for two dimensional multiphase flows with high density and viscosity ratios was simulated to investigate the codes of multiphase in the current study. Two fluid Poiseuille flow was simulated with various values of density and kinematic viscosity ratios with different Re number. The a good comparisons between the current study and the analytic solution were obtain then the L_2-norm errors for these results in Figures (5.2-5.5) are illustrated the convergence with lattice grids. The verification of static bubble flow with density ratio 100 is made and obtained good comparisons between the theoretical (Laplace law) and current computations with dif-

ferent surface tension coefficient values and various radius (see Figure (5.12)). The gravitational acceleration force for rising bubble was studied and the terminal shape with the velocity vectors for rising bubble between the present results at (128×512) lattice grid and Sun & Tao (2010) results were tested (see Figure (5.13)).

A LBM for multiphase flows with high density and viscosity ratios to simulate 2D single and multiple mode Rayleigh-Taylor instability (RTI) is studied. The single RTI at high density up to 100 and 1000 at $Re = 600,\ 3000,\ 5000$ were investigated. It observed that from the simulations are obtained a good result with $\frac{\acute{\rho}_1}{\acute{\rho}_2} = 100$ and 1000 and high Re. Also, the study of the evolution of interface and the convergence of a multiple mode RTI with different values of surface tension coefficient (σ_{12}) and lattice grid for the positions of bubble and spike are made. A good result is obtained by comparing with those in He et al. (1999) for the average density profiles across the depth in multiple mode RTI with various σ_{12}. In addition, the results followed the expected pattern of increased interface complexity with decreasing σ_{12}.

The multiphase using MRT for LBM was developed and three cases of breaking dam problems were studied. The expanding of range of applying high density ratios with large Reynolds number (Re) beyond what was possible with SRT. The results has been agreed well for testing the convergence with grid numbers of the square and rectangular domain of the breaking dams and for both leading edge position and water column height results. The simulations give a good comparisons with with Martin et al. (1952) by using the MRT. Also, comparisons was show agreements when investigated the second case of the Dam break problems with Colagrossi & Landrini (2003). In addition, the wet bed of the dam break problems was studied and show a fine results by comparing with Badarch et al. (2016). Finally, the MRT mode is implemented with breaking dam problems especially for density ratio up to 1000 and high Re numbers which was impossible with SRT model.

The multiphase LB with MRT model improved for different density and viscosity

ratios with large Re to simulate two different scaling for standing waves. The results shown good convergence with lattice grid for density ratio up to 1000 at $Re = 1000$. In the second case, the development of the height of a standing wave for both high and low viscosity was introduced. The high viscosity result agrees well with results of Buick & Greated (1998). As expected the decay rate was reduced for the low viscosity $(Re = 10000)$ standing wave.

9.2 Future work

The LBM multiphase scheme introduced of this thesis is limited to 2D. The model should be extend to three spatial dimensions. So, in order to investigate this, parallelisation would be required with three dimensional model.

The MRT is a more general form of the LBM with a collision matrix where moments of distribution functions as density, momentum are relaxed with different time scales, because of the MRT model is more stable than SRT then it can be investigated with three dimensional model for multiphase LB approach .

Extension of the model to include fluid-structure interactions problems could enable prediction of ship motion.

The extension of multiphase with LBM can be applied at each phase for ship motion structure with solid phase of the problem with need to create new approach to simulate the flow with three phases. It is likely that MRT model would be required for such stability.

Appendix A

Scaling the parameters

The correct conversion between the physical and Lattice Boltzmann (LB) scale is a most important step to simulate the physical problems when implemented in LBM. It is necessary when comparing results obtained from LB simulations to convert to either physical parameters or non dimensional parameters. The converted variables in LB depend on the scaling factor parameters as are explained below

A.1 Direct Method

The relation between physical and LB parameters can be illustrated directly by the grid size Δx and the time step Δt in table (A.1) and used to convert the physical parameters unit to LB and vice versa (Jain 2010, Inamuro et al. 1997).

Table A.1: Convert physical parameters unit to LB and vice versa.

Parameter	Units	Physical	Lattice Boltzmann	Conversion
Density	Kg/m^3	ρ_{Phy}	ρ_{LB}	$\rho_{Phy} = \rho_{ref}\,\rho_{LB}$
Grid size	m	Δx_{Phy}orΔy_{Phy}	$\Delta x_{LB} = \Delta y_{LB} = 1$	—
length	m	x_{Phy}	x_{LB} or l_x	$x_{Phy} = \Delta x_{Phy}\, x_{LB}$
Time space	s	Δt_{Phy}	$\Delta t_{LB} = 1$	—
lattice speed	m/s	$c_{Phy} = \frac{\Delta x_{Phy}}{\Delta t_{Phy}}$	$c_{LB} = \frac{\Delta x_{LB}}{\Delta t_{LB}} = 1$	—
Velocity	m/s	$u_{Phy} = \frac{\Delta x_{Phy}}{\Delta t_{Phy}}$	$u_{LB} = \frac{\Delta x_{LB}}{\Delta t_{LB}} = 1$	$u_{Phy} = \frac{\Delta x_{Phy}}{\Delta t_{Phy}}\, u_{LB}$
Speed of sound	m/s	$c_{s_{Phy}} = \frac{1}{\sqrt{3}} \frac{\Delta x_{Phy}}{\Delta t_{Phy}}$	$c_{s_{LB}} = \frac{1}{\sqrt{3}} \frac{\Delta x_{LB}}{\Delta t_{LB}} = \frac{1}{\sqrt{3}}$	$c_{s_{Phy}} = \frac{\Delta x_{Phy}}{\Delta t_{Phy}} c_{s_{LB}}$
Acceleration	m/s^2	$a_{Phy} = \frac{\Delta u_{Phy}}{\Delta t_{Phy}}$	$a_{LB} = \frac{\Delta u_{LB}}{\Delta t_{LB}}$	$\Delta u_{Phy} = \frac{\Delta x_{Phy}}{\Delta t_{Phy}}\, \Delta u_{LB}$ so $a_{Phy} = \frac{\Delta x_{Phy}}{\Delta t^2_{Phy}}\, a_{LB}$
Kinematic viscosity	m^2/s	$\nu_{Phy} = c^2_{s_{LB}} \frac{(\tau - 0.5)\Delta x^2_{Phy}}{\Delta t_{Phy}}$	$\nu_{LB} = c^2_{s_{LB}} \frac{(\tau - 0.5)\Delta x^2_{LB}}{\Delta t_{LB}}$	$\nu_{Phy} = \frac{\Delta x^2_{Phy}}{\Delta t_{Phy}}\, \nu_{LB}$

A.2 The Governing equations for the physical system

The equations of fluid mechanics problem represent conservation of mass and momentum. The conservation of mass guaranteed by the equation of the continuity in which the velocity field is divergence free, as defined below

$$\nabla_{phy} \,.\, \mathbf{u}_{phy} = 0\,, \tag{A.2.1}$$

where the subscript "phy" refers to the physical system. The Navier-Stokes equations, are given by

$$\partial_{t_{phy}}\, \mathbf{u}_{phy} + (\mathbf{u}_{phy} \,.\, \nabla_{phy})\, \mathbf{u}_{phy} = -\frac{1}{\rho_{o,phy}}\, \nabla_{phy}\; p_{phy} + \nu_{phy}\, \nabla^2_{phy}\, \mathbf{u}_{phy}\,. \tag{A.2.2}$$

Non dimensions of the parameters is necessary for the LBM.

A.3 The non-dimensional scaling

The dimensionless variables is represented by removing the units of the parameters. The "nd" subscript refer to non-dimensional scale. The characteristic length $l_{0,phy}$ and the characteristic time $t_{0,phy}$ is used to convert the parameters from physical units (phy) that were introduced by governing equations (A.2.1) and (A.2.2) to the non-dimensional units (nd). The characteristic length $l_{0,phy}$ can be define as length of an obstacle, radius of bubble or length of the fluid that needs $t_{0,phy}$ time or period scale for developing of the flow. These quantities used to find the non dimensional length l_{nd} and non-dimensional time t_{nd} scale from the physical length l_{phy} and time t_{phy} are illustrated according to the relations below (Latt 2008)

$$t_{nd} = \frac{t_{phy}}{t_{0,phy}}, \quad \text{and} \quad l_{nd} = \frac{l_{phy}}{l_{0,phy}}. \tag{A.3.1}$$

According to dimensional analysis, the same technique is used to convert the other parameters which can be represented as

$$u_{phy} = \frac{l_{0,phy}}{t_{0,phy}}\, u_{nd},\ \partial_{t_{phy}} = \frac{1}{t_{0,phy}}\, \partial_{t_{nd}},\ \nabla_{phy} = \frac{1}{l_{0,phy}}\, \nabla_{nd},\ P_{phy} = \rho_{0,phy}\, \frac{l_{0,phy}^2}{t_{0,phy}^2}\, P_{nd}\,. \tag{A.3.2}$$

By substitution the above parameters into eqs (A.2.1) and (A.2.2), the dimensionless of the governing equation is obtained as

$$\frac{l_{0,phy}}{t_{0,phy}^2}\partial_{t_{nd}}\ \mathbf{u}_{nd} + \frac{l_{0,phy}}{t_{0,phy}^2}\left(\mathbf{u}_{nd}\ .\ \nabla_{nd}\right)\mathbf{u}_{nd} = -\frac{l_{0,phy}}{t_{0,phy}^2}\nabla_{nd}\ p_{nd} + \frac{\nu_{nd}\, t_{0,phy}}{l_{0,phy}^2}\ \nabla_{nd}^2\ \mathbf{u}_{phy}\,.$$

Multiplying by $\frac{t_{0,phy}^2}{l_{0,phy}}$, yield

$$\partial_{t_{nd}} \mathbf{u}_{nd} + (\mathbf{u}_{nd} \,.\, \nabla_{nd})\, \mathbf{u}_{nd} = -\nabla_{nd}\ p_{nd} + \frac{1}{Re}\, \nabla_{nd}^2\, \mathbf{u}_{phy}\,, \tag{A.3.3}$$

where

$$Re = \frac{l_{0,phy}^2}{\nu_{nd}\, t_{0,phy}}\,. \tag{A.3.4}$$

By setting the reference parameters in the non dimensional scale as

$$l_{0,nd} = \frac{l_{0,phy}}{l_{0,phy}} = 1\,, \tag{A.3.5}$$

and

$$t_{0,nd} = \frac{t_{0,phy}}{t_{0,phy}} = 1\,. \tag{A.3.6}$$

Since the Re is dimensionless unit for that it has same quantity in the physical and non dimensional scale, can be written as

$$Re = \frac{1}{\nu_{nd}}\,, \tag{A.3.7}$$

and from this non dimensional property of Re that leads to viscosity in the non dimensional scale defined as

$$\nu_{nd} = \frac{1}{Re}\,. \tag{A.3.8}$$

A.4 Conversion of the non-dimensional to Lattice Boltzmann units

Assuming dimensionless length and time scales $l_{0,nd} = t_{0,nd} = 1$. The step size (Δx) and the time steps (Δt), can be written as

$$\Delta x = \frac{l_{0,nd}}{l_x} = \frac{1}{l_x}\,, \tag{A.4.1}$$

and

$$\Delta t = \frac{t_{0,nd}}{N_{iteration}} = \frac{1}{N_{iteration}}\,. \tag{A.4.2}$$

Dimensionless analysis is used a base to convert the other parameters from non-dimensional to LB units and the "LB" subscript refers to the Lattice Boltzmann. The length and time factors are (λ_x) and (λ_t), respectively. They are used to define the other parameters, such as velocity factor (λ_u):

$$\frac{u_{nd}}{u_{LB}} = \lambda_u, \quad \text{so }, u_{nd} = \frac{\lambda_x}{\lambda_t}\, u_{LB}\,,$$

which results as

$$u_{nd} = \frac{\Delta x}{\Delta t}\, u_{LB}\,, \tag{A.4.3}$$

and from the viscosity in eq. (A.3.8), can be obtained as

$$\nu_{nd} = \frac{\Delta^2 x}{\Delta t}\, \nu_{LB}\,, \tag{A.4.4}$$

and thus

$$u_{LB} = \frac{\Delta t}{\Delta x}\, u_{nd}\,, \tag{A.4.5}$$

and

$$\nu_{LB} = \frac{\Delta t}{\Delta^2 x}\, \nu_{nd} = \frac{\Delta t}{\Delta^2 x} = \frac{1}{Re}\,. \tag{A.4.6}$$

Since reference length and time is unity $(l_{0,nd} = t_{0,nd} = 1)$, so

$$u_{0,nd} = \frac{l_{0,nd}}{t_{0,nd}} = 1\,. \tag{A.4.7}$$

Therefore from eq. (A.4.5)

$$u_{LB} = \frac{\Delta t}{\Delta x}\,. \tag{A.4.8}$$

In general, non dimensional parameters such as Reynolds number (Re) and Froude number (Fr) can be used to obtain the unknown parameters in Lattice Boltzmann scaling. The relation between the three scales of Reynolds number (Re) and Froude number (Fr) is same, so

$$Re_{phy} = Re_{LB} \quad \text{which means} \quad Re_{LB} = \frac{U_{LB}\, L_{LB}}{\nu_{LB}},$$

and similarly,

$$Fr_{phy} = Fr_{LB}.$$

Thus as

$$Fr_{LB} = \frac{U_{LB}}{\sqrt{g_{LB}\, L_{LB}}},$$

where (g_{LB}) is the lattice gravity. In addition, If the valued of the Re, velocity, length are known in the LB leads to determine lattice kinematic viscosity (ν) from Re. Then from the ν, the relaxation time (τ) can defined

$$\tau = 3\,\nu + 0.5$$

Also, The lattice time space can be obtained according to low Ma number with an other relation by knowing the lattice grid space and the lattice viscosity (ν) as

$$\Delta t_{LB} = \frac{U_{LB}\,\Delta x_{LB}}{U_{phy}}$$

or the lattice time space can be found with respect to lattice gravity (g_{LB}) which is define as an external force (Nils 2007).

$$g_{phy} = \frac{\Delta x_{LB}\, g_{LB}}{(\Delta t_{LB})^2}\,, \quad \text{that give as} \quad \Delta t_{LB} = \sqrt{\frac{g_{LB}\, L_{LB}}{g_{phy}}}.$$

Appendix B

Chapman-Enskog Expansion for Solving Multiphase Flow

B.1 Chapman-Enskog expansion for recovery the pressure-less Navier -Stokes equations

In this section, the LBGK equation

$$g_i(\mathbf{x}+c_i\Delta t, t+\Delta t) - \ g_i(\mathbf{x},t) = -\frac{\Delta t}{\tau_g}(g_i(\mathbf{x},t) - g_i^{(eq)}(\mathbf{x},t)) + \Delta t\ B_i, \tag{B.1.1}$$

with the equilibrium distribution function of D_2Q_9

$$g_i^{(eq)} = \ \omega_i \left[\frac{(c_{i\alpha}.\mathbf{u}^*)}{c_s^2} + \frac{(c_{i\alpha}.\mathbf{u}^*)^2}{2c_s^4} - \frac{u^{*2}}{2c_s^2}\right] + \omega_i \frac{k}{\rho}\ G_{\alpha\beta}c_{i\alpha}c_{i\beta} - v_i\frac{k}{2\rho}\ |\nabla\phi|^2, \tag{B.1.2}$$

where c_s is speed of sound, $c_{i\alpha}$ is the velocity with index $\alpha = (x, y) = (1, 2)$ or also $\beta = (x, y) = (1, 2)$ and

$$w_i = \begin{cases} \frac{4}{9}, & \text{for } i = 0, \\ \frac{1}{9}, & \text{for } i = 1, 2, 3, 4, \\ \frac{1}{36}, & \text{for } i = 5, 6, 7, 8. \end{cases} \tag{B.1.3}$$

$$v_i = \begin{cases} \frac{-5}{3\,c^2}, & \text{for } i = 0, \\ \frac{3\,w_i}{c^2}, & \text{for } i = 1, 2, \cdots, 8. \end{cases} \tag{B.1.4}$$

are weight functions and

$$G_{\alpha\beta} = \frac{9}{2\,c^4}\left(\frac{\partial\phi}{\partial x_\alpha}\frac{\partial\phi}{\partial x_\beta}\right) - \frac{9}{4\,c^4}\left(\frac{\partial\phi}{\partial x_\gamma}\frac{\partial\phi}{\partial x_\gamma}\right)\,\delta_{\alpha\beta}, \tag{B.1.5}$$

leads to the macroscopic (pressure-less) Navier-Stokes equations

$$\begin{aligned}\frac{\partial u^*_\alpha}{\partial t} + u^*_\beta\,\frac{\partial u^*_\alpha}{\partial x_\beta} = \frac{k}{\rho}\,\frac{\partial}{\partial x_\beta}\left\{\left(\frac{\partial\phi}{\partial x_\gamma}\frac{\partial\phi}{\partial x_\gamma}\right)\delta_{\alpha\beta} - \left(\frac{\partial\phi}{\partial x_\alpha}\frac{\partial\phi}{\partial x_\beta}\right)\right\} + \frac{\partial}{\partial x_\beta}\left\{\frac{\mu}{\rho}\left(\frac{\partial u^*_\alpha}{\partial x_\beta} + \frac{\partial u^*_\beta}{\partial x_\alpha}\right)\right\} \\ - \mu\,\left(\frac{\partial u^*_\alpha}{\partial x_\beta} + \frac{\partial u^*_\beta}{\partial x_\alpha}\right)\,\frac{\partial}{\partial x_\beta}\,\frac{1}{\rho} + \frac{B_\alpha}{\rho},\end{aligned} \tag{B.1.6}$$

where

$$\frac{\mu}{\rho} = \nu = c_s^2\left(\acute{\tau}_g - \frac{1}{2}\,\Delta t\right). \tag{B.1.7}$$

The multi-scale expansions are introduced,

$$g_i = g_i^{(0)} + \varepsilon g_i^{(1)} + \varepsilon^2 g_i^{(2)} + O(\varepsilon^3) \tag{B.1.8}$$

$$\partial_t = \partial_{to} + \varepsilon\partial_{t1} + O(\varepsilon^2) \tag{B.1.9}$$

$$\partial_\alpha = \partial_{\alpha o} + O(\varepsilon^1). \tag{B.1.10}$$

where ε is a small number known as Knudsen number, which is, the ratio between the mean free path and the microscopic length scale, and ∂_t and ∂_α are the derivatives with respect to space and time, respectively. ∂_{to} is represented to be the time scale for fast advective scale, while ∂_{t1} is the slow diffusive scale. By starting with the second order Taylor series expanding the lattice BGK (LBGK) equation (B.1.1) without force term, reads

$$\varepsilon(\partial_t + c_{i\alpha}\partial_\alpha)g_i + \frac{\varepsilon^2}{2}(\partial_t + c_{i\alpha}\partial_\alpha)(\partial_t + c_{i\beta}\partial_\beta)g_i + O(\varepsilon^3) = -\frac{1}{\acute{\tau}_g}(g_i - g_i^{(eq)}), \tag{B.1.11}$$

where $\acute{\tau}_g = \tau_g/\Delta t$ the dimensionless relaxation time. Inserting equations (B.1.8), (B.1.9) and (B.1.10) into eq.(B.1.11), yield

$$\varepsilon(\partial_{to} + c_{i\alpha}\partial_{\alpha o})g_i^{(0)} + \varepsilon^2\left\{\partial_{t1}\, g_i^{(0)} + (\partial_{to} + c_{i\alpha}\partial_{\alpha o})g_i^{(1)} + \frac{1}{2}(\partial_{to} + c_{i\alpha}\partial_{\alpha o})(\partial_{to} + c_{i\beta}\partial_{\beta o})g_i^{(0)}\right\}$$
$$+ O(\varepsilon^3) = -\frac{1}{\acute{\tau}_g}\left[g_i^{(0)} + \varepsilon g_i^{(1)} + \varepsilon^2 g_i^{(2)} - g_i^{(eq)}\right] + O(\varepsilon^3). \tag{B.1.12}$$

Equating the coefficients of each order ε, at the zeroth-order of ε is obtained as

$$g_i^{(0)} = g_i^{(eq)}, \tag{B.1.13}$$

and at the first-order of ε

$$(\partial_{to} + c_{i\alpha}\partial_{\alpha o})\, g_i^{(eq)} = \frac{-1}{\acute{\tau}_g} g_i^{(1)}, \tag{B.1.14}$$

and at the second-order of ε

$$\partial_{t1}\, g_i^{(eq)} + (\partial_{to} + c_{i\alpha}\partial_{\alpha o})\, g_i^{(1)} + \frac{1}{2}(\partial_{to} + c_{i\alpha}\partial_{\alpha o})(\partial_{to} + c_{i\beta}\partial_{\beta o})\, g_i^{(eq)} = \frac{-1}{\acute{\tau}_g} g_i^{(2)}, \tag{B.1.15}$$

equation (B.1.15) can be written as follows

$$\partial_{t1}\, g_i^{(eq)} + \left[\frac{2\,\acute{\tau}_g - 1}{2\,\acute{\tau}_g}\right] (\partial_{to} + c_{i\alpha}\partial_{\alpha o})\, g_i^{(1)} = -\frac{1}{\acute{\tau}_g} g_i^{(2)}, \tag{B.1.16}$$

To evaluate zeroth-, first-, second- and third-order moments of equilibrium distribution functions Eq.(B.1.2), the properties of the generalized lattice tensor according to (Guo & Shu 2013) for D_2Q_9 are required as follows

$$\sum_i w_i = 1 \tag{B.1.17a}$$

$$\sum_i w_i c_{i\alpha} = 0 \tag{B.1.17b}$$

$$\sum_i w_i c_{i\alpha} c_{i\beta} = c_s^2 \delta_{\alpha\beta} \tag{B.1.17c}$$

$$\sum_i w_i c_{i\alpha} c_{i\beta} c_{i\gamma} = 0 \tag{B.1.17d}$$

$$\sum_i w_i c_{i\alpha} c_{i\beta} c_{i\gamma} c_{i\delta} = c_s^4 \left(\delta_{\alpha\beta}\, \delta_{\gamma\delta} + \delta_{\alpha\gamma}\, \delta_{\beta\delta} + \delta_{\alpha\delta}\, \delta_{\beta\gamma}\right) \tag{B.1.17e}$$

$$\sum_i w_i c_{i\alpha} c_{i\beta} c_{i\gamma} c_{i\delta} c_{i\theta} = 0\,. \tag{B.1.17f}$$

$G_{\alpha\beta}$ in equation(B.1.5) can be written as

$$G = \frac{9}{2c^4}\begin{bmatrix} G_{11} & G_{12} \\ G_{21} & G_{22} \end{bmatrix},$$

where

$$G_{11} = -G_{22} = \frac{1}{2}\left[(\frac{\partial\phi}{\partial x_1})^2 - (\frac{\partial\phi}{\partial x_2})^2\right] \quad \text{and} \quad G_{12} = G_{21} = \frac{\partial\phi}{\partial x_1}\frac{\partial\phi}{\partial x_2}, \tag{B.1.18}$$

the zeroth-order moment of equilibrium distribution function is evaluated as follows

$$\sum_i g_i^{(eq)} = \frac{1}{c_s^2}\sum_i \omega_i\, c_{i\alpha}.u_\alpha^* + \frac{1}{2\,c_s^4}\sum_i \omega_i\, c_{i\alpha}\, c_{i\beta}\, u_\alpha^*\, u_\beta^* - \frac{1}{2\,c_s^2}\sum_i \omega_i\, u_\gamma^*\, u_\gamma^* + \frac{k}{\rho}\sum_i \omega_i\, G_{\alpha\beta} c_{i\alpha} c_{i\beta} - \frac{k}{2\rho}\sum_i v_i\, |\nabla\phi|^2,$$

from eqs. (B.1.17) yields,

$$\sum_i g_i^{(eq)} = \frac{1}{c_s^2}(0) + \frac{1}{2\,c_s^2}\, u_\beta^*\, u_\beta^* - \frac{1}{2\,c_s^2}\, u_\gamma^*\, u_\gamma^* + \frac{k}{\rho}(0) - \frac{k}{2\rho}(0) = 0\,, \tag{B.1.19}$$

the first-order moments of equilibrium distribution function is competed as follows

$$\sum_i c_{i\alpha}\, g_i^{(eq)} = \frac{1}{c_s^2}\sum_i \omega_i\, c_{i\alpha}\, c_{i\beta}\, u_\beta^* + \frac{1}{2\,c_s^4}\sum_i \omega_i\, c_{i\alpha}\, c_{i\beta}\, c_{i\delta}\, u_\beta^*\, u_\delta^* - \frac{1}{2\,c_s^2}\sum_i \omega_i\, c_{i\alpha}\, u_\beta^*\, u_\beta^* + \frac{k}{\rho}\sum_i \omega_i\, G_{\beta\delta}\, c_{i\alpha} c_{i\beta} c_{i\delta} - \frac{k}{2\rho}\sum_i v_i\, c_{i\alpha} |\nabla\phi|^2,$$

by substituting eqs. (B.1.17) into above equation

$$\sum_i c_{i\alpha} g_i^{(eq)} = \frac{1}{c_s^2}(c_s^2\,\delta_{\alpha\beta}\,u_\beta^*) + \frac{1}{2\,c_s^4}(0) - \frac{1}{2\,c_s^2}\,(0) + \frac{k}{\rho}(0) - \frac{k}{2\rho}(0) = u_\alpha^*\,. \tag{B.1.20}$$

The second-order moments of the equilibrium distribution function ($\pi_{\alpha\beta}^{(0)} = \sum_i c_{i\alpha}\,c_{i\beta}\,g_i^{(eq)}$) is evaluated as below

$$\begin{aligned}\sum_i c_{i\alpha}\,c_{i\beta}\,g_i^{(eq)} &= \frac{1}{c_s^2}\sum_i \omega_i\,c_{i\alpha}\,c_{i\beta}\,c_{i\delta}\,u_\delta^* + \frac{1}{2\,c_s^4}\sum_i \omega_i\,c_{i\alpha}\,c_{i\beta}\,c_{i\delta}\,c_{i\gamma}\,u_\delta^*\,u_\gamma^* \\ &- \frac{1}{2\,c_s^2}\sum_i \omega_i\,c_{i\alpha}\,c_{i\beta}\,u_\gamma^*\,u_\gamma^* + \frac{k}{\rho}\sum_i \omega_i\,G_{\delta\gamma}\,c_{i\alpha}c_{i\beta}c_{i\delta}\,c_{i\gamma} \\ &- \frac{k}{2\rho}\sum_i v_i\,c_{i\alpha}\,c_{i\beta}|\nabla\phi|^2,\end{aligned}$$

from eqs. (B.1.17), yields

$$\begin{aligned}\sum_i c_{i\alpha}\,c_{i\beta}\,g_i^{(eq)} &= \frac{1}{c_s^2}(0) + \frac{c_s^4}{2\,c_s^4}(\delta_{\alpha\beta}\,\delta_{\delta\gamma} + \delta_{\alpha\delta}\,\delta_{\beta\gamma} + \delta_{\alpha\gamma}\,\delta_{\beta\delta})\,u_\delta^*\,u_\gamma^* - \frac{c_s^2}{2\,c_s^2}\,\delta_{\alpha\beta}\,u_\gamma^*\,u_\gamma^* \\ &+ \frac{k}{\rho}c_s^4\,(\delta_{\alpha\beta}\,\delta_{\delta\gamma} + \delta_{\alpha\delta}\,\delta_{\beta\gamma} + \delta_{\alpha\gamma}\,\delta_{\beta\delta})\,G_{\delta\gamma} - \frac{k}{2\rho}|\nabla\phi|^2\,\delta_{\alpha\beta}\,, \\ &= \frac{1}{2}(\delta_{\alpha\beta}\,u_\gamma^*\,u_\gamma^* + \delta_{\alpha\delta}\,u_\delta^*\,u_\beta^* + \delta_{\alpha\gamma}\,u_\beta^*\,u_\gamma^*) - \frac{1}{2}\,\delta_{\alpha\beta}\,u_\gamma^*\,u_\gamma^* \\ &+ \frac{k}{9\,\rho}(2\,G_{\alpha\beta} + G_{\gamma\gamma}\,\delta_{\alpha\beta}) - \frac{k}{2\rho}\frac{\partial\phi}{\partial x_\gamma}\frac{\partial\phi}{\partial x_\gamma}\,\delta_{\alpha\beta}\,, \\ &= u_\alpha^*\,u_\beta^* + \frac{2\,k}{9\,\rho}\left[\frac{9}{2c^4}\left(\frac{\partial\phi}{\partial x_\alpha}\frac{\partial\phi}{\partial x_\beta}\right) - \frac{9}{4c^4}\left(\frac{\partial\phi}{\partial x_\gamma}\frac{\partial\phi}{\partial x_\gamma}\right)\delta_{\alpha\beta}\right] - \frac{k}{2\rho}\frac{\partial\phi}{\partial x_\gamma}\frac{\partial\phi}{\partial x_\gamma}\delta_{\alpha\beta}\,,\end{aligned}$$

thus

$$\sum_i c_{i\alpha}\,c_{i\beta}\,g_i^{(eq)} = \pi_{\alpha\beta}^{(0)} = u_\alpha^*\,u_\beta^* + \frac{k}{\rho}\left(\frac{\partial\phi}{\partial x_\alpha}\frac{\partial\phi}{\partial x_\beta}\right) - \frac{k}{\rho}\left(\frac{\partial\phi}{\partial x_\gamma}\frac{\partial\phi}{\partial x_\gamma}\right)\delta_{\alpha\beta}\,, \tag{B.1.21}$$

the third-order moments of equilibrium distribution function is evaluated as follow

$$\begin{aligned}\sum_i c_{i\alpha}\, c_{i\beta}\, c_{i\gamma}\, g_i^{(eq)} = &\frac{1}{c_s^2}\sum_i \omega_i\, c_{i\alpha}\, c_{i\beta}\, c_{i\gamma}\, c_{i\delta}\, u_\delta^* + \frac{1}{2\,c_s^4}\sum_i \omega_i\, c_{i\alpha}\, c_{i\beta}\, c_{i\gamma}\, c_{i\delta}\, c_{i\theta}\, u_\delta^*\, u_\theta^* \\ &- \frac{1}{2\,c_s^2}\sum_i \omega_i\, c_{i\alpha}\, c_{i\beta}\, c_{i\gamma}\, u_\delta^*\, u_\delta^* + \frac{k}{\rho}\sum_i \omega_i\, G_{\delta\theta}\, c_{i\alpha}\, c_{i\beta}\, c_{i\gamma}\, c_{i\delta}\, c_{i\theta} \\ &- \frac{k}{2\rho}\sum_i v_i\, c_{i\alpha}\, c_{i\beta}\, c_{i\gamma}\, |\nabla\phi|^2,\end{aligned}$$

from eqs. (B.1.17), yields

$$\sum_i c_{i\alpha}\, c_{i\beta}\, c_{i\gamma}\, g_i^{(eq)} = \frac{c_s^4}{c_s^2}\left(\delta_{\alpha\beta}\,\delta_{\delta\gamma} + \delta_{\alpha\delta}\,\delta_{\beta\gamma} + \delta_{\alpha\gamma}\,\delta_{\beta\delta}\right) u_\delta^*\,,$$

then,

$$\sum_i c_{i\alpha}\, c_{i\beta}\, c_{i\gamma}\, g_i^{(eq)} = c_s^2\left(\delta_{\alpha\beta}\, u_\gamma^* + \delta_{\beta\gamma}\, u_\alpha^* + \delta_{\alpha\gamma}\, u_\beta^*\right). \tag{B.1.22}$$

The zero and first moments of distribution function and equilibrium distribution function are defined as follow

$$\sum_i g_i = \sum_i g_i^{(eq)} = 0 \quad \text{and} \quad \sum_i c_{i\alpha}\, g_i = \sum_i c_{i\alpha}\, g_i^{(eq)} = u_\alpha^*. \tag{B.1.23}$$

From equations (B.1.8), (B.1.13) and (B.1.23), yield

$$\sum_i g_i^{(k)} = 0 \quad \text{and} \quad \sum_i c_{i\alpha}\, g_i^{(k)} = 0 \quad \text{for} \quad k > 0\,. \tag{B.1.24}$$

Now, by taking the zeroth-order moment of equation (B.1.14)

$$\partial_{to} \sum_i g_i^{(eq)} + \partial_{\alpha o} \sum_i c_{i\alpha}\, g_i^{(eq)} = -\frac{1}{\acute{\tau}_g} \sum_i g_i^{(1)}\,,$$

from zeroth- and first-order moments of of equilibrium distribution function Eqs. (B.1.19) and (B.1.20) with eq. (B.1.24), yields

$$\partial_{\alpha o}\, u_\alpha^* = 0\,. \tag{B.1.25}$$

By taking the first-order moment of equation (B.1.14), reads

$$\partial_{to} \sum_i c_{i\alpha}\, g_i^{(eq)} + \partial_{\beta o} \sum_i c_{i\alpha}\, c_{i\beta}\, g_i^{(eq)} = -\frac{1}{\acute{\tau}_g} \sum_i c_{i\alpha}\, g_i^{(1)}\,,$$

from first- and second-order moments of equilibrium distribution function Eqs. (B.1.20) and (B.1.21) with eq. (B.1.24), yields

$$\partial_{to}\, u_\alpha^* + \partial_{\beta o} \left[\frac{k}{\rho}\left(\frac{\partial \phi}{\partial x_\alpha}\frac{\partial \phi}{\partial x_\beta}\right) - \frac{k}{\rho}\left(\frac{\partial \phi}{\partial x_\gamma}\frac{\partial \phi}{\partial x_\gamma}\right)\,\delta_{\alpha\beta} + u_\alpha^*\, u_\beta^*\right] = 0\,. \tag{B.1.26}$$

The first-order moment of equation (B.1.16)

$$\partial_{t1} \sum_i c_{i\alpha}\, g_i^{(eq)} + \left[\frac{2\,\acute{\tau}_g - 1}{2\,\acute{\tau}_g}\right]\left\{\partial_{to} \sum_i c_{i\alpha}\, g_i^{(1)} + \partial_{\beta o} \sum_i c_{i\alpha}\, c_{i\beta}\, g_i^{(1)}\right\} = \frac{-1}{\acute{\tau}_g} \sum_i c_{i\alpha}\, g_i^{(2)}\,,$$

from eqs. (B.1.20) with eq. (B.1.24), yields

$$\partial_{t1}\, u_\alpha^* + \left[\frac{2\,\acute{\tau}_g - 1}{2\,\acute{\tau}_g}\right]\,\partial_{\beta o} \sum_i c_{i\alpha}\, c_{i\beta}\, g_i^{(1)} = 0\,. \tag{B.1.27}$$

From eq. (B.1.14), ($\pi^{(1)}_{\alpha\beta} = \sum_i \, c_{i\alpha} \, c_{i\beta} \, g^{(1)}_i$) can be evaluated as follow

$$\pi^{(1)}_{\alpha\beta} = \sum_i c_{i\alpha} c_{i\beta} g^{(1)}_i = -\acute{\tau}_g \left\{ \partial_{to} \sum_i c_{i\alpha} \, c_{i\beta} \, g^{(eq)}_i + \partial_{\gamma o} \sum_i \, c_{i\alpha} \, c_{i\beta} \, c_{i\gamma} \, g^{(eq)}_i \right\} , \quad \text{(B.1.28)}$$

By using the definitions of eqs. (B.1.21) with eq. (B.1.22), reads

$$\begin{aligned} \pi^{(1)}_{\alpha\beta} \; = & - \acute{\tau}_g \left\{ \partial_{to} \left[\frac{k}{\rho} \left(\frac{\partial \phi}{\partial x_\alpha} \frac{\partial \phi}{\partial x_\beta} \right) - \frac{k}{\rho} \left(\frac{\partial \phi}{\partial x_\gamma} \frac{\partial \phi}{\partial x_\gamma} \right) \, \delta_{\alpha\beta} + u^*_\alpha \, u^*_\beta \right] \right\} \\ & - \acute{\tau}_g \, \partial_{\gamma o} \, c_s^2 \left(\delta_{\alpha\beta} \, u^*_\gamma + \delta_{\beta\gamma} \, u^*_\alpha + \delta_{\alpha\gamma} \, u^*_\beta \right) , \end{aligned}$$

by substituting eq. (B.1.25), yields

$$\begin{aligned} \pi^{(1)}_{\alpha\beta} \; = & - \acute{\tau}_g \partial_{to} \left[\frac{k}{\rho} \left(\frac{\partial \phi}{\partial x_\alpha} \frac{\partial \phi}{\partial x_\beta} \right) - \frac{k}{\rho} \left(\frac{\partial \phi}{\partial x_\gamma} \frac{\partial \phi}{\partial x_\gamma} \right) \, \delta_{\alpha\beta} \right] - \acute{\tau}_g \left(u^*_\beta \partial_{to} \, u^*_\alpha + u^*_\alpha \partial_{to} \, u^*_\beta \right) \\ & - \acute{\tau}_g \, c_s^2 \left(\partial_{\beta o} \, u^*_\alpha + \partial_{\alpha o} \, u^*_\beta \right) . \end{aligned} \quad \text{(B.1.29)}$$

To evaluate $\partial_{to} \, u^*_\alpha$ and $\partial_{to} \, u^*_\beta$, by taking zeroth-order moments of eq. (B.1.14) as follow

$$\partial_{\gamma o} \, u^*_\gamma = 0 . \quad \text{(B.1.30)}$$

and first-order moments of eq. (B.1.14) as follow

$$\partial_{to} \, u^*_\alpha + \partial_{\gamma o} \, \pi^{(0)}_{\alpha\gamma} \; = 0 , \quad \text{(B.1.31)}$$

also

$$\partial_{to}\, u^*_\beta + \partial_{\gamma o}\, \pi^{(0)}_{\beta\gamma} \;= 0\,, \tag{B.1.32}$$

then,

$$\begin{aligned}
\partial_{to}\, u^*_\alpha &= -\partial_{\gamma o}\, \pi^{(0)}_{\alpha\gamma} \\
&= -\partial_{\gamma o}\left[\frac{k}{\rho}\left(\frac{\partial\phi}{\partial x_\alpha}\frac{\partial\phi}{\partial x_\gamma}\right) - \frac{k}{\rho}\left(\frac{\partial\phi}{\partial x_\beta}\frac{\partial\phi}{\partial x_\beta}\right)\delta_{\alpha\gamma} + u^*_\alpha\, u^*_\gamma\right] \\
&= -\partial_{\gamma o}\,\frac{k}{\rho}\left(\frac{\partial\phi}{\partial x_\alpha}\frac{\partial\phi}{\partial x_\gamma}\right) + \partial_{\alpha o}\,\frac{k}{\rho}\left(\frac{\partial\phi}{\partial x_\beta}\frac{\partial\phi}{\partial x_\beta}\right) - \partial_{\gamma o}\,\left(u^*_\alpha\, u^*_\gamma\right)\,,
\end{aligned} \tag{B.1.33}$$

also

$$\begin{aligned}
\partial_{to}\, u^*_\beta &= -\partial_{\gamma o}\, \pi^{(0)}_{\beta\gamma} \\
&= -\partial_{\gamma o}\,\left[\frac{k}{\rho}\left(\frac{\partial\phi}{\partial x_\beta}\frac{\partial\phi}{\partial x_\gamma}\right) - \left(\frac{k}{\rho}\frac{\partial\phi}{\partial x_\alpha}\frac{\partial\phi}{\partial x_\alpha}\right)\,\delta_{\beta\gamma} + u^*_\beta\, u^*_\gamma\right] \\
&= -\partial_{\gamma o}\,\frac{k}{\rho}\left(\frac{\partial\phi}{\partial x_\beta}\frac{\partial\phi}{\partial x_\gamma}\right) + \partial_{\beta o}\,\frac{k}{\rho}\left(\frac{\partial\phi}{\partial x_\alpha}\frac{\partial\phi}{\partial x_\alpha}\right) - \partial_{\gamma o}\,\left(u^*_\beta\, u^*_\gamma\right)\,,
\end{aligned} \tag{B.1.34}$$

by substituting eqs. (B.1.33) and (B.1.34) into eq. (B.1.29), yields

$$\begin{aligned}
\pi^{(1)}_{\alpha\beta} = &-\acute{\tau}_g \partial_{to}\left[\frac{k}{\rho}\left(\frac{\partial\phi}{\partial x_\alpha}\frac{\partial\phi}{\partial x_\beta}\right) - \frac{k}{\rho}\left(\frac{\partial\phi}{\partial x_\gamma}\frac{\partial\phi}{\partial x_\gamma}\right)\delta_{\alpha\beta}\right] - \acute{\tau}_g\, c_s^2\,(\partial_{\beta o}\, u^*_\alpha + \partial_{\alpha o}\, u^*_\beta) \\
&- \acute{\tau}_g\left\{-u^*_\beta\,\partial_{\gamma o}\,\frac{k}{\rho}\left(\frac{\partial\phi}{\partial x_\alpha}\frac{\partial\phi}{\partial x_\gamma}\right) + u^*_\beta\,\partial_{\alpha o}\,\frac{k}{\rho}\,\left(\frac{\partial\phi}{\partial x_\beta}\frac{\partial\phi}{\partial x_\beta}\right) - u^*_\beta\,\partial_{\gamma o}\big(u^*_\alpha\, u^*_\gamma\big)\right\} \\
&- \acute{\tau}_g\left\{-u^*_\alpha\,\partial_{\gamma o}\,\frac{k}{\rho}\left(\frac{\partial\phi}{\partial x_\beta}\frac{\partial\phi}{\partial x_\gamma}\right) + u^*_\alpha\partial_{\beta o}\frac{k}{\rho}\,\left(\frac{\partial\phi}{\partial x_\alpha}\frac{\partial\phi}{\partial x_\alpha}\right) - u^*_\alpha\,\partial_{\gamma o}\big(u^*_\beta\, u^*_\gamma\big)\right\}\,.
\end{aligned} \tag{B.1.35}$$

Now substitute eq. (B.1.35) into eq. (B.1.27), reads

$$\partial_{t1}u^*_\alpha - \left(\acute{\tau}_g - \frac{1}{2}\right)\partial_{\beta o}\left\{\partial_{to}\left[\frac{k}{\rho}\left(\frac{\partial\phi}{\partial x_\alpha}\frac{\partial\phi}{\partial x_\beta}\right) - \frac{k}{\rho}\left(\frac{\partial\phi}{\partial x_\gamma}\frac{\partial\phi}{\partial x_\gamma}\right)\delta_{\alpha\beta}\right] + c_s^2(\partial_{\beta o}u^*_\alpha + \partial_{\alpha o}, u^*_\beta)\right\}$$
$$- \left(\acute{\tau}_g - \frac{1}{2}\right)\partial_{\beta o}\left\{-u^*_\beta\partial_{\gamma o}\frac{k}{\rho}\left(\frac{\partial\phi}{\partial x_\alpha}\frac{\partial\phi}{\partial x_\gamma}\right) + u^*_\beta\partial_{\alpha o}\frac{k}{\rho}\left(\frac{\partial\phi}{\partial x_\gamma}\frac{\partial\phi}{\partial x_\gamma}\right) - \partial_{\gamma o}\left(u^*_\alpha u^*_\beta u^*_\gamma\right)\right\}$$
$$- \left(\acute{\tau}_g - \frac{1}{2}\right)\partial_{\beta o}\left\{-u^*_\alpha\partial_{\gamma o}\frac{k}{\rho}\left(\frac{\partial\phi}{\partial x_\beta}\frac{\partial\phi}{\partial x_\gamma}\right) + u^*_\alpha\partial_{\beta o}\frac{k}{\rho}\left(\frac{\partial\phi}{\partial x_\gamma}\frac{\partial\phi}{\partial x_\gamma}\right)\right\} = 0\,.$$

which can be multiplied to $\varepsilon = \Delta t$, the term that contain $(u^*_\alpha u^*_\beta u^*_\gamma)$ is $O(Ma^3)$ Mach number can be neglected (Guo & Shu 2013) and simplified to,

$$\varepsilon\partial_{t1}u^*_\alpha - \partial_{\beta o}\partial_{to}\left\{\left(\acute{\tau}_g - \frac{1}{2}\right)\frac{k\Delta t}{\rho}\left(\frac{\partial\phi}{\partial x_\alpha}\frac{\partial\phi}{\partial x_\beta}\right)\right\} + \partial_{\alpha o}\partial_{to}\left\{\left(\acute{\tau}_g - \frac{1}{2}\right)\frac{k\Delta t}{\rho}\left(\frac{\partial\phi}{\partial x_\gamma}\frac{\partial\phi}{\partial x_\gamma}\right)\right\}$$
$$- \partial_{\beta o}\left\{c_s^2\Delta t\left(\acute{\tau}_g - \frac{1}{2}\right)(\partial_{\beta o}u^*_\alpha + \partial_{\alpha o}u^*_\beta)\right\} + u^*_\beta\partial_{\beta o}\partial_{\gamma o}\left\{\left(\acute{\tau}_g - \frac{1}{2}\right)\frac{k\Delta t}{\rho}\left(\frac{\partial\phi}{\partial x_\alpha}\frac{\partial\phi}{\partial x_\gamma}\right)\right\}$$
$$- u^*_\beta\partial_{\beta o}\partial_{\alpha o}\left\{\left(\acute{\tau}_g - \frac{1}{2}\right)\frac{k\Delta t}{\rho}\left(\frac{\partial\phi}{\partial x_\gamma}\frac{\partial\phi}{\partial x_\gamma}\right)\right\} + u^*_\alpha\partial_{\beta o}\partial_{\gamma o}\left\{\left(\acute{\tau}_g - \frac{1}{2}\right)\frac{k\Delta t}{\rho}\left(\frac{\partial\phi}{\partial x_\beta}\frac{\partial\phi}{\partial x_\gamma}\right)\right\}$$
$$- u^*_\alpha(\partial_{\beta o})^2\left\{\left(\acute{\tau}_g - \frac{1}{2}\right)\frac{k\Delta t}{\rho}\left(\frac{\partial\phi}{\partial x_\gamma}\frac{\partial\phi}{\partial x_\gamma}\right)\right\} = 0\,. \qquad \text{(B.1.36)}$$

In order to recover pressure-less Navier-Stokes momentum equation (B.1.6), by adding eq. (B.1.36) to eq. (B.1.26), yielding

$$\begin{aligned}
\partial_t u^*_\alpha = &-\partial_{\beta o}\left[\frac{k}{\rho}\left(\frac{\partial\phi}{\partial x_\alpha}\frac{\partial\phi}{\partial x_\beta}\right)-\frac{k}{\rho}\left(\frac{\partial\phi}{\partial x_\gamma}\frac{\partial\phi}{\partial x_\gamma}\right)\delta_{\alpha\beta}+u^*_\alpha u^*_\beta\right]\\
&+\partial_{\beta o}\partial_{to}\left\{\left(\acute{\tau}_g-\frac{1}{2}\right)\frac{k\Delta t}{\rho}\left(\frac{\partial\phi}{\partial x_\alpha}\frac{\partial\phi}{\partial x_\beta}\right)\right\}-\partial_{\alpha o}\partial_{to}\left\{\left(\acute{\tau}_g-\frac{1}{2}\right)\frac{k\Delta t}{\rho}\left(\frac{\partial\phi}{\partial x_\gamma}\frac{\partial\phi}{\partial x_\gamma}\right)\right\}\\
&+\partial_{\beta o}\left\{c_s^2\Delta t\left(\acute{\tau}_g-\frac{1}{2}\right)(\partial_{\beta o}u^*_\alpha+\partial_{\alpha o}u^*_\beta)\right\}-u^*_\beta\partial_{\beta o}\partial_{\gamma o}\left\{\left(\acute{\tau}_g-\frac{1}{2}\right)\frac{k\Delta t}{\rho}\left(\frac{\partial\phi}{\partial x_\alpha}\frac{\partial\phi}{\partial x_\gamma}\right)\right\}\\
&+u^*_\beta\partial_{\beta o}\partial_{\alpha o}\left\{\left(\acute{\tau}_g-\frac{1}{2}\right)\frac{k\Delta t}{\rho}\left(\frac{\partial\phi}{\partial x_\gamma}\frac{\partial\phi}{\partial x_\gamma}\right)\right\}-u^*_\alpha\partial_{\beta o}\partial_{\gamma o}\left\{\left(\acute{\tau}_g-\frac{1}{2}\right)\frac{k\Delta t}{\rho}\left(\frac{\partial\phi}{\partial x_\beta}\frac{\partial\phi}{\partial x_\gamma}\right)\right\}\\
&+u^*_\alpha(\partial_{\beta o})^2\left\{\left(\acute{\tau}_g-\frac{1}{2}\right)\frac{k\Delta t}{\rho}\left(\frac{\partial\phi}{\partial x_\gamma}\frac{\partial\phi}{\partial x_\gamma}\right)\right\}=0\,. \qquad \text{(B.1.37)}
\end{aligned}$$

In the RHS of eq.(B.1.37), the terms $\partial_{\beta o}\partial_{to}\Big\{\big(\acute{\tau}_g-\frac{1}{2}\big)\frac{k\Delta t}{\rho}\big(\frac{\partial\phi}{\partial x_\alpha}\frac{\partial\phi}{\partial x_\beta}\big)\Big\}$, $\partial_{\alpha o}\partial_{to}\Big\{\big(\acute{\tau}_g-\frac{1}{2}\big)\frac{k\Delta t}{\rho}\big(\frac{\partial\phi}{\partial x_\gamma}\frac{\partial\phi}{\partial x_\gamma}\big)\Big\}$, $u^*_\beta\partial_{\beta o}\partial_{\gamma o}\Big\{\big(\acute{\tau}_g-\frac{1}{2}\big)\frac{k\Delta t}{\rho}\big(\frac{\partial\phi}{\partial x_\alpha}\frac{\partial\phi}{\partial x_\gamma}\big)\Big\}$, $u^*_\beta\partial_{\beta o}\partial_{\alpha o}\Big\{\big(\acute{\tau}_g-\frac{1}{2}\big)\frac{k\Delta t}{\rho}\big(\frac{\partial\phi}{\partial x_\gamma}\frac{\partial\phi}{\partial x_\gamma}\big)\Big\}$, $u^*_\alpha\partial_{\beta o}\partial_{\gamma o}\Big\{\big(\acute{\tau}_g-\frac{1}{2}\big)\frac{k\Delta t}{\rho}\big(\frac{\partial\phi}{\partial x_\beta}\frac{\partial\phi}{\partial x_\gamma}\big)\Big\}$ and $u^*_\alpha(\partial_{\beta o})^2\Big\{\big(\acute{\tau}_g-\frac{1}{2}\big)\frac{k\Delta t}{\rho}\big(\frac{\partial\phi}{\partial x_\gamma}\frac{\partial\phi}{\partial x_\gamma}\big)\Big\}$ have small parameter k multiplying to Δt and thus can be eliminated. After using these simplification into eq. (B.1.37), yields

$$\begin{aligned}
\partial_t u^*_\alpha+\partial_{\beta o}\left(u^*_\alpha u^*_\beta\right)=&\frac{k}{\rho}\,\partial_{\beta o}\left\{\left(\frac{\partial\phi}{\partial x_\gamma}\frac{\partial\phi}{\partial x_\gamma}\right)\delta_{\alpha\beta}-\left(\frac{\partial\phi}{\partial x_\alpha}\frac{\partial\phi}{\partial x_\beta}\right)\right\}\\
&+\partial_{\beta o}\left\{c_s^2\Delta t\left(\acute{\tau}_g-\frac{1}{2}\right)(\partial_{\beta o}u^*_\alpha+\partial_{\alpha o}u^*_\beta)\right\}=0\,. \qquad \text{(B.1.38)}
\end{aligned}$$

By using the continuity equation (B.1.25), reads

$$\partial_t u^*_\alpha + u^*_\beta\,\partial_{\beta o}\,(u^*_\alpha) = \frac{k}{\rho}\,\partial_{\beta o}\left\{\left(\frac{\partial\phi}{\partial x_\gamma}\frac{\partial\phi}{\partial x_\gamma}\right)\,\delta_{\alpha\beta} - \left(\frac{\partial\phi}{\partial x_\alpha}\frac{\partial\phi}{\partial x_\beta}\right)\right\} + \partial_{\beta o}\left\{c_s^2\Delta t\left(\acute{\tau}_g - \frac{1}{2}\right)(\partial_{\beta o}u^*_\alpha + \partial_{\alpha o}u^*_\beta)\right\} = 0\,. \tag{B.1.39}$$

After adding the force term the eq. (B.1.39) correspond to the (pressure-less) momentum Navier-Stokes equation (B.1.6).

B.2 Chapman-Enskog expansion for satisfying the Cahn-Hilliard equation

In this section, the same technique is used to derive that the LBGK equation

$$f_i(\mathbf{x} + c_i\Delta t, t + \Delta t) - \ f_i(\mathbf{x}, t) = -\frac{\Delta t}{\tau_f}\Big(f_i(\mathbf{x}, t) - f_i^{(eq)}(\mathbf{x}, t)\Big)\,, \tag{B.2.1}$$

with the equilibrium distribution function of $D_2\,Q_9$

$$f_i^{(eq)} = H_i\,\phi + v_i\,\frac{M}{\tau_f - \frac{1}{2}\Delta t}\,M_\phi + \phi\,\omega_i\left[\frac{(c_{i\alpha}.\mathbf{u})}{c_s^2} + \frac{(c_{i\alpha}.\mathbf{u})^2}{2c_s^4} - \frac{u^2}{2c_s^2}\right]\,, \tag{B.2.2}$$

where

$$H_i = \begin{cases} 1, & \text{for } \ i = 0, \\ 0, & \text{for } \ i = 1, 2, 3, \cdots, 8 \end{cases} \tag{B.2.3}$$

is weight functions. The diffusive interface motion modelled by Cahn-Hilliard (CH) equation may be recovered.

$$\frac{\partial \phi}{\partial_t} + \nabla .(\phi \, \mathbf{u}) = M \, \nabla^2 \, M_\phi \, , \tag{B.2.4}$$

where M diffusive coefficient (Mobility) and

$$M_\phi = \beta \, \acute{\Psi} - k \, \nabla^2 \, \phi \, , \tag{B.2.5}$$

is the chemical potential, β and k are parameters, Ψ is related to bulk FE density and $\nabla \, \phi$ is the energy gradient. The multi-scale expansions are introduced,

$$f_i = f_i^{(0)} + \varepsilon f_i^{(1)} + \varepsilon^2 f_i^{(2)} + O(\varepsilon^3) \tag{B.2.6}$$

$$\partial_t = \partial_{to} + \varepsilon \partial_{t1} + O(\varepsilon^2) \tag{B.2.7}$$

$$\partial_\alpha = \partial_{\alpha o} + O(\varepsilon^1) \, . \tag{B.2.8}$$

by starting with the second order Taylor series expanding the lattice BGK (LBGK) equation (B.2.1), as

$$\varepsilon \, (\partial_t + c_{i\alpha} \partial_\alpha) \, f_i + \frac{\varepsilon^2}{2} (\partial_t + c_{i\alpha} \partial_\alpha)(\partial_t + c_{i\beta} \partial_\beta) f_i + O(\varepsilon^3) = \frac{-1}{\acute{\tau}_f} (f_i - f_i^{(eq)}) \, , \tag{B.2.9}$$

where $\acute{\tau}_f = \tau_f/\Delta t$ is the dimensionless relaxation time. Inserting equations (B.2.6), (B.2.7) and (B.2.8) into eq.(B.2.9), yields

$$\varepsilon(\partial_{to}+c_{i\alpha}\partial_{\alpha o})f_i^{(0)}+\varepsilon^2\Big\{\partial_{t1}\, f_i^{(0)}+(\partial_{to}+c_{i\alpha}\partial_{\alpha o})f_i^{(1)}+\frac{1}{2}(\partial_{to}+c_{i\alpha}\partial_{\alpha o})(\partial_{to}+c_{i\beta}\partial_{\beta o})f_i^{(0)}\Big\} + O(\varepsilon^3) = -\frac{1}{\acute{\tau}_f}\left[f_i^{(0)}+\varepsilon f_i^{(1)}+\varepsilon^2 f_i^{(2)}-f_i^{(eq)}\right]+O(\varepsilon^3). \tag{B.2.10}$$

Equating the coefficients of each order ε, It observed that at the zeroth-order of ε

$$f_i^{(0)} = f_i^{(eq)}, \tag{B.2.11}$$

and at the first-order of ε

$$(\partial_{to}+c_{i\alpha}\partial_{\alpha o})\, f_i^{(eq)} = -\frac{1}{\acute{\tau}_f}f_i^{(1)}, \tag{B.2.12}$$

and at the second-order of ε

$$\partial_{t1}\, f_i^{(eq)}+(\partial_{to}+c_{i\alpha}\partial_{\alpha o})f_i^{(1)}+\frac{1}{2}(\partial_{to}+c_{i\alpha}\partial_{\alpha o})(\partial_{to}+c_{i\beta}\partial_{\beta o})f_i^{(eq)}=\frac{-1}{\acute{\tau}_f}f_i^{(2)}\,. \tag{B.2.13}$$

Equation (B.2.13) can be written as follow

$$\partial_{t1}f_i^{(eq)}-\Big(\acute{\tau}_f-\frac{1}{2}\Big)(\partial_{to}+c_{i\alpha}\partial_{\alpha o})(\partial_{to}+c_{i\beta}\partial_{\beta o})f_i^{(eq)}=\frac{-1}{\acute{\tau}_f}f_i^{(2)}\,. \tag{B.2.14}$$

By using the properties of the generalized lattice tensor (Guo & Shu 2013) for D_2Q_9, the zeroth-order moment of equilibrium distribution function Eq.(B.2.2) is evaluated as

follow

$$\sum_i f_i^{(eq)} = \phi \sum_i H_i + \frac{M}{\tau_f - \frac{1}{2}\Delta t} M_\phi \sum_i v_i + \frac{\phi}{c_s^2} \sum_i \omega_i \, c_{i\alpha}.u_\alpha + \frac{\phi}{2\, c_s^4} \sum_i \omega_i \, c_{i\alpha} \, c_{i\beta} \, u_\alpha \, u_\beta - \frac{\phi}{2\, c_s^2} \sum_i \omega_i \, u_\gamma \, u_\gamma \, .$$

From eqs. (B.1.17) yields,

$$\sum_i f_i^{(eq)} = \phi + \frac{M}{\tau_f - \frac{1}{2}\Delta t} M_\phi(0) + \frac{\phi}{c_s^2}(0) + \frac{\phi}{2\, c_s^2} \, u_\beta \, u_\beta - \frac{\phi}{2\, c_s^2} \, u_\gamma \, u_\gamma = \phi \, . \tag{B.2.15}$$

The first-order moments of $f_i^{(eq)}$ is computed as follow

$$\sum_i c_{i\alpha} \, f_i^{(eq)} = \phi \sum_i H_i \, c_{i\alpha} + \frac{M}{\tau_f - \frac{1}{2}\Delta t} M_\phi \sum_i v_i \, c_{i\alpha} + \frac{\phi}{c_s^2} \sum_i \omega_i \, c_{i\alpha} \, c_{i\beta}.u_\beta + \frac{\phi}{2\, c_s^4} \sum_i \omega_i \, c_{i\alpha} \, c_{i\beta} \, c_{i\delta} \, u_\beta \, u_\delta - \frac{\phi}{2\, c_s^2} \sum_i \omega_i \; c_{i\alpha} u_\gamma \, u_\gamma \, ,$$

by substituting eqs. (B.1.17) into above equation, yields

$$\sum_i c_{i\alpha} \, f_i^{(eq)} = \phi \, (0) + \frac{M \; M_\phi \, (0)}{\tau_f - \frac{1}{2}\Delta t} + \frac{\phi}{c_s^2} \, c_s^2 \, \delta_{\alpha\beta} \, u_\beta + \frac{\phi}{2\, c_s^4}(0) - \frac{\phi}{2\, c_s^2}(0) = \phi \, u_\alpha \, , \tag{B.2.16}$$

the second-order moments of equilibrium df ($\pi_{\alpha\beta}^{(0)} = \sum_i c_{i\alpha} \, c_{i\beta} \, f_i^{(eq)}$) is evaluated as below

$$\sum_i c_{i\alpha}\, c_{i\beta}\, f_i^{(eq)} = \phi \sum_i H_i\, c_{i\alpha}\, c_{i\beta} + \frac{M\, M_\phi}{\tau_f - \frac{1}{2}\Delta t} \sum_i v_i\, c_{i\alpha}\, c_{i\beta} + \frac{\phi}{c_s^2} \sum_i \omega_i\, c_{i\alpha}\, c_{i\beta}\, c_{i\delta}\, u_\delta + \frac{\phi}{2\, c_s^4} \sum_i \omega_i\, c_{i\alpha}\, c_{i\beta}\, c_{i\delta}\, c_{i\gamma}\, u_\delta\, u_\gamma - \frac{\phi}{2\, c_s^2} \sum_i \omega_i\, c_{i\alpha}\, c_{i\beta}\, u_\gamma\, u_\gamma\,,$$

from eqs. (B.1.17), yields

$$\begin{aligned}\sum_i c_{i\alpha}\, c_{i\beta}\, f_i^{(eq)} &= \phi(0) + \frac{M\, M_\phi}{\tau_f - \frac{1}{2}\Delta t}\frac{3}{c^2}\sum_i \omega_i\, c_{i\alpha}\, c_{i\beta} - \frac{\phi}{c_s^2}(0) \\ &\quad + \frac{\phi\, c_s^4}{2\, c_s^4}(\delta_{\alpha\beta}\,\delta_{\delta\gamma} + \delta_{\alpha\delta}\,\delta_{\beta\gamma} + \delta_{\alpha\gamma}\,\delta_{\beta\delta})\, u_\delta\, u_\gamma - \frac{\phi\, c_s^2}{2\, c_s^2}\,\delta_{\alpha\beta}\, u_\gamma\, u_\gamma \\ &= \frac{M\, M_\phi\, 3\, c_s^2 \delta_{\alpha\beta}}{(\tau_f - \frac{1}{2}\Delta t)\, c^2} + \frac{\phi}{2}(\delta_{\alpha\beta}\, u_\gamma\, u_\gamma + \delta_{\alpha\delta}\, u_\delta\, u_\beta + \delta_{\alpha\gamma}\, u_\beta\, u_\gamma) - \frac{\phi}{2}\,\delta_{\alpha\beta}\, u_\gamma\, u_\gamma \\ &= \frac{M\, M_\phi\, \delta_{\alpha\beta}}{\tau_f - \frac{1}{2}\Delta t} + \frac{\phi}{2}\,\delta_{\alpha\beta}\, u_\gamma\, u_\gamma + \frac{\phi}{2}\,(u_\alpha\, u_\beta + u_\beta\, u_\alpha) - \frac{\phi}{2}\,\delta_{\alpha\beta}\, u_\gamma\, u_\gamma\,,\end{aligned}$$

thus

$$\sum_i c_{i\alpha}\, c_{i\beta}\, f_i^{(eq)} = \frac{M}{\tau_f - \frac{1}{2}\Delta t}\, M_\phi\, \delta_{\alpha\beta} + \phi\, u_\alpha\, u_\beta\,. \tag{B.2.17}$$

The zero and first moments of distribution function and equilibrium distribution function are defined as follow

$$\sum_i f_i = \sum_i f_i^{(eq)} = \phi \quad \text{and} \quad \sum_i c_{i\alpha}\, f_i = \sum_i c_{i\alpha}\, f_i^{(eq)} = \phi\, u_\alpha. \tag{B.2.18}$$

From equations (B.2.6), (B.2.11) and (B.2.18), it observed that

$$\sum_i f_i^{(k)} = 0 \quad \text{and} \quad \sum_i c_{i\alpha}\, f_i^{(k)} = 0 \quad \text{for} \quad k > 0\,. \tag{B.2.19}$$

Now, by taking the zeroth-order moment of equation (B.2.12)

$$\partial_{to} \sum_i f_i^{(eq)} + \partial_{\alpha o} \sum_i c_{i\alpha}\, f_i^{(eq)} = -\frac{1}{\acute{\tau}_f} \sum_i f_i^{(1)}\,,$$

from the zeroth- and first-order moments of of equilibrium distribution function Eqs. (B.2.15) and (B.2.16) with eq. (B.2.19), yielding

$$\partial_{to}\,\phi + \partial_{\alpha o}\,(\phi\, u_\alpha) = 0\,. \tag{B.2.20}$$

By taking the zeroth-order moment of eq. (B.2.14) and simplified to

$$\begin{aligned}
&\partial_{t1} \sum_i f_i^{(eq)} - \Big(\acute{\tau}_f - \frac{1}{2}\Big)\Big\{\partial_{to}\,\partial_{to} \sum_i f_i^{(eq)} + \partial_{to}\,\partial_{\alpha o} \sum_i c_{i\alpha}\, f_i^{(eq)}\Big\} \\
&\quad - \Big(\acute{\tau}_f - \frac{1}{2}\Big)\Big\{\partial_{\beta o}\,\partial_{to} \sum_i c_{i\beta}\, f_i^{(eq)} + \partial_{\beta o}\,\partial_{\alpha o} \sum_i c_{i\beta}\, f_i^{(eq)}\Big\} = -\frac{1}{\acute{\tau}_f} \sum_i f_i^{(2)}\,,
\end{aligned}$$

By substituting eqs. (B.2.15), (B.2.16), (B.2.17) and (B.2.19), yields

$$\partial_{t1}\phi - \left(\acute{\tau}_f - \frac{1}{2}\right)\partial_{to}\left\{\partial_{to}\,\phi + \partial_{\alpha o}\left(\phi\, u_\alpha\right)\right\} - \left(\acute{\tau}_f - \frac{1}{2}\right) \left\{\partial_{\beta o}\,\partial_{to}\left(\phi\, u_\beta\right) + \partial_{\beta o}\,\partial_{\alpha o}\left[\frac{M}{\tau_f - \frac{1}{2}\Delta t}\, M_\phi\, \delta_{\alpha\beta} + \phi\, u_\alpha\, u_\beta\right]\right\} = 0\,, \tag{B.2.21}$$

From eq. (B.2.20), yields

$$\partial_{t1}\phi = \left(\acute{\tau}_f - \frac{1}{2}\right)\partial_{\beta o}\left\{\partial_{to}\left(\phi\, u_\beta\right) + \partial_{\alpha o}\left(\phi\, u_\alpha\, u_\beta\right)\right\} + \frac{\left(\acute{\tau}_f - \frac{1}{2}\right)\partial_{\alpha o}\,\partial_{\alpha o}\, M\, M_\phi}{\left(\acute{\tau}_f - \frac{1}{2}\right)\Delta t}\,, \tag{B.2.22}$$

by multiplying eq. (B.2.22) by $\varepsilon = \Delta t$, It observed that

$$\varepsilon\,\partial_{t1}\phi = \left(\acute{\tau}_f - \frac{1}{2}\right)\Delta t\,\partial_{\beta o}\Big\{\partial_{to}\left(\phi\, u_\beta\right) + \partial_{\alpha o}\left(\phi\, u_\alpha\, u_\beta\right)\Big\} + \partial_{\alpha o}\,\partial_{\alpha o}\, M\, M_\phi\,. \tag{B.2.23}$$

By adding eq. (B.2.23) to the eq. (B.2.20), reads

$$\partial_t\phi + \partial_\alpha\left(\phi\, u_\alpha\right) = \left(\acute{\tau}_f - \frac{1}{2}\right)\Delta t\,\partial_\beta\Big\{\partial_{to}\left(\phi\, u_\beta\right) + \partial_\alpha\left(\phi\, u_\alpha\, u_\beta\right)\Big\} + \partial_\alpha\,\partial_\alpha\, M\, M_\phi\,. \tag{B.2.24}$$

The term that contain $\left(\acute{\tau}_f - \frac{1}{2}\right)\partial_\beta\,\partial_{to}\left(\phi\, u_\beta\right)$ is multiplied by a small parameter Δt can be neglected and the term that contain $\left(\phi\, u_\alpha\, u_\beta\right)$ can be removed, because it has $O(Ma)^3$ Mach number, so

$$\partial_t\phi + \partial_\alpha\left(\phi\, u_\alpha\right) = M\,\nabla^2\, M_\phi\,,$$

which is the Cahn-Hilliard equation.

B.3 Chapman-Enskog expansion for solving pressure Poisson equation

In this section, by applying the Chapman-Enskog expansion to the LB equation for solving pressure Poisson equation

$$h_i^n(\mathbf{x}+c_i\Delta t, t+\Delta t) - h_i^n(\mathbf{x},t) = -\frac{\Delta t}{\tau_h}\left(h_i^n(\mathbf{x},t) - h_i^{(eq,n)}(\mathbf{x},t) \right) - \Delta t\,\omega_i\left(\nabla.\mathbf{u}^*(t)\right), \tag{B.3.1}$$

where n is $n-$ th iteration for the pressure. With the equilibrium distribution function of $D_2\,Q_9$

$$h_i^{(eq,n)} = \omega_i\,\frac{p^n(\mathbf{x},\mathbf{t})}{\rho_o\,c^2}\,, \tag{B.3.2}$$

where

$$\tau_h = \Delta t\left(\frac{1}{2} + \frac{\rho_o\,c^2}{\rho\,c_s^2}\right), \tag{B.3.3}$$

and

$$\nabla.\left(\frac{\Delta t\,\nabla p}{\rho}\right) = \nabla.\mathbf{u}^*\,, \tag{B.3.4}$$

is the Poisson equation. The multi-scale expansions are introduced,

$$h_i^n = h_i^{(0)} + \varepsilon h_i^{(1)} + \varepsilon^2 h_i^{(2)} + O(\varepsilon^3)\,, \tag{B.3.5}$$

$$\partial_t = \partial_{to} + \varepsilon \partial_{t1} + O(\varepsilon^2)\,, \tag{B.3.6}$$

$$\partial_\alpha = \partial_{\alpha o} + O(\varepsilon^1)\,. \tag{B.3.7}$$

By the second order Taylor series expanding the lattice BGK (LBGK) equation (B.3.1), yields

$$\varepsilon\left(\partial_t + c_{i\alpha}\partial_\alpha\right) h_i^n + \frac{\varepsilon^2}{2}(\partial_t + c_{i\alpha}\partial_\alpha)(\partial_t + c_{i\beta}\partial_\beta)\, h_i^n + O(\varepsilon^3) = -\frac{1}{\acute{\tau}_h}(h_i^n - h_i^{(eq,n)}) - \Delta t\, \omega_i\, \nabla.\mathbf{u}^*\,, \tag{B.3.8}$$

where $\acute{\tau}_h = \tau_h/\Delta t$ the dimensionless relaxation time. Inserting equations (B.3.5), (B.3.6) and (B.3.7) into eq. (B.3.8), reads

$$\varepsilon(\partial_{to}+c_{i\alpha}\partial_{\alpha o})h_i^{(0)} + \varepsilon^2\left\{\partial_{t1}h_i^{(0)} + (\partial_{to} + c_{i\alpha}\partial_{\alpha o})h_i^{(1)} + \frac{1}{2}(\partial_{to}+c_{i\alpha}\partial_{\alpha o})(\partial_{to}+c_{i\beta}\partial_{\beta o})h_i^{(0)}\right\} + O(\varepsilon^3) = \frac{-1}{\acute{\tau}_h}\left[h_i^{(0)} + \varepsilon h_i^{(1)} + \varepsilon^2 h_i^{(2)} - h_i^{(eq,n)}\right] - \varepsilon\,\omega_i\,\nabla.\mathbf{u}^* + O(\varepsilon^3). \tag{B.3.9}$$

Equating the coefficients of each order ε, it is observed that at the zeroth-order of ε

$$h_i^{(0)} = h_i^{(eq,n)}\,, \tag{B.3.10}$$

and at the first-order of ε

$$(\partial_{to} + c_{i\alpha}\partial_{\alpha o})\, h_i^{(eq,n)} = -\frac{1}{\acute{\tau}_h}\, h_i^{(1)} - \omega_i\, \nabla.\mathbf{u}^*\,, \tag{B.3.11}$$

and at the second-order of ε

$$\partial_{t1}\, h_i^{(eq,n)} + (\partial_{to} + c_{i\alpha}\partial_{\alpha o})\, h_i^{(1)} + \frac{1}{2}(\partial_{to} + c_{i\alpha}\partial_{\alpha o})(\partial_{to} + c_{i\beta}\partial_{\beta o})\, h_i^{(eq,n)} = -\frac{1}{\acute{\tau}_h}\, h_i^{(2)}\,, \tag{B.3.12}$$

which can be written as follow

$$\partial_{t1}\, h_i^{(eq,n)} + \left(\frac{2\acute{\tau}_f - 1}{2\acute{\tau}_f}\right)(\partial_{to} + c_{i\alpha}\partial_{\alpha o})\, h_i^{(1)} - \frac{\omega_i}{2}\,(\partial_{to} + c_{i\alpha}\partial_{\alpha o})\,\nabla.\mathbf{u}^* = -\frac{1}{\acute{\tau}_h}\, h_i^{(2)}\,. \tag{B.3.13}$$

By using the properties of the generalized lattice tensor (Guo & Shu 2013) for D_2Q_9, the zeroth-order moment of equilibrium distribution function eq. (B.3.2) is evaluated as follow

$$\sum_i h_i^{(eq,n)} = \sum_i \omega_i\, \frac{p^n}{\rho_o\, c^2}\,,$$

from eqs. (B.1.17), yields

$$\sum_i h_i^{(eq,n)} = \frac{p^n}{\rho_o\, c^2}\,, \tag{B.3.14}$$

the first-order moments of equilibrium distribution function is competed as follow

$$\sum_i c_{i\alpha}\, h_i^{(eq,n)} = \sum_i c_{i\alpha}\, \omega_i\, \frac{p^n}{\rho_o\, c^2}\,.$$

By substituting eqs. (B.1.17) into above equation, yields

$$\sum_i c_{i\alpha}\, h_i^{(eq,n)} = 0\,. \tag{B.3.15}$$

The second-order moments of equilibrium distribution function is evaluated as below

$$\sum_i c_{i\alpha}\, c_{i\beta}\, h_i^{(eq,n)} = \sum_i c_{i\alpha}\, c_{i\beta}\, \omega_i\, \frac{p^n}{\rho_o\, c^2}\,,$$

from eqs. (B.1.17), yields

$$\sum_i c_{i\alpha}\, c_{i\beta}\, h_i^{(eq,n)} = c_s^2\, \delta_{\alpha\beta}\, \frac{p^n}{\rho_o\, c^2}\,, \tag{B.3.16}$$

the zero and first moments of distribution function and equilibrium distribution function are defined as follow

$$\sum_i h_i^n = \sum_i h_i^{(eq,n)} = \frac{p^n}{\rho_o\, c^2}\,, \tag{B.3.17}$$

from equations (B.3.5), (B.3.10) and (B.3.17), it observed that

$$\sum_i h_i^{(k)} = 0\,. \tag{B.3.18}$$

Now, by taking the zeroth-order moment of equation (B.3.11), yields

$$\partial_{to} \sum_i h_i^{(eq,n)} + \partial_{\alpha o} \sum_i c_{i\alpha}\, h_i^{(eq,n)} = -\frac{1}{\acute{\tau}_h} \sum_i h_i^{(1)} - \sum_i \omega_i\, \nabla.\mathbf{u}^* \,,$$

then,

$$\partial_{to} \left(\frac{p^n}{\rho_o\, c^2}\right) = -\nabla.\mathbf{u}^* \,, \tag{B.3.19}$$

and the zeroth-order moment of equation (B.3.13), yields

$$\partial_{t1} \sum_i h_i^{(eq,n)} + \left(\frac{2\acute{\tau}_f - 1}{2\acute{\tau}_f}\right) \left(\partial_{to} \sum_i h_i^{(1)} + \partial_{\alpha o} \sum_i c_{i\alpha}\, h_i^{(1)}\right) - \frac{1}{2}\, \partial_{to} \sum_i \omega_i\, \nabla.\mathbf{u}^* - \frac{1}{2}\, \partial_{\alpha o} \sum_i \omega_i\, c_{i\alpha}\, \nabla.\mathbf{u}^* = -\frac{1}{\acute{\tau}_h} \sum_i h_i^{(2)} \,,$$

which can be simplified to,

$$\partial_{t1} \sum_i h_i^{(eq,n)} + \partial_{\alpha o} \left(\frac{2\acute{\tau}_f - 1}{2\acute{\tau}_f}\right) \sum_i c_{i\alpha}\, h_i^{(1)} - \frac{1}{2}\, \partial_{to} \sum_i \omega_i\, \nabla.\mathbf{u}^* = 0 \,. \tag{B.3.20}$$

From eqs. (B.3.11) and (B.1.17), yields

$$\partial_{t1} \sum_i h_i^{(eq,n)} - \partial_{\alpha o} \left(\frac{2\acute{\tau}_f - 1}{2}\right) \sum_i c_{i\alpha} \Big((\partial_{to} + c_{i\beta}\partial_{\beta o})\, h_i^{(eq,n)} + \omega_i\, \nabla.\mathbf{u}^* \Big) - \frac{1}{2}\, \partial_{to}\, \nabla.\mathbf{u}^* = 0 \,.$$

Then,

$$\partial_{t1}\sum_i h_i^{(eq,n)} - \partial_{to}\,\partial_{\alpha o}\Big(\frac{2\acute{\tau}_f - 1}{2}\Big)\sum_i c_{i\alpha}\,h_i^{(eq,n)} - \partial_{\alpha o}\Bigg(\Big(\frac{2\acute{\tau}_f - 1}{2}\Big)\,\partial_{\beta o}\sum_i c_{i\alpha}\,c_{i\beta}\,h_i^{(eq,n)}\Bigg) - \partial_{\alpha o}\Big(\frac{2\acute{\tau}_f - 1}{2}\Big)\sum_i c_{i\alpha}\,\omega_i\,\nabla.\mathbf{u}^* - \frac{1}{2}\,\partial_{to}\,\nabla.\mathbf{u}^* = 0\,,$$

and from eqs. (B.1.17), (B.3.14), (B.3.15) and (B.3.16), it observed that

$$\partial_{t1}\Big(\frac{p^n}{\rho_o\,c^2}\Big) - \partial_{\alpha o}\left(\Big(\frac{2\acute{\tau}_f - 1}{2}\Big)\,\frac{c_s^2}{\rho_o\,c^2}\,\partial_{\beta o}\,\delta_{\alpha\beta}\,p^n\right) - \frac{1}{2}\,\partial_{to}\,\nabla.\mathbf{u}^* = 0\,,$$

then,

$$\partial_{t1}\Big(\frac{p^n}{\rho_o\,c^2}\Big) - \partial_{\alpha o}\left(\Big(\acute{\tau}_f - \frac{1}{2}\Big)\,\frac{c_s^2}{\rho_o\,c^2}\,\partial_{\alpha o}\,p^n\right) - \frac{1}{2}\,\partial_{to}\,\nabla.\mathbf{u}^* = 0\,. \tag{B.3.21}$$

By multiplying eq. (B.3.21) by $\varepsilon = \Delta t$ and adding with eq. (B.3.19), yields

$$\partial_t\Big(\frac{p^n}{\rho_o\,c^2}\Big) - \partial_{\alpha o}\left(\Big(\acute{\tau}_f - \frac{1}{2}\Big)\,\frac{\Delta t\,c_s^2}{\rho_o\,c^2}\,\partial_{\alpha o}\,p^n\right) - \frac{\Delta t}{2}\,\partial_{to}\,\nabla.\mathbf{u}^* = -\nabla.\mathbf{u}^*\,. \tag{B.3.22}$$

The term that contain $\frac{1}{2}\,\partial_{to}\,\nabla.\mathbf{u}^*$ is multiplied by a small parameter Δt can be neglected and when $\partial_t\,(p^n) \longrightarrow 0$ eq. (B.3.22) becomes,

$$\nabla.\left(\Big(\acute{\tau}_f - \frac{1}{2}\Big)\,\frac{\Delta t\,c_s^2}{\rho_o\,c^2}\,\nabla.\,p^n\right) = \nabla.\mathbf{u}^*\,, \tag{B.3.23}$$

which identical to the diffusive Poison equation eq. (B.3.4), that satisfies

$$\left(\acute{\tau}_f - \frac{1}{2}\right) \frac{c_s^2}{\rho_o\, c^2} = \frac{1}{\rho}\,. \tag{B.3.24}$$

Since $\acute{\tau}_h = \tau_h/\Delta t$, so

$$\tau_h = \Delta t \left(\frac{1}{2} + \frac{\rho_o\, c^2}{\rho\, c_s^2}\right).$$

Appendix C

The discretization of the first and second derivative

The first and second order derivative can be calculated by central finite difference approximations for equation according to Lee & Lin (2005) as follows:
The first order derivation in the x-direction:

$$\frac{\partial \phi}{\partial x}|_{(i,j)} = \frac{1}{3}(\phi(i+1,j) - \phi(i-1,j)) + \frac{1}{12}(\phi(i+1,j+1) - \phi(i-1,j-1)) + \frac{1}{12}(\phi(i+1,j-1) - \phi(i-1,j+1)), \quad \text{(C.0.1)}$$

and in the y-direction:

$$\frac{\partial \phi}{\partial y}|_{(i,j)} = \frac{1}{3}(\phi(i,j+1) - \phi(i,j-1)) + \frac{1}{12}(\phi(i+1,j+1) - \phi(i-1,j-1)) + \frac{1}{12}(\phi(i-1,j+1) - \phi(i+1,j-1)), \quad \text{(C.0.2)}$$

where i and j refer to the grid coordinate.

The second order derivative can be computed as:

$$\frac{\partial \phi^2}{\partial x_k^2}|_{(i,j)} = \frac{-20}{6}(\phi(i,j) + \frac{4}{6}(\phi(i+1,j) + \phi(i-1,j) + \phi(i,j+1) + \phi(i,j-1)) + \frac{1}{6}(\phi(i+1,j+1) + \phi(i-1,j+1) + \phi(i+1,j-1) + \phi(i-1,j-1)), \quad \text{(C.0.3)}$$

and

$$\frac{\partial \phi^2}{\partial x \, \partial y}|_{(i,j)} = \frac{1}{4}(\phi(i+1, j+1) - \phi(i+1, j-1) - \phi(i-1, j+1) + \phi(i-1, j-1)), \quad \text{(C.0.4)}$$

where i, j and k refer to the grid coordinate.

Bibliography

Allen, S. M. & Cahn, J. W. (1976), 'Mechanisms of phase transformations within the miscibility gap of fe-rich fe-al alloys', *Acta Metallurgica* **24**(5), 425–437.

Anderson, D. & McFadden, G. (1996), 'A Diffuse-Interface description of fluid systems, National Institute of Standards and Technology', *Gaithersburg, MD, Report No. NISTER* **5887**.

Ba, Y., Liu, H., Li, Q., Kang, Q. & Sun, J. (2016), 'Multiple-relaxation-time color-gradient lattice boltzmann model for simulating two-phase flows with high density ratio', *Physical Review E* **94**(2), 023310.

Badalassi, V., Ceniceros, H. & Banerjee, S. (2003), 'Computation of multiphase systems with phase field models', *Journal of computational physics* **190**(2), 371–397.

Badarch, A., Tokuzo, H. & Narantsogt, N. (2016), Hydraulics application of the free-surface lattice boltzmann method, *in* '2016 11th International Forum on Strategic Technology (IFOST)', IEEE, pp. 195–199.

Banari, A. (2014), 'Lattice Boltzmann simulation of multiphase flows; application to wave breaking and sea spray generation'.

Banari, A., Janßen, C., Grilli, S. T. & Krafczyk, M. (2014), 'Efficient gpgpu implementation of a lattice boltzmann model for multiphase flows with high density ratios', *Computers & Fluids* **93**, 1–17.

Bao, Y. B. & Meskas, J. (2011), 'Lattice Boltzmann method for fluid simulations',

Department of Mathematics, Courant Institute of Mathematical Sciences, New York University .

Benzi, R., Biferale, L., Sbragaglia, M., Succi, S. & Toschi, F. (2006), 'Mesoscopic modeling of a two-phase flow in the presence of boundaries: the contact angle', *Physical Review E* **74**(2), 021509.

Botella, O. & Peyret, R. (1998), 'Benchmark spectral results on the lid-driven cavity flow', *Computers & Fluids* **27**(4), 421–433.

Bruneau, C.-H. & Jouron, C. (1990), 'An efficient scheme for solving steady incompressible navier-stokes equations', *Journal of Computational Physics* **89**(2), 389–413.

Buick, J. & Greated, C. (1998), 'Lattice boltzmann modeling of interfacial gravity waves', *Physics of Fluids* **10**(6), 1490–1511.

Buick, J. & Greated, C. (2000), 'Gravity in a lattice boltzmann model', *Physical Review E* **61**(5), 5307.

Cahn, J. W. & Hilliard, J. E. (1958), 'Free energy of a nonuniform system. i. interfacial free energy', *The Journal of chemical physics* **28**(2), 258–267.

Chapman, S. & Cowling, T. (1970), 'The mathematical theory of non-uniform gases, cambridge univ', *Press, Cambridge, England* .

Chen, G.-Q., Huang, X., Zhang, A.-M. & Wang, S.-P. (2019), 'Simulation of three-dimensional bubble formation and interaction using the high-density-ratio lattice boltzmann method', *Physics of Fluids* **31**(2), 027102.

Chen, H., Chen, S. & Matthaeus, W. H. (1992), 'Recovery of the Navier-Stokes equations using a lattice-gas Boltzmann method', *Phys. Rev. A* **45**(8), R5339.

Chen, S. & Doolen, G. D. (1998), 'Lattice boltzmann method for fluid flows', *Annual review of fluid mechanics* **30**(1), 329–364.

Clift, R., Grace, J. R. & Weber, M. E. (2005), *Bubbles, drops, and particles*, Courier Corporation.

Colagrossi, A. & Landrini, M. (2003), 'Numerical simulation of interfacial flows by smoothed particle hydrodynamics', *Journal of computational physics* **191**(2), 448–475.

Contreras, J. O. et al. (2013), 'Efficient algorithms for the realistic simulation of fluids'.

Dabbaghitehrani, M. (2013), 'Lattice Boltzmann method for two immiscible components', *Master of Science Thesis. Stockholm, Royal Institute of Technology* .

Deng, G., Piquet, J., Queutey, P. & Visonneau, M. (1994), 'Incompressible flow calculations with a consistent physical interpolation finite volume approach', *Computers & fluids* **23**(8), 1029–1047.

d'Humieres, D. (1994), 'Generalized lattice-Boltzmann equations', *Rarefied gas dynamics- Theory and simulations* pp. 450–458.

d'Humieres, D. (2002), 'Multiple–relaxation–time lattice boltzmann models in three dimensions', *Philosophical Transactions of the Royal Society of London. Series A: Mathematical, Physical and Engineering Sciences* **360**(1792), 437–451.

Dong, B., Yan, Y., Li, W. & Song, Y. (2010), 'Lattice boltzmann simulation of viscous fingering phenomenon of immiscible fluids displacement in a channel', *Computers & Fluids* **39**(5), 768–779.

Enright, D., Marschner, S. & Fedkiw, R. (2002), Animation and rendering of complex water surfaces, *in* 'ACM Transactions on Graphics (TOG)', Vol. 21, ACM, pp. 736–744.

Fakhari, A. & Lee, T. (2013), 'Multiple-relaxation-time lattice boltzmann method for immiscible fluids at high reynolds numbers', *Physical Review E* **87**(2), 023304.

Fakhari, A., Mitchell, T., Leonardi, C. & Bolster, D. (2017), 'Improved locality of the phase-field lattice-boltzmann model for immiscible fluids at high density ratios', *PHYSICAL REVIEW E Phys Rev E* **96**, 053301.

Fakhari, A. & Rahimian, M. H. (2010), 'Phase-field modeling by the method of lattice boltzmann equations', *Physical Review E* **81**(3), 036707.

Frisch, U., Hasslacher, B. & Pomeau, Y. (1986), 'Lattice-gas automata for the Navier-Stokes equation', *Phys. Rev. Let.* **56**(14), 1505.

Ghia, U., Ghia, K. N. & Shin, C. (1982), 'High-resolutions for incompressible flow using the Navier-Stokes equations and a multigrid method', *J. Comput. Phys.* **48**(3), 387–411.

Ginzburg, I. & Steiner, K. (2003), 'Lattice Boltzmann model for free-surface flow and its application to filling process in casting', *J. Comput. Phys.* **185**(1), 61–99.

Golberg, M. A. (1995), 'The method of fundamental solutions for poisson's equation', *Engineering Analysis with Boundary Elements* **16**(3), 205–213.

Grunau, D., Chen, S. & Eggert, K. (1993), 'A lattice boltzmann model for multiphase fluid flows', *Physics of Fluids A: Fluid Dynamics* **5**(10), 2557–2562.

Gunstensen, A. K., Rothman, D. H., Zaleski, S. & Zanetti, G. (1991), 'Lattice boltzmann model of immiscible fluids', *Physical Review A* **43**(8), 4320.

Guo, Z. & Shu, C. (2013), *Lattice Boltzmann method and its applications in engineering*, Vol. 3, World Scientific.

Guo, Z., Zheng, C. & Shi, B. (2002), 'Discrete lattice effects on the forcing term in the lattice boltzmann method', *Physical Review E* **65**(4), 046308.

Harris, S. (2004), *An introduction to the theory of the Boltzmann equation*, Courier Corporation.

He, X., Chen, S. & Zhang, R. (1999), 'A lattice boltzmann scheme for incompressible multiphase flow and its application in simulation of rayleigh–taylor instability', *Journal of Computational Physics* **152**(2), 642–663.

He, X. & Doolen, G. D. (2002), 'Thermodynamic foundations of kinetic theory and lattice boltzmann models for multiphase flows', *Journal of Statistical Physics* **107**(1-2), 309–328.

He, X. & Luo, L.-S. (1997*a*), 'A priori derivation of the lattice Boltzmann equation', *Phys. Rev. E* **55**(6), R6333.

He, X. & Luo, L.-S. (1997*b*), 'Theory of the lattice Boltzmann method: From the Boltzmann equation to the lattice Boltzmann equation', *Phys. Rev. E* **56**(6), 6811.

He, X., Zou, Q., Luo, L.-S. & Dembo, M. (1997), 'Analytic solutions of simple flows and analysis of nonslip boundary conditions for the lattice boltzmann bgk model', *Journal of Statistical Physics* **87**(1-2), 115–136.

Hirt, C. W. & Nichols, B. D. (1981), 'Volume of fluid (VOF) method for the dynamics of free boundaries', *J. comput. phys.* **39**(1), 201–225.

Hodges, B. R., Street, R. L. & Zang, Y. (1996), A method for simulation of viscous, nonlinear, free-surface flows, *in* '20th Symposium on Naval Hydrodynamics', pp. 791–809.

Holdych, D., Rovas, D., Georgiadis, J. G. & Buckius, R. (1998), 'An improved hydrodynamics formulation for multiphase flow lattice-boltzmann models', *International Journal of Modern Physics C* **9**(08), 1393–1404.

Hou, S., Zou, Q., Chen, S., Doolen, G. & Cogley, A. C. (1995), 'Simulation of cavity flow by the lattice Boltzmann method', *J. Comput. Phys.* **118**(2), 329–347.

Hua, J. & Lou, J. (2007), 'Numerical simulation of bubble rising in viscous liquid', *Journal of Computational Physics* **222**(2), 769–795.

Huang, H., Huang, J.-J., Lu, X.-Y. & Sukop, M. C. (2013), 'On simulations of high-density ratio flows using color-gradient multiphase lattice boltzmann models', *International Journal of Modern Physics C* **24**(04), 1350021.

Huang, H., Sukop, M. & Lu, X. (2015), *Multiphase lattice Boltzmann methods: Theory and application*, John Wiley & Sons.

Huang, H., Thorne Jr, D. T., Schaap, M. G. & Sukop, M. C. (2007), 'Proposed approximation for contact angles in shan-and-chen-type multicomponent multiphase lattice boltzmann models', *Physical Review E* **76**(6), 066701.

Huang, J., Shu, C., Feng, J. & Chew, Y. (2012), 'A phase-field-based hybrid lattice-boltzmann finite-volume method and its application to simulate droplet motion under electrowetting control', *Journal of Adhesion Science and Technology* **26**(12-17), 1825–1851.

Inamuro, T., Ogata, T., Tajima, S. & Konishi, N. (2004), 'A lattice Boltzmann method for incompressible two-phase flows with large density differences', *J. Comput. Phys.* **198**(2), 628–644.

Inamuro, T., Yoshino, M. & Ogino, F. (1997), 'Accuracy of the lattice boltzmann

method for small knudsen number with finite reynolds number', *Physics of Fluids* **9**(11), 3535–3542.

Jacqmin, D. (1999), 'Calculation of two-phase Navier–Stokes flows using phase-field modeling', *J. Comput. Phys.* **155**(1), 96–127.

Jain, P. K. (2010), Simulation of two-phase dynamics using lattice boltzmann method (LBM), PhD thesis, University of Illinois at Urbana-Champaign.

Janssen, C. F., Grilli, S. T. & Krafczyk, M. (2013), 'On enhanced non-linear free surface flow simulations with a hybrid LBM–VOF model', *Comput. Math. Appl.* **65**(2), 211–229.

Janssen, C. F., Krafczyk, M., Grilli, S. et al. (2010), Modeling of wave breaking andwave-structure interactions by coupling of fully nonlinear potential flow and lattice-Boltzmann models, *in* 'The Twentieth International Offshore and Polar Engineering Conference', International Society of Offshore and Polar Engineers.

Janssen, C. & Krafczyk, M. (2010), 'A lattice Boltzmann approach for free-surface-flow simulations on non-uniform block-structured grids', *Comput. Math. Appl.* **59**(7), 2215–2235.

Janssen, C. & Krafczyk, M. (2011), 'Free surface flow simulations on GPGPUs using the lbm', *Comput. Math. Appl.* **61**(12), 3549–3563.

Johansson, J. (2010), 'Efficient implementation of the Particle Level Set method'.

Körner, C., Thies, M., Hofmann, T., Thürey, N. & Rüde, U. (2005), 'Lattice Boltzmann model for free surface flow for modeling foaming', *J. Stat. Phys.* **121**(1-2), 179–196.

Koshizuka, S. & Oka, Y. (1996), 'Moving-particle semi-implicit method for fragmentation of incompressible fluid', *Nuclear science and engineering* **123**(3), 421–434.

Lallemand, P. & Luo, L.-S. (2000), 'Theory of the lattice Boltzmann method: Dispersion, dissipation, isotropy, galilean invariance, and stability', *Phys. Rev. E* **61**(6), 6546.

Lallemand, P., Luo, L.-S. & Peng, Y. (2007), 'A lattice boltzmann front-tracking method for interface dynamics with surface tension in two dimensions', *Journal of Computational Physics* **226**(2), 1367–1384.

Latt, J. (2008), 'Choice of units in lattice Boltzmann simulations', *Freely available online at http://lbmethod. org/_media/howtos: lbunits. pdf* .

Latva-Kokko, M. & Rothman, D. H. (2005), 'Static contact angle in lattice boltzmann models of immiscible fluids', *Physical Review E* **72**(4), 046701.

Leclaire, S., Reggio, M. & Trépanier, J.-Y. (2012), 'Numerical evaluation of two recoloring operators for an immiscible two-phase flow lattice boltzmann model', *Applied Mathematical Modelling* **36**(5), 2237–2252.

Lee, T. & Lin, C.-L. (2005), 'A stable discretization of the lattice boltzmann equation for simulation of incompressible two-phase flows at high density ratio', *Journal of Computational Physics* **206**(1), 16–47.

Li-shi, L. (2000), 'The lattice-gas and lattice Boltzmann methods: past, present, and future'.

Liang, H., Li, Y., Chen, J. & Xu, J. (2019), 'Axisymmetric lattice boltzmann model for multiphase flows with large density ratio', *International Journal of Heat and Mass Transfer* **130**, 1189–1205.

Liu, H., Valocchi, A. J. & Kang, Q. (2012), 'Three-dimensional lattice boltzmann model for immiscible two-phase flow simulations', *Physical Review E* **85**(4), 046309.

Lord, R. (1900), 'Investigation of the character of the equilibrium of an incompressible heavy fluid of variable density', *Scientific Papers* pp. 200–207.

Luo, L.-S., Liao, W., Chen, X., Peng, Y., Zhang, W. et al. (2011), 'Numerics of the lattice boltzmann method: Effects of collision models on the lattice boltzmann simulations', *Physical Review E* **83**(5), 056710.

Márkus, A. & Házi, G. (2008), 'Determination of the pseudopotential gradient in multiphase lattice boltzmann models', *Physics of Fluids* **20**(2), 022101.

Martin, J. C., Moyce, W. J., Martin, J., Moyce, W., Penney, W. G., Price, A. & Thornhill, C. (1952), 'Part iv. an experimental study of the collapse of liquid columns on a rigid horizontal plane', *Philosophical Transactions of the Royal Society of London. Series A, Mathematical and Physical Sciences* **244**(882), 312–324.

Mei, R., Luo, L.-S. & Shyy, W. (1999), 'An accurate curved boundary treatment in the lattice Boltzmann method', *comput. phys.* **155**(2), 307–330.

Nadiga, B. & Zaleski, S. (1995), 'Investigations of a two-phase fluid model', *arXiv preprint comp-gas/9511003* .

Nils, T. (2007), 'Physically based animation of free surface (ph. d thesis)'.

Osher, S. & Fedkiw, R. (2006), *Level set methods and dynamic implicit surfaces*, Vol. 153, Springer Science & Business Media.

Osher, S. & Sethian, J. A. (1988), 'Fronts propagating with curvature-dependent speed: algorithms based on Hamilton-Jacobi formulations', *J. comput. physics.* **79**(1), 12–49.

Penrose, O. & Fife, P. C. (1990), 'Thermodynamically consistent models of phase-field type for the kinetic of phase transitions', *Physica D: Nonlinear Phenomena* **43**(1), 44–62.

Qian, Y.-H., d'Humières, D. & Lallemand, P. (1992), 'Lattice bgk models for navier-stokes equation', *EPL (Europhysics Letters)* **17**(6), 479.

Raiskinmäki, P., Koponen, A., Merikoski, J. & Timonen, J. (2000), 'Spreading dynamics of three-dimensional droplets by the lattice-boltzmann method', *Computational Materials Science* **18**(1), 7–12.

Reis, T. & Phillips, T. (2007), 'Lattice boltzmann model for simulating immiscible two-phase flows', *Journal of Physics A: Mathematical and Theoretical* **40**(14), 4033.

Ren, F., Song, B., Sukop, M. C. & Hu, H. (2016), 'Improved lattice boltzmann modeling of binary flow based on the conservative allen-cahn equation', *Physical Review E* **94**(2), 023311.

Rothman, D. H. & Keller, J. M. (1988), 'Immiscible cellular-automaton fluids', *Journal of Statistical Physics* **52**(3-4), 1119–1127.

Rothman, D. H., Zaleski, S. & Powell IV, A. C. (1998), 'Lattice-gas cellular automata: Simple models of complex hydrodynamics'.

Rowlinson, J. & Widom, B. (1982), 'Molecular theory of capillarity 1982', *Clarendon: Oxford* p. 56.

Rüde, U. & Thürey, N. (2004), Free surface lattice-Boltzmann fluid simulations with and without level sets, *in* 'Vision, Modeling, and Visualization 2004: Proceedings, November 16-18, 2004, Standford, USA', IOS Press, p. 199.

Sahin, M. & Owens, R. G. (2003), 'A novel fully implicit finite volume method applied to the lid-driven cavity problem—part i: High reynolds number flow calculations', *International journal for numerical methods in fluids* **42**(1), 57–77.

Sankaranarayanan, K., Kevrekidis, I., Sundaresan, S., Lu, J. & Tryggvason, G. (2003), 'A comparative study of lattice boltzmann and front-tracking finite-difference methods for bubble simulations', *International Journal of Multiphase Flow* **29**(1), 109–116.

Sankaranarayanan, K., Shan, X., Kevrekidis, I. & Sundaresan, S. (2002), 'Analysis of drag and virtual mass forces in bubbly suspensions using an implicit formulation of the lattice boltzmann method', *Journal of Fluid Mechanics* **452**, 61–96.

Scardovelli, R. & Zaleski, S. (1999), 'Direct numerical simulation of free-surface and interfacial flow', *Annual review of fluid mechanics* **31**(1), 567–603.

Shan, X. & Chen, H. (1993), 'Lattice boltzmann model for simulating flows with multiple phases and components', *Physical Review E* **47**(3), 1815.

Shan, X. & Doolen, G. (1995), 'Multicomponent lattice-boltzmann model with interparticle interaction', *Journal of Statistical Physics* **81**(1-2), 379–393.

Shan, X. & He, X. (1998), 'Discretization of the velocity space in the solution of the Boltzmann equation', *Phys. Rev. L.* **80**(1), 65.

Shan, X., Yuan, X.-F. & Chen, H. (2006), 'Kinetic theory representation of hydrodynamics: a way beyond the Navier–Stokes equation', *J. Fluid Mech.* **550**(1), 413–441.

Shao, J. & Shu, C. (2015), 'A hybrid phase field multiple relaxation time lattice boltzmann method for the incompressible multiphase flow with large density contrast', *International Journal for Numerical Methods in Fluids* **77**(9), 526–543.

Sharp, D. H. (1983), Overview of rayleigh-taylor instability, Technical report, Los Alamos National Lab., NM (USA).

Sidik, N. A. C., Khan, A. A., Kermani, E., Manshor, A. H. & Jahanshaloo, L. (2013), The use of mrt-lattice Boltzmann method for the prediction of fluid solid flow, *in* 'IOP Conference Series: Materials Science and Engineering', Vol. 50, IOP Publishing, p. 012037.

Sofonea, V., Lamura, A., Gonnella, G. & Cristea, A. (2004), 'Finite-difference lattice boltzmann model with flux limiters for liquid-vapor systems', *Physical Review E* **70**(4), 046702.

Sterling, J. D. & Chen, S. (1996), 'Stability analysis of lattice boltzmann methods', *Journal of Computational Physics* **123**(1), 196–206.

Succi, S. (2001), *The lattice Boltzmann equation: for fluid dynamics and beyond*, Oxford university press.

Sukop, M. (2006), *DT Thorne, Jr. Lattice Boltzmann Modeling Lattice Boltzmann Modeling*, Springer.

Sun, D. & Tao, W. (2010), 'A coupled volume-of-fluid and level set (voset) method for computing incompressible two-phase flows', *International Journal of Heat and Mass Transfer* **53**(4), 645–655.

Swift, M. R., Orlandini, E., Osborn, W. & Yeomans, J. (1996), 'Lattice boltzmann simulations of liquid-gas and binary fluid systems', *Physical Review E* **54**(5), 5041.

Swift, M. R., Osborn, W. & Yeomans, J. (1995), 'Lattice boltzmann simulation of nonideal fluids', *Physical review letters* **75**(5), 830.

Takada, N., Misawa, M., Tomiyama, A. & Fujiwara, S. (2000), 'Numerical simulation of two-and three-dimensional two-phase fluid motion by lattice boltzmann method', *Computer Physics Communications* **129**(1-3), 233–246.

Taylor, G. I. (1950), 'The instability of liquid surfaces when accelerated in a direction perpendicular to their planes. i', *Proceedings of the Royal Society of London. Series A. Mathematical and Physical Sciences* **201**(1065), 192–196.

Thürey, N., Körner, C. & Rüde, U. (2005), 'Interactive free surface fluids with the lattice Boltzmann method', *Technical Report05-4. University of Erlangen-Nuremberg, Germany* .

Thürey, N. & Rüde, U. (2009), 'Stable free surface flows with the lattice Boltzmann method on adaptively coarsened grids', *Comput. Visual. Sci.* **12**(5), 247–263.

Tölke, J. (2002), 'Lattice boltzmann simulations of binary fluid flow through porous media', *Philosophical Transactions of the Royal Society of London. Series A: Mathematical, Physical and Engineering Sciences* **360**(1792), 535–545.

Torrey, M. D., Cloutman, L. D., Mjolsness, R. C. & Hirt, C. (1985), NASA-VOF2D: a computer program for incompressible flows with free surfaces, Technical report, Los Alamos National Lab., NM (USA).

Tryggvason, G., Bunner, B., Esmaeeli, A., Juric, D., Al-Rawahi, N., Tauber, W., Han, J., Nas, S. & Jan, Y.-J. (2001), 'A front-tracking method for the computations of multiphase flow', *Journal of computational physics* **169**(2), 708–759.

Viggen, E. M. (2009), 'The lattice Boltzmann method with applications in acoustics', *Master's Thesis, NTNU Trondheim, Norway* .

Xu, A. (2005), 'Finite-difference lattice-boltzmann methods for binary fluids', *Physical Review E* **71**(6), 066706.

Yu, D., Mei, R., Luo, L.-S. & Shyy, W. (2003), 'Viscous flow computations with the method of lattice Boltzmann equation', *Progress in Aerospace Sciences* **39**(5), 329–367.

Yu, Y., Chen, L., Lu, J. & Hou, G. (2014), 'A coupled lattice Boltzmann and particle level set method for free-surface flows', *ScienceAsia* **40**(3), 238–247.

Yu, Z., Fan, L.-S. et al. (2010), 'Multirelaxation-time interaction-potential-based lattice boltzmann model for two-phase flow', *Physical Review E* **82**(4), 046708.

Zhao, Y. (2008), 'Lattice Boltzmann based PDE solver on the GPU', *The visual computer* **24**(5), 323–333.

Zhao, Z., Huang, P., Li, Y. & Li, J. (2013), 'A lattice boltzmann method for viscous free surface waves in two dimensions', *International Journal for Numerical Methods in Fluids* **71**(2), 223–248.

Zheng, H., Shu, C. & Chew, Y.-T. (2006), 'A lattice boltzmann model for multiphase flows with large density ratio', *Journal of Computational Physics* **218**(1), 353–371.

Zou, Q. & He, X. (1997), 'On pressure and velocity boundary conditions for the lattice Boltzmann BGK model', *Phys. Fluids.* **9**(6), 1591–1598.

Zu, Y. & He, S. (2013), 'Phase-field-based lattice boltzmann model for incompressible binary fluid systems with density and viscosity contrasts', *Physical Review E* **87**(4), 043301.